Université de Montréal

A FOUR DIMENSIONAL SPATIO-TEMPORAL EMG MAPPING TECHNIQUE FOR STUDY OF THE NEURO-MUSCULO-SKELETAL SYSTEM

by

Enrique J. de la Barrera

Département de Chirurgie

Faculté de médecine

Thèse présentée à la Faculté des études supérieures
en vue de l'obtention du grade de
Philosophiae Doctor (Ph.D.)
en sciences biomédicales

Novembre, 1997

Université de Montréal
Faculté des études supérieures

Cette thèse intitulée :

A FOUR DIMENSIONAL SPATIO-TEMPORAL EMG MAPPING TECHNIQUE FOR STUDY OF THE NEURO-MUSCULO-SKELETAL SYSTEM

Présentée par :

Enrique J. de la Barrera

a été évaluée par un jury composé des personnes suivantes :

Dr. Bertrand Arsenault, Ph.D. ……………….. président du jury

Dr. Charles-Hilaire Rivard, m.d. ……………. directeur de recherche

Dr. Morris Duhaime, m.d. ………………….. codirecteur de recherche

Dr. Michel Bertrand, Ph.D., ing. ……………... membre du jury

Dr. Serge Roy, Ph.D., ……………………… examinateur externe

Dr Pierre Mathieu, D.SC.,............................... representant du doyen

Thèse acceptée le : 02.11.1998

Université de Montréal
Faculté des études supérieures

Cette thèse intitulée :

A FOUR DIMENSIONAL SPATIO-TEMPORAL EMG MAPPING TECHNIQUE FOR STUDY OF THE NEURO-MUSCULO-SKELETAL SYSTEM

Présentée par :

Enrique J. de la Barrera

a été évaluée par un jury composé des personnes suivantes :

Dr. Bertrand Arsenault, Ph.D. ………………… président du jury

Dr. Charles-Hilaire Rivard, m.d. …………… directeur de recherche

Dr. Morris Duhaime, m.d. …………………… codirecteur de recherche

Dr. Michel Bertran, Ph.D., ing. ……………… membre du jury

Dr. Serge Roy, Ph.D., ………………………… examinateur externe

Dr. Pierre Mathieu, D.Sc. ing. ……………… représentant du doyen

Thèse acceptée le : 3 de décembre de 1998

SUMMARY

A comprehensive description of human movement (HM) as a multi-dimensional process, with its implicit narrative aspects, is still some ways off from the present modeling of the neuro-musculo-skeletal system (NMSS). Three main factors responsible for this situation are identified as: the current changing views on the mechanisms of the central nervous system; the lack of visual image to the behavior of NMSS; and the ongoing re-conceptualization of movement and posture. This thesis proposes to reconsider the NMSS as a non-linear open system. From this point of view, HM can be regarded in terms of action development with posture playing a fundamental role in the elaboration of adaptability during movement execution.

The main working hypothesis assume that multi-dimensional features of actions movement can be characterized from a spatio-temporal electromyographic (EMG) patterns of muscle activation. The problem is then defined as the production of a dynamic internal image of the ensemble of muscle activities involved in action development in such a way that, both global and individual, EMG patterns can be elucidated.

The solution proposes the generation of a spatio-temporal mapping image of muscle activity coupled with movement cinematic image. This implies a simultaneous measurement of the potential distribution on the skin surface and movement dynamics. However, this type of EMG measurement requires an electrode capable of recording high fidelity signals from local muscle activity. Since transient noises exist within the SEMG signal's bandpass, these must be suppressed at the detection stage.

The solution was found in the selectivity properties of the spatial filtering technique induced by the construction of a Laplacian discrete function, and developed from the point of view an optimal electrode's geometrical configuration, such as found on a Laplacian electrodes. While Laplacian electrodes have been reported to enhance selectivity, the conditions under which this type of measurement might be valid remain uncertain.

To this end, the selectivity assumption was confirmed by means of a theoretical analysis, and the requirements for the validity of an EMG Laplacian measurement were defined. In addition, the sensitivity to disturbances related to skin/electrode interface, as well as the selectivity, sensitivity and stability dependence of the Laplacian spatial filter to changes in action potential (AP) conduction velocity (CV) were investigated and confirmed by means of physiological experiments.

The technique was implemented and validated by means of a physiological experiment of the lower leg performing an ergo-cycle. In view of the fact that only twelve Laplacian electrodes were available and that the performed movement is cyclic, it was possible to devise a 2-D "virtual array" of 12 by 17 electrodes. This procedure permitted the averaging of surface EMG (rms wise) and motion data; thus, producing the most likely representation of the phenomenon through a single cycle. Data collected under controlled slow and rapid speed conditions permitted a comparative analysis of the strategies used by the CNS in development of distinctive spatio-temporal pattern of muscle activation. From the analysis of the results, a movement functional programming mechanism is manifested in a spatio-temporal EMG pattern of muscle activation and these patterns are task specific.

RÉSUMÉ

Le monde biomédical ressent actuellement un besoin urgent d'outils nouveaux donnant accès à une description quantitative des mécanismes fonctionnels et opérationnels du système neuro-musculo-squelettique (SNMS). De tels outils ont plusieurs applications pertinentes à l'analyse multidimensionnelle du mouvement humain; particulièrement en médecine en permettant d'établir une représentation objective et analytique du schéma corporel du patient selon le processus pathologique en cause, les thérapeutique et les pronostics envisagés. Cependant les diverses méthodes et techniques de mesure actuellement utilisées doivent apporter une analyse plus réaliste des modèles de représentation du SNMS. Une description analytique de mouvement humain en tant que processus multidimensionnel présentant ses aspects les plus variés et implicites est encore de l'ordre du concept. Une série d'arguments analytiques est présentée dans le Chapitre I afin de décrire les raisons expliquant cette situation. Les principaux facteurs responsable de cette situation y sont identifiés. Il s'agit des changements d'optique actuels quant au fonctionnement du système nerveux central (SNC), du manque de représentation visuelle du SNMS; et du devenir de la re-conceptualisation du mouvement et de la posture.

Cette thèse repose sur les conclusions de cette discussion ainsi que sur l'approche scientifique moderne du phénomène (par laquelle maintenant le phénomène peut raconter sa propre histoire). Le SNMS est alors considéré comme un système non-linéaire et en boucle ouvert, échangeant continuellement information et énergie avec les environnements interne et externe. De ce point de vue, le mouvement humain peut être considéré comme un développement d'actions -- plutôt que comme le développement du mouvement -- où la posture joue un rôle fondamental dans l'élaboration de l'équilibre et dans l'adaptation du système aux conditions internes et externes pendant l'exécution du mouvement.

Les hypothèses principaux de cet travail sont relié au fait que les électrodes Laplaciennes ne sont pas caractérisées par un filtre présentant une fonction de transfert équivalente à celle d'une électrode double différentielle et que l'élaboration d'une image dynamique de l'ensemble des activités musculaires est possible a partir d'une mesure Laplacienne de la distribution de potentiel de surface représentant des activités musculaire localisé.

Le but principal de cette thèse peut être ainsi défini comme étant l'élaboration d'une image dynamique interne de l'ensemble des activités musculaires impliquées dans le développement de l'action de telle façon que les patrons d'activation EMG, dans leur globalité et/ou individuellement, puissent être élucidés et analysés.

De façon à introduire les différents aspects décrits du phénomène, la solution proposée a consisté en la création d'une cartographie spatio-temporelle de l'activité musculaire couplée à la description cinématique du mouvement étudié. Les données spécifiques, nécessaires à la construction de cette image dynamique peuvent être obtenues en effectuant des mesures simultanées de la distribution de potentiel électrique enregistré à la surface la peau et de l'analyse du mouvement. Ce type d'EMG de surface (SEMG) requiert un type d'électrode pouvant enregistré un signal de haute fidélité, représentant l'activité locale musculaire, et épuré des bruits transitoires.

La description de la physiologie musculaire et des propriétés du volume conducteur, présentée au Chapitre II, laisse voir que le signal SEMG produit est aléatoire. Ce signal est également dénaturé de part la position relative de l'électrode en fonction de l'orientation des fibres musculaires; de part la position des points d'innervation; de part la polarité directionnelle des potentiels d'action; ainsi que de la présence de signaux non-propagés. Ces contraintes, regroupées sous l'appellation « bruits transitoires », existent dans la bande passante du signal SEMG. Il est donc quasiment impossible de filtrer ce bruit lorsqu'il est enregistré. Il doit donc être supprimé dès la détection du signal. La solution envisagée est basée sur les propriétés sélectives de la technique de filtrage spatial associées à l'élaboration d'une fonction Laplacienne discrète. Ce principe de détection sélective, épurée du bruit transitoire, fut développée en manipulant la géométrie de l'électrode.

Le Chapitre III est constitué des diverses étapes essentielles au développement d'une configuration géométrique optimale de l'électrode. Cette dernière prend une forme concentrique ou Laplacienne. Cependant, même si les électrodes Laplaciennes possèdent une plus grande sélectivité, les conditions d'application sous lesquelles ce type de mesure demeure valide sont imprécises. Le principal argument est relié au fait que les électrodes Laplaciennes semblent être caractérisées par un filtre présentant une fonction de transfert équivalente à celle d'une électrode double différentielle (configuration tripolaire) qui ne considèrent pas l'effet perturbant d'une zone d'équipotentiels rapprochés près de l'électrode. De façon à valider cette propriété de sélectivité, une analyse mathématique comparative de l'effet d'intégration spatiale reliée à la surface de l'électrode sur le SEMG (considérant la contribution d'une zone d'équipotentiels rapprochés) fut effectuée, pour des électrodes monopolaire, bipolaire, double différentielle et concentrique. Cette analyse théorique a permis de confirmer cette prémisse sur la sélectivité de l'électrode Laplacienne en plus d'identifier les conditions d'application valides pour une telle mesure EMG. Par comparaison avec la double différentielle, les principaux avantages de la configuration Laplacienne tiennent à l'obtention d'une image plus précise de la source émettrice ainsi qu'à un effet négligeable de la polarité du signal et de l'orientation des fibres musculaires. Il fut également précisé que la fonction de transfert de l'électrode Laplacienne possède un facteur d'amplification très faible (moins de 1.5) lorsque comparée à une électrode double différentielle (gain de 16). Ce résultat soulève d'autres questions en regard de la sensibilité du filtre face aux variables reliées à la dimension temporelle, variables pouvant affecter sa forme et sa performance en terme de sélectivité. De plus, à cause de son faible gain et de la pondération relativement importante du centre de l'électrode, cette dernière est probablement plus sensible aux perturbations affectant la condition de l'interface peau/électrodes, ce qui engendrerait un ratio signal/bruit (RSB) moins intéressant.

Cette sensibilité des électrodes Laplaciennes aux perturbations de l'interface peau/électrode, de même que sa dépendance aux changements de vitesse de conduction (VC), en terme de sélectivité, de sensibilité et de stabilité, furent étudiées lors d'études physiologiques présentées au Chapitre IV. Des signaux SEMG furent recueillis simultanément avec une matrice d'électrodes Laplaciennes et bipolaires. Les caractéristiques temporelles ainsi que fréquentielles des signaux filtrés "spatialement" purent ainsi être comparées aux signaux filtrés par l'électrode bipolaire. Pour ce faire, le niveau de bruit à la surface de la peau fut enregistré chez 5 sujets, pendant une durée de deux secondes. Ces enregistrements furent effectués au début et à la fin de la session expérimentale. Des potentiels d'action provoqués par stimulation furent également enregistrés simultanément à l'impulsion électrique inductrice. Ces données furent utilisées pour vérifier la fonction de transfert des filtres tel que développé théoriquement ainsi que pour évaluer le RSB des électrodes. De plus, le SEMG ainsi que les données de force furent enregistrés pour des conditions expérimentales exigeant des contractions en rampe, des efforts en paliers ou des contractions isométriques et volontaires conduisant à la fatigue. Ces données furent corrélées aux événements neurophysiologiques impliquant l'activation de différents types de fibre musculaire générant et contrôlant la force requise. Les résultats montrent que les électrodes Laplaciennes atténuent de façon similaire le bruit et le signal et, que malgré une faible amplification, un bon RSB peut être obtenu si l'interface peau/électrode est de bonne qualité. L'aire de l'électrode centrale doit également être augmentée pour obtenir un signal représentatif des activités musculaires locale. Les fonctions de transfert théoriques semblent représentatives de celles calculées à partir des données expérimentales. La sensibilité et la sélectivité des électrodes Laplacienne à l'information locale confirment que la configuration Laplacienne exprime les caractéristiques d'un filtre passe-haut. De plus, les signaux obtenus à partir des électrodes bipolaires et Laplacienne partagent le même contenu fréquentiel, se différenciant uniquement en fonction de la distribution de ces fréquences. Ainsi, la sensibilité et la sélectivité des électrodes Laplaciennes à l'information locale sont évidentes de part la pondération accrue des composantes de haute fréquence, validant ainsi sa capacité à produire une image plus précise de la source locale sans interférence des bruits transitoires. Finalement, les électrodes Laplaciennes apparaissent comme très stables lors des variations de vitesse de conduction.

Au Chapitre V, la technique de cartographie spatio-temporelle électromyographique est développée, mise en application et validée. Cette technique consiste à mesurer les potentiels de surface en utilisant une matrice d'électrodes Laplaciennes en synchronisation avec une mesure stéréovidéographique de la cinématique du mouvement. La position spatiale de chaque électrode formant la matrice est obtenue en utilisant un numérisateur 3D par champs magnétiques (Flock of Bird). Ces coordonnées sont ensuite utilisées pour former un maillage tri-dimensionnel et construire une représentation visuelle tri-dimensionnelle de la surface anatomique explorée. Une cartographie de la distribution du potentiel est établie en interpolant les données EMG entre les points de collecte du signal à un instant précis, formant ainsi une « coupe » temporelle de l'activité musculaire. Une séquence de ces coupes temporelles peut être produite et superposée à la représentation 3D de la surface anatomique, formant ainsi une vue dynamique des activités musculaires. Finalement, cette vue dynamique est synchronisée avec les données dynamiques du mouvement pour former une représentation 4D du SNMS. La contribution individuelle de chaque muscle, en intensité et en durée d'activité, peut ainsi être identifiée à chaque étape du mouvement. La direction de propagation de la distribution du potentiel d'action permet d'identifier la direction des vecteurs de force selon les différents repères anatomiques du segment étudié. La stratégie fonctionnelle et opérationnelle du CNS peut alors être approchée et interprétée par la lecture des patrons spatio-temporels d'activation musculaire.

Cette technique fut appliquée et validée lors d'une étude physiologique de la jambe lors de mouvements réalisés sur une bicyclette stationnaire. Bien que seulement 12 électrodes Laplacienne furent disponibles pour cette évaluation, il fut possible d'obtenir une "matrice virtuelle" de 12 par 17 électrodes Laplacienne en considérant le mouvement étudié comme cyclique et hautement répétitif. Cette procédure permit d'obtenir une représentation EMG (rms) et cinématique moyenne hautement représentative des phénomènes au cours d'un cycle typique du mouvement. L'enregistrement des données pour une vitesse de pédalage lente et rapide permit une analyse comparative des stratégies utilisées par le SNC pour l'élaboration de divers schémas ou patrons spatio-temporels d'activation musculaire. Il semble évident, à partir de l'analyse des résultats, que le mécanisme de programmation de l'effectivité du mouvement est représenté par un tracé électromyographique spatio-temporel de l'activation musculaire et que ce tracé est spécifique de la nature de la tâche réalisée.

TABLE OF CONTENTS

Chapter One : **NEURO-MUSCULO-SKELETAL MOVEMENT**

Chapter Two : **ELECTROMIOGRAPHY**

Chapter Three : **ELECTRODE SPATIAL FILTERING SYSTEM**

Chapter Four : **BIPOLAR CONCENTRIC ELECTRODE`S EXPERIMENTS**

Chapter Five : **SPATIO-TEMPORAL EMG MAPPING TECHNIQUE**

LIST OF TABLES

LIST OF FIGURES

LIST OF ACRONYMS AND ABBREVATION

A/D	Analog to digital
AP	Action potential
APO	Ankle point object
ARMA	Auto-regressive moving average

BCE	Bipolar concentric electrode
BLE	Bipolar linear electrode
CNS	Central nervous system
CV	Conduction velocity
DFT	Discrete Fourier transform
EEG	Electroencephalography (electroencephalogram)
ECG	Electrocardiography (electrocardiogram)
EMG	Electromyography (electromyogram)
FFT	Fourier transform
FPO	Foot point object
HM	Human movement
HPO	Hip point object
IVC	Isometric voluntary contraction
KPO	Knee point object
LBCE	Large bipolar concentric electrode
LMSRL	Least mean square regression line
MDF	Median frequency
MNF	Mean frequency
MS	Motor system
MSS	Musculo-skeletal system
MU	Motor unit
MVC	Maximal voluntary contraction
MUAP	Motor unit action potential
NMS	Neuro-muscular system
NMSS	Neuro-musculo-skeletal system
PDF	Probability density function
PSD	Power spectrum density
PPO	Pedal point object
RMS	Root mean square
SBCE	Small bipolar concentric electtrode
SEMG	Surface electromyography (electromyogram)
SNR	Signal to noise ratio

"Namer of the thousand names, maker of meanings, transformer of the world, your parents and the parents of your parents continue in you. You are not a fallen meteor, but a brilliant shooting star launched towards the skies. You are the meaning of the world, and when you clarify your meaning you illuminate the earth. When you lose your meaning, the earth becomes darkened and the abyss opens."

Silo

To

Xochilt,
Francisco, Marianella
Paola

« Toi qui donnes milles noms, toi qui donnes du sens, toi qui transformes le monde, tes pères et les pères de tes pères se perpétuent en toi. Tu n'es pas un bolide qui tombe, mais une brillante flèche qui vole vers les cieux. Tu es le sens du monde et, quand tu clarifies ton sens, tu illumines la terre. Lorsque tu perds ton sens, la terre s'obscurcit et l'abîme s'ouvre. »

Silo

ACKNOWLEDGEMENTS

Very seldom one has the chance to thank the people who have contributed to our formation and growth in life. First, I would like to take this unique opportunity to publicly thank my parents and ancestors for opening my future, for encouraging me to follow my passions and showing me a way to give life a meaning. Their presence, although no longer in this world, have been with me as the inspiration and guiding light in the creative work of this thesis. Also, this work reflects the generous effort and support of a long list of people who have made materially possible to be accomplished it.

My special thanks go to my advisor and friend Dr Charles-Hilaire Rivard; his support, trust and patience have been proven in many ways, not only by giving me ample freedom in my work, but also by providing with wise advice, a working environment and living resources when I most need them. I also like to thank Dr Christine Coillard for those many long illuminating conversations on anatomy, neuro-musculo-skeletal pathologies and our favor crazy theme, so fundamental in this thesis, chaos! I am grateful to my good friend and colleague Dr Michel Lereoux for helping with the dynamic experimental set-up and protocols, and his moral support. I also must thank Dr Daniel Bourbonnais, from the IRM.

My thanks also go to my family, also a main source of energy, hope and inspiration in this work, especially my little one Xochilt, Paola, Marianella, Francisco and Dinath for their support and encouragement. Very special thanks also go to my partner Nathalie Alos, who has been by my side all through the good and bad moments, always encouraging and supporting me in all the thinkable possible ways; I do know we share the pride of this work. Thank also to my good friend Brenda Lee for her supportive friendship and for helping me with the tedious work of proof reading and corrections.

I like to thank Jerome Deziel and Daniel Marineau from the IRM, for lending their facilities in the construction of the concentric electrodesFinally, I like to thank the friends at the Hopital Ste Justine for their co-operation in the development of this thesis, particularly Johanne B, Linda, Andre.

FOREWORD

The current technical interest in, and fascination with, human movement has, in fact, a long multi-faceted history. From Aristotle (384-322 B.C.) to Bernstein (1967) the phenomenon of human movement has been studied and reported from a number of points of view and diverse interests. In this endeavor, the analytical tools have ranged from pure logic to mathematical modeling. Current models are nowadays assisted by the most sophisticated computer technology and scientific advances in the various related fields. Consequently, the battery of knowledge accumulated on human movement has increased both in quantity and quality with interest now being emphasized, more and more, on its practical application. Although such new insights have rich import for the study of human movement, and their practical applications have contributed enormously to the improvement of the quality of human life, they have also introduced new complications.

Most modern models have taken reductionist principles to a high degree of complexity. They have thus become very specialized in particular aspects of human movement but unable to explain concomitant and structural features of the same phenomenon, such as planning, generation, control and co-ordination of multi-joints movement and posture. This specialization is now under challenge. Increasingly, scientists from a variety of disciplines concerned with the study of human movement are no longer able to limit their scope to the principles of their own field, (i.e.: mechanical, physiological, behavioral). Nowadays scientists are beginning to consider the meaning and significance of "neuro-musculo-skeletal movement". The human being is now understood as a plastic being whose movements not only allow him to continuously adapt himself to dynamic changes in his internal and external environments but also to modify simultaneously his environment and his own psycho-physic structure with his actions. From this point of view, it is evident that the limited scope of any one field of principles will reveal only a fraction of the entire spectrum of human movement.

The framework, subject and objective of this thesis were inspired by this new scientific vision, a vision which has been the product of a slow shift from the classical geometrical-mechanical view to a description of nature in which the narrative element is essential.

Natural phenomena, such as human movement, now "tell us their history". We now know that most phenomena in nature are non-linear open systems whose dynamic is developed as a concomitant and structured process. But to include these new narrative aspects in our description of nature we require new tools, and new views of space and time.

The concrete subject of this thesis is a technology which permits the integration of its parameters: a new type of electromyography that displays a visual image of the multidimensional process of the neuro-musculo-skeletal system. This technology acts both to raise and to focus arguments for such interrelated topics as "normal movement", "posture and movement", "static and dynamic equilibrium", "patterns of movement", "movement as a dynamic adaptive response to changing conditions" and "changes in patterns of movement related to status of the system".

And so, while this thesis is oriented around a novel kind of electromyography, its larger objective is twofold: first to present some basic arguments that allow us to reconsider the neuro-muscular and musculo-skeletal systems as one non-linear open system, and second, to begin to develop the tools (or conditions) that will empower an understanding of human movement as a multidimensional process with implicit narrative aspects. This thesis therefore functions within but is not about the study of human movement, and its functional anatomy or neurophysiology. It is about, rather, some specific technical tools that will allow production of a "dynamic internal image" of the neuro-musculo-skeletal process which is involved in the generation, control and coordination of human movement.

The specific contribution of this thesis is therefore its furtherance of a concrete mapping of the muscles activity process and investigative frame of reference for the neuro-musculo-skeletal system.

CHAPTER ONE

NEURO-MUSCULO-SKELETAL MOVEMENT

1.1 INTRODUCTION

Traditionally, the various specific disciplines such as neuro-physiology, functional anatomy, motor control, motor behavior, kinesiology, electromyography and biomechanics have specialized in particular aspects of HM. These disciplines, while differing in approach and particular interest, are mostly complementary and have thus contributed to an inter-disciplinary understanding of the general phenomenon of HM. In fact, some such as biomechanics and electromyography have often lent themselves as general analytical or validation tools. In short, none is an isolated science, sufficient unto itself in methods, knowledge or contribution, but rather together they have generated the composite science of HM. In spite of its unifying action this new science is today found in a transition stage. Three fundamental factors account for this situation.

First, scientists from different fields now increasingly share the view that traditional theories on HM are based upon assumptions that are not longer tenable and that the predictions deriving from these theories have, somehow, been falsified by recent findings about movement and posture (Cordo, 1990; Reed, 1989, 1990; Rothwell, 1994; Winter, 1985). This is, of course, a controversial claim and therefore deserves a scrutiny which is beyond the scope of this thesis. However, what is not controversial is that perspectives on movement and posture are undergoing considerable change and that a new understanding is emerging to replace a number of traditional views. The particular group of traditional assumptions under revision concern the idea that the central nervous system (CNS) is an input/output mechanism and that motor responses are generated in a hierarchical chain command.

Second, the lack of a visual representation to the behavior of the neuro-musculo-skeletal system (NMSS) has made difficult to establish a direct relationship between the central command (CNS) and the motor system (MS) during the process of planning, generation, co-ordination and control of movement. Many biological systems (i.e. cardiovascular) do lend themselves to study in vivo and therefore to direct measurement of forces acting on it and/or within it. However, in the case of the neuro-musculo-skeletal system, due to ethical considerations and the difficulty of controlling the many variables involved, the acting forces can not be measured directly (i.e. by means of force transducers and/or implanted electrodes). Even the use of animal models is limited here, because no other species has an anatomy that is both structurally and functionally similar to that of humans and used in a comparable manner. For these reasons, muscle actions are estimated using non-invasive methods, such as electromyogram (EMG) and/or mathematical models (single joint system). Both of these methods have proved to be insufficient to establish a direct dynamic relationship between the central nervous system and the motor system.

Third, there is an increasing need for practical application of the new emerging hypothesis on posture and movements (clinical implementation). This need is viewed currently not so much as a response to the pragmatic economic tendency of science for survival, but rather as a response to the pressing need to validate or test many of new germinating perspectives on posture and movement. This is particularly true for those assumptions concerning the adaptive developmental stages of posture and movement (i.e., infancy, puberty). The need for implementation and/or validation of the emerging hypothesis, (which today can be found in most fields of science), has given a more predominant role to applied research, especially in the medical field, where clinical and therapeutic applications are in great demand.

These three main factors -- the ongoing change of view on movement and posture, the lack of visual feed-back on the behavior of NMSS and the need for applied research -- are all implicit in the vast range of questions today surrounding the theme of "neuro-musculo-skeletal movement", and they shall therefore be considered the research framework of this thesis.

They each derive naturally from an analysis of the historical background of the human movement sciences, they are inter-related, and will be tacitly implicated throughout the work that constitutes this thesis.

1.2 HISTORICAL BACKGROUND

Most ideas of HM were developed intuitively by the great neurologists of the last century, such as Duchenne, Beevor, Jackson, Sherrington and Huxley. These ideas remain essentially the same today, even when dressed up in the latest scientific and technological jargon. In fact these fundamental ideas, which have stemmed from the main concept of chain command, are the only justification for treating the various areas of the NMSS separately in a discussion and investigation of HM. Descartes (1649) took great effort to demonstrate that human actions were either mechanical responses to stimuli or voluntary responses to commands issued from the mind or brain. A few years later, Borelli (1685) published his "De Motu Animalium", perhaps known as the first biomechanical analysis approached from a mathematical point of view. But, it was Newton (1686) who laid the foundation of modern dynamics with his "Principia Mathematica Philosophiae Naturalis".

From these dualistic theories, based on a causal point of view, emerged the experimental procedures to study reflex responses in decorticated animal models as well as the bases of theoretical motor control and biomechanical models. This legacy, while including a great deal of knowledge, has also begotten the assumption that there are some particular tasks or aspects of movement that each area of the CNS is best adapted to control, whether by virtue of its anatomical connections with other areas or because of the peculiarities of its internal circuitry. Traditionally, theories supporting the various disciplines involved in human movement sciences have thus assumed that motor behavior is built up out of mechanistic units that are expressed in relatively unchanging forms in different actions, units such reflexes and central pattern generators. This has been essentially a reductionist approach and follows naturally from analysis of hierarchical control. So in the hierarchy of structures that sub-serves motor functions, the spinal cord forms the lowest level, with the brain stem and the cerebral cortex forming the higher levels. However, later findings (Rothwell, 1994) suggest that each of these higher levels contains several anatomically distinct areas that project in parallel to the spinal cord. In fact, a characteristic feature of most these areas is that, like the sensory system, they are organized in a somatotopic fashion -- movements of adjacent body parts, controlled by neighboring parts of each area of the brain. Thus, the motor cortex contains a complete motor map of the body just as the nearby somatic sensory cortex contains a complete map of the body surface. According to Rothwell (1994), there are two associated structures, the cerebellum and the basal ganglia, which are not involved directly in producing movement, but seem to modulate the corticospinal and the brain stem systems that control the motor neurons and related spinal inter-neurons. Finally, based on the above arguments it could be proposed that since internal state variables exist at different hierarchical levels in the NMSS, the kinematics of movement might be conceptualized as emerging from: a structured and concomitant interaction between top-level commands; various internal states; and kinetic as well as informational coupling to/from environment. It is evident here that what is undergoing change is a conceptual scientific model, that is, the sphere of mental preconceptions that have structured the observance of empirical phenomena

1.2.1 The Neuro-Musculo-Skeletal System

The NMSS can be described as the actuator and effector system of a structure which is in continuous and simultaneous interaction with its internal and external environment. The function of this system is to bring about movement of the body in part and as a whole while adapting the responses to new conditions in order to maintain the homeostasis. In addition, the system provides protection for the body and its other organ systems. Normal functioning of the system can be described as the type of adaptive behavior which allows the structure to maintain its integrity while developing itself in a continuous interaction with its environment. The best adaptation is that which is achieved with the lest resistance from the environment, the least effort in work and the minimum energetic waste. These functional requirements are essentially reflected in the unique properties of the tissues that constitute the component parts of system, and the manner in which these parts are put together into functional sub-units and set into action by the nervous system. This is manifested by: the various degrees of rigidity and resilience found in bone, cartilage, ligament and tendon; the contractile properties of the muscle; the conductive properties of the nerve; and the afferent/efferent circuitry connecting the central nervous system with the proprioceptive apparatus and the peripheral nervous system. In short, it seems evident that the integral analysis of HM can not be restricted to a simple study of single and/or multiple joint systems. That is, a study of the multi-dimensional process of planning, generation, co-ordination and control of movement must also take into account the "functional and operational relationship" between the skeletal segments in motion, the muscles that produce the motor force and a nervous system controlling the movement, and the condition and status of the system within its internal/external environment.

This is indeed an extremely complex problem, as well as a very ambitious enterprise, one that scientists from different fields have being dealing with for centuries. Historically scientists have simplified the problem by breaking the NMSS into two sub-systems, the neuro-muscular and the musculo-skeletal systems, thus originating the two basic disciplines, neurophysiology and biomechanics. However, as discussed, the breadth and complexity of the field caused these disciplines to fragment into many sub-disciplines, each evolving and specializing in particular aspects of HM. Today, scientists from the component disciplines are attempting to subsume their specialty under the title of "movement sciences". The category and scope of these subsumed disciplines is not quite clear yet, since they overlap in many aspects of their research and often lend support to each other as models and/or validation tools.

For purposes of analysis here, we will recognize here two main disciplines that deal with the neuro-muscular system (NMS) and the musculo-skeletal system (MSS); they are respectively motor control and kinesiology. Motor control concerns itself with the behavioral and physiological aspects of programming, preparation and generation of movement and therefore, with problems such as stability, adaptation, co-ordination, regulation of movements.

Kinesiology, on the other hand, concerns itself with functional anatomical and biomechanical aspects of movement performance, and therefore with biomechanical responses to movement which must obey the physical laws of mechanics such gravity, reactive forces, strength, tonus, stress, strain, etc. Both disciplines essentially deal with the same fundamental problem, namely, the functional relationship between the central command (CNS) and the skeletal segments in motion, where the role of muscular system (MS) is not only viewed as the actuator and effector of motion, but also as the actual dynamic link between the central command and the skeletal structure. The problem is thus reduced to measurement of the muscle activity, (forces), involved in the motor control strategies that are responsible for the biomechanical behavior of motion (and posture). In this sense, motor control deals with the forward problem and kinesiology deals with the inverse problem. However, since in-vivo internal forces and moments at a joint are difficult to measure directly, several methods have been developed to estimate muscle force.

1.2.2 Estimation of Muscle Force

Muscle force has traditionally been estimated through electromyogram (EMG) and/or mathematical models. Both of these methods have complications of their own. The EMG/force conversion is not always linear and differs from muscle to muscle. Mathematical models, on the other hand, are highly indeterminant and many assumptions have been necessary to simplify them. Furthermore, EMG is often used to drive or validate mathematical models, and this raises serious concerns about the reliability of some of the neurophysiological, anatomical and biomechanical assumptions which they have made. In spite of these complications, great advances have been made by these methods in understanding the many variables involved in estimating muscle force, in defining the role and function of muscles in the equilibrium, and in the loading of single and multiple joint systems. Some of the primary advantages and disadvantages of these methods, considering the synergistic and antagonist muscles participating in the loading of the system, are discussed below.

The integrated EMG (IEMG) has been used to quantify the level of activity of muscles and to assess muscle function in the absence of maximal voluntary contraction, (MVC). The technique consists in simultaneously measuring the reactive force or torque produced by the joint system and the EMG activity of those muscles that are thought to contribute to the responsive force. Normally measurements are performed under isometric conditions. The relationship between the generated force and the IEMG is established using linear regression methods. The resulting EMG-to-force conversion function is then approximated. This relating function is not always linear and often researchers have obtained different relationships according to the method used, (Perry and Bekey, 1981; Woods and Bigland-Ritchie, 1983; Solomonow et al., 1987; Stokes et al. 1987). Discrepancies in results may lay in the fact that EMG-force relationship is dependent upon metabolic, functional, structural and control properties of the muscle (i.e., muscle state, size and length, fiber composition, motor unit recruitment, firing rate, etc.). Furthermore, surface EMG (SEMG), although providing global information on muscle activity, is not limited to anatomical borders and is thus sensitive to distortions of the electric current field in the volume conductor. Moreover, the system is mechanically redundant (there are more muscles than it is needed to perform a task); consequently a single specific force acting on a skeletal joint or segment can be generated by an infinite combination of muscles forces (Van Eijden et al., 1990; Zajac, 1993). Also a particular muscle can generate a particular force in many different fashions in response to the demands of the system and therefore the EMG activity level might not be fully representative of the force level, (Zuk, 1962; Woods and Bigland-Ritchie, 1983). For instance, Solomonow et al. (1987) in a study of slow and fast twitch muscles (soleus and gastrocnemius) found that for the soleus, the EMG/force curves were linear in first 50 to 70% of MVC and non-linear for the remainder up to 100% of MVC. All motor units were fully recruited by the time the initial 30 to 40% of the MVC was reached and the rest of the force was achieved by the firing rate increase. The gastrocnemius on the other hand recruited all the units to obtain the initial 50% of MVC in a linear fashion and rest of the force was obtained by progressive increase of firing rate in a non-linear manner.

Biomechanical models are also used to calculate the forces in a joint system, (trunk and limbs), by considering the balance between external loads, body weight loads and the muscle force required to maintain equilibrium. The purpose of these models is at least two-fold: to analyze the nature, distribution and magnitude of forces exerted through the joint system and to predict the changes in stress that might occur in various postures and activities. Mathematical formulations predicting muscle, ligament and joint forces usually involve solution of an inverse dynamics problem, followed by solution of a distribution problem. In this, there are at most six equations of equilibrium (three force and three moment equations) to be satisfied, but there are far more than six muscle forces to be computed. Normally, reactive forces and moments are calculated by the partitioning technique, which consists in partitioning the reaction force and moments at a given level into restorative tissue components and calculating the size of compression and shear forces on that level. A complex system such as this is, of course, highly indeterminant, since the number of parameters involved outnumber the available number of equations defining the dynamic equilibrium of the interconnected joint segments. In order to circumvent the many constraints imposed by the system and to reduce the number of unknowns, the various existing models have simplified the actual system by approximating the action of several muscles into a single force-equivalent. Another complicating factor in biomechanical models, (particularly those of the trunk), is the contribution of the ligamentous structures and silent muscles which act as ligament when extended to their full length. These passive structures contribute to the forces acting on the joint system only when they are in a tightened position.

Later models have used mathematical optimization techniques to include the synergy and antagonist activity in the prediction of force about joints. For instance, in studies of the trunk, some models have managed to include up to twenty-two muscles (Bean et al., 1988; Pedersen et al., 1987). The assumption here is that the central nervous system distributes commands to the musculature to create movement, but in such a way as to minimize a function such as tissue stress-strain, energy utilization or fatigue. A major concern with this optimization scheme is that it cannot facilitate co-contraction, for this would generate additional compression to the joints. So while the idea that the CNS optimizes a function is a plausible one, it is simply unclear what that function might be and what the effects would be on the system. Other models have used video-optical technology with external load measuring devices and IEMG data to include more accurate posture and motion kinematics of the joint system (McGill and Norman, 1986). These are EMG driven models and although they may achieve a better anatomical fidelity and introduce a dynamic component into the picture, the main disadvantage still rests in the problem of an adequate relationship between EMG and force.

Most recently, some researchers have derived models from more accurate features obtained from morphological anatomical studies of the trunk muscles (Bogduk et al., 1992). These models rely strongly on: the geometric and morphological arrangement of the trunk muscles and vertebrae; the muscles physiological cross-sectional area; and a force coefficient relating this area to maximal force capacity. It includes 49 fascicles of the lumbar back muscles and considers the relative motion between vertebrae as well as changes in muscle lengths and the orientation of individual fascicles. These models provide an accurate description of all muscle fascicle attachments and use vector analysis efficiently, but do not consider an EMG/force relationship to drive the model. Instead, they replace the EMG/force relationship by a force-muscle-fascicle coefficient, leaving the EMG data as a validation method.

1.2.3 The Dynamic Systems Approach

A brief point about the motor control approach is called for here by the important role of the CNS in controlling and modulating the many muscles exerting forces to maintain bodily equilibrium. It is practically impossible to conceive of a model to estimate muscle force from a system that is highly redundant if we do not know how these forces are modulated and/or how the muscles counteract each other. These questions have been investigated by studying the EMG pattern of activity from solicited muscles (Crenna et al., 1987; Diener et al., 1988; Oddson and Thorstensson, 1987). Some of the main findings have been that muscle activation strategies are different for fast and slow voluntary movements. Not only might different muscles be solicited at a given time but the reaction time and duration of activity will also be different for different muscles. Some movements are performed synergistically, while others use antagonist or co-contraction activity. It has also been demonstrated that some patterns in the control of voluntary movement are task specific. The apparent implication of this finding is that there is some fixed synergy, referred to as "generalized motor program", which incorporates variant and invariant characteristics. Only one "template", that is, would be required to control a certain set of movements, which in turn would include adaptive “sub-templates” as responses to perturbations of the equilibrium. The battery of “sub-templates” is thought to grow with maturation and experience, thus providing the system with more efficiency and adaptability. If this is the case, then we must take the CNS into consideration and introduce these "templates" into our models. However, the lack of visual feedback for the behavior of the NMSS has made this difficult to achieve.

1.2.4 Posture and Movement

Traditionally, the analysis of movement has been limited to study of the development of input/output neural mechanisms underlying both bodily support and perturbation. And so, according to this point of view, posture has been treated as one of the sensorimotor mechanisms, with local stimuli from muscles, joints and the inner ear being integrated in the cerebellum and perhaps elsewhere and then channeled out in the form of signals modifying both phasic and tonic reflex. However, many scientists now believe that this sort of model of neural functioning, based on the traditional reflex hierarchy theories, is oversimplified (Edelman, 1987; Oddson and Thorstensson, 1986; Reed, 1989; Cordo, 1990). A new approach is emerging that regards posture, or rather postural development, as a key functional component of movement which gathers diverse processes, (perceptual as well as motor), and serves not only to execute actions but also to maintain bodily orientation to the environment in accordance with homeostatic demands. From this standpoint, sensory signals are not channeled into singular sensory mapping regions; instead they are the results of an active exploratory processes involving complex and distributed control of movements of the head and limbs, and in turn produce specific spatio-temporal patterning of input neural activities throughout the CNS (Easter et al., 1985; Rothwell, 1994).

The absence of a viable account of posture has meant that motor studies have been regarded primarily as movement development rather than action development (i.e. goal or task oriented movement). Action development is understood as the development of the adaptive flexible nesting of movement and posture so as to achieve intended outcomes (Berstein, 1967; Reed, 1990). Although posture has always played an essential role in clinical procedures, (which is one of the chief interest of this thesis), it has had a less significant role in both theory and experimental practice. To study action development entirely in terms of movement development is quite misleading, because the role of posture is fundamental in the development of flexible adaptability during movement execution. Therefore, greater efforts need to be put to the study of how such flexibility develops in general and the role of the adaptive postural development as a response to perturbations of the system, in specific. In this regard, clinical insight has been in the vanguard of our understanding of movement and posture, and research and theory are only beginning to catch up with the contemporary point of view on human movement sciences.

1.3 THE EMERGING POINT OF VIEW ON HUMAN MOVEMENT

Until recently, we have been studying and analyzing HM in the terms of a Newtonian-Cartesian system, rather than in those of an open non-lineal system in dynamic interaction with its surrounding systems. In other words, we have been regarding movement as "what develops", a point changing position in the space through time giving rise to a trajectory, instead of as an "adaptive development of a series of action movements". As discussed, this does not imply that the advances on human movement acquired to date are wrong, but rather that they have become insufficient to understand the phenomenon in its multidimensional aspects. In the last 50 years there have been many attempts to provide an unifying model of

HM, mainly by breaking the phenomenon down into sub-systems and sub-sub-systems and then proceeding to analyze each through reductionist models drawn from classical science. Today we realize that this point of view is unable to explain structural and concomitant aspects of HM. In fact, the definition of natural phenomena in terms of physical laws is a conception of our occidental world that is presently being tested in every field of science.

Historically, the concept of "law" was based on ideas of certitude and determinism where time, space and matter were the fundamental existential dimensions. In light of Newton's work, time, space and matter were distinctive concepts by which future and past become reversible in the eyes of a passive observer. This was a machinist model of natural phenomena. Later, Boltzmann introduced the entropic concepts of irreversibility and probability, and Einstein placed the observer back into the system by establishing a relationship between space and time with matter remaining independent. The machine now looked different, for indeed it depended where you stood within it and how many times you observed the phenomenon; but it was still a deterministic machine. Then Planck introduced a constant defining the interaction between a quantum system, forcing us to revise our concepts of coordinates and momenta; and Bohr linked the new quantum physics to the structure of atoms (and later of molecules) showing that there exist discrete sequences of electron orbits. For Bohr, Plank's constant defined the interaction between a quantum system and the measuring device as "non-decomposable". Subsequently, Schrödinger's equations accounted for irreversibility and discontinuity at the time of measurement and Heisenberg's uncertainty principle accounted for the system's probabilistic aspects.

These findings had a tremendous influence on the ways that sciences were practiced, for it meant that now we were required to decide which of a multiplicity of irreducible representations we were going to measure and about which our experimental questions were going to be posed. This was the beginning of the end of the departure from classical physics with its univocal notion of "objectivity", since this view recognized only one objective description as complete and this was independent of the way in which the system was to be observed. Classical science tended to emphasize stability, order, uniformity and equilibrium. It concerned itself mostly with closed systems and linear relationships in which small inputs uniformly yielded small results.

Modern science, on the other hand, concerns itself mainly with open systems, chaotic systems, giving particular attention to those aspects of reality, such as disorder, instability, diversity, disequilibrium, temporality and relationships which are non-linear (where small inputs can trigger massive consequences). The blatant contradiction between the classical and modern sciences, however, is only apparent. According to Ilya Prigogine, (who won the Nobel Prize in 1977 for his work on the thermodynamics of non-equilibrium systems), the machine paradigm is still the reference point for physics and the core model of science in general. Prigogine and Stengers (1984) argue that the old universal laws are not universal, but do apply to local physical realms. Prigogine and his colleagues, the "Brussels school", in a comprehensive theory of change hold that while some parts of the universe may operate like machine, these are closed systems forming at best a small part of the physical universe, and that most phenomena of interest to us are open systems exchanging energy or matter and information with their environment.

If biological systems form part of these open systems as they surely must, then any attempt to understand them in mechanistic term is doomed to be insufficient.

1.4 THE CLINICAL INTEREST IN HUMAN MOVEMENT

Static and dynamic positions of reference are the patient's functional equilibrium positions and it is according to these references that the clinician will evaluate the patient's disease, and severity, progression and efficiency of treatment. Thus, the clinician knows that points of stability must be controlled in order to support points of mobility. The mechanism by which actions are realized seems to be functionally organized and therefore, movement may be viewed as organized by the conditions inherent in the system-surround and orchestrated along some task-goal. Further, from a developmental point of view, control over the musculature proceeds as a proximal/distal dialectic and thus, there is also a progressive integration of proximal/distal control into a functional whole. Co-ordination of the system demands a differential (task/surround specific) appropriation of control (Rothwell, 1994). These conditions are quite the inverse from those presented in experimental settings, since here the mechanical constraints specify the control needed in a task. As well, an effective, appropriate, control changes as both system and environment change; co-ordination of proximal and distal motor systems with the periphery must therefore occur at all points in the movement process.

How this co-ordination reflects itself will be influenced by the system's ability to anchor its parts as a tool in order to free the extension of other parts into space. That is, in clinical terms the form of a movement (series of action movement) must emerge in compliance with the physical and mechanical reality of the surround and the psycho-physical structure of the system. From a clinical point of view, these constraints can be regarded as operational principles guiding the organization of the structure; posture and stability thus take a different connotation for the clinicians. Conversely, in an experimental settings, most physical and mechanical constraints are controlled in order to elucidate the functional principles guiding the system. Nevertheless, medical specialists as well as scientists from different backgrounds today are well aware that a true understanding of HM requires knowledge on both, the functional and operational mechanisms, by which the central nervous system integrates proprioceptive input and coordinates the activity of the muscles in a way that each will contribute properly to the intended movement. Today, there is no question that the psycho-physic structure is organized according to meaningful limits that orient its equilibrium, that is, its pattern of organization. The capacity of the structure to remain "stable" in the face of major external/internal adjustments is given by a central command which coordinates the processes between the individual, his body and his environment. Due to the fact that the human structure is modifiable, benefits as well as disturbances may be imposed equally by the individual, its body and the external environment. However, it is not clear which are the spatio-temporal factors contributing to the ultimate organization of movement and which are the meaningful limits that orient a stable equilibrium. These questions are of great concern, from both the functional and operational point of view.

1.5 KEY THEMES AND CONCEPTS

To this point, a number of themes and concepts have been presented as a series of arguments leading to the formulation of the working questions. The most important of these arguments can be summarized as follows:

- different anatomical pathways may be used to estimate muscle activity under various conditions and statuses of the system;
- normal functioning of the system can be described as an adaptive behavior that allows the structure to maintain its integrity while developing itself in a continuous interaction with its environment;
- movement must be conceptualized as emerging from a structured and concomitant interaction between CNS commands, various internal states and kinetics of the system as well as informational coupling to/from environment;
- muscles generate and modulate their force in a manner that is proper to the demands of the system as described above;
- a fixed synergy (generalized motor program) is expressed in a muscle activation pattern which incorporates variant and invariant characteristics of the system;
- such muscle activation patterns, based upon the principles of interdependence and homeostasis, should be regarded as a multi-dimensional dynamic process in movement development;
- postural development is an integral component of movement development and is implicitly expressed in specific the spatio-temporal patterning of input neural activities throughout the CNS;

- from the point of view of these observations, the NMSS can be regarded as a non-lineal open system exchanging information and energy with its environment;
- the functional and operational narrative aspects of movement development could be elucidated from the spatio-temporal patterning of muscles activity involved in the execution of movement.

1.6 RESEARCH QUESTIONS

Human movement is a natural phenomenon whose dynamic is given as a concomitant and structured process between CNS, various internal states and kinetic as well as informational coupling to/from environment. According to this description of movement, the NMSS can be modeled as a non-lineal open system. The main problem, however, is to establish a relationship between the central command and the skeletal segments in motion. Such a relationship can be regarded as a visual representation to the behavior of the NMSS. Since the muscular system is the (actuator and effector) link between the central command and the skeletal structure, and since movement development is expressed in specific spatio-temporal patterning of muscle activities, the solution must then be found precisely in the spatio-temporal patterning of muscle activity. Therefore, from the analysis and observations presented up to this point, the following research questions are raised:

1) Is it possible to characterize multi-dimensional features of movement from spatio-temporal patterns of muscle activation? and if so;
2) Are these spatio-temporal patterns related to particular type of movement dynamic (task specific)?

These have been the driving questions of this thesis research; they are found implicit in the underlying rationale of the various observations and analysis carried until now, and consequently formalized in the following section.

1.7 DEFINITION OF THE PROBLEM

The narrative aspects of the movement phenomenon might be depicted and deciphered from the ensemble of EMG patterns or "spatio-temporal orchestration of muscle activity". Consequently, from this point of view, the problem can be defined as:

> **the production of a dynamic visual representation of the ensemble of muscle activities involved in movement development in a manner that, both globally and individually, EMG patterns can be elucidated.**

This assumes that is possible to estimate temporal variations of potential of distribution on the skin surface from local potential distribution (EMG activity). Which implies that local EMG signal should be recorded bi-dimensionally on the skin surface independently from muscles location, muscle fiber direction, location of innervation points, action potential directional polarity and non-propagated signals. Solutions to these problems are often found in the selectivity properties of two dimensional spatial filtering techniques, induced by the construction of a Laplacian discrete function using a multi-electrode configuration, (Broman et al., 1985; Masuda et al., 1985; Reucher et al., 1987). This solution, in our case, represents a further problem since multi-electrode recording requires a large number of recording channels. An alternative solution is to search a geometric configuration that meets the Laplacian characteristics but that requires lesser number of recording channels. One choice would be to use active double-differential electrodes -- which can reduce the number of recording channels by one third -- but, the performance of this type of electrode configuration is muscle fiber direction dependent and therefore a better candidate might be the circular concentric electrode configuration. However, this latter configuration has been reported to enhance local selectivity under the assumption that its spatial transfer function is equivalent to that of a double differential (Bhullar et al., 1990). This assumption seems to lack solidity and therefore a suitable spatial filter configuration must be further investigated.

1.8 WORKING HYPOTHESES

The hypotheses derived from assumptions implicit in the research questions and definition of the problem, and they are formulated as follows:

First hypothesis:

> Circular concentric electrodes configuration have a transfer function which makes them more selective than double differentials.

This hypothesis is supported by the fact that a circular concentric offers a closer geometric representation of the Laplacian discrete function and thus, its spatial filter characteristics are expected to enhance local selectivity differently.

Second hypothesis:

> Spatio-temporal variations of EMG potential distribution on the skin surface can be adequately recorded by a two dimensional array of Laplacian electrodes.

This hypothesis assumes that there is a type of Laplacian electrodes which are capable of recording local EMG activity (first hypothesis).

Third hypothesis:

> Multidimensional features of movement can be characterized from spatio-temporal EMG patterns of muscle activation.

This hypothesis is based on the two previous hypothesis and the existence of a fixed synergy (generalized motor programming mechanism) which is task-dependent.

1.9 METHODOLOGY

Present video technology lends itself perfectly to measuring movement dynamics, but how to measure multidimensional EMG signals in a way that is both, global and localized is a problem. The proposed solution has been to measure the surface potential distribution on the skin surface by means of a two dimensional array of Laplacian electrodes. To achieve the various steps leading to the production of a spatio-temporal representation of muscle activity during the execution of a movement, the proposed methodology is out-lined in the following stages:

1.- Research and develop an electrode system that meets the required characteristics of a two dimensional spatial filter.
2. Test and validate the electrode system.
3. Measure local surface EMG activity with a two dimensional array of these electrodes while simultaneously recording the movement dynamics.
4.- Perform the recording of these signals under at least two different conditions (i.e. slow and fast movement).
5.- Use this data to estimate the potential distribution on the skin surface; and;
6. Construct a spatio-temporal EMG mapping of muscle activity correlated with movement dynamics.

1.10 OBJECTIVE OF THE RESEARCH

The objectives of this thesis research are twofold: first to present some basic arguments leading to future consideration of the neuro-muscular and musculo-skeletal systems as one non-lineal open system, and second, to develop technical tools needed to convey the multi-dimensional features of HM.

The first objective was achieved in previous sections through an analysis and discussion of the changing views regarding the traditional tenets. The main concepts found undergoing present changes are those concerning motor mechanisms of the central nervous system; muscle force estimation methods; movement and posture; scientific methodology and approach on human movement studies; and the clinical interest on HM.

The second objective, which forms the bulk of the thesis, will concern principally the measuring device and representation of the experimental data. The systematic development of these objectives in the following chapters will, finally, lead to demonstrate the feasibility to produce a dynamic internal image capable to depict some of the neuro-musculo-skeletal processes involved in the generation, control and co-ordination of HM. First, a summary of the fundamental knowledge of EMG is presented in Chapter Two together with a discussion of the main factors involved in the generation and detection of the EMG signal as well as the various hypotheses used in processing the signal to extract pertinent information on the system. Chapter Three investigates various electrode system configurations and electrode geometries, aiming for the development of a Laplacian or spatial filter electrode that meets our requirements. Chapter Four reports on series of experimental tests run on the Laplacian electrode with the aim to validate its spatial filter characteristics. Chapter Five describes a limited implementation of the electrode to provide a "proof-of-concept" for spatio-temporal EMG mapping. To this end, the technique is developed, tested and validated experimentally. Finally, global conclusions, some possible applications and research works are proposed for future consideration under the section of General Conclusions.

CHAPTER TWO

ELECTROMYOGRAPHY

2.1. INTRODUCTION

This chapter discusses the main factors involved in the generation and detection of the EMG signal, as well as the way in which these affect the content of the signal throughout the detecting and data processing stages. A brief review of muscle physiology is presented in the next section, followed by a review of the detection process involving different electrode configurations and their filter ability to suppress non-delayed signals. Due to its non-invasive nature, surface EMG (SEMG) is often preferred over intra-muscular or indwelling EMG, and this review will therefore focus mainly on SEMG. However, special emphasis will be given to the geometric factors, because among these, the electrodes' morphology plays a key role in the detected signal. This will be followed by a review of the various hypotheses used in processing the SEMG and their ability to enhance the signal's time and frequency domain features. Finally, an analysis of the main factors affecting the content of the SEMG will be reviewed with the conclusions leading to the systematic analysis of electrode spatial filtering system in Chapter Three.

2.2. PHYSIOLOGY OF SKELETAL MUSCLE

The CNS is in continuos communication with the periphery by means of peripheral nerves (PNS). Data of the present status of the internal and external environment is transmitted to the CNS in the form of stimuli via afferent peripheral nerves. The CNS responds in turn with instructions to organs, muscles and tissues which are transmitted via efferent peripheral nerves. Such stimuli data and instructions responses are carried by transient electrical impulses called neural action potentials (NAP).

2.2.1 Generation of Muscle Action Potential

A skeletal muscle consists of a number of motor units, which in turn consist of number of muscle fibers innervated by the terminal branches of a single α-motoneuron whose cell body is located in the anterior horn of the spinal cord. When the efferent NAP reaches its target via the α-motoneuron, in this case the muscle end-plate or innervation point, it will cause changes in the permeability of the neural membrane to calcium ions that move from the extracellular space across the neural membrane into the nerve terminal. Calcium ions then bind to molecules inside the nerve terminal and cause the chemical transmitter acetylcholine (ACh) to be release from synaptic vesicles in the terminal membrane. The ACh diffuses across the gap between the nerve terminal and the muscle fiber membrane and binds to receptors in the fiber membrane. This binding, in turn, causes permeability changes to sodium and potassium in the muscle fiber membrane resulting in a propagated muscle action potential (AP).

2.2.2 Muscle Conduction Velocity

This depolarization (AP) begins at the neuromuscular junction, and propagates in opposite direction, towards both ends the muscle fiber at a speed referred to as the muscle conduction velocity (CV). The CV varies from approximately 2 m/sec for the smallest fibers to 5 m/sec for the largest. The intracellular potential contains frequencies of up to about 10 KHz. The lowest frequency components are generated by the slow depolarization currents, coming from extended regions of previously depolarized membrane. The middle frequencies constituting the bulk of the gross EMG come from the active depolarization region, perhaps a few millimeters long. The highest frequencies come from the sharp boundary between open and closed sodium gates at the leading edge of the actively propagating potential. The CV is dependent on the internal longitudinal resistance, which is related to the diameter of the fiber, resistance of the core plasma, and the membrane capacitance. Rosenfalk, 1969; Andreassen and Rosenfalk, 1981).

2.2.3. Muscular Contraction

As the AP propagates, the depolarization is also transmitted toward the interior of the fiber where it leads to an increase in calcium permeability, this activates the contractile proteins (troponin molecules) contained within the muscle fiber cells, a process known as excitation-contraction coupling. The characteristics of the generation of this ionic current and its propagation which are much the same in skeletal muscle and unmyelinated nerve cells, are basic to the physiological understanding of the electrical phenomena leading to muscle contraction. The rise and decline of muscle force produced by a single AP is called twitch. Since the time course of a twitch is relatively slow compared to the time course of an AP, several APs can occur within the period of a single twitch, thus adding force by causing more calcium to be released. Maximum tension or tetanus is reached when sufficient calcium accumulates within the intracellular space to saturate the troponin molecules.

2.2.4 Motor Units

The motor units are the motor output of the CNS and are responsible for both movement and maintenance of posture. A motor unit (MU) is composed of a motoneuron, an axon and its muscle unit. This latter, in turn, is the ensemble of fibers innervated by a single motor axon. Fibers belonging to the same motor unit (MU) are widely dispersed throughout a muscle; different MUs intermingle in a manner that territories of 10 to 30 MUs may overlap to some extent in any one region of the muscle. Although MUs vary widely in their properties, the muscle fiber within a single muscle unit are quite homogeneous. Muscle fibers are generally classified into three main groups according to their speed of contraction and fatigability: fast twitch-fatigable (FF), fast twitch-fatigue resistant (FR) and slow twitch-fatigue resistant (S). The force produced by a MU is correlated with the speed of contraction and fatigability of its muscle fibers, as well as with the number of muscle fibers that are innervated by its motoneuron. The S fibers produce the smallest force; they are recruited first and remain active as other MUs are recruited to reach or maintain the required force. The largest forces are produced by FF fibers. Slow-twitch fibers are usually referred to as Type I muscle fibers and fast-twitch fibers as Type II muscle fibers. In addition, groups of muscle fibers (collectively known as a fascicle) are surrounded by blood vessels and connective tissue which inserts into portions of specialized connective tissue (tendons), and in turn usually connect each muscle end to rigid links (i.e. bones). Rigid links connected by synovial joins together with muscles, neurons and sensory receptors form skeletal articulation (i.e. single or multiple joint system). Depending on the role that the muscle plays in a particular joint system, its fascicles and fibers are oriented in different directions in relation to their attachment to tendinous and bonny tissues. If fibers run obliquely to the long axis, the muscle is referred to as pennate, because of its resemblance to a feather. Unipennate muscles have a single tendon running over one side. Multipennate muscles have aponeuroses of tendinous material which approach the belly of the muscle from both ends, with fibers running only a short distance from one aponeurosis to the other.

2.2.5. Control of Muscular Contraction

The CNS and PNS control the required level of muscle tension by modulating the number and firing rate of recruited motoneurons. These two factors are determined by the synaptic activity on the cell body of each motoneuron, which in turn is a function of the activity of the descending upper motoneurons and the efferent activity emanating from the peripheral sensors (proprioceptors and exterceptors). Even though the relative contribution of motor unit recruitment to muscle force varies between muscles, the modulation scheme appears to be in a orderly fashion. Thus, force is initially generated through use of a percentage of the maximum recruitment of the muscle's motor units, and then through variation of their discharge rate. One important factor underlying orderly recruitment appears to be motor unit size. This effect is described as the size principle: the motor unit with the smallest motoneurons is recruited first and those with the largest motoneuron are recruited last. This group organization of motoneurons is referred to as a motor unit pool. (Basmajian and De Luca, 1985). Orderly recruitment seems to relieve the brain of concern with this level of detail in the performance of movement, recruitment order is therefore largely predetermined by spinal chord mechanisms.

2.2.6. Detection of Extracellular Action Potentials

The presence of an extracellular potential field in the neighborhood of an active fiber is due to an external medium that behaves like a volume conductor in which passive spatial conduction of the membrane current takes place. A quantitative description of this current field is hampered by the anisotropic and inhomogeneous character of the extracellular medium. However, by making a number of simplifications it is possible to describe the conduction phenomena mathematically (Rosenfalk,1969; Plonsey,1974; de Weird 1984). Extracellular detected APs from active fibers in situ usually have a triphasic wave shape, depending on the way in which the potentials are detected. The triphasic wave shape corresponds to the second derivative of the intracellular AP. The amplitude of the extracellular detected AP markedly decreases with increasing observation distance from the active fiber; near the fiber it is inversely proportional to the distance, whereas further away it is approximately inversely proportional to the square of the distance (Rosenfalk,1969).

Due to both a geometric and a temporal dispersion, the action potential of muscle fibers belonging to the same motor unit is not precisely synchronized in either time or space. The geometric dispersion, resulting from the different observation distances to each fiber, makes the effect of volume conduction different for each AP. The temporal dispersion, resulting from spatial scattering of the neuromuscular junction which produces different arrival time at the detecting electrode, results in a broadening or even cancellation of APs. The effect of volume conduction, beginning from the intracellular AP, can be modeled as conduction through a high pass and a low pass filter (Gath and Stalberg, 1977, 1979). The high pass filter represents the relationship between the intracellular and extracellular AP directly outside the fiber, while the low pass filter represents the spread of the AP in the external medium.

2.2.7 Detection of Motor Units Action Potentials

The extracellular electric field detected with an electrode is generated by a number of muscle fibers from many MUs. The sum of these single fiber contributions is referred to as MU action potential (MUAP). The shape and amplitude of a MUAP are determined by the number of MUs active within the electrode's pickup volume, their spatial arrangement in relation to the electrode and their activation time. Further changes in the wave shape and amplitude are produced due to conduction through the volume conductor which acts as a low pass filter. A sequence of MUAPs is known as MUAP train. The firing sequence of MUAPs is described by the firing rate which is calculated from the inverse of the firing interval. The firing rates of different motor units within a muscle and across muscles are controlled in tightly bound manner and are significantly cross-correlated with a near-zero phase shift. The unison behavior of the firing rates is called the common drive (De Luca, 1984). This phenomenon indicates that the nervous system controls the motor units in a non-individual fashion.

2.2.8 Detection of Electromyograms

Each active MUAP has an associated current field in the surrounding volume conductor. This field is comprised of the non-linear sum of the electrical fields generated by the individual muscle fibers of the motor unit. Two electrodes may be used to detect the potential difference between any two points inside or on the boundaries of the volume conductor. The potential detected by the electrode pair is the weighted sum of the contributions of the different generators. The weight (filter function) of each component is determined by the distance of the corresponding source from the detection electrode pair and the anisotropy of the tissue. The detection electrode pair itself introduces an additional filtering function related to the electrode size and geometry and inter-electrode distance (Lindstrom and Magnuson, 1977).

During voluntary contractions, MUAPs are almost asynchronous and the resulting potential difference between the detection electrodes is stochastic, with a probability density function that is approximately Gaussian if a sufficiently large number of active MUs contribute to the electrode potential. When the probability distribution is normal, its variance is a measure of the spread of a peak in the EMG record at a specific amplitude. In other words, the variance is a function of the number of spikes occurring in the EMG weighted by the square of their amplitude. This function represents the muscle behavior and gives a good estimate of the signal to noise ratio. A weak variance indicates a density concentration around the mean value and consequently gives a good estimate of the level of muscle activity. Furthermore a zero mean value (unbiased) indicates that the estimator is precise (providing that the noise is uncorrelated to the EMG signal).

2.3. DETECTION ELECTRODES

The two main types of electrodes are surface (or skin) and percutaneous (wire and needle) electrodes. They are used either singularly or in pairs, and referred to as monopolar or bipolar, respectively. Surface electrodes are normally used to detect gross EMG signals consisting of the electrical activity from numerous individual MUs within the boundary or pickup volume of the detection surface. To detect activity from single motor units or single fibers it is usually necessary to insert the electrodes directly into a muscle. In addition, surface electrodes can be constructed as either passive or active. The passive electrode consists of a detection surface that senses the current on the skin through its skin-electrode interface. In the active configuration, the input impedance of the electrodes is greatly increased by an electronic circuit, rendering the electrode less sensitive to the impedance of the skin-electrode interface. Usually cleaning the skin surface by means of light abrasion and application of an electrolyte gel is sufficient to form a low impedance contact between the electrode and the skin. The lack of chemical equilibrium at the metal-electrolyte junction sets up a polarization potential that may vary with temperature fluctuations, sweat accumulation, changes in the electrolyte concentration of the gel, relative movement of the metal and skin and the amount of current flowing into the electrodes. The polarization potential has both a DC and AC component. The AC component is greatly reduced by providing a reversible chloride exchange interface with the metal of the electrode. The DC component of the polarization potential is nullified by using the differential technique (bipolar) in conjunction with differential amplifiers.

2.3.1. Bipolar Electrode Configuration

The SEMG signal may be described as a space distribution of an electric potential travelling along the direction of the muscle fibers from the innervation point to the fiber's ends at a velocity ν. The space and time description of the signal are related by the following basic equations which holds for a periodic signal as well as for each frequency component of a non-periodic signal:

$$\nu = \lambda f_t = \lambda / T; \qquad f_s = 1/\lambda = f_t / \nu \tag{2.1}$$

where: ν = conduction velocity (CV), [m/s]; λ = wavelength, [m]; f_t = frequency in the time domain, [Hz or cycles/s]; T = period, [s]; and f_S = frequency in the space domain, [cycles/m]. At any given time, the differential amplifier output is the difference of two space samples of the signal from the two detection surface separated by the interelectrode distance d. If distances are measured with respect to the middle of the inter-electrode spacing, then the filtered effect induced by the electrode and its transfer function can be described as follows (Lindstron, 1970):

$$\Phi_d(t) = \Phi\left(t + \frac{d}{2\nu}\right) - \Phi\left(t - \frac{d}{2\nu}\right) \tag{2.2}$$

$$\Phi_d(t) = \Phi(t) \otimes \left[\delta\left(t + \frac{d}{2v}\right) - \delta\left(t - \frac{d}{2v}\right) \right] \qquad (2.3)$$

where $\Phi(t)$ is a single signal moving from one electrode to the other; d is the inter-electrode distance; v is the conduction velocity; δ is the Dirac impulse and $\otimes$ is the convolution operator, yielding the following transfer function

$$H(f) = 2j \sin \pi f \frac{d}{v} \qquad (2.4)$$

$$|H(f)|^2 = 4 \sin^2 \pi f \frac{d}{v} \qquad (2.5)$$

The expressions (2.4) and (2.5) show zeros of the transfer function for frequencies multiple of $f = d/v$; this phenomenon is referred to as dip and is sometime used in estimation of the CV. Lindstrom and Magnusson (1977), have demonstrated that expression (2.4) allows a separation between the filtering effect due to the bipolar configuration and the degradation induced by the distance between the active MU and electrode. They estimate the transfer function as:

$$H(f) = \frac{K_0(2\pi h / v)}{K_0(2\pi a / v)} \qquad (2.6)$$

where the fiber is considered as an infinite cylinder of radius a, orthogonally distance h from the measurement point; K_0 is the modified Bessel function of the second kind, order zero.

2.3.2. Multipolar Electrode Configuration

Electrode developments have expanded to multipolar configuration or electrodes arrays, also referred to as multielectrode systems. This kind of electrode, although in extensive use for some time in EEG and ECG, have found an application now in the detection of EMG signal. The first, and most important hypothesis, which is not true for EMG signals, concerns the pure delay condition between recording sites. Broman et al., (1985a,b), have stated that largely overestimated results of CV were obtained by differential electrode sets in spite of good correlation values. They demonstrated that SEMG are a mixture of delayed and undelayed signals. In order to overcome this problem, they suggested a double differential electrode set acting as a Laplacian filter (see Figure 2.1b). Using this layout they obtained consistent CV results. This was also reported by Reucher et al., (1987), who demonstrated the difference between monopolar, bipolar and tripolar configuration.

Multielectrode systems are useful for the analysis of a spatial two-dimensional cartography of the EMG potentials (Homma et al., 1986; Yamada et al., 1987). Multielectrode systems also permit localization of motor points (Sadoyama et al., 1985) and determination of more precision conduction velocity and direction of MUAP propagation (de la Barrera and Milner, 1991). The disadvantages of these layouts lie in the large electrode size and the lower signal amplitude. These limitations can be incompatible with constraints in either distance between motor points areas or signal to noise ratio.

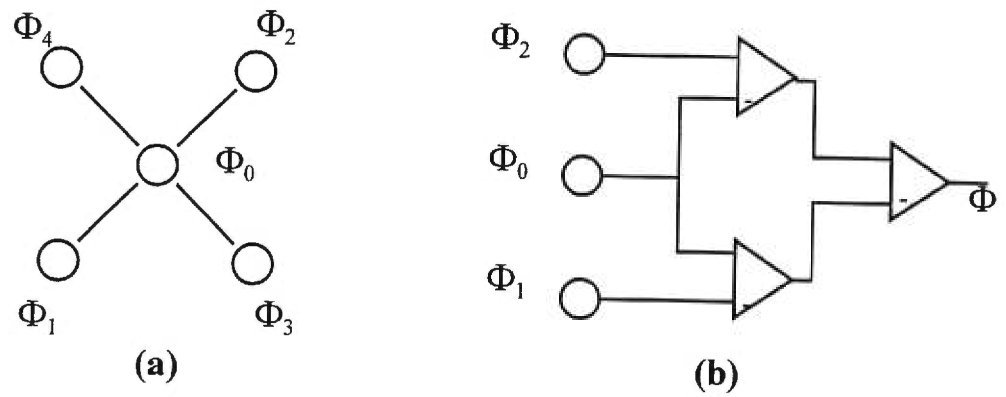

Figure 2.1 **Laplacian estimate for local activity detection.** (a) Classical bidimensional layout used in EEG applications. (b) Monodimensional approximation as per Broman et al.,(1985a).

The main objective of multipolar configuration is to minimize the integrating effect of bipolar sets, by reducing the recording field of the underlying electrical activity as much as possible. This results in a higher selectivity in the detection process of the signal. This selectivity can be analyzed from the current density divergence (discussed in more detail in the next chapter), which is equivalent to the assessment of the Laplacian electrical potential on the surface of the skull. The Laplacian estimate can be obtained with a five-electrode system (Figure 2.1a), leading to a first order estimate (Nunez, 1981):

$$\nabla^2\Phi = \frac{\partial^2\Phi}{\partial x^2} + \frac{\partial^2\Phi}{\partial y^2} \approx (\Phi_1 + \Phi_2 + \Phi_3 + \Phi_4) - 4\Phi_0 \quad (2.7)$$

Based on the assumption of unidirectional variation of electrical potential, the signal propagates in the direction 1-0-2, the estimate reduces to:

$$\nabla^2\Phi \approx (\Phi_1 + \Phi_2) - 2\Phi_0 \quad (2.8)$$

This signal can be constructed from a double-differential amplification layout (Figure 2.1.b), as proposed by Broman et al., (1985a) and Reucher et al., (1987a,b). The filtering effect induced by this configuration can be obtained in a similar manner as for the bipolar configuration, under the same propagation assumptions:

$$H(f) = 2\left(\cos 2\pi f \frac{d}{v} - 1\right) \quad (2.9)$$

The transfer function is real and again exhibits zeros for frequencies which are proportional to the CV.

2.3.3. Electrode Configuration and Global Parameters

The effects of electrode configuration on global parameters of the SEMG signal have been investigated by several researchers using mainly single or double electrode layouts. In a comprehensive study, Van Boxtel et al., (1984), analyzed the effect of size, location, direction and interelectrode distance on some SEMG parameters (mean rectified EMG and equivalent bandwidth). They observed that neither electrode size nor interelectrode distance influence these parameters, as long as rectified SEMG was normalized with respect to maximal contraction values, considering a minimal interelectrode distance of 10 mm. However, they did find statistically significant, although small absolute, differences between horizontal and vertical derivations in their specific electrode location.

Masuda et al., (1985) using an electrode array of 13 electrodes, which lead 12 differential electrodes along the muscle fiber direction, noticed that potential polarity was inverted from one side to the other of the innervation area and that electrodes closer to the motor point location showed smaller delays with respect to the earliest signals. Sollie et al., (1985 a,b), demonstrated that near the innervation zone and the tendon, the effects of generation and extinction of the signal are important and that potential propagates with a constant shape and velocity in only a limited region. This region was found to be between the innervation point and the tendon, a conclusion confirmed by Roy et al., (1986), Masuda et al., (1988), and Saitou et al., (1991).

Sollie et al., (1985 a,b) also found that a misalignment of 15° with respect to muscle fiber direction generates a 6.7 % error in CV estimates. Similarly, Lynn (1979) found a 12 % error in the estimation of CV for a misalignment of 10° and Sadoyana et al. (1985) found that for misalignment between 10° and 15° the cross-correlation values are greater than 0.9 but they drop dramatically for misalignments greater that 15°. However, Schneider et al., (1991) have carried out a theoretical study on the influence of tissue inhomogeneity on the recorded SEMG signal. They concluded that fluctuation of CV along muscle fibers cannot be attributed solely to the influence of the electrode's proximity to innervation points and/or electrodes' misalignments, but that fluctuations along the muscle fiber can also be attributed to variations in fiber diameter and that up to 10 % can be attributed to inhomogeneity of tissue conductivity between the active fiber and the recording electrode.

In another theoretical study, Cunnigham and Hogan (1981) found that the frequency components of the signal are also affected by refraction and redirection of the signal at the muscle/fat boundary. Lower frequency components of the signal are more refracted toward the vertical at the muscle/fat boundary than high frequency components. The magnitude of this refractive effect is somewhat offset by signal redirection in the anisotropic muscle tissue. They concluded that higher frequency components from active fiber closer to the muscle/fat boundary will contribute more than lower frequency components from active fibers deeper in the muscle. These conclusions were confirmed by de la Barrera and Milner (1994). Using arrays of surface electrodes, they investigated the effects of fatty tissue and electrode orientation on the selectivity of SEMG and found that the selectivity of the surface electrodes increased as the skin fold thickness decreased; action potential were more rapidly attenuated and underwent less low-pass filtering. Conversely, the ability of surface electrode to localize EMG source deteriorated as the amount of subcutaneous fat between the surface recording site and the active fibers increased. For subjects with higher skin fold thickness, the median frequency of signals were lower and electrode misalignment was less critical.

De Luca et al., (1987), investigated the effect of recruitment and firing rate on the global parameter and found that the force threshold of motor units recruited below 20 % maximum voluntary contraction (MVC) increased while their firing rate decreased. Conversely, the force of motor units recruited above 25 % MVC decreased while their average firing rate increased. Blinowska and Verroust (1987) found that the discharge of motor units became more synchronized as the force level increased and that discharge frequency peak may emerge in the low frequency power spectrum if synchronization occurs.

2.4. PROCESSING HYPOTHESES OF THE EMG SIGNAL

A number of time and frequency domain attributes have been used to describe the EMG signal. Among the time domain attributes are the average rectified value (ARV), the root mean square value (RMS), muscle fiber CV, peak and peak-to-peak amplitude, duration and area of the M-wave (the response to electrically elicited contraction). Among the frequency domain attributes are the mean (MNF) and median (MDF) frequency of the EMG signal power spectrum density function (PSD). This section discusses some of the basic concepts used in computation of these attributes, as they concern the recurrent hypotheses and tests encountered in the analysis of time dependent parameters. Their value and the time course reflect physiological correlates which have been used to detect or monitor pathologies and to describe neuro-musculo-skeletal properties. Statistically, the myoelectric signal may be considered as a bandlimited stochastic process with a Gaussian distribution, (Basmajian and De Luca, 1985). Although the Gaussian property is seldom verified in SEMG signals, it is demonstrated in some precise experimental conditions, (Inbar et al., 1987). Stationarity of a random process is produced by the fact that the moments of probability density function (PDF) do not depend on the specific instant when they are computed. In addition, for signals like SEMG, these statistical moments are assessed from a single record, requiring assumption of ergodicity, i.e., the ability of a single infinite time-series to entirely describe the PDF of the random variables (attributes) associated with the process. Usually, a simple parameter computation can be achieved for time windows without any control of stationarity, in which case the statistical characteristics of such parameters will remain unknown (excluding any statistical method for comparison and classification). Further, no specific relation can be formally established between time and spectral domains.

Often wide sense stationarity (WSS) is confined to test the time-invariant characteristic of the mean and the autocorrelation function. The problem arises when WSS stationarity must be assessed on experimental samples and more often than not, (for practical reasons), an insufficient number of sample records are utilized to achieve relevant tests from average estimates. It is then necessary to hypothesize ergodicity to allow mean and correlation estimation from time windows on a single sample record rather than on many samples as theoretically required. In any case, mean-ergodicity seems to be a reasonable assumption for SEMG according to Slutsky's theorem, thus a process is mean-ergodic if:

$$\frac{1}{T}\int_0^T R(\tau)\,d\tau \;-\!\!\!\xrightarrow[T\to\infty]{}\; 0 \qquad (2.10)$$

with $R(\tau)$ as the autocorrelation function, a sufficient condition of mean ergodicity is $R(\tau)\rightarrow 0$ as $\tau\rightarrow\infty$. This condition can reasonable be considered as satisfied for SEMG. Since the power spectral density function (PSD) is defined for WSS signals only, SEMG may be considered, in most cases, as WSS during relatively low level and short contractions , 20 to 30 % MVC , up to 20 to 40 seconds. If the contraction level is increased, the WSS hypothesis holds for shorter epochs, 0.5 to 1.5 s at 50 to 80 % MVC, (Balestra et al., 1988).

The time course of time and frequency domain attributes is generally computed by subdividing the signal in epochs during which the WSS hypothesis holds and the selected variables (attributes) are computed over each epoch. The attributes then become function of time, i.e., changes in the median frequency of the PSD during fatigue experiments. The PSD function, (also refers to as raw periodogram), is computed by taking the square modulus of the discrete Fourier transform of the selected epoch in the SEMG signal. This technique gives a spectral estimate in which the single spectral line is affected by a standard deviation of 100 %. Moving averages of the PSD of the selected epoch helps to smooth or reduce the random fluctuations with a consequent lost of resolution. However, one must be careful in finding the balance between smoothing and resolution, for it might have an effect on the area distribution of the PSD and thus change artificially the attributes, i.e., shifting of the median frequency. In conclusion, for all these reasons, it is essential to define local stationarity before under taking any study involving spectral estimates. On the other hand some authors (Xiong and Shwedyk, 1987; Englehart and Parker, 1994; Merleti and Lo Conte, 1995 a,b), dealing with non-stationary models consider global SEMG as the product between a zero-mean stationary Gaussian process and a time varying variance coefficient (i.e. spectral dispersion, skewness and kurtosis coefficients). This model applies well to periodic dynamic contractions and/or stimulated contractions where no fatigue process is involved.

However, it is not always necessary to use such a complicated model. For instance, in an experiment consisting in pedaling an ergocycle at rates from 50 to 120 rpm, Helal and Duchene (1989) demonstrate that the non-stationary aspects of SEMG were located only in the 0 to 10 Hz frequency band. Similarly, Englehart and Parker (1994), show that non-stationary behavior markedly influences estimates of features describing motor unit firing pattern and consequently, the low portion of the SEMG power spectral density. They add some factor that may affect the degree of stationarity of experimentally generated SEMG: the duration of the contraction (i.e. fatigue); means of force production (i.e. active loading produce more jitters than passive loading); and level of contraction (i.e. a firing rate that is more susceptible to greater fluctuation at higher levels of contraction).

2.4.1 Time Domain Parameters

The most classical signal processing application to SEMG are the ARV and the RMS. The ARV is the area under the rectified signal during a time interval duration *T* and divided by *T*, providing a mean voltage value of the signal $\Phi(t)$:

$$ARV_{\Phi} = \frac{1}{T}\int_{-T/2}^{T/2} \left|\Phi(t)\right| dt \qquad (2.11)$$

This kind of SEMG representation is often used to compare signal evolution with respect to other parameters such as force; however its drawback lies in the difficulty of relating it to an actual energy or power estimate. In this sense a far more reliable parameter is the signal's RMS. The RMS value is obtained by dividing the energy of the signal during a time interval of duration *T* by the value of *T*, thus providing the mean power value whose square root is the RMS and expressed as:

$$RMS_{\Phi} = \left[\frac{1}{T}\int_{-T/2}^{T/2} \Phi^{2}(t)\,dt\right]^{1/2} \qquad (2.12)$$

If we now consider two signals, $\Phi_x(t)$ and $\Phi_y(t)$, the discrete cross-correlation function between the two signals at times τ before (or after) the current values of $\Phi_x(t)$ can be estimated over a time interval T as:

$$R_{xy}(\tau) = \frac{1}{n_d(T-\tau)}\sum_{i=1}^{n_d} \Phi_{xi}(t)\Phi_{yi}(t-\tau) \qquad (2.13)$$

$$R_{xy}(\tau) = \lim_{T\to\infty} E\left[R_{xy}(\tau, T, n_d)\right] = R_{yx}(-\tau) \qquad (2.14)$$

where $R_{xy}(\tau)$ is the average cross-correlation function over n_d contiguous segments, each of these epochs of length *T* and with *E*[ ] representing the expected value over the epochs ensemble index n_d ; where $(i-1) \leq t \leq iT$ and $i = 1,2,\ldots,n_d$. The estimated auto-correlation functions $R_{xx}(\tau)$ and $R_{yy}(\tau)$ are particular cases of $R_{xy}(\tau)$, where $\Phi_x(t) = \Phi_y(t)$. The cross-correlation coefficient function provides a normalized measurement of the cross-correlation values. It is defined as follows:

$$\rho_{xy}(\tau) = \frac{R_{xy}(\tau)}{\sqrt{R_{xx}(0)R_{yy}(0)}} \qquad (2.15)$$

which satisfies $-1 \leq \rho_{xy} \leq 1$. If the distance d between two collinear pair of electrodes is known, then the CV v can be estimated as $v = d/\tau$.

2.4.2 Frequency Domain Parameters

Two main frequency parameters have been used to describe the spectrum of the EMG signal, its MNF (or centroid) and the MDF. The use of MNF was first introduced by Lindstrom and Magnusson (1977), and the MDF by Stulen and De Luca (1981). The PSD MDF is defined as the frequency that divides the power spectrum into two regions having the same amount of power, thus:

$$\int_0^{MDF} P(f)\,df = \int_{MDF}^{\infty} P(f)\,df = \frac{1}{2}\int_0^{\infty} P(f)\,df \qquad (2.16)$$

The MNF is defined by:

$$MNF = \frac{\int_0^{\infty} fP(f)\,df}{\int_0^{\infty} P(f)\,df} \qquad (2.17)$$

The MNF can be estimated with a lower relative error while the MDF is less sensitive to added white noise and is therefore more reliable for tracking of spectral compression. However, both estimates are affected by a standard deviation that increases with decreasing epoch duration (Balestra et al., 1988). In general, for a zero mean signal with PSD within the bandwidth 0-F, sampled at $f_S = 2F$, the moment of order n of the normalized PSD (PSD with unit area) with respect to the y axis is given by:

$$M_n = \int_0^{\infty} f^n P(f)\,df \qquad (2.18)$$

where $P(f)$ is the PSD.

2.4.3. Indices of spectral shape changes

The power moments defined in Equation (2.18) can be used as descriptors of PSD shape. Indeed, if the SEMG signal is assumed to be generated by an equivalent field source propagating at a certain depth, a change of CV from v_0 to v_1 implies a time scaling of the signal by a factor of $k = v_0/v_1$ (Lindstrom and Magnusson, 1977). And if we further assume the possibility of amplitude scaled by a factor of h, then we can consider the two signals $\Phi_x(t)$ and $\Phi_y(t) = h\Phi_x(kt)$. If $\Phi_x(t)$ has a Fourier transform $X_x(f)$, PSD $P_x(f) = |X_x(f)|^2$, and auto-correlation function $R_{xx}(\tau)$, then $\Phi_y(t)$ has a Fourier transform, PSD and auto-correlation function defined by:

$$X_y(f) = \frac{h}{k} X_x\left(\frac{f}{k}\right), \tag{2.19}$$

$$P_y(f) = \frac{h^2}{k^2} P_x\left(\frac{f}{k}\right),$$

(2.19)

$$R_{yy} = \frac{h^2}{k^2} R_{xx}(k\tau)$$

The lag of the zero crossing of the auto-correlation function is defined as the lowest value of τ_0 for which $R_{xx}(\tau_0) = 0$. The MNF, MDF and τ_0 of $\Phi_y(t)$ are given by:

$$f_{ymean} = kf_{xmean}; \qquad f_{ymed} = kf_{xmed}; \qquad \tau_{0y} = \tau_{0x}/k \tag{2.20}$$

Further more, from Equations (2.11) and (2,12) we can define the ARV and RMS value of $\Phi_y(t)$ over the time interval 0-T as:

$$ARV_y = \frac{1}{T}\int_0^T |h\Phi_x(kt)|dt,$$

(2.21)

$$RMS_y = \left[\frac{1}{T}\int_0^T h^2\Phi_x^2(kt)\,dt\right]^{1/2}$$

Amplitude changes between two epochs of duration T_e may be defined by the ratio ARV_y / ARV_x or RMS_y / RMS_x. If k changes slowly with time, it may be assumed to be constant within epoch of duration T_e over which the PSD, the auto-correlation function and the values of ARV and RMS are estimated. Then , Φ_x could be considered as the signal of reference epoch at $t = 0$ and Φ_y as the signal of a second epoch taken t seconds later. From Equations (2.20) and (2.21) the following relations can be made:

$$k(t) = \frac{f_{med}(t)}{f_{med}(0)} = \frac{f_{mean}(t)}{f_{mean}(0)} = \frac{\tau_0(t)}{\tau_0(0)} = \frac{v(t)}{v(0)} \qquad (2.22)$$

$$h(t) = k(t)\frac{ARV(t)}{ARV(0)} = \left[k(t)\right]^{1/2}\frac{RMS(t)}{RMS(0)} \qquad (2.23)$$

where t now indicates the time along the contraction at which the epoch for calculation of the variables is taken and v is the CV. The above ratios are normalized values of the SEMG signal variables; therefore estimates of frequency and amplitude scaling factors $k(t)$ and $h(t)$ may be computed from normalized spectral and amplitude variable. If the SEMG signal is progressively scaled during sustained contraction, the regression coefficient and the correlation coefficient of the mean square regression line of normalized MNF versus MDF, and normalized CV versus one of the spectral variables, would both be unity (Merletti and Lo Conte, 1995). This would indicate pure spectral compression and reliable estimates of k and h. Values that differ from unity indicate a change in the signal and spectral shape, suggesting that factors other than CV affect the signal (i.e. changes in the firing patterns of motor units, changes in synchronization between motor units and recruitment of new motor units). In such cases, the estimates of $k(t)$ and $h(t)$ depend on the variables used (f_{mean}, f_{med}, τ_0). Information about spectral changes may be provided by higher moment descriptor of the spectrum.

Since the normalized PSD may be viewed as a probability density function, indicators commonly adopted for probability density function characterization may be used. Lower moment descriptors such as mean and median values are dimensional quantities, however higher moments descriptors such as skewness and kurtosis are non-dimensional quantities that characterize only the shape of the distribution. The skewness (third moment) characterizes the degree of asymmetry of the distribution around its mean. A positive value of skewness signifies a distribution with an asymmetric tail extending out towards higher values of the mean; conversely, a negative value indicates a distribution whose tail extends toward lower values of the mean. The kurtosis (fourth moment), on the other hand, measures the relative peakedness (positive value) or flatness (negative value) of the distribution with respect to a normal distribution. The moment of order n of the PSD of Φ_y, $M_{y,n}$ is related to the moment of order n of the PSD of Φ_x, $M_{x,n}$ by:

$$M_{y,n} = h^2 k^{n-1} M_{x,n}; \quad \frac{M_{y,n}}{M_{y,0}} = k^n \frac{M_{x,n}}{M_{x,0}} \tag{2.24}$$

By using Pearson's second coefficient of skewness $S_p = 3(f_{mean} - f_{med}) / \sigma$, a moment-based estimate of MDF can be defined as $f_{med} = f_{mean} - \sigma S_p / 3$. The mean frequency is M_1 / M_0, the zero crossing density of the signal is $\sqrt{M_2/\pi}$ (Papoulis, 1965) and the spectral dispersion (variance) is $\sigma^2 = M_2 - M_1^2$. The coefficient of skewness is:

$$S_p = \frac{(M_3 - 3M_2M_1 + 2M_1^3)}{\sigma^3} \tag{2.25}$$

and the coefficient of kurtosis is :

$$K_p = \frac{(M_4 - 4M_3M_1 + 6M_1^2M_2 - 3M_1^4)}{\sigma^4} \tag{2.26}$$

As mentioned before, these two latter coefficients are not affected by scaling and therefore they may be used as shape change indicators. Another scale-insensitive index is the coefficient of variation C_p, defined for a normalized PSD as:

$$C_p = \left[\frac{M_2}{M_1^2 - 1}\right]^{1/2} \tag{2.27}$$

Following the same rational adopted in Equations (2.22) and (2.23), the normalized PSD showing progressive scaling without shape changes is:

$$\frac{C_p(t)}{C_p(0)} = 1; \qquad \frac{S_p(t)}{S_p(0)} = 1; \qquad \frac{K_p(t)}{K_p(0)} = 1; \tag{2.28}$$

where $C_p(t)$, $S_p(t)$ and $K_p(t)$ are the coefficients of variation, skewness and kurtosis respectively at time t during a sustained contraction. These coefficients derive from spectral estimates based on the Fourier analysis and can therefore be affected by the phenomenon of frequency leakage (related to windowing) and frequency resolution (related to the finite signal time support). To avoid these problems, a compromise should be made between length of the epochs, type of window used and length of the zero padding. An alternative to avoid these problems is the autoregressive analysis of the SEMG signal.

2.4.4. Time-Series Analysis of EMG

Some of the factors that can strongly biased the results and interpretation of SEMG signals are: large variance estimates; implicit assumption of stationarity and ergodicity; and/or signal equal zero outside the interval of interest. These are signal conditioning and processing problems and will become more critical for dynamic measurements such as signature characterization of behavioral movement patterns, functional discrimination, time evolution or comparison with other parameters like exerted force. Parametric or autoregressive identification methods (i.e. AR, ARMA models) avoid these problems, since they make no commitment to the signals outside the interval of interest and allow a compact signal description by means of p coefficients. The AR model is actually preferred for its implementation simplicity. So, in the case of the AR model, p coefficients define a filter with p poles, no zeros and an infinity long impulse response (IIIR filter). The common approach is to model the sequence from a white noise driving input with zero mean and variance σ^2. Thus, each sample of the signal s_t is assumed to be a linear combination of p previous samples (time-series) plus an uncorrelated error term n_t,

$$s_t = -\sum_{k=1}^{p} a_k s_{t-k} + n_t \qquad (2.29)$$

This particular description is equivalent to the assumption that the signal is the output of a filter whose input has a flat spectrum (white noise or delta function) and whose transfer function is defined by:

$$H(z) = \frac{1}{1 + \sum_{k=1}^{p} a_k z^{-k}} \qquad (2.30)$$

$$H(\omega) = \frac{1}{\sum_{k=1}^{p} a_k e^{-j\omega k}} \qquad (2.31)$$

in the z and ω domain respectively, hence the PSD estimate is:

$$P(\omega) = \frac{\sigma^2}{\left| 1 + \sum a_k e^{-j\omega k} \right|^2} \qquad (2.32)$$

In other words, if the signal generation model defined by equation (2.29) is valid, then the EMG signal can be described by the coefficient vector $\{a_k\}$ or the set of poles of $H(z)$ or $H(\omega)$. In reality the infinite impulse response of the filter will be truncated and the PSD defined by equation (2.32) will be different from that defined by $P(f) = |\mathfrak{I}[s(t)]|^2$, where $\mathfrak{I}$ indicates the Fourier transform (FFT). If the signal is not stationary, the coefficient $\{a_k\}$ provides a local description of the signal. Many algorithms are found for the estimation of the a_k coefficient; the most common is to multiplying both sides of the equation (2.29) by s_{t-j} with $j=1,2,...p$ taking the expected value of both sides and considering $E[s_{t-j}n_t]=0$, (uncorrelated noise), for any j yields the following set of linear equations, whose solution provides p a_k coefficients:

$$\begin{bmatrix} R(0) & . & . & . & R(p) \\ . & . & & & . \\ . & & . & & . \\ . & & & . & . \\ R(p) & . & . & . & R(0) \end{bmatrix} \begin{bmatrix} 1 \\ a_2 \\ . \\ . \\ a_{p+1} \end{bmatrix} = \begin{bmatrix} \sigma^2 \\ 0 \\ . \\ . \\ 0 \end{bmatrix} \qquad (2.33)$$

Notice that the p and a_k coefficients in equation (2.33) are related to the first p samples of the autocorrelation function of the signal, therefore that the signal can be interpreted as the output of a p+1 points prediction filter with mean square error σ^2. If the PSD of the error is uniform (white noise), this interpretation corresponds to the maximum entropy spectral estimation (Diemont and Maranzana, 1985).

The efficiency of this method depends on the right choice of the model order p. Choosing a model with too low an order results in a smoothing of the spectrum, whereas that with too high an order introduces spurious information in the spectrum. Diemont and Maranzana, (1985), compared the FFT and the autoregressive algorithms and found that a model order of 4 or 5 was sufficient to allow good estimates of the MDF and MNF for voluntary SEMG. Similarly, Merletti and Lo Conte, (1995), found that orders of 4 to 6 appear satisfactory for voluntary SEMG and orders of 8 to 11 are preferable for electrically elicited SEMG.

Finally, it is important to underline that the a_k and p coefficients are strictly mathematical descriptors of the signal and have no direct physiological correlate. However, some authors have studied the variance of the estimates of the autoregressive model coefficients and described their changes with physiological events, (like force, temperature or fatigue, etc.), by tracing their value in subsequent epochs of usually 256 samples, (Graupe and Cline, 1975; Inbar and Noujaim, 1984; Sheriff and Gregor, 1986; Paiss and Inbar, 1987; Hefftner et al., 1988; Ju et Minamitani,1990; Chang and Hwang, 1991).

2.5. FACTORS AFFECTING THE EMG SIGNAL

The factors affecting the content of the EMG signal can be of an anatomical, physiological or physical nature, such as the anatomical configuration of the muscle, the physiological properties of the muscles and surrounding media, the control scheme of the peripheral nervous system or the characteristics of the instrumentation utilized to detect and observe the phenomenon. These factors are well summarized in an recent article by Merletti et al. (1992). These researchers classify the factors affecting the content of the signal into three mayor groups: geometric factors, factors determining the mean and probability density function of CV, and factors determining the length and potential distribution of the polarized zones of the muscle fibers. The two latter factors relate to the fiber constituency of the active motor unit pool, to blood flow and to ionic shift across the muscle fiber membrane. All of these factors are ultimately related to the level of activation of the muscle and are therefore time variant.

Conversely, geometric factors are related to the tissue and electrode system spatial filtering, and the electrode location with respect to muscle fiber direction and the innervation zone and tendons. Since geometric factors are assumed to be time invariant during sustained contractions, the detected EMG signals are a function of the sources of electric field and their CV. In turn, CV, median (MDF) and mean (MNF) frequency of the myoelectric signal power spectral density functions are functions of muscle fiber diameter, intramuscular temperature and intra- and extra-cellular hydrogen concentration (pH). In addition to these factors, the control scheme of the peripheral nervous system should be taken into account, since the active motor unit pool may change during a sustained contraction due to the recruitment or derecruitment of some motor units. Further, additional factors can be introduced by hypotheses concerning conditioning and processing the SEMG signal. Choosing a proper method that can hold these hypothesis dependent directly upon the type of information or attributes to be extracted from the signal, which in turn is dependent upon the measuring conditions.

2.6. CONCLUSIONS

SEMG signals are very complex signals to be interpreted in physiological terms. Their complexity arises from the random nature of the electromyographic phenomenon and the many additional factors that can influence the content of the signal. The signal generation process exist within the detection process, both of which are implicit in the measurement arrangements and the hypotheses used in conditioning and processing the signal. The many factors influencing the content of the SEMG signal have been discussed for the generation, detection and processing processes. The main problems in dealing with SEMG signal lie in the stationarity assumption of the signal and the electrode configuration. In the end, both of these problems are highly related to the detecting electrode's morphology. In most electrodes, their surface integration effect renders the first hypothesis concerning the pure delay condition between recording sites null for some SEMG signals.

The second hypothesis relates to the electrode orientation with respect to the average muscle fiber direction and the third hypothesis concerns electrode location in reference to innervation points and tendon. Due to the fact that muscle fibers' anatomical arrangement and the filtering property of the conductive tissues change during the generation-detecting process, the surface electrodes provide a global measurement which reflects a distribution (including non-delayed signals) rather than a single value of the generation source (delayed signals only). In other words, the actual recorded signal is a mixture of propagated and non-propagated activities and rarely a pure propagated wave can be obtained.

CHAPTER THREE

ELECTRODE SPATIAL FILTERING SYSTEM

3.1 INTRODUCTION

This chapter discusses the role played by the electrode geometry and electrode system configuration in the information carried within the recorded SEMG signal. Particular emphasis is given to the spatial filtering characteristics of the electrode surface detection area and the electrode configuration in its ability to influence the delayed and non-delayed components of the signal. The most common solutions used to overcome this selectivity problem are discussed in conjunction with the non-delayed characteristics of the signal and the filtering characteristics of the electrode system. Next, optimal configurations and geometry are analyzed theoretically for their ability to reduce the influence of the non-propagated components of the signal. Finally, the conclusions aim to elucidate the specifications of an electrode system capable of responding to the various constraints presented by the generation and detection of the SEMG signal.

3.2. SPATIAL MEASUREMENT OF THE SEMG SIGNAL

From an engineering point of view, the SEMG signal is measured by sampling the two-dimensional spatial surface potential distribution by means of transducers, (electrodes), at chosen measuring sites through time. Details in the excitation process of MUAPs generate slight variations in the electric potential field at the skin surface which must then be transformed by suitable filters to distinct alterations of the measured MUAPs impulse transient conforming to the signal. However, interference in the MUAPs electric potential field is introduced by non-delayed components which are also integrated into the MUAPs electric field. Such components must be properly taken into account and be consequently suppressed by the filtering process at the measuring stage.

3.2.1 Spatial Filtering of the Electrode System

An analysis of the bipolar arrangement, which is the most selective conventional non-invasive measurement configuration, shows that the system of electrodes and amplifier constitutes the first stage filter. This first stage pre-filter is a spatial filter whose transfer function is dependent upon the geometry, interelectrode distance of the electrode system and the muscle CV. Subsequent filtering stages of the time signal are not capable of compensating for certain properties of the bipolar pre-filter. Such properties are related to the spatial integration of the electrode system (i.e. surface electrode do not discriminate among the possible sources of EMG signals propagating through the electrode's detection volume, a phenomenon refer to as cross-talk) and the inversion of polarity of a signal impulse when the excitation-propagation in the muscle is oppositely directed, (i.e. at innervation points and tendons).

Indeed, SEMG signals are known to be a mixture of delayed and non-delayed signals. Broman et al., (1985 a,b), investigating the cross-talk phenomenon, attribute the non-delayed activity to the non-homogeneous and anisotropic properties of the volume conductor. Reucher et al., (1987a) found these assumptions in agreement with their findings, however, they added that non-propagated disturbances are also due to the deformation of the electric current field at bone and to the double depolarization at the endplates and at the tendon. In addition, misalignment of the bipolar electrodes with respect to the active muscle fiber artificially reduces the interelectrode distance, thus producing a reduction effect on the CV. Sadoyama et al., (1985) proposed that theoretically the conduction velocity should be inversely proportional to the cosine of the misalignment, and their experimental values agreed with their theoretical values in the range of -15° to 10° of misalignment.

To summarize, the superposition of minutely phase shifted action potential in the vicinity of the innervation zones results in a relative increase in the high frequency components of the SEMG signal. Similarly, at either end of the muscle fiber, the relative impedance of the tendon tissue truncates the action potentials and increase the high frequency content of the signal. Further, it can be shown that an additional relative increase in the high frequency components may be introduced by a relative reduction of CV due to misalignment of the electrode pair. Moreover, selectivity of surface electrode is not limited to the anatomical border; volume conducted signals from other active sources in the vicinity will consequently contaminate those from the muscle of interest. These four non-delayed components of the signal are to be considered as transient noise affecting the frequency content of the measured SEMG signal and must be duly dealt with at the first pre-filter stage. In other words, the SEMG signal must be free of transient noise in order to be properly considered and interpreted as an authentic representation of the excitation-contraction phenomenon linking the neuro-muscular system to musculo-skeletal system through movement.

3.2.2 Conditions Required for the Filter Characteristics

The enhancement of spatial SEMG signals of the observed MUAPs which are located close to the filter axis (electrode system) requires certain filter characteristics (Reucher et al, 1987b):

a) Unchanged location of the signal maximum after filtering. Thus, the negative maximum of the input signal should be converted to an upward peak (as per EMG standard) of the output signal.

b) Sharpening of the signal peak; meaning a diminution of the distance between the central zero crossing of the input and output signals.

c) Reduction of the pickup area by attenuation of the signal amplitudes of MUAPs that are more distant in lateral direction and /or in depth with respect to the active muscle fibers of the observed MUs of interest.

While requirement a) predicates only a conservation of the signal, it does not necessarily assure an improvement of the signal features; these advantages are postulated by requirements

b) and c). In order to conserve the signal peak, phase distortion must be avoided. These are zero with filters having linear phase frequency characteristics, thus:

$$H(f_t) = \left|H(f_t)\right| \cdot e^{\frac{-j2\pi f_t d}{v} n}, k = const. \tag{3.1}$$

where d is the interelectrode distance and v is the CV. Here, all frequency components are delayed by the same phase delay time constant k. The exact moments when an excitation passes by under the spatial filter with no phase delay, ($k = 0, 1, \ldots, n$), are known as dips and they are sometimes used to estimate the CV. On the other hand, when the peak polarity is to be inverted by filtering, $(-j2\pi f_t d/v)k = \pi$ can be chosen. Therefore, suited filter transfer functions are characterized by:

$$H(f_t) = \left|H(f_t)\right|, (k = 0)$$

or

$$H(f_t) = -\left|H(f_t)\right|, \left(\frac{2\pi f_t d}{v} k = \pi\right) \tag{3.2}$$

These filters are a subgroup of those characterized by:

$$H(f_t) = real \bullet\!\!-\!\!\circ\, h(\tau) = h(-\tau) \tag{3.3}$$

where $h(\tau)$ is the filter impulse response. Filters with real $H(f_t)$ that do not fulfill Equation (3.2) for all frequencies because of periodical phase reversal (i.e., $H(f_t) = \cos(k2\pi f_t d/v)$) are also suited, when the phase reversal frequencies are out of the signal frequency range. So, based in these observations two conditions are defined for the requirements of the spatial filter characteristics as follow:

<u>Condition 1</u>: $h(\tau) = h(-\tau)$ and no phase reversal of $H(f_t)$ within the signal band pass frequency range.

<u>Condition 2</u>: $H(f_t)$ = high-pass transfer function, that is as far as the high frequency components within the frequency range concerns.

Generally speaking, when condition 1 is fulfilled, there is no delay of the signal peak due to phase influence. However, a small delay may still occur due to the frequency dependent attenuation in $H(f_t)$, that is, when the signal is not completely symmetrical on both sides of its peak. Further, a symmetrical $h(\tau)$ provides the advantage that the shape and polarity of the output signal remains unchanged, regardless of the direction (positive or negative) that the excitation field propagates along the muscle fibers. Nevertheless, although the signal peak can be conserved by a filter with a symmetrical $h(\tau)$, the width of the signal is increased, which contradicts the above mentioned requirement b). The width of the signal peak is determined particularly by the spatially low frequency components. Since the volume conductor behaves as low pass filter, the influence of the higher spatial frequencies decreases with increased distance between the measuring site and the excitation from active muscle fibers. An approach to meet the requirements b) and c) is the attenuation of the lower frequencies component. Some of the classical approach, which meet the requirement and conditions outlined above, are discussed in the next section.

3.2.3 Methods to Filtering of Transient Noise

A common approach to overcome the transient noise problems, discussed in Section 3.2.2, has been directed towards the measurement of the surface Laplacian of the potential, where spatial filters are devised at the pre-filter stage by involving some of the second spatial partial derivatives of the potential on the body surface. In practice, this can be obtained form the weighted summation of the signals from more than two electrodes, which amounts to an estimation the Laplacian, and thus forming the spatial filter output signal, (Broman et al., 1985; Reucher et al., 1987a,b; Clancy and Hogan, 1994, 1995). Specifically, in this kind of configuration, electrodes of a single spatial filter are arranged in a longitudinal or a two dimensional array with the effective measuring site being, for instance, the array center. Assuming that separate EMG sites are spatially correlated but temporally uncorrelated, the output signal of the system derives an optimal amplitude estimator. In addition, different methods have been used in combination to improve the signal to noise ratio (SNR). For instance, Broman et al., (1985) used the technique of double differentiation of a longitudinal electrode array at the pre-amplifying stage. Reucher et al., (1987) improved the signal by means of weighting functions applied to a two dimensional array. Clancy and Hogan, (1994) achieved a good SNR by temporal whitening of individual signals from a two dimensional array follow by a spatio-temporal moving-average root mean square (MARMS) filter.

Generally speaking, in order for the electrode system to efficiently suppress non-propagated disturbances, their spatial wave lengths must be long compared to the interelectrode length of the spatial high-pass filter system. If this is not the case, signal peaks that are not directly correlated with the propagation of the action potential will probably occur in the pre-filter output signals. Reucher et al., (1987) using a compact spatially multiple differentiating configuration (total filter length 8 mm), observed non-propagated disturbances only near the tendons but never at the innervation sites, and concluded that their filter configuration was very effective in suppressing these latter disturbances. Broman et al., (1985) used a configuration of four bar electrodes with an interelectrode distance of 10 mm to produce a double differentiation on three pair of electrodes, and thus with a total equivalent filter length 40 mm, demonstrated that their configuration was efficient to suppress only long wave disturbances such as those volume conducted from far distances (cross-talk).

Clancy and Hogan (1995) used an array of 2 by 4 electrodes placed latitudinally across the biceps and triceps muscle of the elbow, and then assuming that EMG waves were spatially and temporally correlated they proceeded with two filter operations. They first filtered each respective site with a temporal whitening filter derived from the PSD's of each site and second, filtered the whitened sequences via n-input, n-output linear transformation, (with n being the n-site signal). These inverse filters orthogonalize the data samples, thus allowing a detection algorithm to operate in each output sample independently on the bases of the temporally whitened, spatially uncorrelated samples. According to these authors, their method performs at its best between 10 to 75 % maximum voluntary contraction, doubling or tripling the SNR.

It is obvious that these methods have their advantages and disadvantages. Further, each method evidently biases to some extent its solution to particular aspects of the transient noises problem previously described. Broman et al., (1985) concentrated on the cross-talk problem and therefore the double differentiation configuration solution only apply to suppression of undelayed signals from extremely distant source. Taken into consideration the small geometry and the specific disturbances, this configuration can be assumed to act in practice as a matched filter approach. On the other hand, Reucher et al., (1987) were concerned with disturbances from innervation zones. They not only succeeded in suppressing this kind of disturbance but also managed to device a highly selective spatial filter ideal for the study of individual MUs or very small muscles, like those of the hand. However, this kind of configuration has little influence in practice in reducing cross-talked signal, since the spectral content of these disturbances are in the spectral band of the undisturbed signal. Further, it loses a portion of the global information of the muscle when used in other areas of the body or situations where subjects have thicker layer of fat. The obvious solution to these inconvenience is to increase the electrodes' diameter and spacing, with the disadvantage of increasing the spatial filter configuration.

Finally, Clancy and Hogan, (1995) were interested in isolating particular site signals from the influence of neighboring signals for multiple control of prostheses and therefore it can be said also in the problem of cross-talk. They achieved this quite well, however their method is cumbersome and although the system can be devised conveniently in an hybrid circuit, it does not make practical the study of whole muscle systems. Further, they did not provide information concerning other types of disturbances.

3.3. ELECTRODE SPATIAL INTEGRATION EFFECTS

Most of the studies concerning the electrode effect on SEMG degradation are related mainly to electrical properties of the electrode itself (Geddes and Baker, 1989), to the electrode-electrolyte-skin interface (Geddes et al., 1987) or to the configuration of the electrode system (Broman et al., 1985; Reucher et al., 1987; Clancy and Hogan, 1995). However, little attention has been paid in the literature to the integration effect of the electrode detection area and geometry. Traditionally, this integration has normally been described in terms of the simple addition of filtered motor units activities within a *detection point*, and thus considers the electrode's surface detection area negligible. In fact, the most popular model has been described by De Luca (1984), who constructed SEMG from impulse trains randomly distributed and added, after filtering under an electrode of a type often considered as a zero-surface detection point.

Only a few works deal with the effect of a single (or several) MU under an electrode whose surface is not negligible (Helal and Bouissou, 1992). On the other hand, most works try to resolve spatially distributed muscle electrical activity by estimating the surface Laplacian from a body surface potential measured by means of electrode arrays. Just a few researchers have tried to measure the surface Laplacian of the potential directly from the skin surface, (Fattorusso and Tilmant, 1949; van Oosterom and Strackee, 1983; Bhullar et al, 1990; He and Cohen, 1992). This has been achieved through use of a center electrode encircled by a coaxial ring electrode; however none of these researchers have analyzed the requirements and conditions under which this measurement might be valid (outlined in Section 3.2.2, page 47).

Further, all of these measurements have been performed on ECG signals with the sole exception of Bhullar et al., (1990), who proposed an electrode set composed of a central circular electrode surrounded by a second active electrode made of a ring, and then surrounded by a third ring electrode acting as a reference. In their analysis they considered the electrode set to act as a double differential configuration and therefore obtained a transfer function similar to that shown in Equation 2.9 (page 31, Chapter Two). Even though this kind of configuration clearly enhances selectivity, the assumption of double differential configuration made lacks solidity and therefore it must be confirmed by also taking into account in the analysis the contribution of closed equipotential surface near the recording electrode.

In the following section, the effects of spatial integration are discussed in conjunction with the Laplacian effects of a circular concentric electrode, also referred to as bipolar concentric or coaxial or Laplacian electrodes. A mathematical analysis of the electrode's spatial integration effect on the SEMG is presented for monopolar, bipolar, double differential and bipolar concentric or Laplacian electrodes. This theoretical analysis is inspired by Helal and Bouissou's (1992) work on monopolar configurations, which to date is the only work available on the particular theme of the electrode's surface spatial integration effects. On this basis, a theoretical analysis is carried out using electrode system models based on the classical muscle fiber model develop by Lindstrom (1970).

3.3.1. Lindstrom's Muscle Fiber Model

According to Lindstrom (1970) and Rosenfalck (1969), the electric field in a biological medium depends upon the charge distribution and the electric permeability. From the classical model made of an infinite cylinder developed by Lindstrom (1970), it is assumed that a single action potential moving along a muscle fiber can be modeled as an infinite cylinder (see Figure 3.1 below). The electrical potential must satisfy the Laplace equation and the boundary condition on the membrane surface. Based on these conditions and by using the frequency domain approach, Lindstrom has demonstrated that the Fourier transform of the electric potential can be found in cylindrical coordinates as:

$$V(r, x, f) = \frac{1}{v} \frac{J_0(j2\pi rf/v)}{J_0(j2\pi af/v)} \vartheta(f/v) e^{j2\pi xf/v} \tag{3.1}$$

where: f is the frequency [cycles/m]; $\vartheta(f/v)$ is the spatial action potential of the fiber (as well as the boundary condition $r = a$); v is the conduction velocity [m/s]; r and x are the cylindrical coordinates defined from the axis system in Figure 3.1 [m]; and $J_n(\chi)$ is the nth-order Bessel function of the first kind. Based on this model and Equation (3.1), the transfer function for the various proposed configuration and geometry can be found in the sections to follow.

3.3.2 Transfer Function of a Monopolar Electrode

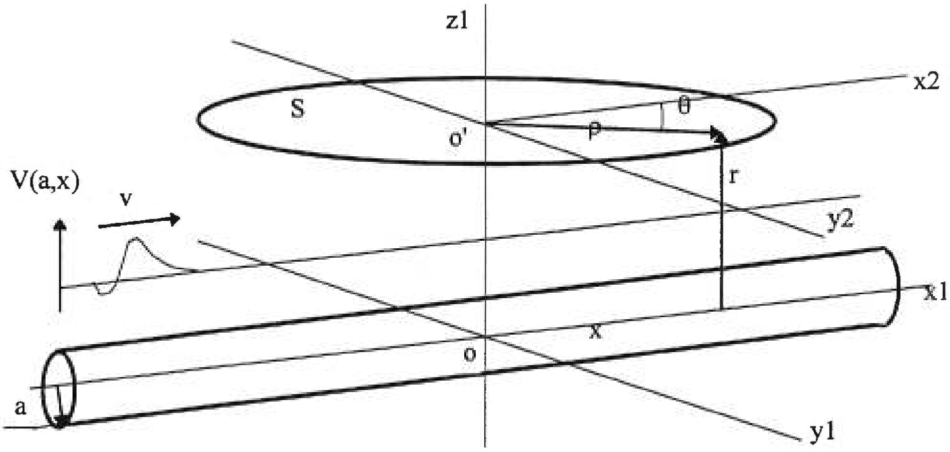

Figure 3.1 <u>**Monopolar electrode model**</u>: points of the surface S can be specified in cylindrical coordinates (r,φ,x) in the (O, x1,y1,z1) axis system. Given the axial symmetry of the cell, φ can be ignored. Muscle fiber runs along axis x1. The center of the electrode is located at the coordinates (r,0). Assuming an axial symmetry of the membrane properties, the electrical potential is denoted as V(r,x). A spatial action potential φ(x), moving with velocity *v* along the fiber, is also the boundary condition for the potential V(a,x), where *a* is the radius of the cell. The surface electrode is described by a conducting disk with diameter *d* placed on the skin. Each point of the disc is specified in polar coordinates (ρ,θ) in the (0',y2,x2) axis system, (as proposed by Helal and Bouissou, 1992).

Considering the electrode on the surface of the skin as a disk without resistance and with a constant internal potential, it is then assumed that the electrode itself alters the observable field distribution (see Figure 3.1 above). Further, from the superposition principle and considering the linear property of the Fourier transform, the detected potential in the electrode can be calculated using the following integral, (as per Helal and Bouissou, 1992):

$$V_m(r,d,f) = \frac{1}{S}\int_S\int V(r,x,f)\,dS \tag{3.2}$$

where d and S are the diameter and the surface of the electrode, respectively. In order to simplify the model, two further assumptions must be made: that the value of x at the electrode center is zero and that the fiber depth is much greater than the electrode diameter ($r >> d$). Next, it is considered that r remains constant at each point of the disc. Then, introducing equation (3.1) into equation (3.2), the detected potential can be computed as:

$$V_m(r,d,f) = \frac{1}{S}\int_S\int \frac{1}{v}\frac{J_0(j2\pi rf/v)}{J_0(j2\pi af/v)}\vartheta(f/v)e^{j2\pi xf/v}dS \tag{3.3}$$

$$= V(r,0,f)\frac{2}{S}\int_{\rho=0}^{d/2}\int_{\theta=0}^{\pi} e^{j2\pi f\rho\cos\theta/v}\rho\, d\rho\, d\theta \tag{3.4}$$

(from Helal and Bouison, 1992), where ρ and θ are the cylindrical coordinates; $V(r,0,f)$ is the Fourier transform of the potential at the center of the electrode; and $x = \rho\cos\theta$. Then, as proposed by Helal and Bouissou, the transfer function for a monopolar electrode can be defined as:

$$H_m(d,f) = \frac{V_m(r,d,f)}{V(r,0,f)} = \frac{2}{S}\int_{\rho=0}^{d/2}\rho\left[\int_{\theta=0}^{\pi} e^{j2\pi f\rho\cos\theta/v}d\theta\right]d\rho \tag{3.5}$$

Using Helal and Bouissou method to solve the integral, the transfer function is obtained as (see Appendix I for the demonstration):

$$H_m(d,f) = \frac{2J_1(\pi df/v)}{\pi df/v} \tag{3.6}$$

From Figure 3.2 below, we observe that the spatial integration of a monopolar electrode results in a low pass filter effect which is dependent on the d/v ratio and the Bessel function $J_1(\pi df/v)$. The shape of the monopolar surface electrode filter is given by the ratio $J_1(\pi df/v)/(\pi df/v)$. Notice also that the spatial integration induces dips corresponding to the zero value of the Bessel function $J_1(\pi df/v)$. The effects of diameter d and CV v on the filter function are depicted in Figure 3.3 below. Notice that an increase of the diameter causes a reduction in the cut off frequency with a faster roll off of the filter function which results in a spectrum compression towards low frequencies, thus giving more predominance to the low frequency content of the signal. Conversely a reduction of the electrodes diameter results in a broadening of the spectrum towards higher frequency with a higher cutoff frequency and a slower roll off rate, thus higher frequency components will contribute more to the total energy of the signal.

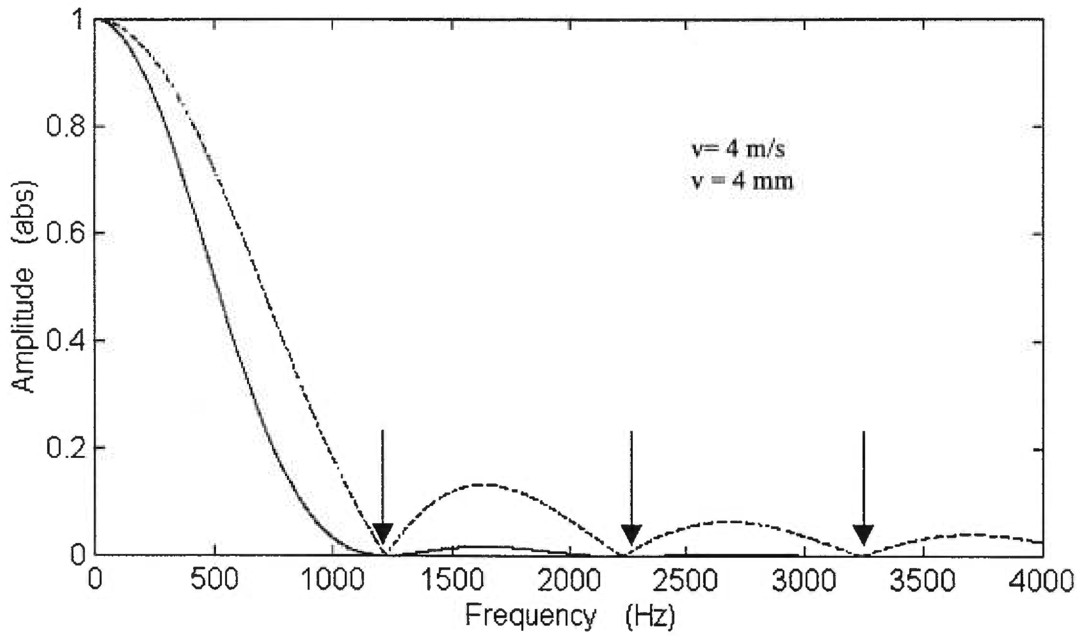

Figure 3.2 **Monopolar electrode transfer function plot**. Solid line indicates the square of the function. Dashed line indicates the Bessel function ratio $J_1(\pi df/v)/(\pi df/v)$ representing the transfer function. Notice that the function has real values. Dips are indicated by the arrows.

Since the bulk of SEMG energy is expected within the 20 to 300 Hz bandpass range with a median frequency between 120 to 170 Hz, it is obvious from these observations that a larger electrode offers a the better signal to noise ratio (SNR) but also induces the lowest cutoff frequency in the transfer function. Less dramatic changes are observed for changes in the CV, higher CVs produce a shift towards higher frequencies and lower CVs result in a compression of the spectrum towards lower frequencies, (expected from the relationship $f_t = v/\lambda$.).

These theoretical results on the monopolar electrode filter properties are quite consistent with those described by Lindstrom (1970) and Helal and Bouissou (1992). Based on these observation we corroborate that the surface of the electrode, as well as tissues, acts a low pass filter on the SEMG signal. Furthermore, just as in the tissue transfer function (see Equations 2.4, 2.5 and 2.6, page 28, Chapter Two), the electrode transfer function in Equation (3.6) also depends on the f/v ratio, meaning that the direct relationships between the CV and spectral moments can still be verified, (Hannaford and Lehman, 1986).

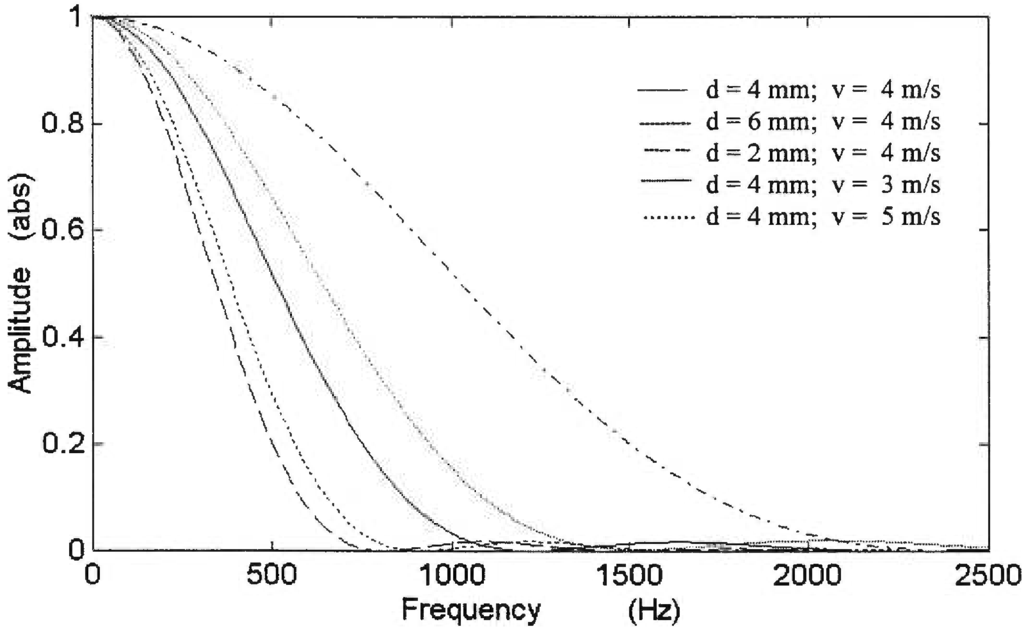

Figure 3.3. Effects of the electrode diameter and CV. Plot of monopolar transfer function as a function of the electrode diameter *d* and conduction velocity *v*.

3.2.2 Transfer Function of a Bipolar Electrode

To calculate the bipolar electrode transfer function including the spatial integration of the electrode area, reasoning similar to that for the monopolar electrode can be followed. Again for simplicity, it can be assumed that the Fourier transform of the potential at the center of both electrodes is the same. And both disks of diameter *d*, representing the electrodes, are considered without resistance and with a constant internal potential. The value *x* at the center of the electrodes is -*h*/2 and *h*/2, respectively, with *h* being the interelectrode distance (see Figure 3.4 below). The distance *r* from the electrodes to the fiber is the same for both disk at all times and remains constant; it is also assumed that *r* >> *d*, therefore the detected potential in the middle of a bipolar electrode system can be calculated using Equation 3.5 as:

$$H_b(d,f,h) = \frac{2}{S_1}\int_{\rho=0}^{d/2}\int_{\theta=0}^{\pi} e^{j2\pi f(-h/2+\rho\cos\theta)/v}\rho\, d\rho\, d\theta$$

$$+\frac{2}{S_2}\int_{\rho=0}^{d/2}\int_{\theta=0}^{\pi} e^{j2\pi f(h/2+\rho\cos\theta)/v}\,\rho d\rho d\theta \qquad (3.7)$$

where h is the interelectrode distance; ρ and θ are the cylindrical coordinates, $x_1 = -h/2 + \rho\cos\theta$ and $x_2 = h/2 + \rho\cos\theta$.

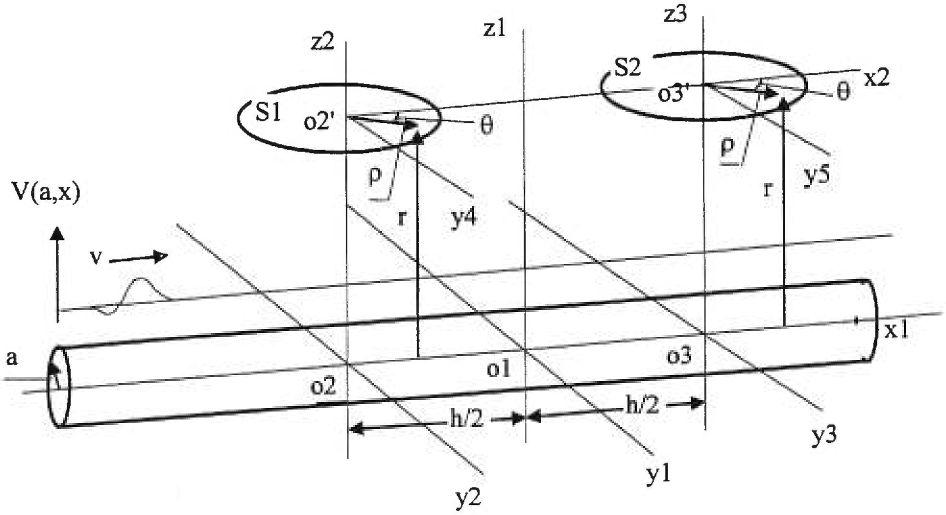

Figure 3.4 **Bipolar electrode model**: points of the surfaces S1 and S2 can be specified in cylindrical coordinates (r,φ,x) in reference to the (O1, x1,y1,z1) axis system. Given the axial symmetry of the cell, φ can be ignored. Muscle fiber runs along axis x1. The center of the electrodes are located at the coordinates (r,-h/2) and (r,h/2), respectively. Assuming an axial symmetry of the membrane properties, the electrical potential is denoted as V(r,x). A spatial action potential ϕ(x), moving with velocity *v* along the fiber, is also the boundary condition for the potential V(a,x), where *a* is the radius of the cell. The surface electrodes are described by a conducting disks with diameter *d* placed on the skin. Each point of the disks is specified in polar coordinates (ρ,θ) in the (02',y4,x2) axis system and (ρ,θ) in the (03',y5,x2) axis system.

Solving the integral, the transfer function for a bipolar electrode is defined as (see Appendix I for demonstration):

$$H_b(d,f,h) = \left[\frac{1 - e^{j2\pi fh/v}}{e^{j\pi fh/v}}\right] \times \frac{2J_1(\pi df/v)}{\pi df/v} \qquad (3.8)$$

Equation 3.8 above provides a more complete mean for study of the surface electrode properties. Notice that in reality the shape of the transfer function for a bipolar electrode is given by the product of the interelectrode distance effects and the electrode's spatial integration effects. In fact, using Euler's exponential relation $e^{j\theta} - e^{-j\theta} = 2j\sin\theta$ it can be demonstrated that the first term on the right side of Equation 3.8 indeed corresponds to Lindstrom's transfer function for a bipolar electrode with negligible surface area ($H_b = 2j\sin\pi fh/v$, Equation 2.4, page 29, Chapter Two), conversely the second term is the transfer function corresponding to the spatial integration of the monopolar electrode as shown in Equation 3.6. Both of these effects are illustrated in Figure 3.5 below.

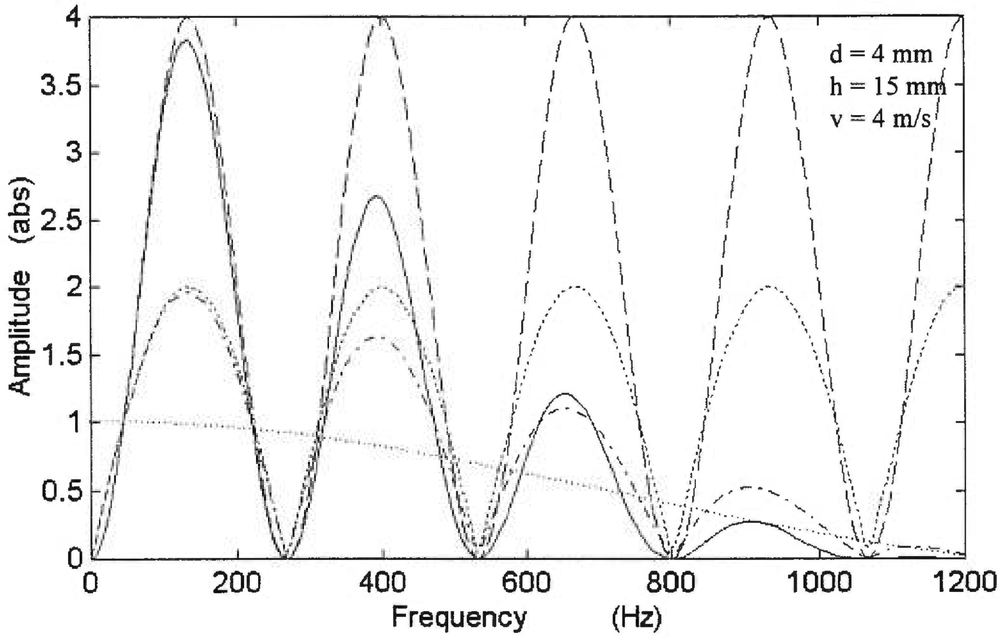

Figure 3.5 **Bipolar electrode transfer function plot.** Small dotted line indicates the Bessel function ratio $J_1(\pi df/v)/(\pi df/v)$ representing the spatial integration effects of the monopolar electrode. Large dotted line indicates the first term of the function $(1-e^{j2\pi fh/v})/e^{j\pi fh/v} = 2j\sin\pi fh/v$ representing the effect of the interelectrode distance. Dash-dotted line indicates resultant bipolar electrode transfer function. Solid line indicates the square of the function. Dashed line indicates the square of the first term of the function. Notice that the function has imaginary values. Dips are indicated at the zero value of the function.

The sinusoidal filter shape representing the effect of the interelectrode distance in the transfer function for the bipolar configuration is depicted in large dotted line, with the dashed line indicating its square. Observe that including the influence of the spatial integration of the electrode's surface detection area in the transfer function (see Equation 3.6), does not result in a significant change in the shape of the transfer function. Indeed, it will produce only a slight attenuation of the signal with a slight shift of the spectrum towards low frequencies. Observe as well that the transfer function depends on the ratio *fh/v* , showing dips at frequencies *f* = k *v/h*, for all k = 0,1,2,....n, and therefore that direct relationships between CV and the spectral moment can still be confirmed. Since phase reversals are expected at dip frequencies, then condition 2 (high pass filter, see Section 3.2.3) is fulfilled for frequencies *f* < *v*/2*h*; however condition 1 is not fulfilled since the zero crossing of the output signal will be at *h*/2, thus at a point when the maximum of the input signal is at the center of the electrode array.

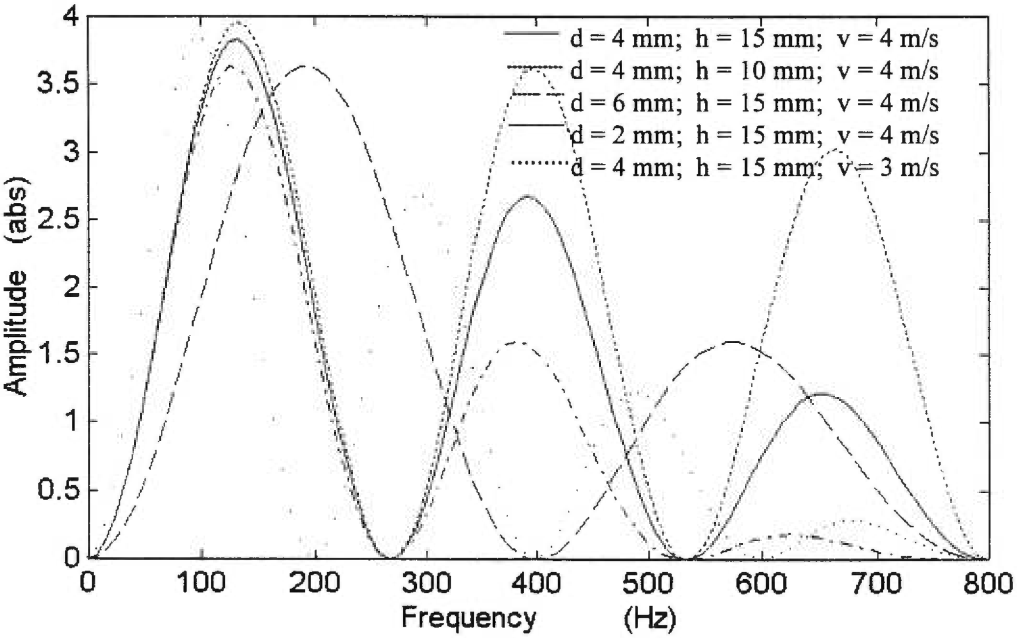

Figure 3.6 **Effects of the electrode diameter, CV and interelectrode distance.** The square of the bipolar transfer function for various combination of *d*, *h* and *v* are depicted as indicated by the different line style.

Furthermore, two excitations propagating in opposite directions will yield different output signals with inverted polarities of the signal peaks. Under these conditions, even when the electrode's surface spatial integration effects are taken into consideration, the bipolar configuration still shows a better SNR and higher selectivity than the monopolar configuration and the diameter of the electrode plays a minor role in the shape of the filter as compared to the interelectrode distance (solid line in Figure 3.5). Consequently, the filter can be considered as a low bandpass matched filter, the effect of which is dependent on the d/v ratio, the Bessel function $J_1(\chi)/\chi$, the h/v ratio and the $\sin(\omega)$ function.

The influence of the electrode diameter d, the interelectrode distance h and the CV v on the shape of the bipolar surface electrode filter is depicted in Figure 3.6 above. As mentioned before, the interelectrode distance h has the strongest influence on the shape of the filter function, overriding the influence of the diameter d in the spatial integration effect seen for a monopolar. In this case, a reduction in the inter electrodes distance h results in shifting the spectrum towards high frequencies (dashed line compared to solid line in Figure 3.6) with an increase in the filter's bandwidth. This again is expected from the relationship $f_t = v/\lambda$; signals with a wave length longer than the interelectrode distance will be more strongly suppressed, thus enhancing the signal's high frequency content.

On the other hand, a reduction of the interelectrode distance h results in a reduction of the SNR with an increase in the power of the signal, which can be inferred from a lower amplitude and a larger area under the filter function curve due to the increase in the bandwidth.

Conversely, a reduction in the CV v results in a compression of the spectrum with a shift towards lower frequencies, thus the CV also has a strong influence in the bandwidth of the filter, a phenomenon which again should be expected from $f_t = v/\lambda$. It is worth mentioning here that since MUAPs with different CV contribute to the SEMG signal, the shape of the electrode filter should be expected to change as the CV changes during the detection process. This is discussed in more detail at the end of this chapter. On the other hand, changes in diameter are related more to the SNR; the larger the diameter the smaller the SNR and the smaller the diameter the higher the SNR, thus selectivity can be controlled by the diameter size.

3.2.3 Transfer Function of a Double Differential Electrode

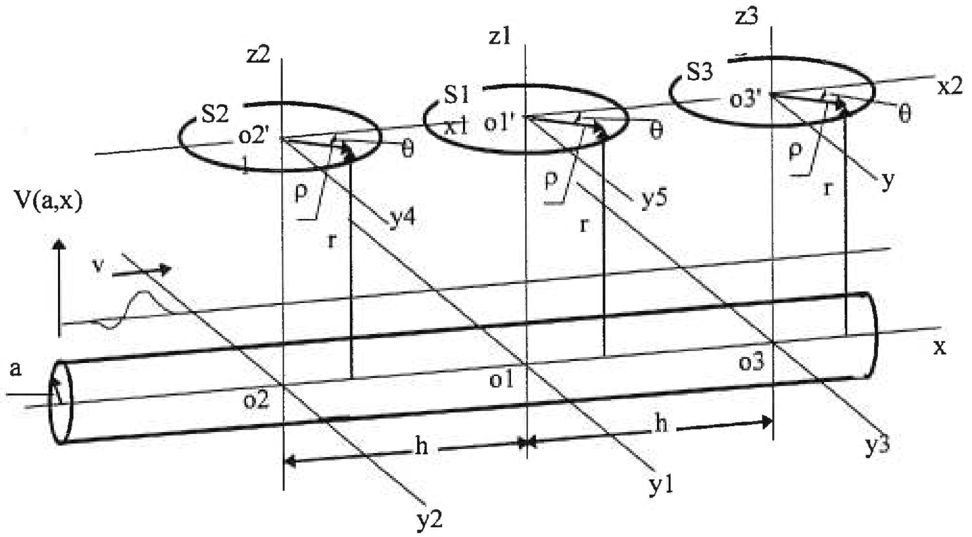

Figure 3.7 **Double differential electrode model**: points of the surfaces S1, S2 and S3 can be specified in cylindrical coordinates (r,φ,x) in reference to the (O1, x1,y1,z1) axis system. Given the axial symmetry of the cell, φ can be ignored. Muscle fiber runs along axis x1. The center of the electrodes are located at the coordinates (r,-h),(r,0) and (r,h), respectively. Assuming an axial symmetry of the membrane properties, the electrical potential is denoted as V(r,x). A spatial action potential ϕ(x), moving with velocity v along the fiber, is also the boundary condition for the potential V(a,x), where *a* is the radius of the cell. The surface electrodes are described by a conducting disks with diameter *d* placed on the skin. Each point of the disks is specified in polar coordinates (ρ,θ) in the (02',y4,x2) axis system for *S*2, (ρ,θ) in the (01',y5,x2) axis system for *S*1 and (ρ,θ) in the (03',y6,x2) system for *S*3.

Continuing the same reasoning; the transfer function of a double differential electrode system can be calculated by applying all assumptions made until now to the double differential model. In this case, however, the electrodes are represented by 3 disks with the central disk located at the coordinated system (O1',x1,y5,z2), as shown in Figure 3.7 above. The value *x* at the center of each of the electrode disks is -*h*, zero and *h*, respectively, with *h* being the interelectrode distance (see Figure 3.7); if ρ and θ are expressed in cylindrical coordinates, therefore $x_1 = -h/2 + \rho\cos\theta$ and $x_2 = h/2 + \rho\cos\theta$. The distance *r* from the electrodes to the fiber is the same for the three disks at all times and remains constant. Again, it also is assumed that $r >> d$, therefore the detected potential in the middle of the tripolar electrode system can be calculated using Equation 3.5 as:

$$H_{dd}(d,f,h) = \frac{2}{S_1}\int_{\rho=0}^{d/2}\int_{\theta=0}^{\pi} e^{j2\pi f(-h+\rho\cos\theta)/v}\rho\, d\rho\, d\theta$$

$$+\frac{2}{S_3}\int_{\rho=0}^{d/2}\int_{\theta=0}^{\pi} e^{j2\pi f(h+\rho\cos\theta)/v}\rho\, d\rho\, d\theta$$

$$-2\frac{2}{S_1}\int_{\rho=0}^{d/2}\int_{\theta=0}^{\pi} e^{j2\pi f\rho\cos\theta/v}\rho\, d\rho\, d\theta \qquad (3.9)$$

Solving the integral, the transfer function for a double differential electrode including the spatial integration effect is defined as (see Appendix I for demonstration):

$$H_{dd}(d,f,h) = \left[\frac{1+e^{j4\pi fh/v}-2e^{j2\pi fh/v}}{e^{j2\pi fh/v}}\right] \times \frac{2J_1(\pi df/v)}{\pi df/v} \qquad (3.10)$$

From Equation 3.10 above, notice that the shape of the transfer function for a double differential electrode is also given by the product between the interelectrode distance effects and the electrode's spatial integration effects. Again, using Euler's exponential relationship $e^{j\theta}+e^{-j\theta}=2\cos\theta$, it can be shown that the first term of the right side of Equation 3.10 corresponds to the transfer function for a double differential electrode configuration where the electrode's surface area is considered negligible ($H_{dd}= 2[\cos(2\pi fh/v)-1] = -2\sin^2(2\pi fh/v)$, Equation 2.9, page 31, Chapter Two). Conversely, the second term of Equation 3.10 is the transfer function corresponding to the spatial integration of the monopolar electrode as shown in Equation 3.6. Notice that with this configuration the phase $\pi/2$ of the bipolar filter has been transformed into the a phase π, allowing the double differential filter to fulfill Equation 3.3 and therefore remain independent of the direction of the excitation propagation. Also since the phase is constant = π, the impulse response is symmetrical, fulfilling condition 1. Observe as well that, the high pass filter characteristics (condition 2 is fulfilled) are much more pronounced for frequencies $f < v/2h$ than with the bipolar filter.

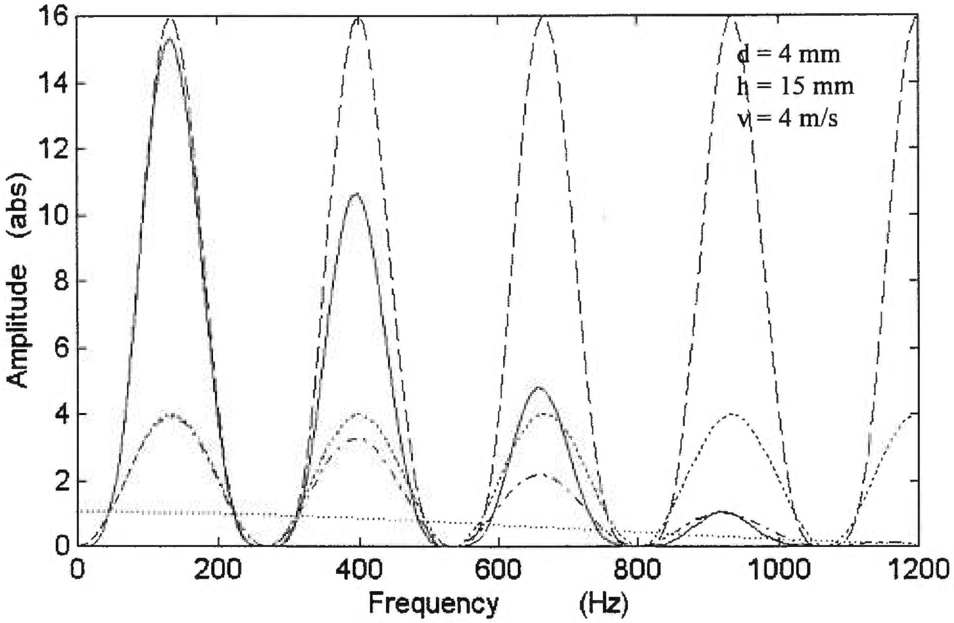

Figure 3.8 **Double differential electrode transfer function plot.** Small dotted line indicates the Bessel function ratio $J_1(\pi df/v)/(\pi df/v)$ representing the spatial integration effects of the monopolar electrode. Large line indicates the first term of the function $(1+e^{j4\pi fh/v}-e^{j2\pi fh/v})/\ e^{j2\pi fh/v} = -2\sin^2(2\pi fh/v)$, representing the effect of the interelectrode distance. Dash-dotted line indicates resultant double differential electrode transfer function. Solid line indicates the square of the function. Dashed line indicates the square of the first term of the function. Notice that the function has real values. Dips are indicated at the zero value of the functions.

Both effects, the interelectrode distance and the electrode's surface spatial integration, are illustrated in Figure 3.8 above. The sinusoidal shape of the transfer function for the double differential configuration indicates only the interelectrode effect and is depicted in large dotted line, with the dashed line indicating its square value. The low pass shape of the Bessel ratio transfer function indicates the spatial integration effect of the electrode's surface area, depicted in small dotted line. The first observation that can be made from Figure 3.8 below is that, compared to the bipolar configuration (see Figure 3.5), the double differential configuration has doubled the gain with a slight compression on the bandwidth.

The implication is that a faster roll-off is obtained for essentially the same bandwidth, thus enhancing the frequency content at the center frequency with a rapid suppression of the lower and higher frequencies components. The practical implication is that a higher selectivity is achieved for frequencies around the center frequency of the transfer function. Again, since the transfer function depends on the ratio *fh/v* , showing dips at frequencies $f = k\ v/h$, for all k = 0,1,2,....n, the direct relationships between CV and spectral moment can still be confirmed.

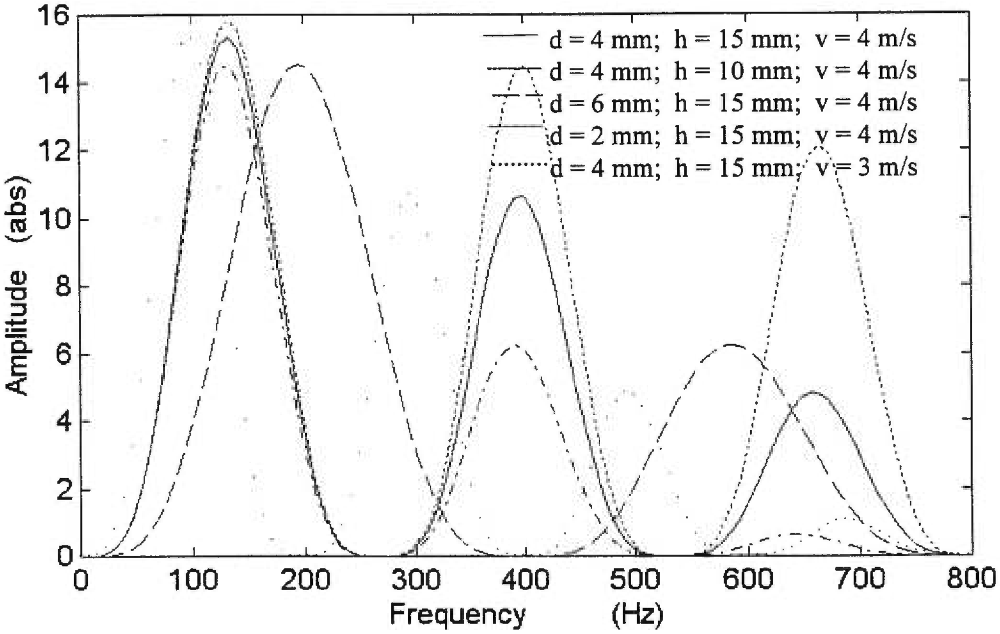

Figure 3.9 **Effects of the electrode diameter, interelectrode distance and CV.** The square of the double differential transfer function for various combination of *d*, *h* and *v* are depicted as indicated by the different line style.

The effects of the electrode diameter *d*, the interelectrode distance *h* and CV *v* on the shape of the filter can be appreciated from Figure 3.9 above. These effects are very similar to those observed for a bipolar configuration. Here again we notice that the influence of the interelectrode distance *h* overrides the influence of the diameter *d* on the shape of the filter. The main difference in comparison with the bipolar configuration is that the spectrum amplitude has been increased in its square value, with a slight reduction in the bandwidth (see Figures 3.7 and 3.9 for comparison). As for the interelectrode distance *h* and CV *v*, these two parameters still have a major influence in the bandwidth of the spectrum and the diameter *d* has even less influence in the SNR ratio than that observed for the bipolar configuration. Once again, it should be kept in mind that the parameters *h* and *d* are time invariable and that they depend mainly on the electrode system geometry and configuration and detection setup. The CV parameter *v*, however, is time dependent and therefore will introduce a dynamic constraint on the shape of the filter. Observe once more that a reduction in the CV *v* results in a compression of the spectrum with a shift towards lower frequencies and increase of the filter's gain. Conversely, an increase in the CV *v* results in an expansion of the bandwidth with a shift towards higher frequencies and a reduction of the filter's gain. In other words, the CV has a strong influence on the bandwidth and gain of the filter, as can be expected from the relation $f_t = v/\lambda$.

3.2.3 Transfer Function of a Concentric Electrode

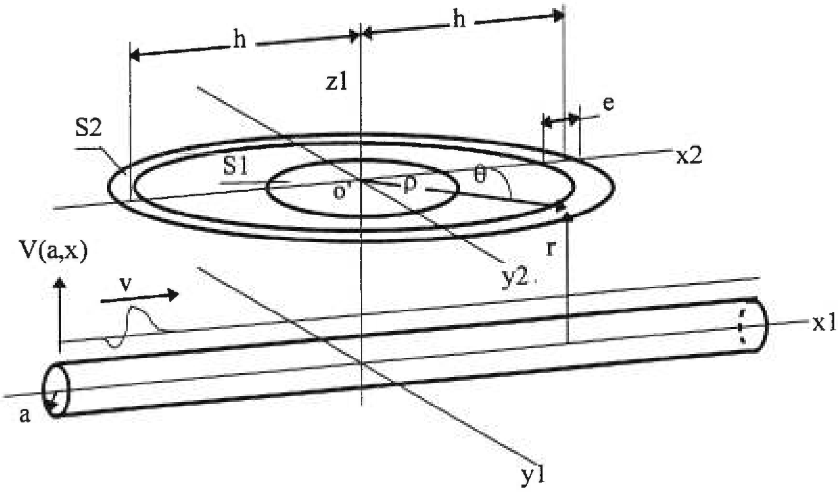

Figure 3.10 **Concentric electrode model**: points of the surfaces S1 and S2 can be specified in cylindrical coordinates (r,φ,x) in reference to the (O, x1,y1,z1) axis system. Given the axial symmetry of the cell, φ can be ignored. Muscle fiber runs along axis x1. The concentric electrodes are located at the coordinates (r,0). Assuming an axial symmetry of the membrane properties, the electrical potential is denoted as V(r,x). A spatial action potential φ(x), moving with velocity *v* along the fiber, is also the boundary condition for the potential V(a,x), where *a* is the radius of the cell. The surface electrodes are described by a conducting disks placed on the skin with diameter *d* for the inner disk and $h=(d_2+d_1)/4$ for the outer ring of thickness $e=(d_2-d_1)/2$. Each point of the inner disks and outer ring is specified in polar coordinates (ρ,θ) in the (0',y2,x2).

To calculate the transfer function of a concentric electrode, we can model the electrode configuration system on the surface of the skin as a center disk with a concentric ring (see

Figure 3.10 below). If both, disk and ring, are considered without resistance and with a constant internal potential, then it can be assumed that the electrode system itself alters the observable field distribution. Once more, from the superposition principle and considering the linear property of the Fourier transform, the detected potential in the electrode can be calculated using the following integral expression:

$$H_c(d,f,h,e) = \frac{2}{S_2}\int_{d_1/2}^{d_2/2}\int_{\theta=0}^{\pi} e^{j2\pi f\rho\cos\theta/v}\rho\,d\rho\,d\theta$$

$$-\frac{2}{S_1}\int_{\rho=0}^{d/2}\int_{\theta=0}^{\pi} e^{j2\pi f\rho\cos\theta/v}\rho\,d\rho\,d\theta \quad (3.11)$$

where d is the diameter of the center disk; d_1 and d_2 are the internal and external diameters of the concentric ring, respectively; S_1 and S_2 are the surface area of the ring and disk, respectively; ρ and θ are the cylindrical coordinates with $x = \rho\cos\theta$. Two further assumptions are made: the value of x at the common center of the electrodes disk and ring is zero and the fibers depth is much greater than the electrode diameter ($r >> d$). After solving the integral, (see Appendix I for demonstration), the transfer function for a concentric electrode can be defined as:

$$H_c(d,f,h,e) = \left[\frac{(2h+e)J_1\left(\pi f(2h+e)/v\right)}{4\pi fhe/v} - \frac{(2h-e)J_1\left(\pi f(2h-e)/v\right)}{4\pi fhe/v}\right]$$

$$-\left[\frac{2J_1\left(\pi df/v\right)}{\pi df/v}\right] \quad (3.12)$$

where d is the central electrode diameter; h is the interelectrode distance defined as $h = (d_2+d_1)/4$; and e is the ring thickness defined as $e = (d_2-d_1)/2$ (see Figure 3.10); $J_1(\chi)$ is the first order Bessel function of the first kind. Equation 3.12 is composed of two subtracting terms, the first term on the right side of the Equation corresponds to the spatial integration due to the geometry of the ring component, and the second term corresponds to the spatial integration due to the central disk component. This transfer function somehow differs from the structure obtained in the former transfer functions for the bipolar and double differential electrode configuration. However, for comparative purposes, Equation 3.12 can also be expressed as product of the center electrode transfer function. First, let us define the following variables:

$$\lambda_1\chi = \pi f(2h-e)/v; \qquad \lambda_2\chi = \pi f(2h+e)/v;$$

$$\chi = \pi f d/v; \qquad k = S_2/S_1 = 8\,h\,e/d^2,$$

where k is the ratio between the concentric ring surface area and the central disk surface area. Then, after substitution into Equation 3.12 and rearranging, the transfer function for the concentric electrode system is expressed as:

$$H_c(\chi,\lambda_2,\lambda_1,k) = \left[\frac{\lambda_2 J_1(\lambda_2\chi) - \lambda_1 J_1(\lambda_1\chi)}{kJ_1(\chi)} - 1\right] \times \frac{2J_1(\chi)}{\chi} \qquad (3.13)$$

The transfer function for the concentric electrode system is now expressed as a product where the second term in the right side of the equation corresponds to the spatial integration effect of the central electrode, just as in the previous transfer function for the bipolar, (Equation 3.8) and double differential, (Equation 3.9) configuration systems. Notice that, in both versions of the transfer function for the concentric electrode system (Equ 3.12 and 3.13), the interelectrode distance parameter h and the outer ring thickness e are implicit in the geometry of the coaxial ring electrode and also that, in this configuration the diameter d of the center electrode takes a more predominant influence in the shape of the filter function.

The influence of the center electrode Bessel function depends on the surfaces area ratio parameter k. These parameters (h, e, d, k) give already a notion of possible performance improvement and of the increased flexibility in spatial filter design of a 2-D electrode system as required for a true surface Laplacian measurement. In fact, since the EMG source produce negligible charge density in the tissue, (Rosenfalck, 1969), the Laplace equation is valid and can be expressed as:

$$\nabla^2_{xy}\Phi = -\frac{\partial^2\Phi}{\partial z^2} = \frac{\partial^2\Phi}{\partial x^2} + \frac{\partial^2\Phi}{\partial y^2} \qquad (3.14)$$

where $\nabla^2_{xy}\Phi$ represents the divergence of the impressed current which is proportional to the equivalent charge density just inside the body surface, this later is represented by the orthogonal plane x-y to the z axis, (see Figure 3.10 below).

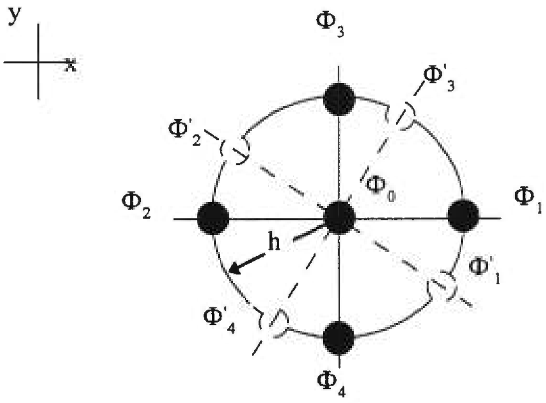

Figure 3.11 **Schematic of a concentric circular Laplacian measurement.** The surface Laplacian (or equivalent charge density) at the center electrode site 0 is estimated from the potential difference between the average potential at equidistant sites 1 to 4 and the center site. Similarly, the potential at the center electrode site 0 is obtained for another average potential difference at sites 1' to 2' if the axes *x*-*y* are rotated around center 0 and so on for sites n'. The potential difference between the average potential over the entire surface of the coaxial ring and the center electrode is the ensemble average of the five point estimation of the surface Laplacian taken over the complete rotation of the axes *x*-*y* around the *z* axis. NOTE: The axis *z* is normal to the plane *x*-*y* and is not seen in this two dimensional representation.

The right side of Equation 3.14 is the two dimensional Laplacian of the electrical potential on the body surface which is negatively proportional to the normal derivative of the current density at the body surface and is proportional to the two dimensional divergence of the tangential components of the current density at the body surface.

Next, the relationship between the two dimensional Laplacian of the potential and the coaxial concentric electrode filter configuration system can be established by considering a set of five unipolar electrode as shown in Figure 3.11 above as follows:

$$\nabla^2_{xy}\Phi = \frac{\partial(\partial\Phi/\partial x)}{\partial x} + \frac{\partial(\partial\Phi/\partial y)}{\partial y} \qquad (3.14)$$

then, the discrete two dimensional Laplacian of the potential at the center electrode Φ_0 can be given by:

$$\approx \left[(\Phi_2 - \Phi_0)/h - (\Phi_0 - \Phi_1)/h\right]/h + \left[(\Phi_3 - \Phi_0)/h - (\Phi_0 - \Phi_4)/h\right]/h$$

thus,

$$\nabla^2_{xy}\Phi \approx \frac{4}{h^2}\left[\frac{1}{4}\sum_{i=1}^{4}\Phi_i - \Phi_0\right] \tag{3.15}$$

where Φ_i is the electrical potential at the i location site and h is the interelectrode distance defined as $h = (d_2 + d_1) / 4$, with d_2 and d_1 being the external and internal diameters of the coaxial ring, respectively. Similarly, since the two dimensional Laplacian of the potential at the center electrode is independent of the coordinate system, then the potential at the center can be defined at any coordinate system x'-y' as:

$$\nabla^2_{x'y'}\Phi \approx \frac{4}{h^2}\left[\frac{1}{4}\sum_{i=1}^{4}\Phi_i - \Phi_0\right] \tag{3.16}$$

and finally, by averaging the estimate over a complete rotation, the two dimensional Laplacian can be obtained as:

$$\nabla^2_{xy}\Phi \approx \frac{4}{h^2}\left[\frac{1}{2\pi h}\int_l \Phi\, dl - \Phi_0\right] \tag{3.17}$$

where the integral is taken around the circle of radius h. And finally, according to expression (3.17), it can be affirmed that the output of the bipolar concentric electrode system is the differential potential between the center electrode potential and the averaged potential over the outer coaxial ring electrode. Thus, the output of the concentric Laplacian electrode is proportional to the magnitude of the two dimensional Laplacian of the normal potential and opposite in sign. The output of the concentric electrode is thereby proportional to the equivalent charge density at the center of the electrode system. The proportionality factor $4/h^2$ of the two dimensional surface Laplacian distribution can also be interpreted as a global attenuation factor, hence a calibration factor. Thus, it has been demonstrated that the concentric electrode configuration is capable of measuring the true surface Laplacian potential distribution. The next step is to prove the capability of the concentric electrode in suppressing non-delayed signals while enhancing local potential distribution. In this respect, since the equivalent charge density can be interpreted as a projection of the actual three dimensional bioelectric source distribution onto the body surface (via Poisson's equation), it would be expected that the equivalent charge distribution would provide a much sharper projection image of the sources than would the surface potential itself (i.e. bipolar or double differential measurement of surface potential).

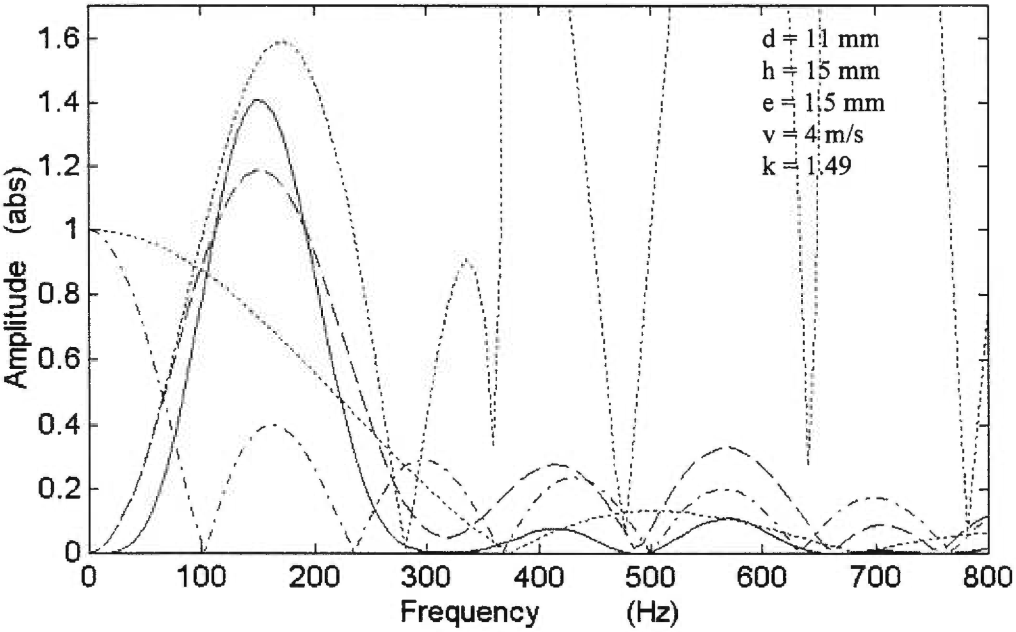

Figure 3.12 **Plot of the concentric electrode transfer function.** Dashed line indicate the transfer function of the system. Solid line indicates the square of the function. Small dotted line is the transfer function of the center disk electrode. Dash-dotted line indicates the absolute value of the transfer function of the ring electrode. Large dotted line indicates the transfer function in function of the area ratio *k* and the Bessel function of the central disk. Large dotted line indicates the transfer function of the central disk.

In other words, the smearing effect of the volume conductor would have much less effect on the surface Laplacian distribution than on the potential distribution. Beside the gain in selectivity, the approximation of $-\partial^2\Phi/\partial z^2$ offers the advantage that the output signal shape is virtually independent of excitation propagation direction *x*, *y* or intermediate. Thus, this two dimensional filter is capable of obtaining signal shapes which are independent of muscle fiber direction. Based on these observations it can be inferred that, contrary to the previous electrode configuration system transfer functions, the spatial integration of the concentric electrode configuration plays a far more predominant role in the filter shape. These effects are more clearly illustrated in Figure 3.12 above. Notice that the phase of the transfer function is constant within the signal band pass range (solid line) and that the filter's shape is fairly symmetrical, thus condition 1 is fulfilled. Also, low frequency components are rapidly suppressed, therefore high pass filter characteristics of condition 2 are fulfilled as well. Further, similarly to the double differential configuration, the zero crossing of the output signal will be at the center electrode, meaning that the filter performance is independent of the direction of the excitation propagation. Observe that as expected, the spatial integration effect of the center electrode (small dotted line) is more predominant for this configuration and that the external ring phase changes more rapidly (dash-dotted line) than the phase of the central disk electrode.

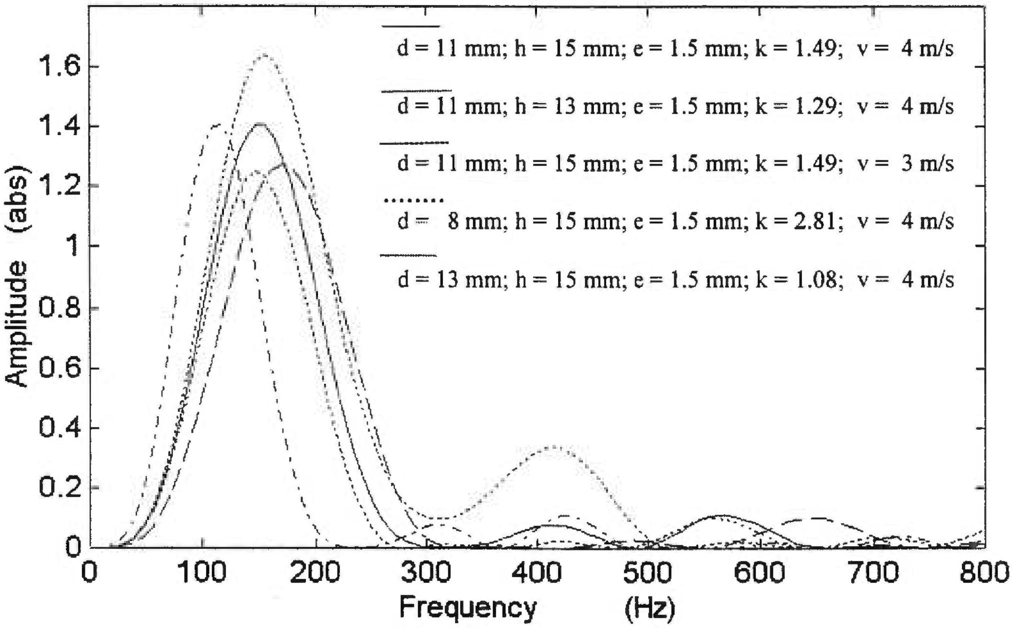

Figure 3.13 **Effects of the electrode diameter, interelectrode distance and CV.** The square of the transfer function for various combination of *d*, *h* , *e* , *k* and *v* are depicted as indicated by the different line style.

It can be interpreted then that the center electrode has the effect of enhancing local information under its area, and that the coaxial ring acts as a sort of gate for the non-propagated frequency components arriving from all directions surrounding the central electrode. The result is a rapid suppression of frequencies under 100 Hz (first phase of the ring function) and over 240 Hz (third phase of the ring function). In other words, the concentric electrode configuration is far more selective, capable of detecting the spatially correlated frequency components while suppressing more efficiently the temporally uncorrelated frequency components. However, even though a direct selective measurement of the surface Laplacian potential distribution is possible by enhancing local activity under the central electrode and by using the ring as gate filter for non-delayed frequency components, this type of configuration also produces a filter with a lower gain. The filter is highly dependent on the surfaces area ration k and the ring size for its shape, that is, since the interelectrode h is defined by the internal and external diameters of the ring. These effects are better appreciated from Figure 3.13 above.

A reduction in the interelectrode distance h shifts the spectrum towards high frequency components, increasing the bandwidth and reducing the gain (dashed line in Figure 3.13). Conversely, an increase in the center electrode diameter d reduces the surfaces area ratio k , narrowing the bandwidth and shifting it slightly towards lower frequencies reducing in the gain (small dotted line). This is expected since a larger diameter will integrate signals from further away. The contrary occurs with a decrease in the central diameter d, (large dotted line). Also observe that the surface area ratio k controls the high frequency limit of the filter's band pass (dips). The coaxial ring thickness e has a very small effect on filter shape and therefore is not shown here. These observations suggest that a proper combination of a central electrode diameter d, a surface area ratio k and an interelectrode distance h should produce a stable and selective filter shape (solid line). These three parameters (d, k and h) alone control the shape and performance of the filter. However, due to possible electrochemical imbalances at the skin-electrode interface produce by larger differences between the inner electrode and the outer ring, a low surface electrode area ratio k should be preferred in filter design.

3.4 DISCUSSION

This chapter has presented a theoretical analysis of the spatial filtering characteristics of the electrode surface detection area and the electrode configuration with respect to their ability to influence both delayed and non-delayed signal components. Particular emphasis has been given to the spatial integration effects of different electrode configuration systems on the shape of the spatial filter and their selectivity to delayed local excitation. To this end, a simple model based on Lindstrom's classical single fiber model and Helal and Bouissou's analysis of the monopolar electrode spatial integration effect has been used. It is underlain by three primary assumptions. First, the muscle conductivity in the transverse axis to the active fibers has been considered to be constant although this has been shown to depend on the frequency (Gielen et al., 1986). Second, the conductance of the electrode-skin interface is assumed to be much higher and frequency dependent (Harry et al, 1986); air conductance is assumed to be nil. Thus, the electrodes have been represented by conducting discs without thickness. Third, is assumed that the electrode diameters are much smaller than the depth ($d<r$), an assumption which does not hold true for active fibers located superficially in the muscle.

In spite of the model's assumptions and simplicity, the theoretical results which it delivers on monopolar, bipolar and double differential electrode filter properties are highly consistent with those reported by previous researchers (Lindstrom, 1973; Broman et al, 1985; Reucher et al, 1987). Inclusion of the spatial integration effects (due to the electrode's area) in the computation of the filter transfer function does not result in significant changes in the filter shape to the bipolar and double differential electrode configurations. Thus, the effects of the electrode spatial integration seem to play a minor role on the shape of the filter for these configuration. However this is not the case for the concentric electrode configuration, including the electrodes surface spatial integration effect allows to take into account contributions from equipotential close to the electrode; thus meeting the conditions of a Laplacian measurement.

The shape of the Laplacian electrode's filter is highly dependent on the central electrode diameter d and the interelectrode distance h as well as the surface electrode ratio k which also contributes to the filter's stability in the high frequency range. It has been demonstrated that the concentric electrode configuration behaves as a true two dimensional Laplacian spatial filter. Suitable spatial filters are desired when certain potential fields must be suppressed at the measuring stage (first stage filtering), in order to obtain a SEMG signal truly representative of the excitation-contraction coupling phenomenon, i.e. when the SEMG signal must be virtually free from transient non-delayed signals. The double differential configuration, although having many advantages, does not behave as a true Laplacian spatial filter since it is based on the assumption of unidirectional variation of the electrical potential. This assumption implies that lateral components from both side of the electrode configuration cancel each other ($\partial^2\Phi/\partial y^2=0$), which is not always necessarily true. In reality, the double differential configuration attenuates partially the non-delayed volume conducted signals arriving to the electrodes laterally, mainly by enhancing delayed signals propagating under the electrodes pickup volume.

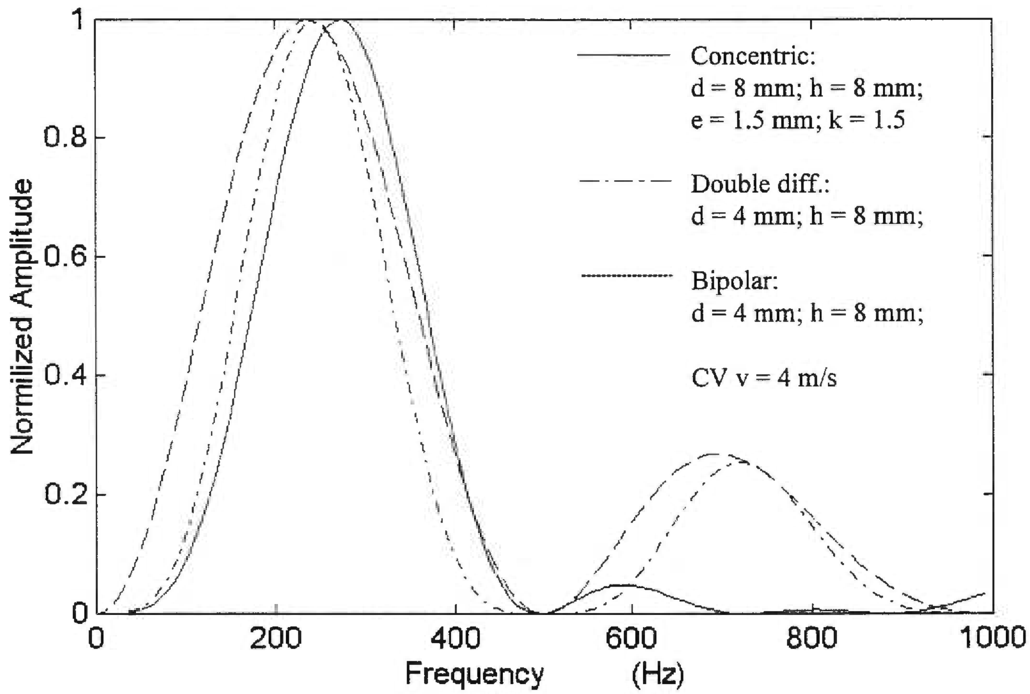

Figure 3.14 **Normalized transfer functions**: The transfer function for concentric, double differential and bipolar electrode configurations are depicted for comparison. (d electrode diameter; h inter-electrode distance; e concentric ring thickness; k area ratio between concentric ring and center electrode).

On the other hand, the surface Laplacian of the potential distribution measured with the concentric configuration is proportional to the normal derivative of the current density at the body surface which is characterized by a particularly strong lateral amplitude attenuation

(Hjorth, 1975; Reucher et al., 1987). If this predicate is correct and since volume conducted signals arriving laterally to the electrode are characterized by their low frequency components, when comparing the concentric Laplacian filter to the double differential filter, we should expect to see a spatial filter suppressing more strongly low frequency components. This would result in a shift of the filter spectrum toward high frequency components but with the same bandwidth for the same interelectrode distance.

To prove this point graphically, the square of normalized filter transfer functions of the bipolar, double differential and concentric electrode configuration with the same interelectrode distance (h = 8 mm) and conduction velocity (v = 4 m/s) are plotted for comparison in Figure 3.14 above. Observe that in the case of the concentric configuration (solid line) the maximum of the spatial signal is emphasized by means of a spatial high-pass filter. The normalized energy is basically the same in both filters, the double differential and concentric configurations; however the median frequency of the concentric configuration is seen shifted towards the high frequency, thus confirming previous expectations.

Notice also the close similarity of the filter shape to the concentric Laplacian and the double differential configurations which demonstrates the excellent suppression of disturbances. It can be said therefore with all confidence that the concentric electrode configuration generates a "normal double differential filter" which retains all the advantages of the double differential electrode configuration and adds a few more at the expense of a lower gain. However, this latter fact is not necessarily a drawback, since the concentric configuration has been shown to be highly selective to local activity and therefore less affected by transient non-propagated noise. In other words, the loss of signal amplitude can be compensated for without restricting the validity of the assumed spatial differentiation. In fact, a global attenuation factor of $4/h^2$ (see Equation 3.17) is inherent to the geometry of the configuration. In practice, this should be considered as a calibration factor.

3.5 CONCLUSIONS

Double differential and circular concentric configurations have Laplacian spatial filter characteristics as it has been verified by the theoretical modeling and arguments presented in this chapter. Comparison between these two spatial filters favors the circular concentric electrode configuration over the double differential configuration. The main advantages of the circular concentric electrode are its provision of a much sharper projection image of the source than would provide the double differential, its capacity to remain unaffected by directional polarity of the signal and most importantly its independence from muscle fiber direction with respect to the electrode orientation.

However, because of its poor gain and the relatively strong weighting of the center electrode signals, the question arises whether other kinds of disturbances affecting the skin/electrode interface (i.e. noise, motion artifacts, effects of sweaty skin, stretching of the skin, etc.) are emphasized by the two dimensional Laplacian spatial filters. Further, due to its high selectivity to local activity this electrode configuration is also sensitive to time dependent variables such as changes in muscle CV, which as previously discussed has an effect on the filters shape and hence its performance. This is a very important point and it rises a second question that involves the SEMG signal processing aspect. Center spectral moments (i.e. RMS, MPF, SD) are CV dependent and as is filter performance. The question is then how stable the filter's sensitivity is to details of the excitation-contraction coupling phenomenon or in other words, how reliable is the concentric Laplacian electrode? These two questions can be investigated only by means of experimental tests, which are presented in the next chapter.

Last, to distinguish uni-dimensional (linear) EMG recordings, (performed by bipolar and double differential electrode configurations), from bi-dimensional (surface Laplacian) EMG recordings, (performed by concentric Laplacian electrode configurations), from here on we will refer to the bipolar configuration as bipolar linear electrode (BLE) and to the concentric Laplacian configuration as bipolar concentric electrode (BCE).

CHAPTER FOUR

BIPOLAR CONCENTRIC ELECTRODE'S EXPERIMENTS

4.1 INTRODUCTION

4.1.1 Selectivity of the Bipolar Concentric Electrode

In the previous chapters it was established that the SEMG recording method must be tailored to a specific task. In this regard, the theoretical modeling analysis presented in Chapter Three led us to conclude that the normal double differentiation or surface Laplacian recording is the best spatial filter configuration for production of a local high spatial resolution SEMG signal free from transient noise. First, it enables a good separation of unrelated electrophysiological activity manifested in the vicinity of the recording electrode from the localized MUAP's activity of interest. Second, it forms a useful prerequisite to estimation of the exact position of the excitation source, independently of the muscle fiber orientation; and of the EMG signal directional polarity and free of non-delayed signals. Such an estimation of the excitation position, performed through time intervals, is the corner stone for the generation of the spatio-temporal mapping of potential distribution at the skin surface.

However, it was also suggested that this two dimensional spatial filter has a lower gain and therefore may be more susceptible to disturbances affecting the skin/electrode interface, thus providing a poor SNR. A second point to be confirmed is the electrode's selectivity and sensitivity to localized sources of interest. A third is the stability of the electrode, particularly in the high pass band of its filter function. Proof of these three points would demonstrate the validity of its filter transfer function and thus the theoretical conclusions derived from the

Laplacian electrode's analysis performed in the previous chapter. The Laplacian spatial filter shape and gain depend on the center electrode diameter *d*, the interelectrode distance *h*, the contact electrodes' surface area ratio *k* and the muscle CV *v*. The first three parameters are time invariant, thus they do not change during the recording process and can be chosen according to a desired filter shape. The CV, on the other hand, relates to the level of activation of the muscle. This parameter is time variant and may change during a contraction due to recruitment or derecruitment of some MUs with different CV, thus inducing changes in filter shape. This behavior, although observable in all filter configurations, might be more critical in the selectivity, sensitivity and stability of the Laplacian configuration.

Given the limitations of the modeling analysis, the selectivity, sensitivity and stability dependence of the Laplacian spatial filter configuration to changes in CV, as well as sensitivity to disturbances related to skin/electrode interface can only be partially investigated and verified by means of physiological experiments. Such experiments must allow to control the main parameters affecting the content of the SEMG signal in a manner that changes in CV can be followed and quantified through out the excitation-contraction phenomenon. To this effect both, the optimization and application of the recorded SEMG signal, must be taken into consideration in the experiment design.

4.1.2 Objective and Framework

In the following experimental study, the previously described two dimensional spatial filtering recording is used to record SEMG signals. The main objectives of this experiment are:

- a) to validate the theoretical transfer function of the bipolar concentric or Laplacian electrodes (BCE);
- b) to test its sensitivity, selectivity and stability to changes in the CV parameter and to noises affecting the skin/electrode interface and;
- c) to defined the best parameters to be used in the design of the BCE to be used in the spatio-temporal mapping technique.

To this end, the time and frequency domain features of spatially filtered SEMG signals are to be evaluated in reference to signals recorded simultaneously with a bipolar linear electrode (BLE), and this implies the recording of signals with an array of bipolar concentric and bipolar linear electrodes. While, signals recorded with a BCE configuration are not affected by fiber orientation and directional polarity, the BLE configuration is so affected; optimization of the SEMG must therefore be also taken into account in the experimental protocol design.

4.2 SELECTION OF THE EXPERIMENTAL PARAMETERS

Based on the conclusions derived from Chapters Two and Three, the main parameters selected for the control of this experiment are: electrode location and orientation relative to the muscle fiber direction and innervation zones (needed for the BLE); muscle length; and level of contraction (related to the number and firing rates of the MUAPTs, thus the control of changes in the muscle CV).

4.2.1 Selection of Muscle

The biceps brachii muscle was chosen for this study because its geometry simplifies interpretation of SEMG signals. The fibers run parallel to the long axis of the muscle forming a relatively long muscle segment free from innervation zones. The average number of fibers in a MU in a normal human biceps has been reported to be approximately 160, (Christensen, 1959). These fibers are distributed randomly throughout a MU's territory, which is between 3 to 10 mm in diameter (Stalberg and Antoni, 1980; Hilton-Brown and Stalberg, 1983). Individual fiber diameters range from 25 to 85 μm and the mean fiber diameter is 50 to 60 μm (Dubowitz and Brook, 1973). Several or more innervation zones can be found in the biceps and their location might vary from individual to individual (Masuda et al., 1985). However, in most individual innervation zones in the biceps are likely to be found around the distal area close to the middle part of the muscle (Saitou et al., 1991); these zones are usually distributed within a line approximately 5 mm wide, transverse and/or perpendicular to the fibers (Aquelonius et al., 1984).

Table I: Conduction Velocities from the Biceps Muscle

STUDIES	C V (m/sec)	
	Mean	± SD
Stalberg (1966)	3.7	0.7
Lynn (1979)	4.3	0.6
Naeije et al., (1983)	4.4	0.4
Sollie et al., (1985 a,b)	5.0	0.6
Hunter et al. (1987)	5.0	N/A
Rababy et al., (1989)	3.6-4.7	N/A

The mean conduction velocity and standard deviation for biceps muscle fibers from several studies are listed in Table I below. Variations in the mean conduction velocity obtained in the different studies can be explained by: the different methods used in estimating the mean values; electrode location and orientation in reference to the fiber direction and innervation zones; amount of fatty tissue in different subjects; different levels of isometric contraction.

4.2.2 Muscle Length and Conduction Velocity

The effects of changes in muscle length on the SEMG signal have been investigated by several authors. Okada (1987) recorded SEMG from the biceps at different elbow angles for a constant level of isometric contraction. He found that the duration of APs increases in proportion to increases in muscle length, but that the amplitude of the signal remains unaffected. This can be explained by the fact that the stretching of fibers produce a relative reduction of the fibers' cross-sectional area; which results in a reduction of the CV and an increase of the AP duration, thus shifting the EMG spectrum towards low frequencies. In addition the muscle belly circumference becomes smaller and so the deeper fibers will contribute to the signal. Shortening of the muscle will produce the opposite effects on the signal. These findings were corroborated by Inbar et al., (1987), who also showed that changes in the SEMG signal due to shifts in the innervation zone are less critical than changes due to muscle length. However, Saitou et al., (1991), found that the mean frequency is highest if the recording electrode is in the vicinity of the innervation zone and that it decreases considerably if changes in muscle length moves the recording electrode away from the innervation zone. In short, changes in the muscle length and shifts in the innervation zone should be avoided, in order to ensure that changes in CV are due to normal physiological changes proper to the MUAP generation process and not to changes in the recording conditions and/or artifacs.

4.2.3 Level of Contraction

Recruitment and firing rate of motor units are a function of time and force. De Luca et al., (1987) found that the force threshold of motor units recruited below 20 % maximum voluntary contraction (MVC) increased while their firing rate decrease. Conversely, the force threshold of motor units recruited above 25 % MVC decreased while their average firing rate increased. Blinowska and Verroust (1987) found that the discharge of motor units became more synchronized as the force level increased. The control of the contraction level is of outmost importance in this experiment. Due to the progressive increase in the firing frequency of MUs initially recruited and to newly recruited MUs with relatively larger spike amplitudes, the content of the SEMG signal will change with the level of contraction (Muro et al., 1983; Broman et al., 1985; Moritani and Muro, 1987). This phenomenon therefore becomes an ideal tool to evaluate changes in the signal's features within the time and frequency domains, and consequently, to evaluate the sensitivity, selectivity and stability of the BCE to the changes in CV. The contraction level parameter can be controlled by having the subjects exert a monitored force under different conditions (i.e. ramp and step isometric contraction) for a short period of time to avoid fatigue. In a separate test, effects of changes in CV can be as well monitored during fatigue.

4.2.4 Optimization of the SEMG Signal

According to the findings discussed until now, recording of the SEMG signal can be optimized if : the differential recording is performed parallel to the fiber direction (Sollie et al., 1985a,b; Masuda and Sodoyama, 1988); the distance between the detecting electrode and the source of the SEMG activity is minimized (Griep et al., 1978; Basmajian and De Luca, 1985); and the electrode array is positioned between the innervation points and the tendon (Masuda et al., 1985; Saitou et al., 1991). Using these criteria, optimization of the SEMG becomes a matter of finding the innervation zone, determining the muscle fiber direction and minimizing the distance from the recording electrode to the active muscle fibers. A regular practice to identify innervation zones is to use a linear array of electrodes and observe the reversal in polarity of the AP; also, in this way shifts in the detection probe with respect to the innervation or tendinous zones can be accounted for when analyzing EMG data. However, if linear array of electrodes are not available, the innervation zones can be found by electrical stimulation, the tendon can be identified by palpation and the fiber direction can be determined by observing the skin deflection while the motor points are electrically stimulated.

4.3 EXPERIMENTAL EQUIPMENT

The experimental equipment consists of a stimulation unit, three types of electrodes, an oscilloscope, a force gauge, an electrode preamplifier, an electrode amplifier (bandwidth 10-1000 Hz, adjustable gain from 10 to 10000), a force amplifier (bandwith 0-100 Hz, adjustable gain), an A/D converter interface, a personal 386 computer equipped with a data acquisition card, and an experimental chair.

The stimulation unit, made by Grass Medical Instruments, consists of a DC variable pulse (square wave) stimulator (Model S48), a stimulus isolation unit (Model SIU), and a constant current unit (Model CCU1) connected in series. The stimulus isolation unit minimizes artifacs and isolates stimulus signal from ground reference by reducing the ground current between the stimulating and recording systems. The constant current unit maintains a constant current output (within 5 %), compensating for impedance fluctuations of the stimulation electrode that might occur from changes in the preparation, (i.e. changes in interelectrode distance between electrode pairs, changes in media conductivity, etc.). For purposes here, the stimulator was set to deliver a current pulse of 0.4 ms duration, the constant unit was set to its intermediate range (between 0.5-5 mA) and the pulse amplitude was adjusted to produce contraction of only a few fibers. The contraction was monitored by visual inspection of the twitch and by a display of the action potential on an oscilloscope. The amplitude of the current was adjusted accordingly to minimize both amplitude and complexity of the action potential.

Three types of electrodes were used in this experiment. The first type were wire electrodes, used to selectively activate only a few fibers, in order to maintain the generation source constant with respect to the detecting electrodes. These stimulation electrodes were made from 25 μm stainless steel enamel coated wire, about 10 cm in length. The enamel coating was removed from both ends, leaving 0.5 mm exposed wire at one end to form the electrode lead (tip) and 20 mm exposed at the other end to be connected to the stimulator. A pair of wires were passed through the cannula of a 27 gauge hypodermic needle (0.5 mm diameter, 15 mm length) leaving the leads exposed at the distal tip of the needle. The lead ends were folded over the needle tip and separated to prevent contact between them. Prior to use, the wire electrodes were sterilized in an autoclave.

The second and third type of electrodes formed a configuration array consisting of two sets of BCE of different coaxial ring diameters and one set of BLE mounted on a Plexiglas frame (Figure 4.1 below). The two sets of BCE were formed by a center electrode contact of 3.5 mm diameter encircled by two coaxial rings of electrode, a first ring of 10 mm inner diameter and 13 mm outer diameter, and a second ring of 16 mm inner diameter and 19 mm outer diameter. The third set of BLE was formed between the center electrode contact and a collinear electrode contact also of 3.5 mm in diameter at an interelectrode distance of 15 mm. The electrode contacts were made of surgical stainless steel. This material was chosen because is an excellent conductor, (high carbon steel), and thus, the diminished polarization potential associated with it is a major benefit, (its dielectric properties are less susceptible to change in presence of perspiration) and it lend itself perfectly to be machined to the desired shape.

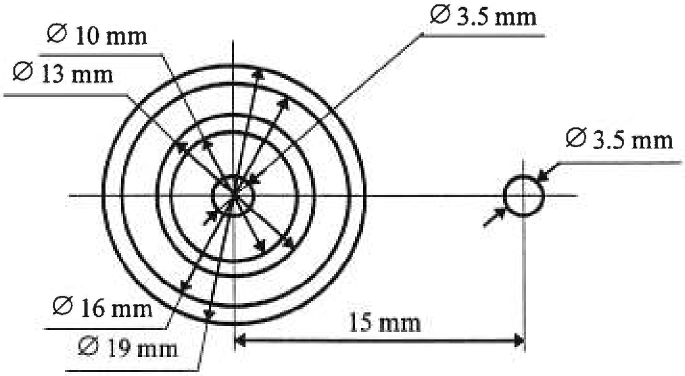

Figure 4.1 **Schematic diagram of the electrode array configuration**. Each coaxial ring forms an individual BCE set with the center electrode, respectively. A third set (BLE) is formed bipolarly between the center electrode and its the collinear electrode.

To minimize the effects of skin shifting, fiber displacement and muscle length changes during electrically stimulated contraction a special chair was suited for the experiment. The chair had an arm rest and straps to secure the subject hand and forearm at the wrist and elbow level, respectively. In this a way the subject sat comfortably with his/her arm at 90 degrees without allowing pronation or supination of the forearm. The subjects were instructed to maintain their shoulders fixed during the experimental trials. By restraining movement of the arm muscle length changes were controlled in a reproducible manner from trial to trial, while skin shift and fiber displacement were minimized. Since during voluntary contractions the control of the aforementioned parameter was less critical, the straps were released in order to measure the isometric force level produced by the biceps, (only a couple of degrees of elbow flexion was needed, since the force gauge wire was set to a constant length and EMG signals were recorded once the required level of contraction was achieved and therefore these parameters would remain unchanged).

The force measurement unit consisted of a force gauge from Intertechnology Inc. with an output of 3 mV/V at 136 Kg and a force amplifier (bandwith 0-100 Hz, adjustable gain). Both ends of the force gauge were attached to flexible steel wires which in turn were fastened, one end to the floor and the other to a handle, respectively. The force amplifier was set at a gain of 4 and the force gauge was calibrated from 0 kg to 15.88 Kg by using a 1.13 Kg step weight. The weight/voltage relationship at a gain of 4 was found by linear regression to be $W = 5.1203*V + 0.0307$; where W is the force in kg and V is the voltage in millivolts.

4.4 DATA ACQUISITION

A data acquisition card (Brain Wave) with a 12 bit resolution and a 12 μs conversion time giving a maximum throughput rate of 60 KHz was used. Data was stored using direct memory access (DMA). A maximum of 16 analog data channels could be collected simultaneously. The card also was equipped with two extra channels to convert digital signals into analog signals, one of these channels was used to trigger the stimulator. Data acquisition and A/D conversion were initiated using the Brain Wave System built-in programs, which were either configured to collect electrically elicited or voluntary contraction SEMG signals, respectively.

4.4.1 Recording Evoked Action Potentials

Stimulation was triggered by a 5 V step from the D/A converter 10.25 ms after data collection began and 220 points representing 54.78 ms of data were collected per channel, (sampling frequency 4016.06 Hz; set by Brain Wave built-in driving program). The Brain Wave system is already fixed to command D/A conversion by either one single or ten impulses at the time, therefore since the stimulator was trigger by D/A conversion, that gave us the choice to collect sets of ten APs. After each set of ten APs were collected, the program automatically computed the average and storage the ten sets plus the average. Individual averaged trial sets, (each of ten electrically evoked APs), were selected previous to storage. Selection was based on visual inspection of the ten individual action potential signals for each channel, which were displayed on the computer screen immediately after the A/D conversion. The criteria for selection of the averaged signals sets included similarity of the shape and amplitude of the action potentials, small stimulus artifacts (minimum interference with the action potential) and high signal to noise ratio. A total of ten averaged sets were collected.

4.4.2 Recording Voluntary Contraction

Maximum voluntary contraction (MVC) was first determined by displaying the maximum possible exerted force by the subject on an oscilloscope. Two types of isometric contraction, step and ramp, and one fatigue test were performed and recorded per subject. First, two trials were recorded in ascending and descending step contractions (steady single contractions maintained at different force levels during 2 seconds). Each trial consisted of eight step force level with each step increasing 10 % from 10 to 80 % MVC for ascending steps and decreasing 10 % from 80 to 10 % MVC for the descending steps. In order to avoid fatigue, a time rest of 60 seconds was allow between steps. Second, two trials per subject were recorded during a progressive increase in force level (ramp, from 0 to 80 % MVC) exerted in 2 s. One set of 2048 points per channel (four channels: three SEMG and one force) representing 2 s (sampling frequency 1024 Hz) was collected for each level of isometric voluntary contraction (step and ramp). Third, two trials per subjects were recorded during fatigue. While the subject maintained a steady force level at 40 % MVC for 3 min, a two-seconds-of-data set per channel were collected every 30 seconds at a sampling frequency of 1024 Hz. Again, data were visually inspected prior to storage. The criteria for selection in this case was a steady force level. In general, it was found that it was easier for the subjects to reproduce force generation under ramp isometric voluntary contraction and fatigue conditions; so given the diversity of experiments run per subject (each experimental seance took approximately 3 hours time), it was judged that the limited number of trials per subject represented sufficient data to confirm theoretical results and observations concluded in Chapter Three.

4.4.3 Subjects

A group of five subject participated in this study, one female and four males, representing an average age group of 33.2 years with a standard deviation of 9.7. Several pre-experimental test using the same configuration array of BLE and BCE have been previously run in various occasions on one subject, the results were always very consistent; consequently it was judged that data from five subjects under a similar experimental set up would suffice, particularly that data from the two first subjects a priory yielded basically similar results. One woman was included in the protocol only as reference to check whether differences could be seen due to muscle composition (i.e. influence of fiber type, fatty tissue). The recording was performed simultaneously over the biceps muscle of the right arm with an electrode array configuration shown in Figure 4.1 above. All subjects were healthy, without any history of neuro-muscular problems affecting the muscle of the upper arm. All subjects were right handed. Subjects gave informed consent to the procedures of the experiment.

4.4.4 SEMG and Force Recording Set-up

The signals from the electrodes were first pre-amplified with a gain of 10 and then fed into a bandpass amplifier with variable gain. The wires connecting the electrodes to the pre-amplifier were about 15 cm in length, these were twisted and shielded with a fine copper mesh which in turn was grounded. The amplifier bandpass was set between 10 and 1000 Hz for data collected at a sampling frequency of 4000 Hz and between 10 and 500 Hz for data collected at a sampling frequency of 1024 Hz. The force signal from the force gauge was amplified with a bandpass between 0 to 100 Hz with a gain of 4. After bandpass amplification, data was digitized and stored on disk for subsequent analysis. (see Figure 4.2 below). In the case of one subject, a fifth channel was added to record the stimulus impulse directly beneath the skin surface (at a depth of approximately 0.5 mm).

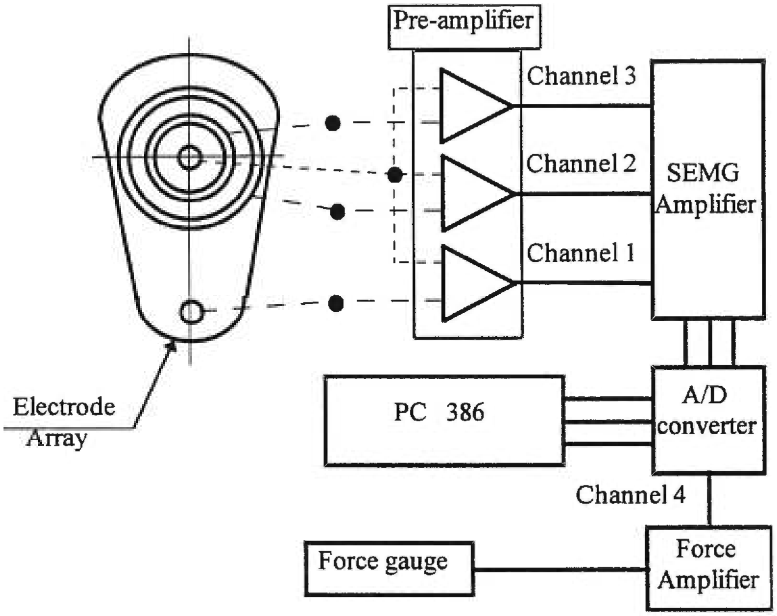

Figure 4.2 **Schematic diagram of the recording configuration**. SEMG signals are recorded simultaneously by the three electrodes configuration array, thus two Laplacian of different coaxial ring diameters and one bipolar electrode used as control reference. The electrode array was place with the bipolar electrode oriented along the muscle fiber direction of the biceps. During isometric voluntary contraction a fourth channel monitoring force level was added to the recording configuration.

4.4.5 Protocol

Subjects sat in the experimental chair with their upper body and shoulders in a straight position while the armrest supported the forearm in a comfortable position, with the elbow flexed approximately 90°. The forearm was strapped to the armrest in order to prevent pronation or supination. Next, the motor points of the biceps muscle were mapped by means of surface electrical stimulation. The skin area over the chosen innervation zone was thoroughly cleaned with surgical alcohol and then a pair of sterilized stimulating electrodes was inserted into the muscle at the most proximal motor point using a 27 gauge hypodermic needle. All subjects had their innervation zones about the middle of the biceps. In three subjects two innervation zones were found running diagonally to the fibers and parallel to each other; in a fourth subject the innervation zones also were diagonally to the fiber but joined in an angle at the lower end. The fifth subject had three innervation zones scatter more perpendicularly to the fibers and forming almost a half-circle. The minimum stimulus current necessary to selectively stimulate only a few muscle fibers was determined (0.4 ms pulse duration, normally between 0.5 and 2.5 mA pulse amplitude). Visual inspection of the skin movement produced by the contraction was used to verify the location and direction of the stimulated muscle fibers. Following selection of the recording area, the skin surface was properly cleaned by means of a light abrasion with alcohol and then the electrode array was placed between the innervation zone and the muscle origin (normally about 10-20 mm proximal from the stimulation electrodes) such that the BLE was directly above the stimulated muscle fibers, oriented in the same direction as the contracting fibers. In all five cases, the recording area was free from innervation zones. The biceps muscle was then stimulated electrically while the subject relaxed and the evoked SEMG signals were recorded using the electrode array in the manner described in Section 4.4.2. Following electrical stimulation, the wire electrodes were removed from the subject and the straps from the wrist released to proceed with the recording of voluntary contractions. The subject's hand was then placed in a supine position holding the force handle. The force handle was previously adjusted in such a manner that the subject's hand rested at the same level as the forearm in a comfortable position. The subject was instructed to prevent flexion or extension of the wrist in order that the force recorded could be well correlated with the biceps activity. Isometric voluntary contraction was then recorded as described in Section 4.4.3. Two seconds of noise level, (no EMG activity), was recorded before and after each recording seance.

4.5 DATA PROCESSING

4.5.1 Processing of Evoked Potentials

Mean amplitude and RMS of the noise were computed for all subjects. The second set of data processed was the stimulus impulse recorded directly beneath the skin surface together with the impulse responses detected by the electrode array (subject E). The aim of the analysis being to confirm the signal to noise ratio (SNR) for each electrode as well as to determine the characteristics of the electrodes' transfer function, this set of data was not filtered. In any event, from experience noise were expected to remain the same through the recording session.

To model the three electrode systems the Steiglitz-McBride method of ARMA modeling was used. It was found that a four zeros, four poles model was sufficient to obtain an almost perfect match with the three recorded electrodes' output. The electrodes' transfer functions were determined using the same ARMA modeling method and later compared to their respective theoretical transfer function, developed in the previous chapter. The third set of data analyzed was the electrically evoked EMG signals. First, the artifacts was removed from the signal. Since the artifact's decay showed a perfect exponential behavior, an exponential curve $(Ae^{t} + C)$ was used. Low and high frequency noise was then removed from the signals using a second order Butterworth digital filter with a 10 to 500 Hz bandpass, thus one fourth of the Nyquist frequency (sampling frequency 4000 Hz). Each signal was then padded with 292 zeros, to form an array of 512 points, and their PSD was computed using the discrete Fourier transform (DFT). PSDs were smoothed using a five point moving average and then normalized to their maximum frequency amplitude. Cross-correlation between signals was computed using the cross-correlation function (equation 2.13 in chapter two). The SNR was determined by computing the ratio between the RMS of the signal and the RMS of the noise level computed in the previous stage.

4.5.2 Processing of Isometric Voluntary Contractions

Data from the ramp isometric voluntary contraction consisted of one force and three SEMG signals. First, a 6 points moving average was applied to the force data to remove high frequency oscillations from the force equipment system (force amplifier was delivering a noisy signal). As for the SEMG signals, these were filtered using a second order Butterworth digital filter with a 30 to 300 Hz bandpass to prevent eventual side-lobbing. The setting allowed by the Brain Wave amplifier was 10-500 Hz bandpass, which it was considered too close to the Nyquist frequency (sampling frequency 1024 Hz). RMS was computed over 2048 points of recorded data using a moving square window of 64 points with an overlap of 32 points. Similarly, PSDs were computed for each channel using a moving Hanning window of 64 points (62.5 ms) with a 32 points overlap (31.25 ms). All widows were padded with 64 zeros to increase resolution of the DFT. This method was found to be the most efficient to analyze the SEMG signals. Larger windows reduced the event's resolution, making it more difficult to track frequency and temporal changes in the signals. Zero padding larger that 64 points produced side lobes at the expense of the main lobe. In order to facilitate comparative analysis between electrode configuration behavior, all PSDs were smoothed using a five point moving average to remove rapid fluctuations and then normalized to their unity area. In order to follow closely PSD shape changes, for comparison purposes; (see section 2.4.3, page 33 for reference), moments of order 1 to 4, plus median frequencies (MDF), and coefficients of skewness, kurtosis and variation were computed for every windowed PSD. All coefficients computed from normalized PSD windows were stored in a 63 point array, and later smoothed by a three point moving average to reduce gross fluctuations, thus representing the most likely temporal and frequency behavior of the two second ramp isometric contraction with a resolution of 32.25 ms. Force and SEMG data from the step isometric voluntary contraction of 10 to 80 % MVC was computed in a similar fashion as described above, delivering one set of coefficients per level of contraction (i.e. MDF, MNF, skewness, kurtosis, variation). Again, each coefficient array of 63 points represented the most likely time-frequency behavior of the two seconds of isometric voluntary contraction at each of the eight contraction levels. Data from the fatigue experiment was processed in a similar manner.

4.6. RESULTS

SEMG data collected under ramp isometric voluntary contraction (IVC) condition were used to track changes in the time and frequency domains and SEMG data collected under step IVC condition served to track changes on the distribution of the signal's spectral components from BLE and BCE configuration.

4.6.1 Sensitivity and Selectivity to Noise

The noise level recorded simultaneously for the three electrode configurations was the first set of data analyzed. Results are presented in Tables II, III and IV below. The amplitude and RMS values of the noise presented in these tables are the mean of averages obtained from five sets recorded at each experimental seance, (i.e. beginning, stimulation-ramp, ramp-step, step-fatigue and end). Raw noise data was used to compute amplitude and RMS values. In each session, no significant changes of RMS noise was observed.

Table II Noise level recorded with the BLE

	RMS value (μV)				AMPLITUDE (μV)			
Subject	Max.	Min.	Mean	Std.	Max.	Min.	Mean	Std.
A	14.11	6.92	9.52	2.14	30.82	15.40	20.87	4.56
B	19.04	9.15	14.36	3.19	40.11	21.02	30.52	6.33
C	32.32	11.45	**22.85**	**6.43**	73.30	28.57	46.66	14.33
D	33.31	13.57	21.29	5.86	62.78	28.61	41.88	11.32
E	12.80	4.43	**7.18**	**2.53**	31.81	9.21	15.25	6.59
Mean	22.32	9.64	15.04	4.02	47.76	20.56	31.04	8.63

The highest mean RMS noise value found for the BLE was 22.85 ±6.43 μV, (see Table II, subject C) and the lowest RMS noise value for the same configuration was 7.18 ±2.53 μV, (see Table II, subject E). The global mean calculated over the five subjects was 15.04 ±4.02 μV. As for the LBCE, the highest mean RMS noise value was found to be 29.05 ±7.97 μV, (see Table III, subject C) and the lowest RMS noise value for the same configuration was 5.85

±2.82 µV, (see Table III, subject E). The global mean calculated over the five subjects was 14.71 ±3.62 µV. The highest mean RMS noise value found for the SBCE was 29.24 ±8.11 µV,(see Table IV, subject C) and the lowest RMS noise value for the same configuration was 5.69 ±2.03 µV, (see Table IV, subject E). The global mean calculated from the mean of all five subjects was 14.48 ±3.68 µV.

Table III Noise level recorded with the LBCE

	RMS value (µV)				AMPLITUDE (µV)			
Subject	Max.	Min.	Mean	Std.	Max.	Min.	Mean	Std.
A	9.96	5.48	7.76	1.48	24.89	7.60	15.59	4.44
B	17.51	11.26	14.18	2.13	44.35	19.58	31.95	6.77
C	44.71	18.62	**29.05**	**7.97**	88.99	35.52	64.10	20.19
D	21.61	10.32	16.72	3.68	48.35	23.46	34.85	7.82
E	11.82	3.28	**5.85**	**2.82**	18.10	6.98	11.27	3.40
Mean	21.12	9.80	14.72	3.62	44.94	18.63	31.55	8.64

Table IV Noise level recorded with the SBCE

	RMS value (µV)				AMPLITUDE (µV)			
Subject	Max.	Min.	Mean	Std.	Max.	Min.	Mean	Std.
A	13.66	3.92	8.24	2.92	29.71	6.40	17.36	7.48
B	16.68	10.86	14.08	2.02	41.86	19.65	31.00	7.54
C	45.50	18.66	**29.24**	**8.11**	91.45	33.29	65.23	20.75
D	19.15	10.14	15.21	3.31	47.59	17.17	31.42	9.75
E	9.50	3.58	**5.69**	**2.03**	16.87	6.79	11.15	3.58
Mean	20.91	9.43	14.48	3.68	45.50	16.66	31.23	9.82

Notice that in general, (with exception of subject C), the noise level from all subjects showed a higher RMS value for the BLE and smaller noise RMS value for the LBCE and SBCE. Observing the overall results, we can confirm that the mean RMS over the five subjects is 15.04 ±4.02 μV for the BLE, 14.71 ±3.62 μV for the LBCE and 14.48 ±3.98 μV for the SBCE. This analysis seems to indicate that (providing a good electrode/skin interface contact, thus lower impedance) the bipolar concentric configuration appears to attenuate the noise in similar manner to which attenuates the signal. This observation, of course, must still be confirmed.

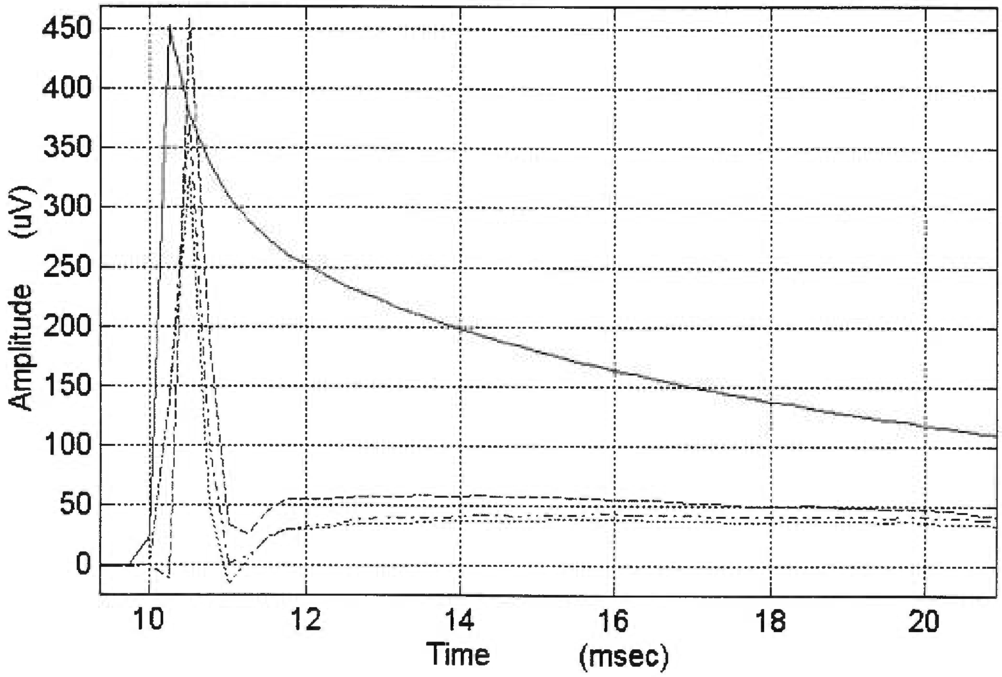

Figure 4.3. **Excitation impulse and systems' impulse response**. Solid line represents the excitation impulse. The systems' impulse response are represented by the dashed line for the BLE configuration, dash-dotted and dotted lines for the BCEs with large and small coaxial ring, respectively.

4.6.2 Validation of the theoretical transfer functions

The second question regarding validity of the theoretical transfer function was investigated by analysis of the impulse response data obtained simultaneously from the three electrode configuration systems to an excitation impulse elicited in the dermis close to the electrodes' array, away from the innervation zone. These impulses are partially depicted in Figure 4.3 above. The solid line represents the impulse fed to the three system electrodes. The dashed line represents the impulse response of the BLE while the dash-dotted line represents the impulse response of the LBCE and the dotted line represents the impulse response of the SBCE. All curves decay asymptotically to zero within 40 to 50 ms (not shown here)

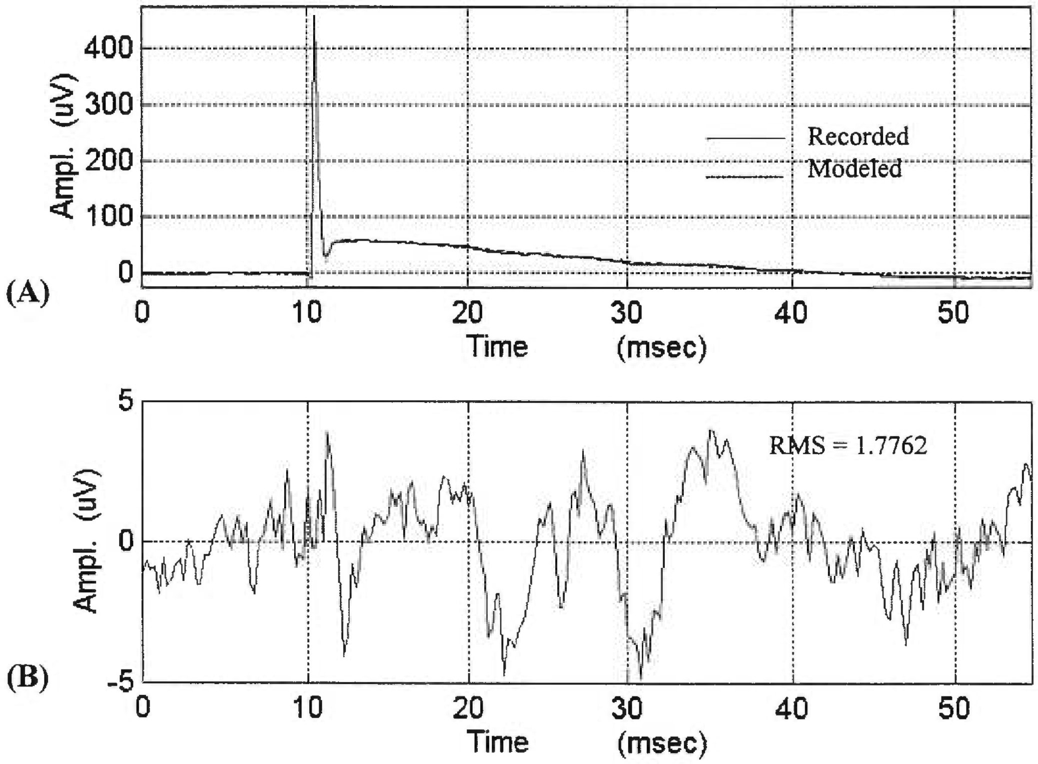

Figure 4.4 **BLE impulse response and error.** (A) Recorded and modeled impulse response of the BLE are represented by the solid and dashed lines, respectively. Notice the perfect matching of the two curves. (B) Curve represents the residual error level between the recorded and modeled impulse responses.

The impulse response of the BLE was modeled with four zeros-four poles ARMA model. As shown in Figures 4.4 B above, the small residual error obtained from subtracting the modeled and recorded responses confirms that the model gives a very good match.

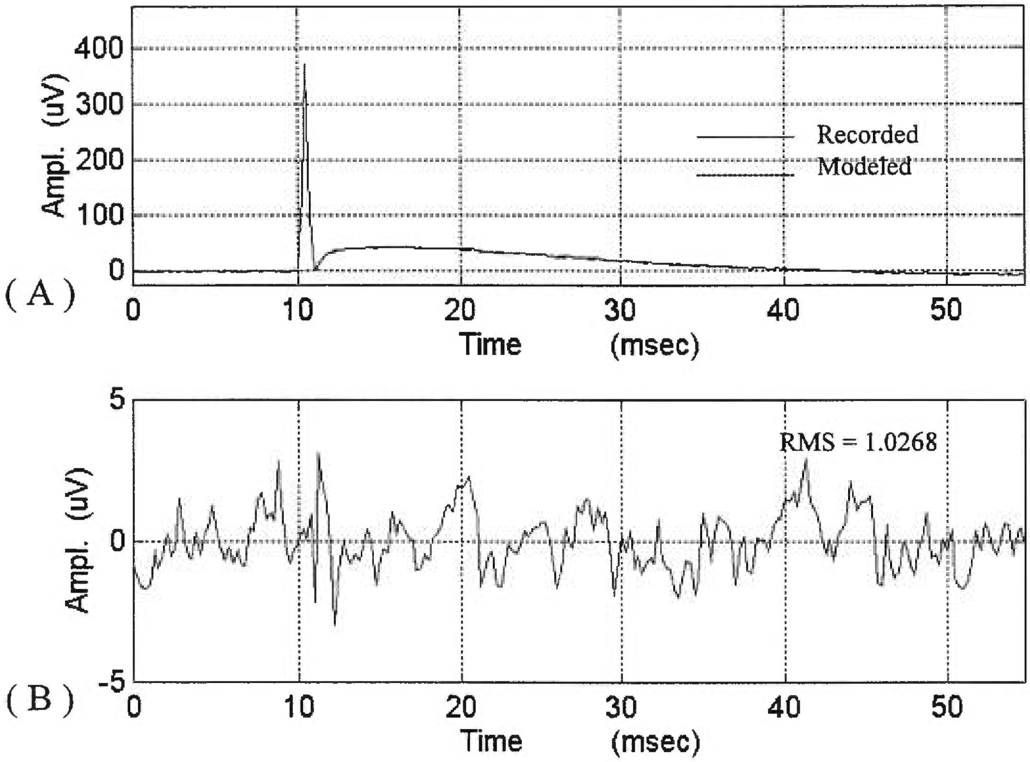

Figure 4.5 **LBCE impulse response and error.** (A) Recorded and modeled impulse response of the LBCE are represented by solid and dashed lines, respectively. Notice the perfect matching of the two curves. (B) Curve represents the residual error level between the recorded and modeled impulse responses

Modeled and recorded impulse response and residual error of the LBCE are depicted in Figure 4.5 above. Once again, a four zeros-four poles ARMA model was able to model the system with a quite good match.

Modeled and recorded impulse response and residual error of the SBCE are depicted in Figure 4.6 below. As with the previous systems, a four zeros-four poles ARMA model was able to produce a good match.

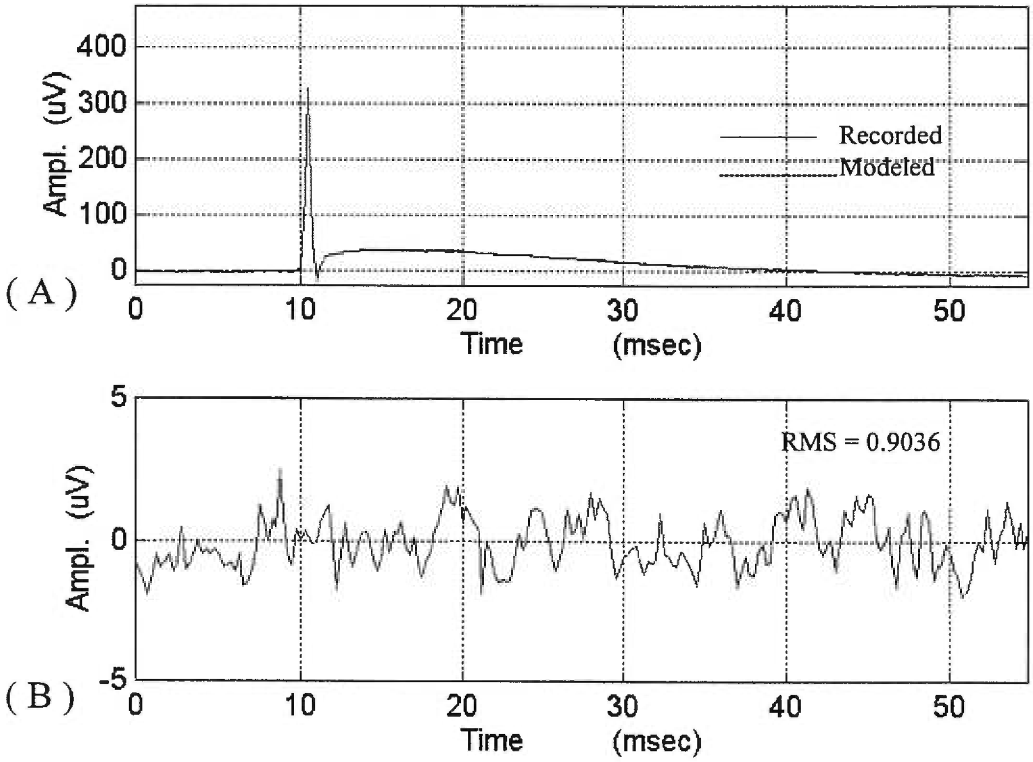

Figure 4.6 **SBCE impulse response and noise.** (A) Recorded and modeled impulse response of the SBCE are represented by solid and dashed lines, respectively. Notice the perfect matching of the two curves. (B) Curve represents the residual error level between the recorded and modeled impulse responses.

The next step in the analysis was to exam whether the transfer functions obtained through the ARMA method correlate to those obtained theoretically in the previous chapter. In order to increase the resolution for the analysis, the sampling frequency of excitation and response impulses was increased to 16000 Hz by means of a half point moving average interpolation. The theoretical transfer functions were computed using Equations 3.8 and 3.12, (developed in chapter three; pages 58 and 67, respectively), in conjunction with the electrodes' dimensions shown in Figure 4.1 of this chapter. The best possible match was obtained for propagation velocities of 14.75 m/s for the BLE, 11.90 m/s for the LBCE and 5.50 m/s for the SBCE Figure 4.7 below depicts the normalized results of the modeled and their respective matched theoretical transfer functions.

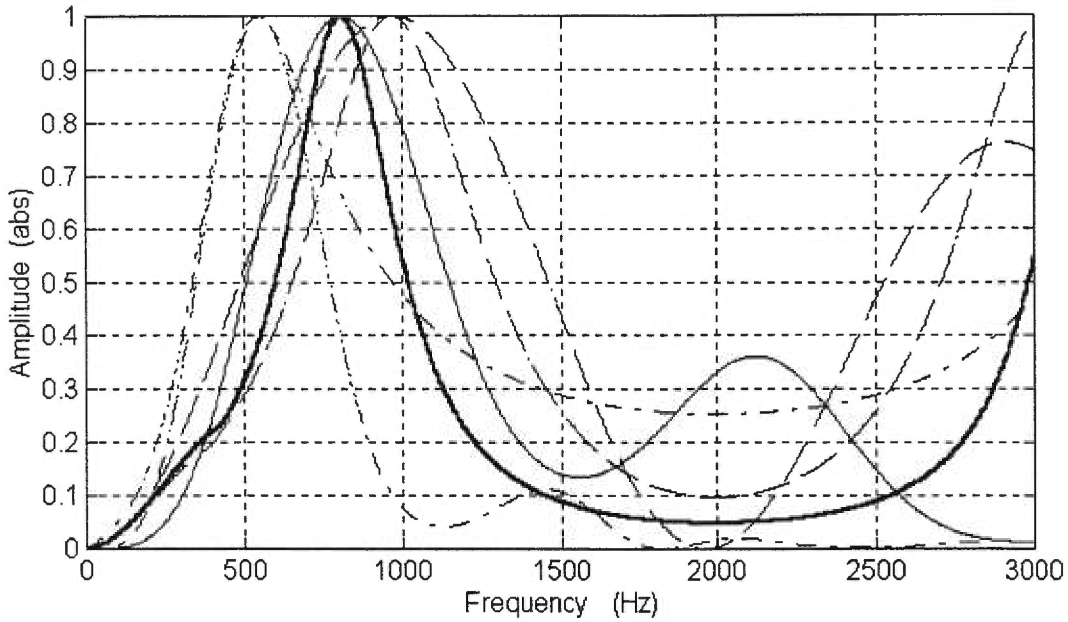

Figure 4.7 **Modeled and theoretical transfer functions**: Dark and light dash lines represent modeled and theoretical BLE's transfer functions, respectively. Dark and light solid lines represent modeled and theoretical LBCE's transfer functions, respectively. Dark and light dash-dot lines represent modeled and theoretical SBCE's transfer functions, respectively.

Before any comparison can be made between the theoretical and modeled results, it must be remembered that the modeled transfer functions in reality correspond to a cascade filtering process, thus $H_m = H_t H_e$, where H_m is the ARMA modeled transfer function computed from the input-output impulses, H_t is the tissue's low-pass filter transfer function and H_e is the theoretical transfer function of electrode configuration system. In other words, the excitation impulse (input) is first low-pass filtered by the dermis tissues before reaching the respective electrode configuration system.

Observe the similarity between the modeled (dark lines) and the theoretical (light lines) filter transfer functions, particularly in the low-pass band side of the functions where the low frequency components of the excitation impulse have been less altered by the tissues media. Conversely, differences seen in the high-pass band side of the functions are explained by the tissue low-pass pre-filtering effects. The performance of this tissue filter (H_t) depends on the depth, velocity and frequency components of the propagating signal (Lindstrom and Magnusson, 1977). In this particular case however, we have a signal (excitation impulse originated at a low depth, about 2 mm from the skin surface) that is actually being *volume conducted* (parallely to the electrodes plane) at a decaying velocity and decreasing amplitude of its high frequency components. This in practice implies that the cut-off and roll-off frequency of the tissue filter (acting orthogonally to the electrodes plane) will be modified differently as the signal is *volume conducted* further from the source. In others words, H_t has the effect of a three dimensional filter, thus $H_t = H_= H_\perp$, where $H_=$ is the filter parallel to the electrodes suppressing the high frequency components and the signal's propagation velocity as it gets further away from its epicenter, and $H_\perp$ is the filter orthogonal to the electrodes which cut-off and roll-off frequency gets modified by the decreasing propagation velocity and attenuation of the high frequency components .

This analysis can be further confirmed from figure 4.7 above, we note that indeed, with respect to the BCEs, the transfer function for the BLE has been shifted toward the higher frequencies. This makes sense since the BLE would have seen the signal first. The tissues, therefore, has had less effect on the higher frequency components of the signal, and thus explaining the higher frequency content seen in the high-pass band side of its modeled transfer function (dark line). Conversely, same high frequency components had been further attenuated by the conductive media by the time they reached the BCEs, thus resulting in a stronger low frequency content seen by the concentric electrodes and lower content of high components on the high frequency band of the modeled filter, thus shifting the filter transfer functions towards lower frequencies.

Further, this analysis is well supported by the fact that different conduction velocities were needed to produced a close match between modeled and theoretical transfer functions. The conduction velocities used to compute the theoretical transfer function were 14.75, 11.90 and 5.50 m/sec for the BLE, LBCE and SBCE, respectively. Notice that the decreasing value of the propagation (conduction) velocities are inversely correlate with the electrode proximity to the electrically generated source. This suggests that the excitation impulse is volume conducted through the media in the same manner as waves propagate through any media. To clarify this point, an analogy can be made with the phenomena observed when a stone is thrown into a water tank; circular wave ripples are formed propagating at lower velocities with longer wave length as they get further away from the epicenter. In short, modeled and theoretical filter transfer functions can be considered very closely matched; the differences observed between them can be explained by the impulse's propagation velocity changes and the low-pass filtering effect of the conductive media.

Another way to verify the theoretical transfer functions could be to perform a spectral analysis on electrically elicited APs. In this case, selective activation of the same motor units enables us to control the depth, the conduction velocity and thus, by the time the AP reaches the three electrode configurations, its frequency content should be almost the same for the three configurations. This implies that the three electrode configurations should detect the same signal, (with a slight delay), and therefore any difference between the simultaneously recorded signals can be attributed solely to their respective electrode filter transfer function performance. Under such conditions the detected AP could be considered as a common impulse exciting equally the three systems. Consequently, each of the simultaneously recorded AP can be considered as the response impulse of the respective electrode configuration system. According to this rational, the APs' PSD of the responses should be representative of the respective systems' transfer function.

Figure 4.8 A below depicts APs recorded simultaneously with the three configuration systems. Observe that the BLE detects a much stronger signal (solid line, 25.81 μV RMS) in comparison to signals from the LBCE (dash line, 10.11 μV RMS) and the SBCE (dash-dot line, 5.18 μV RMS). It must be pointed out that the AP used in this case is the average of ten APs and consequently most of the noise has been reduced by this operation. Since the RMS noise level was 0.54, 0.48 and 0.48 for the BLE, LBCE and SBCE respectively, this a SNR of 47.6 for the BLE, of 21.1 for the LBC and of 11.0 for the SBCE Figure 4.8 B depicts the PSD of the signals normalized to their maximum spectral amplitude. They are similar to the shape of the filter transfer functions obtained in Figure 3.14 of Chapter Three, page 75. As expected, the PSD of the BLE signal is more shifted toward the low frequency components (MDF 125 Hz) than PSD of the signal from the LBCE (MDF 140 Hz) and the SBCE (MDF 156 Hz). These observations are in agreement with the conclusions drawn from the theoretical analysis.

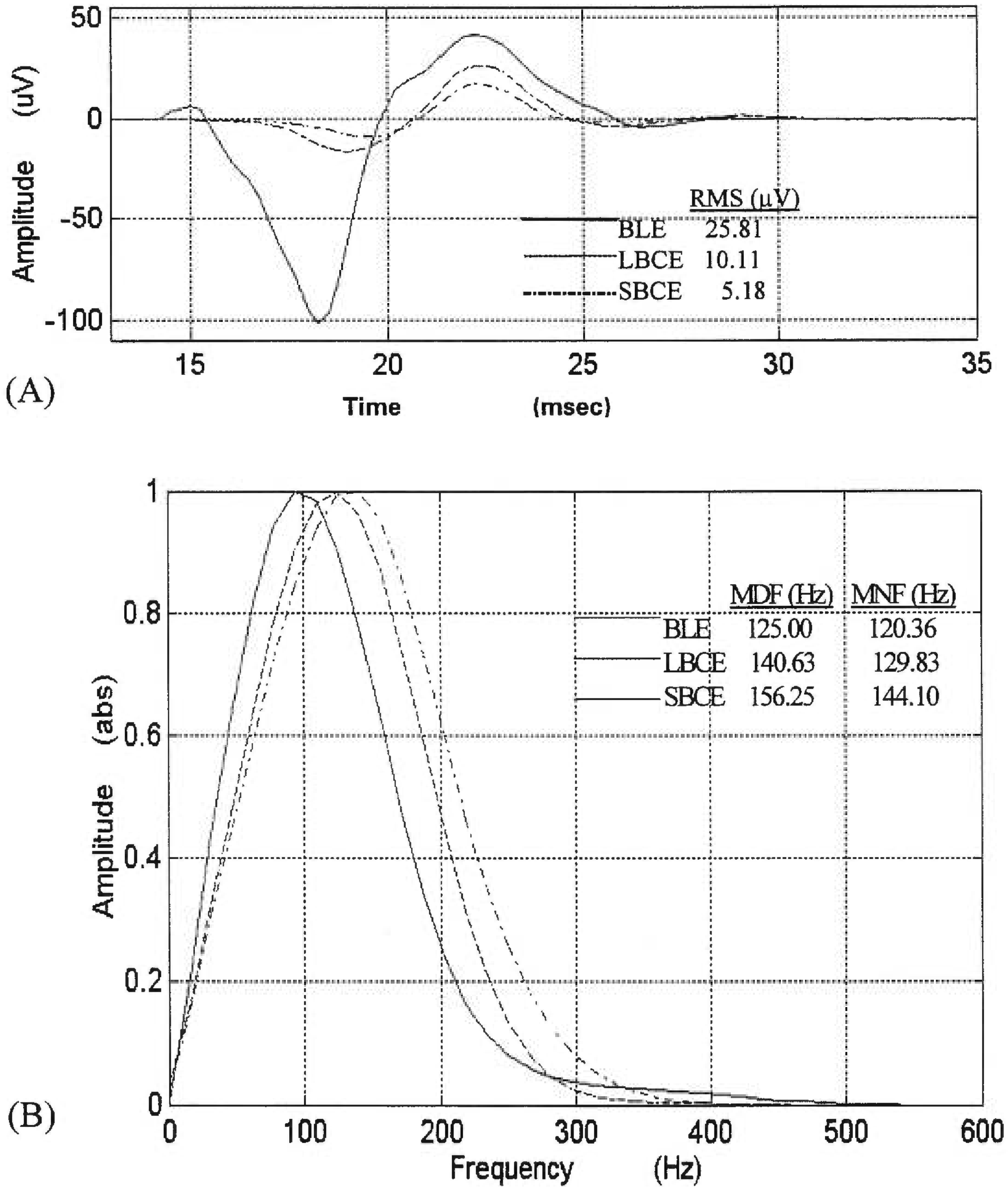

Figure 4.8 **Evoked Action Potentials and their power spectral density.** A) AP averaged over ten APs recorded simultaneously by the three electrode configurations. Differences between depicted APs are due solely to the electrode's spatial filter characteristics from each configuration. B) PSD of the recorded APs are closely shaped to the theoretical electrode transfer functions depicted in chapter three, (see Figure 3.14, page 75, for comparison).

4.6.3 Selectivity and Sensitivity to CV Changes under Ramp IVC

The first set of data analyze here is the ramp IVC up to 80 % MVC. While data from all subjects showed similar results, those of subject **A** were particularly interesting. These results are depicted in Figures 4.9 to 4.12. Force and SEMG signals were recorded simultaneously; however, there is a normal neural lag (delay) of about 200 ms between the SEMG generation and the force generation. This implies that all force events must be correlated with approximately 200 ms lag with respect to the SMEG activity (RMS wise). Figure 4.9 below shows the ramp force up to 80 % MVC and the SEMG RMS from the three electrode configurations. There are seven main events distinguished through the force generation process which can be seen more clearly reflected by the RMS curves.

The force generation process first can be analyzed in general terms from the least mean squares regression line (LMSRL) of the MDF (Figure 4.10 A), LMSRL of the MNF (Figure 4.10 B), LMSRL of the compression coefficient *k* (Figure 4.11 A) and scaling coefficient *h* (Figure 4.11 B). As could be expected, the higher frequency components prevail in the SBCE signal while lower frequency components predominate in the BLE signal. From the LMSRL slope of the MDF and MNF we can observed that BCEs show a faster increase of high frequencies components than the BLE, as the force increases. Notice that in general, the MDF shows a more rapid increase of high frequency components with the increase of force through time than the MNF, particularly the MDF of the LBCE signal (Figure 4.10 A). These observations can be further confirmed from results obtained in Figure 4.11 A, here we see that LMSRL of the compression coefficient *k* for the LBCE a faster spectrum expansion towards higher frequencies than those of the SBCE and the BLE. On the other hand, the evolution through time of the scaling factor *h* (figure 4.11 B) follows very closely the RMS process through time; however, values of the scaling factor *h* for the SBCE signal increase at a much slower rate than those of LBCE and BLE signals. These two latter follow each other very closely for the first 700 ms, after which time the LBCE signal is scaled at a higher rate than the BEC signal. These observations correlate well with the variations beginning at the third event, where the force increase seems to be achieved by modulation of progressively recruited larger fibers (type II), which have higher CVs. Furthermore, since MNF/MDF regression coefficients for the three electrode configurations are not close to the unity value (see Figure 4.10 C), therefore this suggests that spectral changes are influenced by other factors than CV, such as changes in MU's firing patterns, changes in synchronization between MU and recruitment of MU, (Merletti and Lo Conte, 1995).

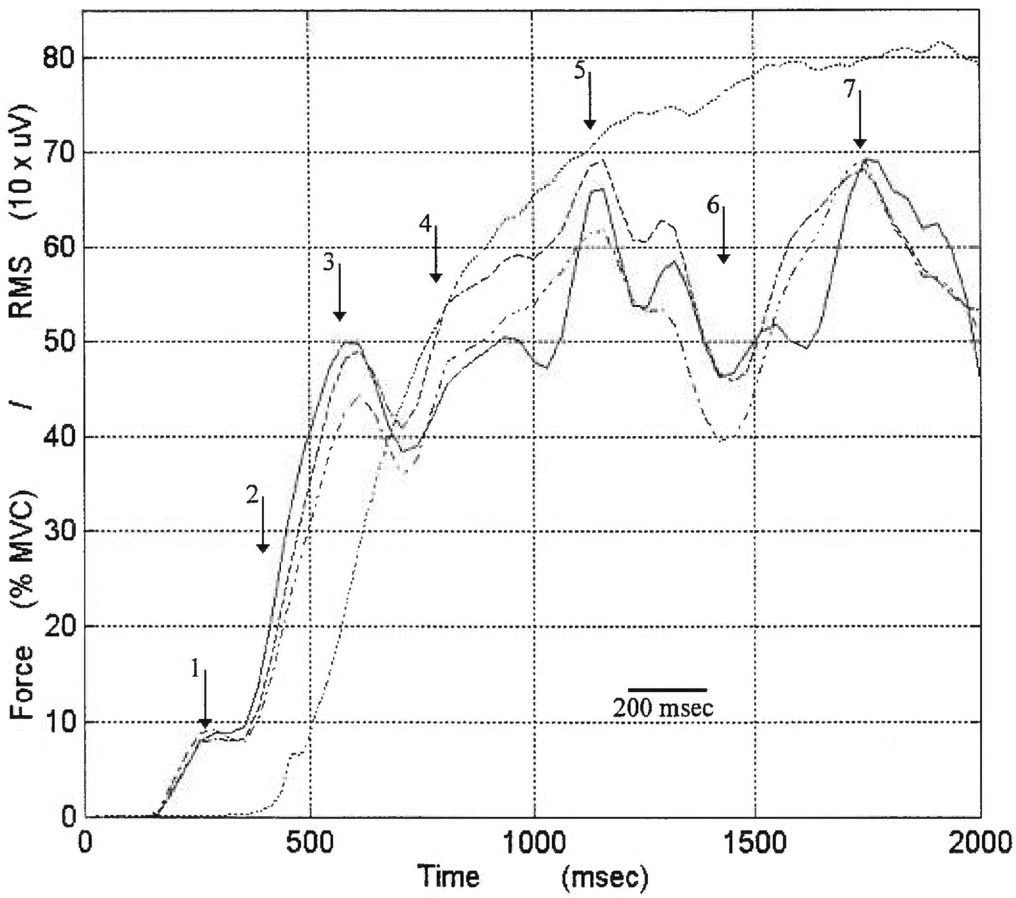

Figure 4.9 **Ramp isometric voluntary contraction**. Dotted line represents 0 to 80 % MVC force. Solid line represents RMS of the BLE SEMG signal while dash and dash-dot lines represent the RMS of the LBCE and SBCE signals, normalized to the maximum value of the BLE's RMS, respectively. Main events through time are depicted by arrows. Force events occur with approximately 200 msec delay.

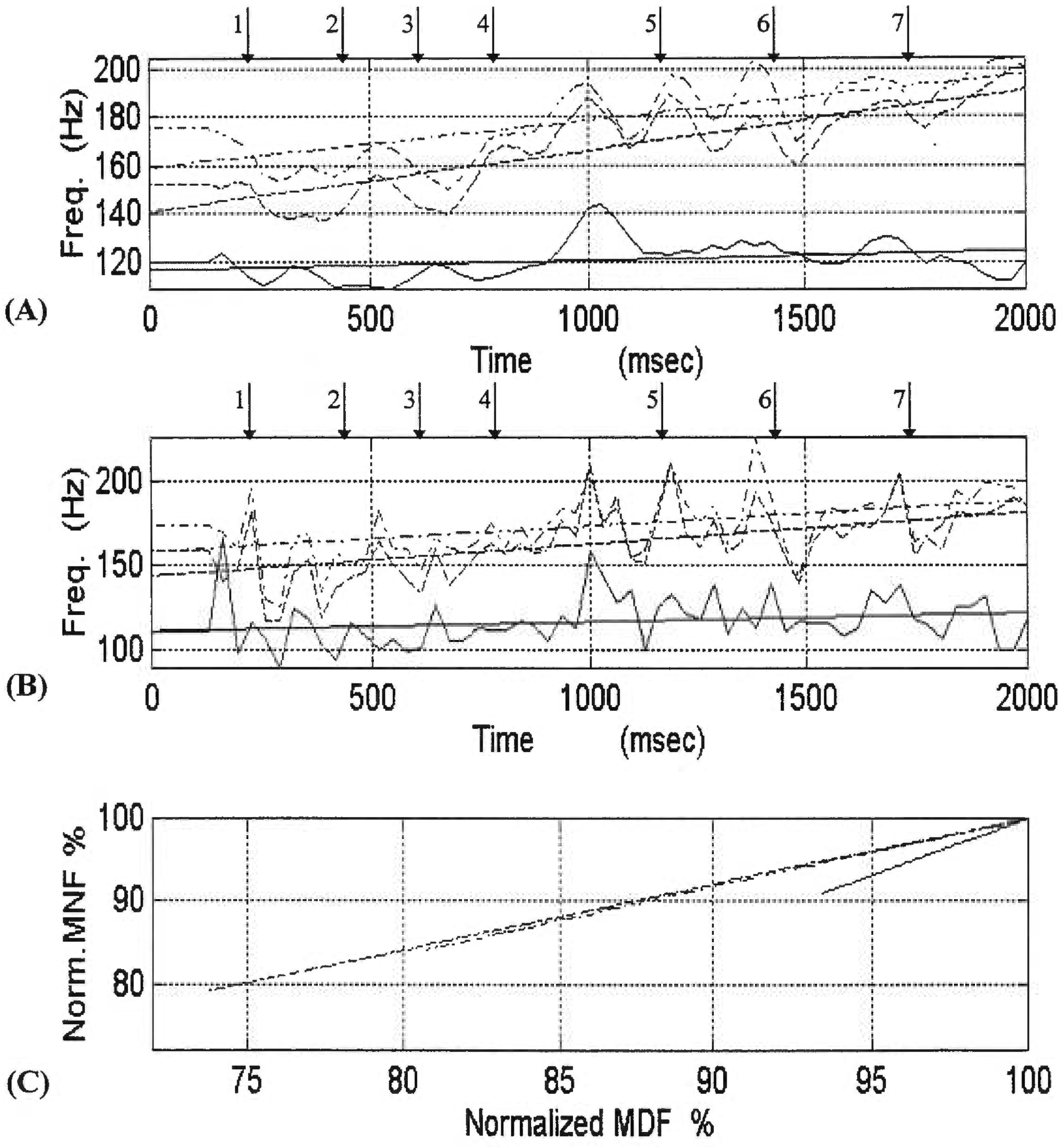

Figure 4.10 **<u>Median and Mean Frequencies</u>: A**) Median frequency variation in time. Solid, dash and dash-dot lines represent MDF from the BLE, LBCE and SBCE signals, respectively. Straight lines represent the least mean square regression of the respective MDF. **B**) Mean frequency variation in time. Solid, dash and dash-dot lines represent MNF from the BLE, LBCE and SBCE signals, respectively. Straight lines represents the least mean square regression of the respective MNF. **C**) Normalized MNF versus normalized MDF. Regression coefficients: 1.38 for BLE (solid line); 0.80 for LBCE (dash line)and; 0.82 for SBCE (dash-dot line).

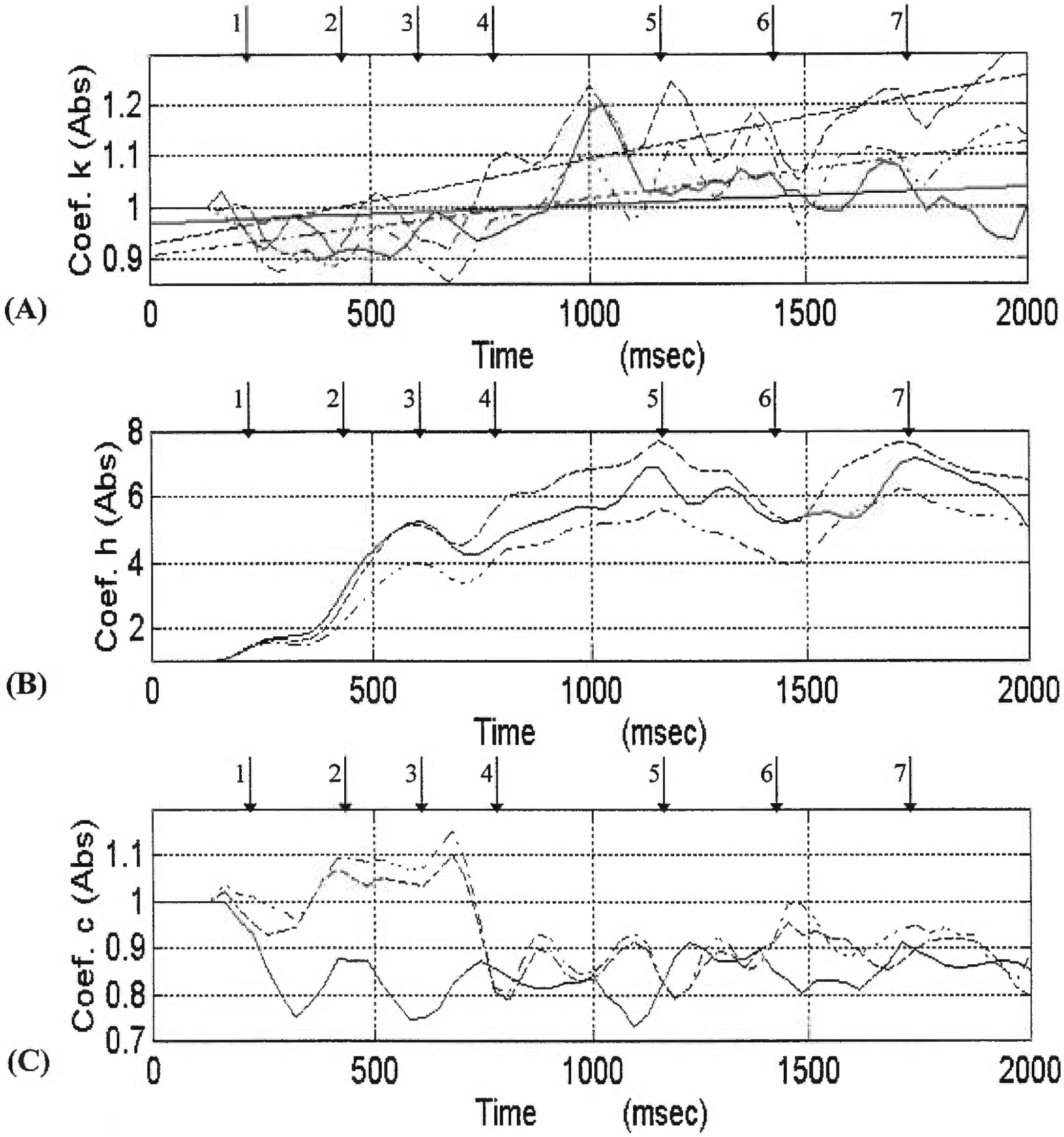

Figure 4.11 **<u>Time evolution of spectral related variables</u>:** Solid, dash and dash-dot lines represent time evolution of variables of BLEC, LBCEC and SBCEC signals, respectively. A) Coefficient of compression k. Values of *k* under the unity indicate spectral compression and over the unity indicate spectral expansion. B) Coefficient of scaling *h*. C) Coefficient of variation *c*. If the PSD shows progressive scaling without shape changes the coefficient *c* is 1. Values of coefficient *c* under 1 indicate progressive scaling with PSD compression, conversely values of *c* over 1 indicate progressive scaling with PSD expansion.

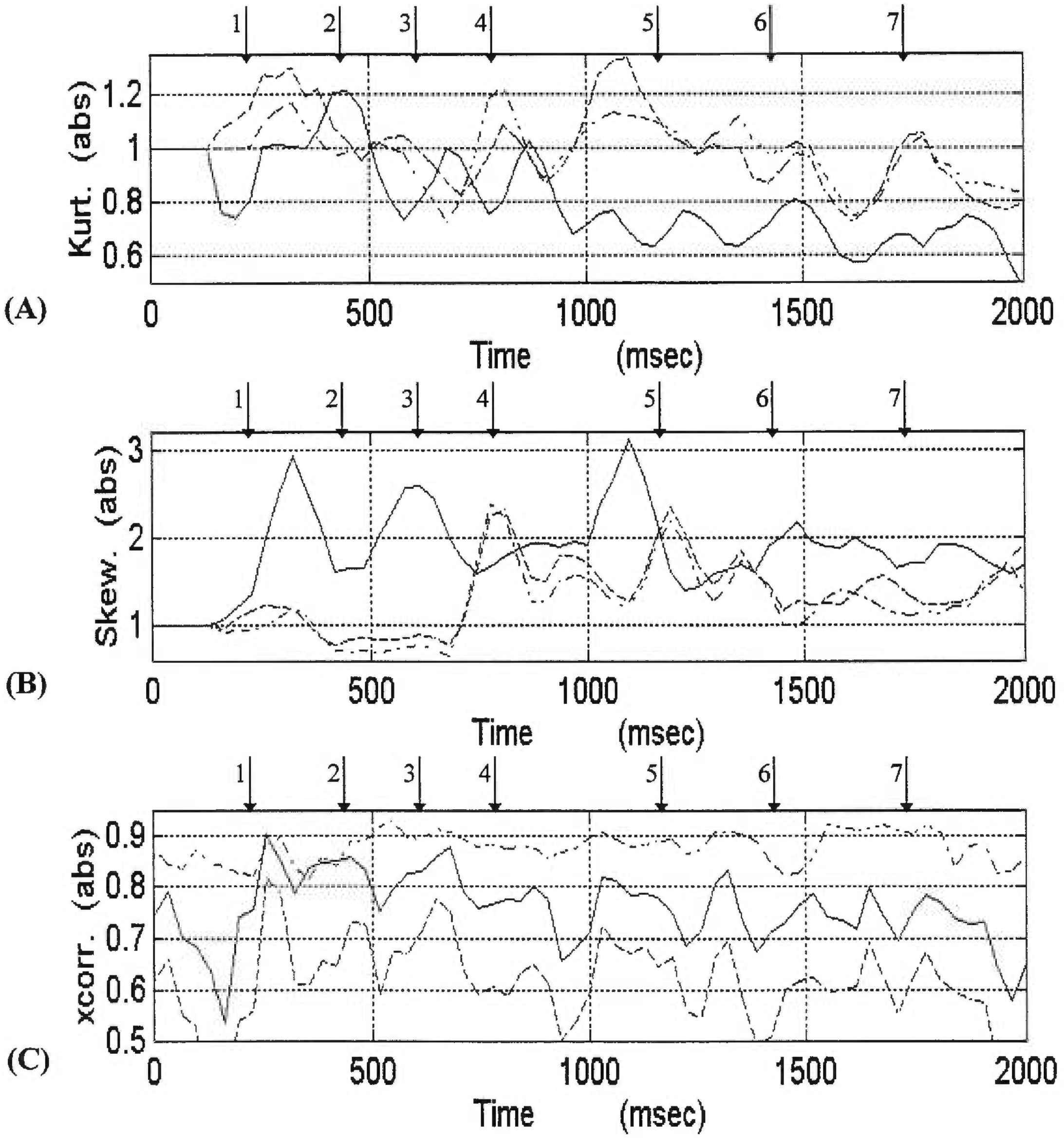

Figure 4.12 **PSD shape changes and SEMG signals cross-correlation**. Normalized indices of spectral shape changes are depicted as: A) coefficient of kurtosis B) coefficient of skewness. Time evolution of coefficients from the BLEC, LBCEC and SBCEC signals are represented by solid, dash and dash-dot lines, respectively. C) Cross-correlation coefficients between SEMG signals: between BLEC and LBCEC signals (solid line); between BLEC and SBCEC signals (dash line) and between LBCEC and SBCEC signals (dash-dot line).

Hence the signal may be expected to contain a mixture of low frequencies (probably given by the increase in firing rate) and high frequencies (probably given by an increase in the recruitment rate of larger fibers), this latter being more predominant. The modulation effect results from the rapid recruitment and derecruitment of the larger fibers. These features (EMG wise) can be better appreciated by a closer time evolution analysis of the various indices of spectral change (Figures 4.10, 4.11 and 4.12) during the force generation process. Observe that between the first and second event the MDF of the signals had decreased (Figure 4.10 A), indicating that slower fibers were recruited first to generate the force from 0 to 28 % MVC (Figure 4.9). The small peaks in MDF seen between these two events, relate to the step force produced for about 100 ms at 250 ms, which demanded a short activation of faster fibers.

These details are well illustrated by the coefficient of variation *c* (Figure 4.11 C). Between events one and two the value of *c* for the BLE has dropped considerably but its compression factor *k* has increased close to the unity value representing an expansion of the spectrum (Figure 4.11 A). This indicates that the changes might be mainly due to a redistribution of the spectrum towards high frequencies components, a conclusion which is confirmed by the rapid increase in the skewness coefficient (Figure 4.12 B) and the value, close to unity, of the kurtosis coefficient (Figure 4.12 A). The RMS begins to increase again at about 350 ms where the step has concluded (Figure 4.9). At this point we see in Figure 4.11, for the BEC signal, its compression coefficient *k* decreasing while its variation coefficient *c* increases; this indicates a compression of the spectrum due to an increase of low frequency components, as result of a further recruitment of slow fibers. This is confirmed by an increase in the kurtosis (peakedness) and a fast decrease in the skewness (low frequency tail) right up to the event two.

Conversely, since BCEs are more selective to high frequencies and yet still capable of including low frequency components, these signals showed a slightly different behavior. First we notice in Figure 4.11 that at about 250 ms, both coefficients, variation *c* and compression *k* drop during the 100 ms of the step force duration, indicating a compression of the spectrum as well and therefore that these changes are not simply due to an increase in high frequency components (faster fibers), as was pointed out in the case of the BLE signal, but rather to a combined effect of an increase in low and high frequency components.

This combined effect is confirmed by a higher increase of the kurtosis factor with a low increase of the skewness factor indicative of a small high frequency tail (Figures 4.12 A and B, respectively). In other words and judging by the small peak frequency which appears in the MDF between events one and two (Figure 4.10 A at about 350 ms), we can only assume that while slower fibers are activated to generate the force level, the appearance of newly recruited faster fibers have allowed the system to maintain the step force for a short period of time.

After the step force finishes at about 350 ms (Figure 4.9, RMS wise), we observe in Figure 4.11 the variation coefficient *c* increasing while the compression coefficient *k* remains fairly constant, suggesting that changes in the spectrum are rather due to a redistribution of frequencies than to a compression or expansion of the spectrum. We notice also that at the same time (350 msec), the spectrum has been shifted towards low frequencies as consequence of a combined effect of an increase of the low frequency components and an increase in the amplitude of the lower high frequency components. In physiological terms, we could interpret from these observations that the force generation from the end of the step event up to 28 % MVC was achieved by a combined additional recruitment of new deeper slow and fast fibers (simultaneous decreased in the kurtosis and skewness factors). This would explain the redistribution of the spectrum towards low frequencies with a decrease in kurtosis and skewness but without significant changes in the compression factor and MDF, (signals from active fibers located further away from the recording electrode are stronger low pass filtered by the conductive media). In short, it begins to become evident that BCE signals are capable of providing more details of the neurophysiological phenomenon of muscle contraction than the BLE signal which provides mainly global information.

The two phase processes observed between events two and three, (increase and decrease of the MDF and coefficient *k*), plus the oscillating changes of the kurtosis of the BCE signals denote more details of the force generation process between 28 to 53 % MVC than that provided by the BLE signal. Accordingly, we notice that the expansion phase of the spectrum towards high frequencies occurs in two stages, beginning with a recruitment of superficial fast fiber which increases the high frequency components of the spectrum, thus producing a flatter shape of the spectrum. In a second stage a further amplitude increase of these newly recruited high frequency components brings about a peaked shape of the spectrum. The compression phase follows with a gradual compression of the spectrum towards low frequencies. Also in two stages, additional deeper fast fibers are recruited in a first stage, thus shifting the peak of spectrum towards lower frequencies in a compression mode; then in a second stage more superficial fast fibers are recruited together with a further recruitment of deeper fast fibers resulting in a flatter spectrum. In both cases, (BLE and BCE signals) we can see that the combined involvement of deep and superficial faster fibers is responsible for the force increase from 28 to 50 % MVC; however the BCE signals provide a more detailed description of the neurophysiological phenomenon involved in the force generation process.

Between events three and four we observe a quite different behavior between BLE and BCE signals (Figure 4.10 A). The MDF of the BCE signals first continues to decrease to a valley (at about 670 ms) only to raise again to a higher value. Notice also that this behavior is paired with those of the RMS (Figure 4.9), the compression coefficient *k* (Figure 4.11 A) and kurtosis (Figure 4.12 A). This means that the changes in the spectrum are first due to a gradual derecruitment of the deeper active fibers coupled with a faster derecruitment of the superficial active fast fiber, bringing about a flatter spectrum in a compression mode towards the low frequencies until just about 670 ms. From this point on, the RMS is increased again by the re-recruitment of the superficial faster fibers, thus producing in turn an expansion of the spectrum (increase of the compression factor k >1, Figure 4.11 A) towards high frequencies, and producing an increase in the skewness and kurtosis factors (Figures 4.12 B and A).

A quite different behavior is observed for the BLE signal between events two and three. Here the MDF first increases to a peak and then decreases to a valley only to slowly increase again (Figure 4.10 A). Notice that this behavior of the MDF is also followed very closely by the compression coefficient *k* (Figure 4.11 A) and the kurtosis (Figure 4.12 A). These changes suggest that the drop in the RMS is due first to a derecruitment of deeper active fast fibers and a concomitant enhancement of the contribution of superficial active fast fibers which in turn produces an expansion of the spectrum (increase of *k*) towards high frequency components, a resulting increase in peakedness (increase of kurtosis) and a reduction in skewness just until about 630 ms. It follows a derecruitment of superficial active fast fibers, which now produces a compression of the spectrum towards the low frequencies with the concomitant reduction in kurtosis and skewness just until about 700 ms. From here on, superficial faster fibers are re-recruited producing an increase of the MDF and an expansion of the spectrum towards high frequencies, thus an increase in kurtosis and skewness. In short, we remark once again that both electrodes configurations describe the same phenomenon, simply in a different order of events, with the BCE able to pick up more information concerning the neurophysiological phenomenon related to muscle contraction.

From event four to event seven we observe that while the MDF of the BCE signals increases in a oscillating mode, the MDF of the BLE signal increases more slowly with less radical changes. Similar behavior is noticed for the various coefficients of spectral change, particularly the compression coefficient *k*, which is directly related to changes in CV. From this observation and the analysis conducted until now, it is obvious that BCE signals reflect with higher fidelity the neurophysiological events resulting in the changes of the RMS during the force generation process from 54 to 80 % MVC. This implies that since more spectral changes are observed for the BCE signal than for the BLE signal, the BCE is more sensitive and selective to local changes in CV.

The main objective of this analysis has been to examine the sensibility and selectivity of the BCE to changes in CV rather than to explore the neurophysiological phenomena involved in muscle force generation. It is felt that this prime objective has been met satisfactorily, therefore further analysis of these particular data is left as an exercise to the interested reader. The question of stability of the BCE remains however.

4.6.4 Stability to Local Changes in CV under Step IVC

The question of the BCE stability can be investigated by an analysis of SEMG data collected under step isometric contraction conditions. This type of experiment allows us to maintain a two seconds of constant contraction at various levels of MVC. The contraction time was sufficiently short to avoid changes in CV due to fatigue and yet long enough to track changes in the signal which might be caused by instability of the BCE filter on its high bandpass.

Generally speaking, similar results were observed from data analyzed across subjects and at various levels of step contraction (10 to 80 % MVC). Consequently the results obtained from subject **B** at 60 % MVC will suffice to illustrate the changes typically observed from this set of experimental data. The results are depicted in Figures 4.13 and 4.14.

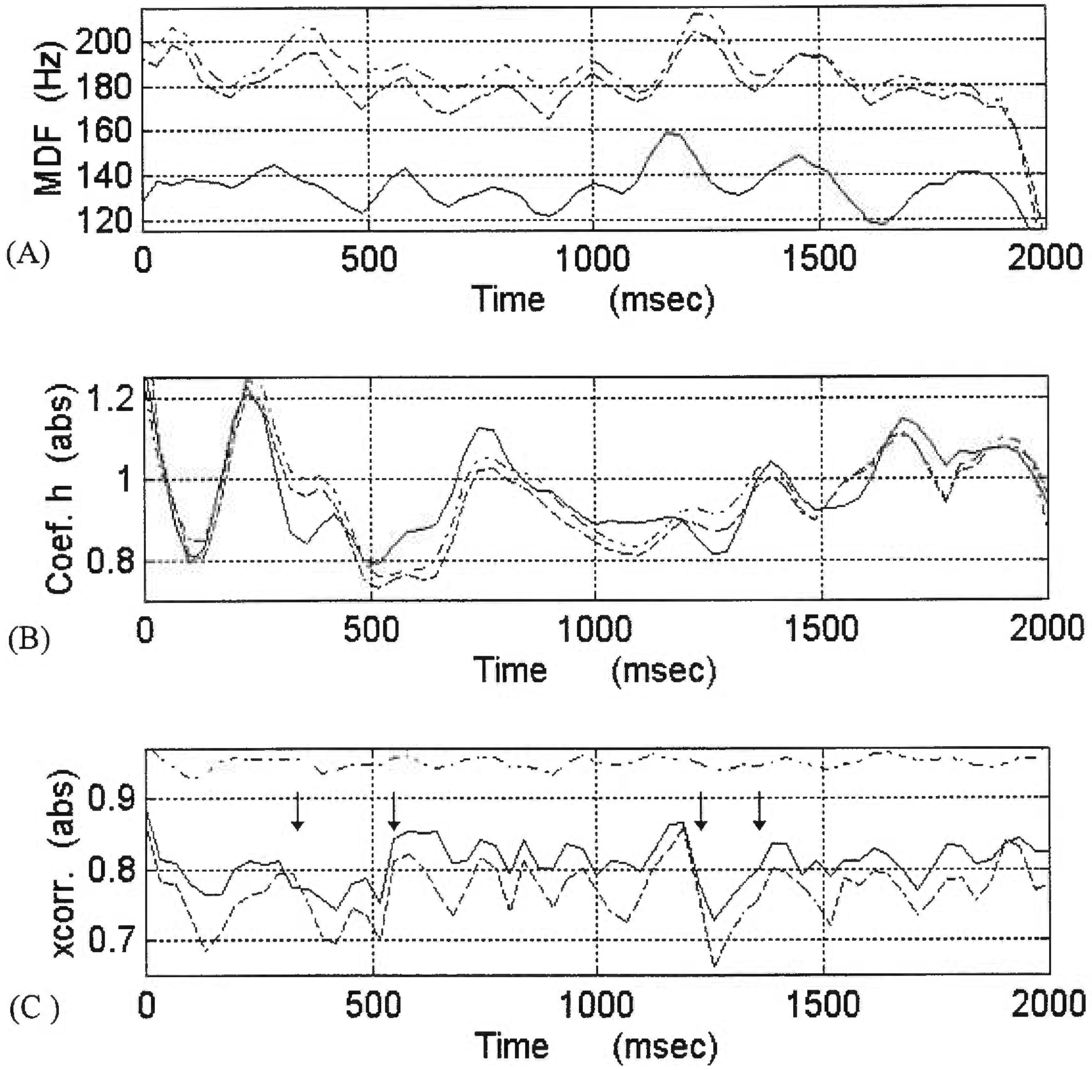

Figure 4.13 Indices of spectral shape changes during step IVC at 60% MVC.
A) Median frequency variation in time: Solid, dash and dash-dot lines depict MDF of BLE, LBCE and SBCE signals, respectively. **B**) Scaling coefficient *h* variation in time: Solid, dash and dash-dot lines represent the scaling coefficient of BLE, LBCE and SBCE signals, respectively. **C**) Cross-correlation factor: Solid, dash and dash-dot depict the correlation coefficient variation in time between BLE and LBCE, between BLE and SBCE and between LBCE and SBCE signals, respectively.

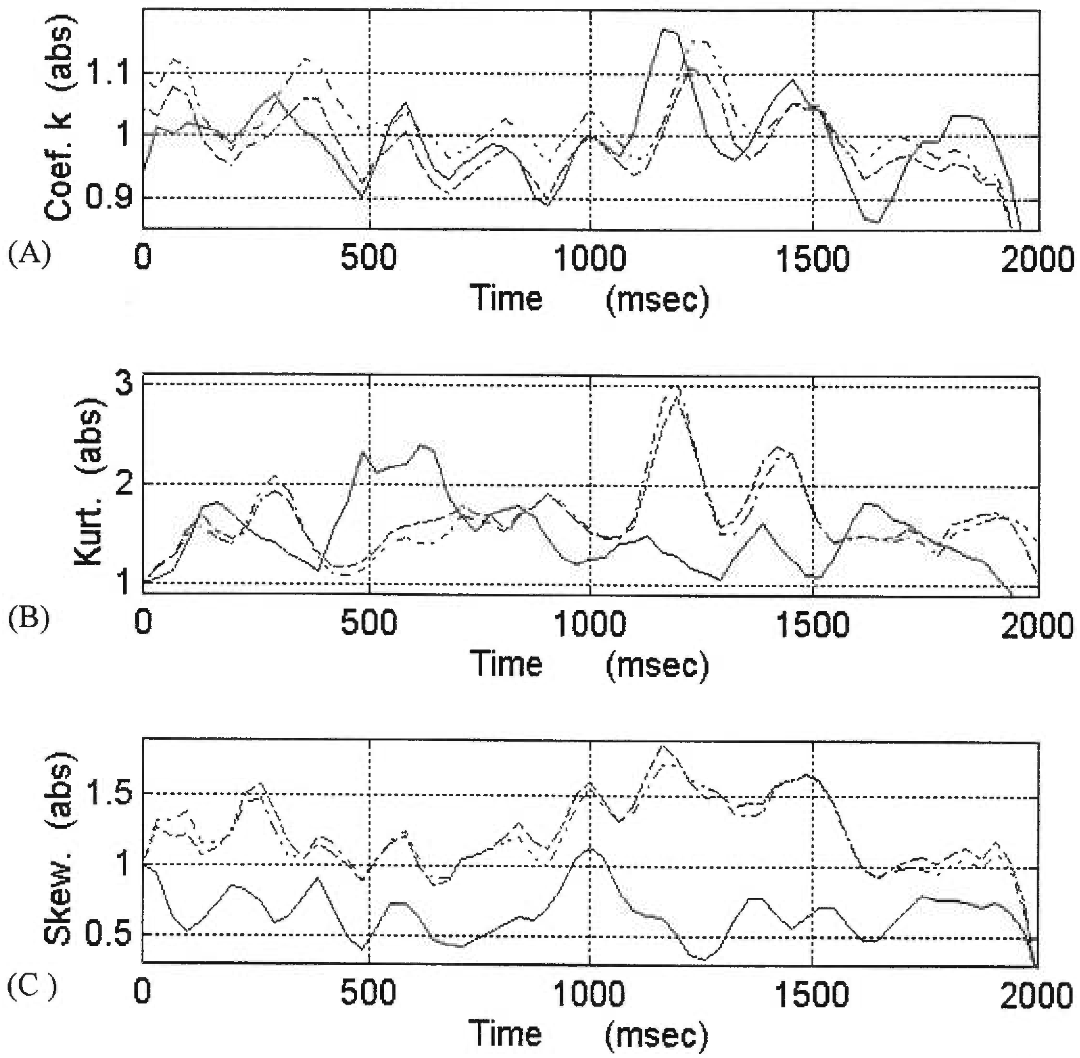

Figure 4.14 <u>**Indices of spectral shape changes during step IVC at 60% MVC**</u>. **A**) Compression coefficient *k* variation in time: Solid, dash and dash-dot lines depict the compression coefficient *k* of BLE, LBCE and SBCE signals, respectively. **B**) Kurtosis coefficient variation in time: Solid, dash and dash-dot lines represent the kurtosis coefficient of BLE, LBCE and SBCE signals, respectively. **C**) Skewness coefficient: Solid, dash and dash-dot depict the skewness coefficient variation in time of BLE, LBCE and SBCE signals, respectively.

From the previous analysis it was remarked that the time evolution of the scaling factor *h* follows very closely that of the RMS, (depicted in Figure 4.13 B below) and therefore for analytic purposes the former will suffice. Note that changes in time of the scaling factors *h*, (and therefore their RMS) from the three electrodes configuration signals follow each other extremely closely. In fact, the cross-correlation factor through time between the BLE and the BCE signals is quite high and fairly constant (about 0.8, Figure 4.13 C), meaning that a high probability exist that these signals carry basically the same information. From Figure 4.13 A, we observe that although the MDF changes through time from the three signals follow each other very closely, that of the BCEC signals is higher than that of the BLEC signal.

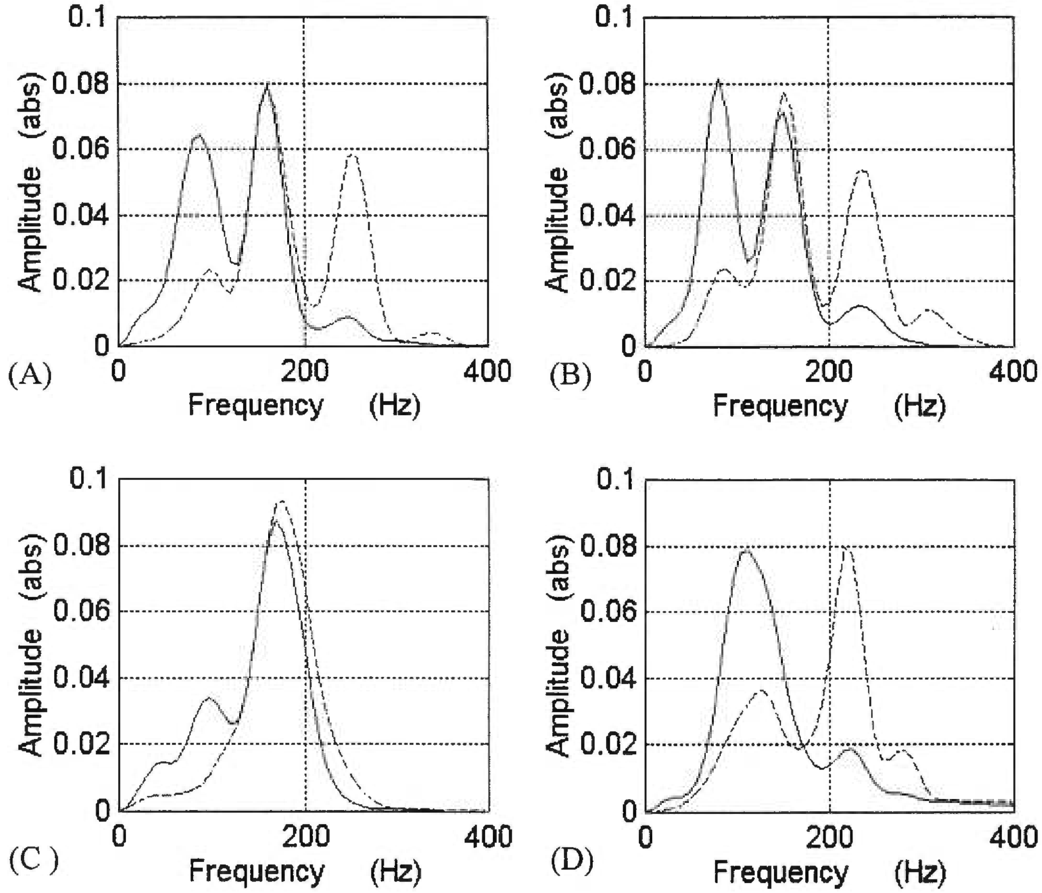

Figure 4.15 **Distribution of spectral components of BLE and LBCE signals**. Illustration of sequential change in spectra of BLE (solid line) and LBCE (dash line) at 350 and 505 ms (**A** and **B**), and at 1200 and 1400 ms (**D** and **C**). Notice that both signal share the same frequency components with different distribution. Low frequency components are emphasized in the BLE signal and high frequency components are emphasized in the LBCE signal.

Further, no drastic changes are observed in the time evolution of the MDF of the BCE signals with respect to that of the BLE signal and in fact, their compression factor *k* varies equally for signals from both electrodes configurations (Figure 4.14 A). These observations indicate that the BCE filter is as stable as the BLE filter. Only two short instances existed where a drop in the cross-correlation factor could be distinguished, (between 350 and 505 ms and between 1200 and 1400 ms, Figure 4.13 C). However, these two instance are not necessarily a sign of BCE filter instability, since they can be explained in terms of the time evolution of the kurtosis and skewness factors (Figure 4.14 B and C). Observe that in the first instance, the kurtosis factor of the BLE signal increases rapidly while same factor decreases slowly for the BCE signals; meanwhile the skewness decreases at an equal rate for both types of signals. This implies that both BLE and BCE signals share the same frequency components and that their common spectrums differ only in their frequency distribution. In other words, between 350 and 505 ms BCE spectrums show higher amplitudes for their high frequency components and lower amplitude for their low frequency components than BLE spectrums, thus explaining a reduction in the kurtosis (flattening of the spectrum). These observations are well illustrated in Figures 4.15 A and B above, which depict typical changes of the spectrum during the designated time.

Conversely in the second instance, between 1200 and 1400 ms, observe the kurtosis coefficient of the BCE spectrum decreases rapidly while that of the BLE decreases slowly, at a time when their skewness coefficient decreases basically at the same rate. These spectrum changes of the BLE and BCE signals are due to the redistribution of their common spectral components as depicted in Figure 4.15 C and D. Observe that in Figure 4.15 C, the bulk of the frequency components are commonly shared and that the BLE includes low frequency components of the signal while high frequency components are enhanced by the BCE. In Figure 4.15 D we can see that even though changes have occurred in the spectrum through time, both signals still carry the same frequency components but with a different frequency distribution, as pointed out before. In short, the BCE filter is found to be as stable as the BLE filter and the differences observed between the BLE and BCE signals are rather due to the selectivity of the BCE to localize signals propagating under the electrode's pick up volume and to its sensitivity to rapid changes in the CV. Sensitivity to rapid changes in CV has been proven mainly for the high bandpass; now we will see if the BCE is also capable of detecting local events characterized by a decrease of CV during muscle fatigue.

4.6.5 Selectivity and Sensitivity to Local Low Frequency Components

The question to be investigated now is whether the BCE, been more selective and sensitive to the signal's high frequency components, can distinguish EMG events that involve as well an increase in low frequency components. The analysis of the SEMG data collected under fatigue condition at 40 % MVC for two minutes show typical results for all subjects; therefore the results obtained from subject **E** will serve to compare spectral changes during fatigue from both electrode configurations. These results are presented in Table V below. First, notice that BLE and LBCE signals show a good cross-correlation factor while the same factor obtained between BLE and SBCE is much lower. Notice however that in both cases the cross-correlation factor is slightly reduced as the MDF of their respective signals decreases through time. The contrary happens for the cross-correlation factor between LBCE and SBCE signals, which is quite high and increases as the MDF of the signals decreases. These observations only confirm the selectivity of the BCE filter to high frequency components; however MDF and MNF of the BCE signals, even though higher, decrease basically at the same rate as the MDF and MNF of the BLE signal, a fact which is shown by the respective slope coefficient of their LMSRL.

In the case of the three signals, the changes in their respective MDF versus MNF through time are very close. In fact the slope and correlation coefficients of the LMSRL of their respective normalized MNF versus normalized MDF were found to be within the unity value (1.03, 1.05 and 1.05 for the BLE, LBCE and SBCE signals, respectively). This implies that changes of the three signals and their respective spectral shapes are due to *pure spectral compression*; no other factors beside the CV affect the signals. Estimates of k and h can be considered very reliable. Observe that the compression coefficient k decreases at the same rate for the three signals (-0.002), meaning that similar conclusions can be derived from the analysis of both types of signal under circumstances where the CV decreases and consequently the low frequency components of the signal increase. Summing up, apart from the BCE selectivity and sensitivity to high frequency components of the signal, no significant differences can be observed between BEC and BCE signals.

Table V Indices of spectral shape changes during fatigue

	Time (seconds)					**Slope**
Cross-corr. between : ↓	**0**	**30**	**60**	**90**	**120**	**coeff.**
BEC and LCEC signals	0.781	0.763	0.755	0.736	0.763	-0.0004
BEC and SCEC signals	0.675	0.657	0.655	0.650	0.644	-0.0002
LCEC and SCEC sign.	0.933	0.937	0.938	0.945	0.947	-0.0001
Median Frequency **MDF** ↓						
BEC signal	135.51	127.73	122.35	105.20	93.24	-0.3569
LCEC signal	190.70	181.27	179.57	152.62	147.06	-0.3840
SCEC signal	200.83	193.14	190.02	162.27	156.99	-0.3952
Mean Frequency **MNF** ↓						
BEC signal	135.24	126.69	120.68	102.39	92.04	-0.3690
LCEC signal	187.90	181.29	176.84	150.68	142.35	-0.4036
SCEC signal	198.19	192.73	188.11	159.69	153.35	-0.4091
Variation coeff. *c* ↓						
BEC signal	0.423	0.443	0.467	0.516	0.552	0.0011
LCEC signal	0.364	0.384	0.374	0.382	0.411	0.0003
SCEC signal	0.356	0.378	0.364	0.377	0.398	0.0003
Scaling coeff. ***h*** ↓						
BEC signal	0.997	1.001	1.067	0.588	1.236	-0.0003
LCEC signal	1.001	1.017	1.141	0.533	0.882	-0.0025
SCEC signal	0.999	0.996	1.121	0.518	0.813	-0.0028
Compression coeff. ***k*** ↓						
BEC signal	0.996	0.939	0.899	0.773	0.685	-0.0026
LCEC signal	1.083	1.030	1.020	0.867	0.835	-0.0022
SCEC signal	1.046	1.006	0.989	0.845	0.818	-0.0021

4.8 DISCUSSION

It is clear from the results analysis that rather limited answers can be provided to the question concerning sensitivity to noise disturbances related to skin/electrode interface, since part of the noise level recorded can also be attributed to the bare minimal EMG activity observed on relaxed subjects or environmental noises. Definitely, in order to draw proper conclusion, this question needs better suited experimental set-up and testing protocol. However, at the light of the partial results obtained with the limited resources at hand, three important conclusion can be inferred from these. In general, signals obtained with the LBCE were about 40 to 45 % (RMS wise) of that obtained with the BLE and considering that the mean average noise level was found to be approximately 15 μV all around, (see Table II, III and IV, pages 93-94) and that typically a 10% MVC was produced by a BLE signal of approximately 100 μV (RMS), then we should expect a SNR of 2.8 (compared to BLE SNR of 6.7); which it is a quite reasonable good SNR, particularly when this will increase as the signal increase.

However, this assumption will hold only providing that a good electrode/skin interface is ensured, which bring us to the second finding: the mean RMS and amplitude values of the noise level for both electrode configuration systems, BLE and BCE, were found to be pretty close to each other and quite consistent across subjects, with one exception. In the particular case of subject C, the discrepancies of RMS and amplitude noise values observed, (in reference to the other subjects), can definitely be attributed to an uneven electrode/skin interface contact of the BCE. This event was indeed produced by the subject's excessive perspiration and skin reaction to the conductive gel. In fact, data has to be collected in two separated experimental seances; the first seance was suspended at the subject's request, the second time the subject was more relaxed and therefore more able to withstand the uncomfortable skin reaction sensation. Thirdly, surface area ratio for the BLE was one, while for the BCE the surface area ratios, (between the centre electrode contact and the coaxial ring contact), were 8.57 and 5.63 for the LBCE and SBCE, respectively. Thus, the bigger the area difference between electrode's contacts, the lower the possibility that the polarization potential (DC noise generated by the lack of chemical equilibrium at the metal-electrolyte junction), can be entirely nullified by the differential technique. Exactly the opposite situation can be observed in the case of subject E, where an excellent electrode/skin interface contact was obtained resulting in the lowest DC noise generated. Conductive gel was applied to all electrodes at the moment when these were placed on the subjects to ensure a good skin/electrode interface contact. As a general rule this practice is quite effective in reducing DC noise, as can be confirmed from the results presented in the Tables II to IV.

Filters' transfer function were computed for each configuration with a four-zeros-four-poles ARMA model using their respective recorded impulse responses; these were compared with their respective theoretical filters' transfer function. A good match was found between the computed and theoretical transfer function, mainly on the low bandpass of the filter. Differences found on the high bandpass, however, are attributed to characteristic of the conductive media rather than to the accuracy of the theoretical transfer function; these differences were extensively discussed in the previous section.

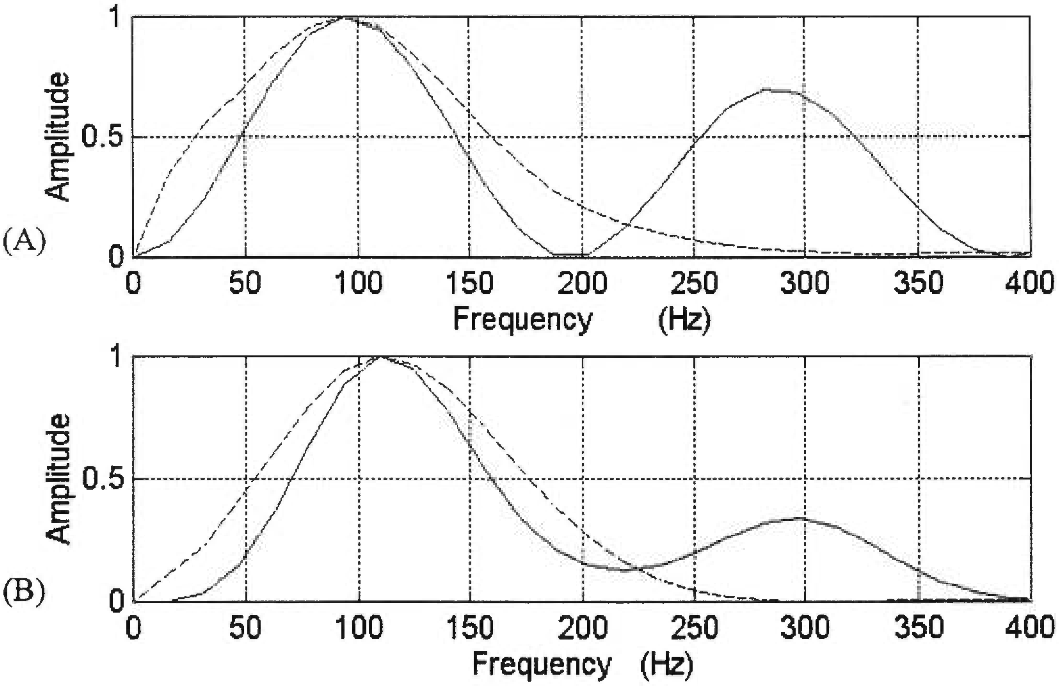

Figure 4.16 **<u>Normalized filter transfer function and AP-PSDs</u>**. Theoretical filter transfer function (solid line) is compared to the PDS (dash line) of an electrical elicited AP considered as the filter's impulse response for the bipolar electrode configuration (A) and the large concentric electrode configuration.

Further validation of these theoretical transfer functions was performed by comparison of PSDs computed from each of the recorded electrically elicited AP. Each the of simultaneously recorded APs were considered as the filter's impulse response of their respective electrode configuration and consequently, their PSD is considered to be representative of their filter transfer function. These are shown in Figure 4.16 above. The theoretical filter's transfer function were computed with the dimensions of their respective electrodes configurations and a CV of 1.6 m/sec. Notice that in both cases, the transfer functions are closely shaped to the PSD; however both PSDs have a broader bandpass than the respective filter transfer function. Since the AP is not a perfect unity impulse, this difference can be attributed to the APs frequency content.

The selectivity and sensitivity of the BCEs to changes in CV was investigated using indices of spectral changes parameters. In this analysis, the estimates of the various indices of spectral changes were obtained from Equation 2.18 to 2.27, Chapter Two, (Merletti and Lo Conte, 1995). These indices depend on spectral variables such as MDF and the four first spectral moments (scale insensitive); and therefore are not affected by the gain of the filters' electrode configurations. In general, it can be said that in comparison to the linear configuration, the concentric configuration was found to be more selective to neuromuscular events reflected from signals containing high frequency components; such selectivity permits as well to assess how deep signals were generated and possible identification of fiber type. Further, concentric configurations were found to be more sensitive to rapid changes in the signals frequency components, and thus providing more details of the neuromuscular events taking place through the generation and control of force.

Given the fact that the concentric configuration emphasizes high frequency components, both its selectivity and sensitivity were as well investigated for low frequency component. Again, these were found to be comparably as good as those of the linear configuration. This was also confirmed during investigation of the filter's stability; the correlation between signals is kept fairly constant trough out physiological changes of the muscle (see Table V); in fact both electrode configuration share the same frequency components (see Figure 4.15), changing only in the distribution of their frequencies.

Finally, regarding stability, in comparison to signals from BLE, signals from BCE showed the variation coefficient changing less drastically while their respective scaling coefficients, MDFs and MNFs changed at the same rate. This is quite understandable given that BCEs are more selective and sensitive localized changes while the BLE is more selective and sensitive to global changes.

4.8 CONCLUSIONS

In light of the experimental results discussed here, it can be concluded that although BLE and BCE signals might show different behavior they describe the same phenomenon. The main difference between these signals, however, lays in their capability to description of the sequence of more localized neurophysiological events. The BLE strongly emphasizes the signal's low frequency components and therefore provides a global description of the events, while the BCE favors high frequency components at a time that includes as well low frequency components; consequently the BCE signal is able to provide a more detailed picture of the neurophysiological events taking place locally.

In definitive, the BCE characteristics described in the theoretical and experimental analysis respond very well to the requirements demanded from an electrode configuration needed to generate a spatio-temporal EMG mapping technique. However, the dimensions of such electrode configuration must be closely controlled, particularly the area ratio between the central electrode and the outer ring, which must be kept closed to its unity value. Two main reasons support this conclusion, first smaller difference between electrode contact areas helps to nullify DC noise generated by the lack of chemical equilibrium at the metal-electrolyte junction; and second, a larger diameter of the centre electrode produces well defined filter's dip, and well limited bandpass. Finally, the outer ring should be sufficiently large as to provide a good gate for local signals carrying the bulk of the neuromuscular information, which has a median frequency in the neighborhood of 120 Hz.

CHAPTER FIVE

SPATIO-TEMPORAL EMG MAPPING TECHNIQUE

5.1 INTRODUCTION

The central problem addressed by this thesis was defined as the production of a dynamic image capable of depicting the ensemble of muscle activities involved in action development in such a way that both global and individual EMG patterns can be elucidated. The solution proposed was to generate a the spatio-temporal mapping of muscle activity coupled with the movement cinematic. For reasons explained in Chapter Two, this kind of SEMG measurement requires an electrode capable of recording high fidelity signals representative of local muscle activity, free from transient noise. The solution was found in the selectivity properties of the spatial filtering technique induced by the construction of a Laplacian discrete function and developed from the point of view of electrode geometry. To this end, Chapters Three and Four were dedicated to the investigation, development, testing and validation a Laplacian electrode with an optimal geometric configuration. Such a configuration was found on a bipolar concentric electrode.

The analysis of experimental results confirmed the selectivity assumption and defined the requirements and conditions for the validity of an EMG Laplacian measurement. Sensitivity to disturbances related to skin/electrode interface, and the selectivity, sensitivity and stability dependence of the Laplacian spatial filter to changes in CV were then investigated through physiological experiments. Results showed that the BCE seems to attenuate noise in a similar manner to that which it attenuates the signal and that in spite of its low gain, a reasonable good SNR can still be obtained if a good skin/electrode interface can be assured and if the central electrode's area is increased. Further, the BCE's selectivity, sensitivity and stability were confirmed by its filter's high pass performance consistency.

In short, provided that certain geometric dimensional requirements are met, the BCE's spatial filtering characteristics furnish localized EMG measurements, which are independent of: muscle fiber direction; location of innervation points; directional polarity; and transient noises (non-propagated signals). Therefore, we are now in a position to implement this electrode in a measurement device that will permit the generation of a dynamic internal image of the muscle orchestration involved in movement execution.

5.2 OBJECTIVE AND FRAMEWORK

Both objectives and framework for this chapter are given by the general objectives proposed and detailed in six stages in Chapter One, page 19. In view of the limited resources available, this chapter is dedicated to develop the conceptual bases of the spatio-temporal EMG mapping technique; further a proof-of-concept is implement and validate by means of a "virtual array of BCE" recording technique. In order to ensure validity of the Laplacian measurement, the BCE's physical dimensions will be first defined according to the requirements demanded by this type of application. This will be followed by the development of the mapping technique in detail. The technique then will be implemented and verified by means of physiological experiments. And finally, a number of possible practical applications of the technique as well as future research will be outlined.

5.3 PHYSICAL DIMENSIONS OF THE BCE

We are now in a position to define the physical dimensions required by the BCE in order to obtain a spatial filter suited to the demands of its particular of application. To this end, three requirements must initially be met:

1) the filter's bandpass must be within the EMG signal's frequency range; thus, between approximately 50 and 350 Hz with a bandpass between approximately 80 and 250 Hz and a median frequency around 170 Hz. These specification are a good compromise between electrode's spatial filter requirement and the electrodes geometrical dimensions, that is,

2) the outer ring's dimension must be large enough to pick up signals with a wave length of the above frequency range but small enough to allow a good resolution between recording sites and;

3) the area ratio between the outer ring and the centre electrodes must be small enough to minimize DC noise generated by an eventual lack of chemical equilibrium at the metal/electrolyte junction.

To fulfil these requirements, the BCE's geometrical dimensions have been defined here as shown in figure 5.1 below. These dimensions give an area ratio of 1.5, which ensures a low DC noise level in the event that poor contact between electrode/skin is produced. Further, the centre to centre distance between electrodes forming the array is 25 mm, with a distance of 10 mm between respective outer rings. This enables a good resolution of surface potential distribution as well as a 5 mm free surface for application of double sided tape to secure the electrode's placement on the skin surface.

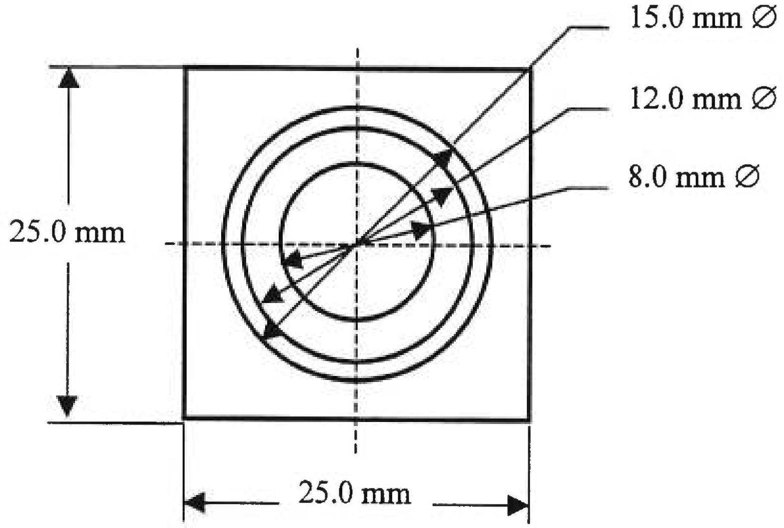

Figure 5.1 **BEC's physical dimensions.** Geometrical dimensions needed to meet the above requirement are depicted.

The theoretical Laplacian filter's transfer function for this geometric configuration can be estimated using Equation 3.12, page 78. Using the above electrode's dimensions, the filter's transfer functions were computed for low and high CVs (3 and 5 m/s, respectively) and the electrode's filter function was estimated using the lower and higher pass limits found. These are depicted in solid line in Figure 5.2 below.

Notice that at a gain of 0.707 = 3dB, the filter's bandpass is between 87 and 250 Hz with a median frequency of 175 Hz, which is sufficiently close to the frequency range where the bulk of the relevant SEMG information is expected to exist. As such, this spatial filter design meets all three requirements for our type of application. We will now proceed to develop the spatio-temporal EMG mapping technique.

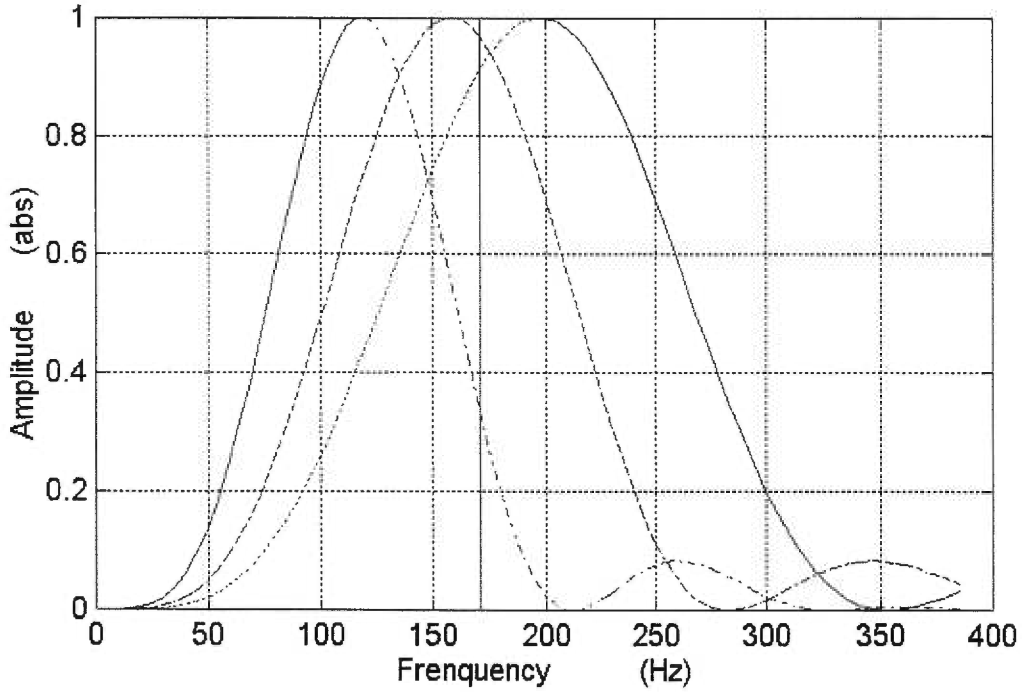

Figure 5.2 **BCE's filter function.** BCE's filter transfer functions are depicted for CVs of 3 m/s (dash-dot line), 4 m/s (dash line) and 5 m/s (dot line). The estimated filter function (solid line) is produced with the lowest and highest pass limits found amongst the computed filter's transfer functions. Median frequency is found at 175.78 Hz.

5.4 SPATIO-TEMPORAL MAPPING TECHNIQUE

The proposed spatio-temporal mapping technique consists in the measurement of EMG surface potentials with a two dimensional array of BCE's, synchronized with movement cinematic measurement through high-speed video technology. The spatial location for each electrode is obtained by a three-dimensional position-orientation-tracking device (BIRD). BIRD data is used to form a two dimensional electrode location's node matrix for each of the X, Y and Z axes. In turn, these node matrices are used to construct a three dimensional visual representation of the explored anatomical surface in a X-Y-Z coordinate system (see example depicted in Figure 5.3 below).

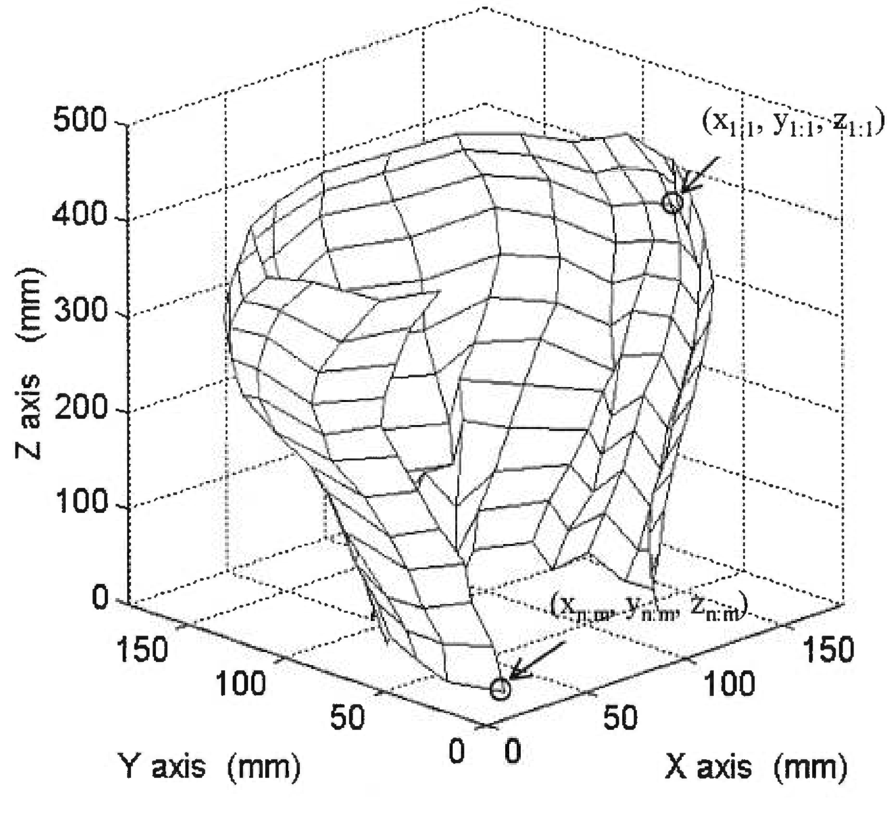

Figure 5.3 **Partial anatomical representation of a left lower leg:** A three dimensional mesh is constructed from the electrodes' spatial location of a *n* by *m* BCE matrix placed over a left lower leg. Each node of the mesh represents an electrode's spatial position. Coordinates of the first and last nodes are indicated.

A two-dimensional EMG data array is formed from the Laplacian potentials measured at a time t_n, (with $t_n = n\Delta t$, where $\Delta t = 1/F_s$; F_s is the sampling frequency and $n = 0,1,2,\ldots N$). A map of the surface potential distribution is constructed by interpolating the EMG data between contiguous nodes of the electrode's array mesh; thus generating a series of temporal mapping slices of the skin surface EMG potential distribution at the measured anatomical area. A temporal sequence of these slices, (from t_0 to t_n), forms a dynamic four-dimensional view of the orchestration of muscle activation involved in the execution of movement. Finally, this dynamic internal image is temporally correlated with the movement cinematic to conform with the requested multi-dimensional visual image to the ensemble of muscle activity for a given movement.

Individual muscle contributions can then expected to be identified at every phase of the movement cinematic, by correlation of the direction of the propagation of potential distributions on the skin surface with the muscular anatomy under the measured area. The ensemble of individual muscle contributions (in intensity and length of activity) will then provide information concerning the spatio-temporal patterns of muscle activity and as such, the functional and operational strategies developed by the CNS to achieve movement in terms of action development.

5.5 SELECTION OF EXPERIMENTAL PARAMETERS

As mentioned, the four dimensional spatio-temporal EMG mapping technique can be implemented and validated only by means of physiological experiments. However, at the time only twelve BCE were available for experimental purposes. This limitation represented the following problem: only a small matrix of 3 by 4 electrodes could be produced to cover an anatomical area; the SEMG data collected would be insufficient to provide a comprehensive image and hence an adequate demonstration and validation of the technique. An alternative solution was to develop a cyclical experiment, where motion-force parameters could be controlled in such a way that the initial experimental and physiological setting conditions could be kept constant through each experimental session. It would then be possible to re-position a 1 by 12 BCE array for each data collection while maintaining the initial settings. This procedure would allow re-positioning of the BCE array as many times as needed to cover the anatomical area of interest, and thus form a "virtual" matrix of N by 12 BCE, where N is the number of re-positioning. Such a physiological experiment was in fact developed using the exercises performed on an ergometer. It had the advantage of enabling collection of SEMG data within a "virtual matrix" of BCE's, that could be synchronized with the motion data.

The main focus of this experiment was therefore its reliability; its ability to maintain the initial experimental and physiological conditions through the many exercise trials needed for full coverage of the anatomical area of interest. To this end, the motion's speed and the force used to produced it were both strictly controlled. This was achieved by keeping the braking torque at a constant crank level and the rpm constant through all trials. In addition, this permitted averaging SEMG (rms) and motion data, thus allowing the most likely representation of the phenomenon through the various phases of a single revolution. To avoid fatigue, a recovery period of about 2 minutes was allowed between recording trials.

5.5.1 Selection of the Anatomical Area

The lower leg was chosen for this experiment because its functional anatomy lent itself perfectly to the test technique. With the exception of the popliteus, all of the lower leg musculature is attached to the bones of the foot. Because both the functional dorsi and plantar flexion motion of the foot are required to exert the forces on a pedal, even when the torque and rpm are maintained constant, the magnitude and direction of forces exerted must vary during the phases of a single revolution. Consequently, different muscles of the lower leg (as well of the thigh) must be solicited, (in length and intensity of activity), at the various phases of a single cycle. Further, since the movement is cyclic and the initial setting conditions are to kept constant, the solicited muscles can be expected to show the same phasic activity through time, and the data can therefore be averaged over several cycles.

5.5.2 Muscle Anatomy of the Lower Leg

Traditionally, the muscle anatomy of the lower leg has been classified in terms of location and function. According to anatomical location, muscles groups are classified as anterior or posterior. These two groups are divided in turn into subgroups or layers.

The anterior muscle group is formed by the anterior extensors (tibialis anterior, extensor digitorum longus and extensor hallucis longus; see figure 5.4 A-C, below) and the lateral subdivision of the peroneal group (peroneus longus and peroneus brevis; see figure 5.4 D-F, below). If the leg is not bearing any weight, the tibialis anterior flexes the foot dorsally and at the same time lifts the medial edge of the foot supination. When the leg is weighted, it approximates the leg to the back of the foot as, for instance, in pedaling (see figure 5.6 C). The extensor digitorum longus produces dorsiflexion of the digit and the foot in the non-bearing leg. However, in the weight-bearing leg its function is the same as the that of the tibialis anterior.

The extensor hallucis longus flexes the great toe dorsally and in the unstressed leg it aids dorsiflexion of the foot. In the weight-bearing leg its function also resembles that of the tibialis, since it brings the leg nearer to the dorsum of the foot. The peroneal group, on the other hand, participates in pronation and plantar flexion (see figure 5.6 A and D, below). The peroneus longus depresses the medial edge of the foot and together with the peroneus brevis is the stronger pronator, also aiding in plantar flexion. The peroneus brevis acts similarly to the peroneus longus.

The posterior flexors muscle group is subdivided into the triceps surae superficial layer (consisting of soleus, gastrocnemius and plantaris; figure 5.5 A-D above), and the deep flexors layer (formed by the tibialis posterior, flexor hallucis longus and flexor digitorum longus; figure 5.5 E-I below). The triceps surae, characterized by its great strength, (it is capable of lifting the entire body), is therefore the plantar flexor par excellence. Full activity of this flexor subgroup is only possible with the knee extended, since with the knee bent the gastrocnemius is already shortened (see figure 5.6 D below). The gastrocnemius, with assistance of the plantaris, is particularly important in pedaling as it is not only involved in flexing the foot but also in flexing the knee joint, and is thus involved in the active and passive force phases through one revolution.

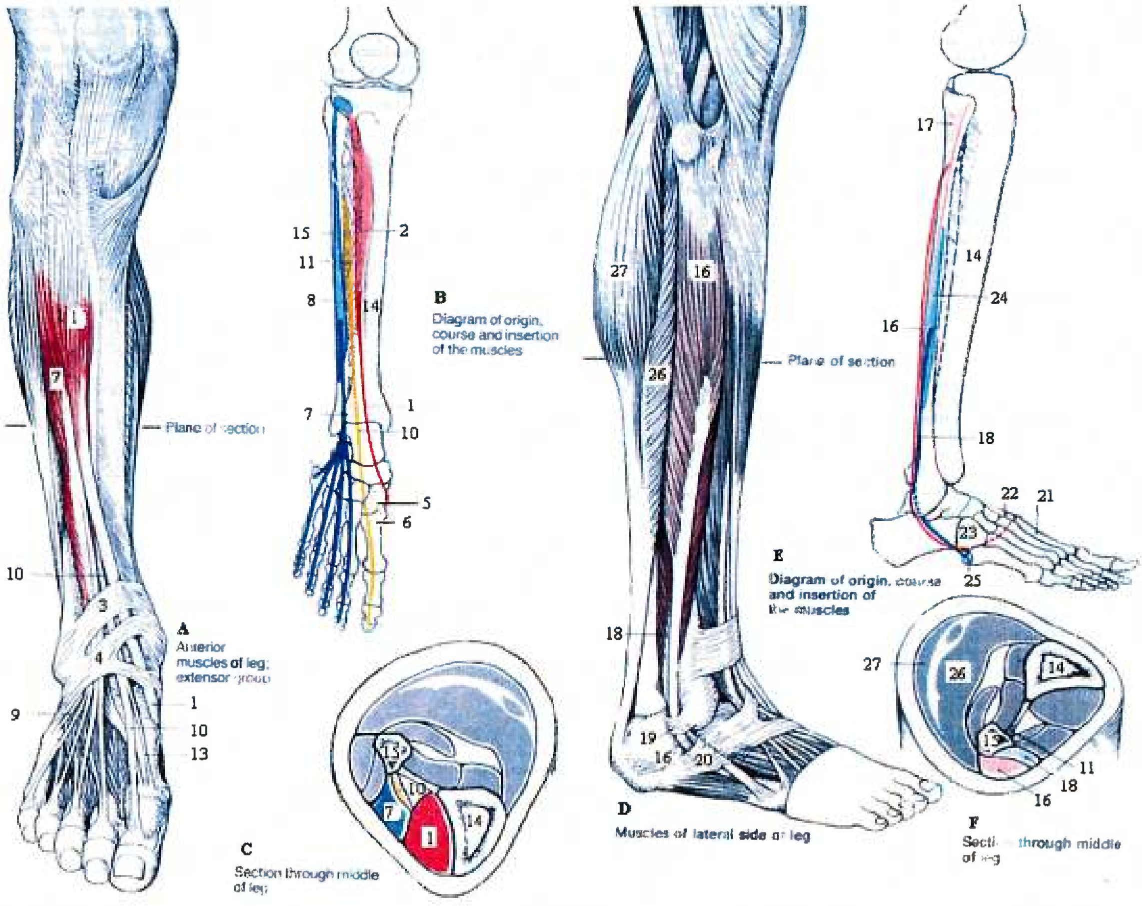
A Anterior muscles of leg: extensor group

B Diagram of origin, course and insertion of the muscles

C Section through middle of leg

D Muscles of lateral side of leg

E Diagram of origin, course and insertion of the muscles

F Section through middle of leg

Figure 5.4 Anterior muscle group: A-C Extensor muscle group; D-F Lateral or peroneal muscle group. (1) Tibialis anterior; (2) Lateral tibial surface; (3) Superior extensor retinaculum; (4) Inferior extensor retinaculum; (5) Medial cuneiform bone; (6) First metatarsal; (7) Extensor digitorium longus; (8) Lateral condyle of the tibia; (9) Peroneus tertius; (10) Extensor hallucis longus; (11) Interosseous membrane; (12) Terminal phalanx; (13) Extensor hallucis accessorius; (14) Tibia; (15) Fibula; (16) Peroneus longus; (17) Capsule of the tibiofibular joint; (18) Peroneus brevis; (19) Superior peroneal retinaculum; (20) Peroneal retinaculum; (21) First metatarsal; (22) Medial cuneiform bone; (23) Cuboid; (24) Lateral fibular surface; (25) Fifth metatarsal; (26) Soleus; (27) Gastrocnemus. (From Platzer)

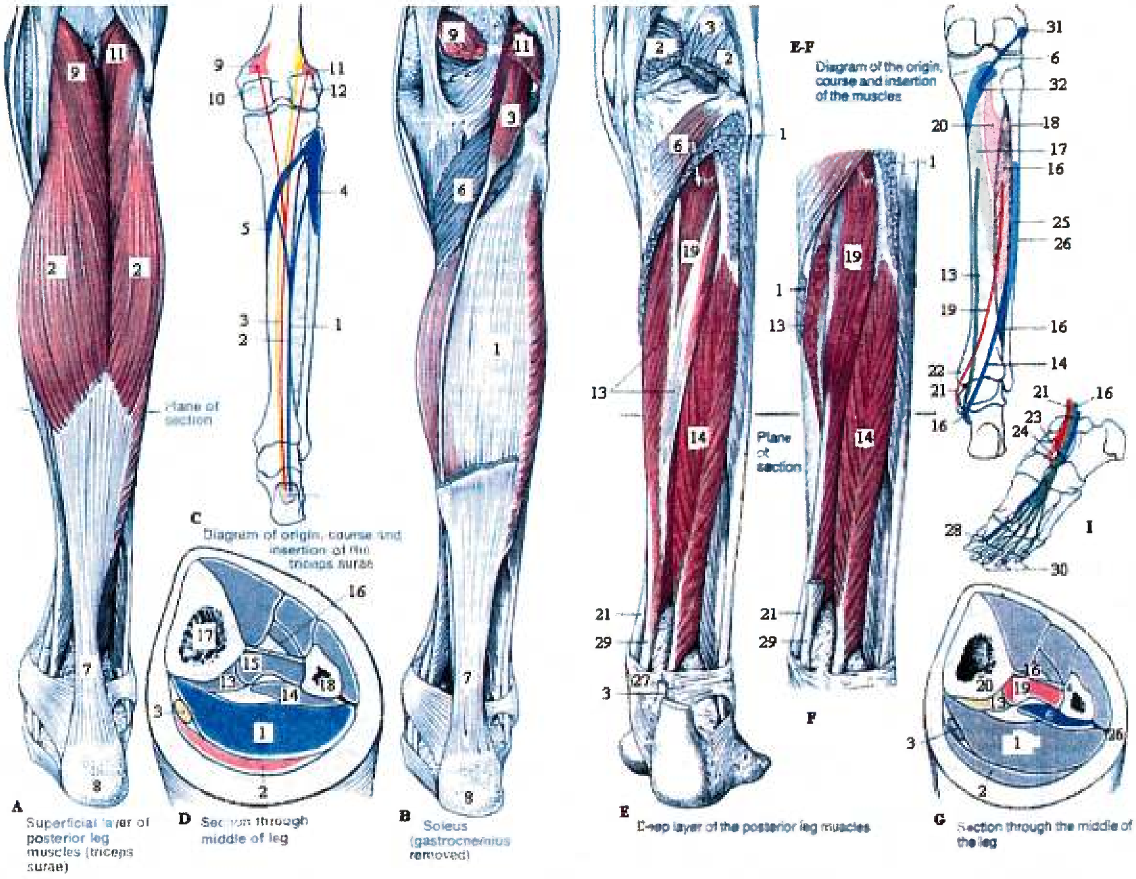

A Superficial layer of posterior leg muscles (triceps surae)

C Diagram of origin, course and insertion of the triceps surae

D Section through middle of leg

B Soleus (gastrocnemius removed)

E-F Diagram of the origin, course and insertion of the muscles

E Deep layer of the posterior leg muscles

F

G Section through the middle of the leg

I

Figure 5.5 **<u>Posterior muscle group</u>: A-E Superficial Layer; F-I Deep Layer**. (1) Soleus; (2) Gastrocnemius; (3) Plantaris; (4) Dorsal fibulal surface; (5) Line of soleus muscle; (6) Popliteus; (7) Achilles tendon; (8) Tuber calcanei; (9) Medial head of the gastrocnemius; (10) Medial femoral condyle; (11) Lateral head of the gastrocnemius; (12) Lateral femoral condyle; (13) Flexor digitorum longus; (14) Flexor hallucis longus; (15) Tibialis posterior; (16) Interosseous membrane; (17) Tibia; (18) Fibula; (19) Tibialis posterior; (20) Adjoining surface of the tibia; (21) Tendon of the tibialis posterior; (22) Medial malleolus; (23) Tuberosity of the navicular bone; (24) Cuneiform bones; (25) Posterior fibulal surface; (26) Posterior crural intermuscular septum; (27) Flexor retinaculum; (28) Phalanx of the first digit; (29) Tendon of the flexor digitorum longus; (30) Phalanx of the lateral digits; (31) Lateral femoral epicondyle; (32) Posterior tibial surface. (From Platzer)

For the deep flexor layer, the tibialis posterior produces plantar flexion and simultaneous supination in the non-weight-bearing leg, while in the stressed leg it approximates the heel to the leg's calf. The flexor hallucis longus supports the arch of the foot, producing plantar flexion of the first digit and assisting in supination.

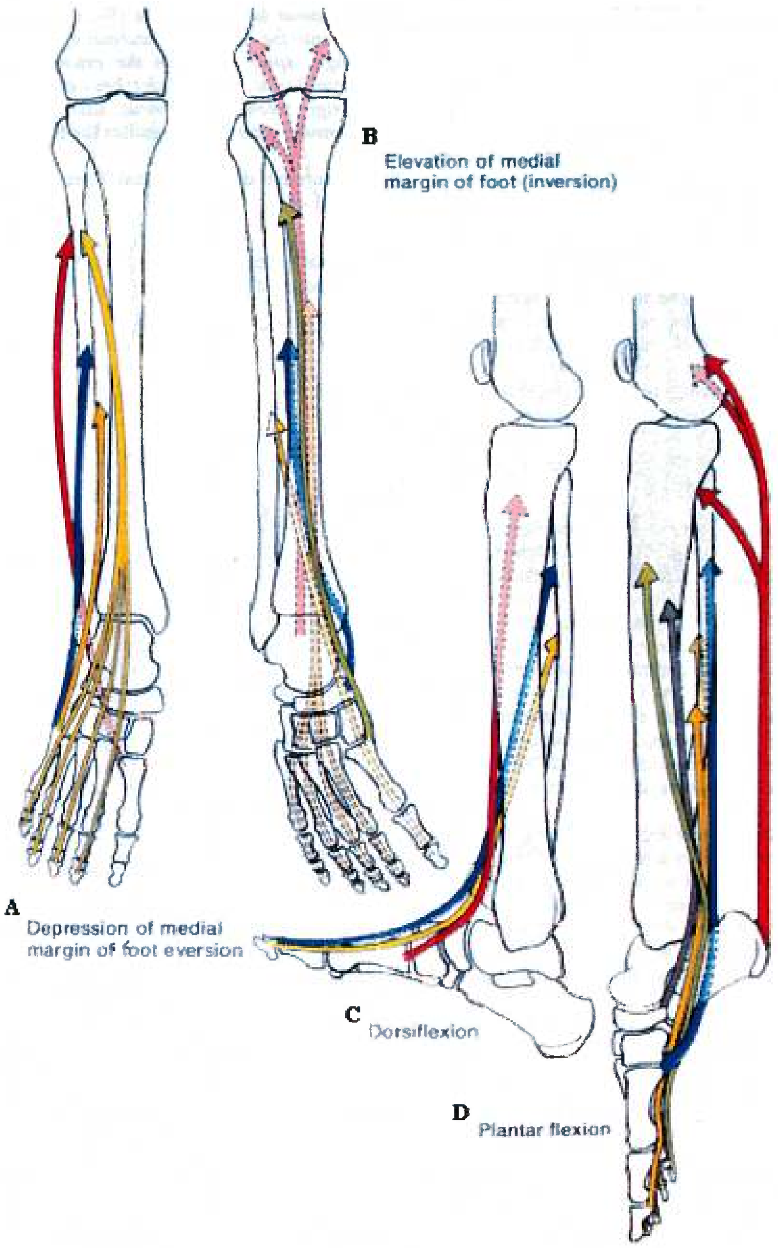

Figure 5.6 __Actions of muscles in the lower leg__. The colors of the arrows show the order of importance of the muscles in each movement as follows: red, blue, yellow, orange, green, brown. **A**.- Pronation: produced by the peroneus longus (red), peroneus brevis (blue), extensor digitorum longus (yellow) and peroneus tertius (orange). **B**.- Supination: produced by the triceps surae (red), tibialis posterior (blue), flexor hallucis longus (yellow), flexor digitorum longus (orange) and tibialis anterior (green). **C**.- Dorsiflexion: carried out by the tibialis anterior (red), extensor digitorum longus (blue) and extensor hallucis longus (yellow). **D**.- Plantar flexion: produced by the triceps surae (red), peroneus longus (blue), peroneus brevis (yellow), flexor digitorum longus (green) and tibialis posterior (brown). (From Platzer)

The flexor digitorium longus platarflexes the digits and the foot in the non-bearing-weight leg. Its also acts as a supinator. In the weight-bearing limb it assists in the support of the plantar arch. Finally, the popliteus, which flexes the knee joint and medially rotates the leg, arises from the lateral femoral epicondyle. The subpopliteal recess, lying between the muscle and the knee joint, is always connected with the joint. It is inserted on the posterior tibial surface.

5.6 EXPERIMENTAL EQUIPMENT

The experimental equipment consists of twelve BCE, an oscilloscope, an A/D interface system, a personal 386 computer equipped with a data acquisition card, a position-orientation tracking system, a motion analysis system and a CCM ergometer (model 3000).

Twelve sets of BCE contact pairs, outer ring and centre disc, were made of surgical stainless steel as per the dimensions shown in Figure 5.1, page 124. A set of contact pairs was mounted on a specially made Plexiglas adapter case of 25 by 30 by 20 mm with a wall thickness of 3 mm. An active bipolar electrode was inserted into the adapter case and kept in place by means of thin copper spring plates which pressed it onto the case's inner wall. The thin copper spring plates served also as connector interface between electrodes' contact as shown in Figure 5.7 below. The active electrodes were manufactured by Liberty Mutual (model MY0111). They have a built-in pre-amplifier circuit with a gain of 4600, a pass-band from 45 to 550 Hz, a common mode-rejection ratio of 95 dB, an input impedance of 10^{14} Ohms and a voltage supply of ± 8 V. Important was that the BCE filter's pass-band (87 to 250 Hz) is within the active electrode pre-amplifier's pass-band.

The A/D interface system amplifies EMG signals and supplies the power to the electrodes' pre-amplifier circuit. At the same time it serves as a connector between the BCE array and the A/D converter. It consists of twelve individual amplifiers (each with a bandwidth from 2 to 1000 Hz and adjustable gain from 1 to 26.6), a power supply transformer and twelve individual connector jacks.

EMG signals were collected using a 16 channels data acquisition card (Brain Wave) with a 12 bit resolution and a 12 μsec conversion time, giving a maximum throughput rate of 60 KHz. The card is also equipped with two extra channels to convert digital to analog signals. One of these channel was used to synchronize data acquisition with the motion analysis system. Data acquisition and A/D conversion were initiated using the built-in Brain Wave program which utilizes direct memory access (DMA).

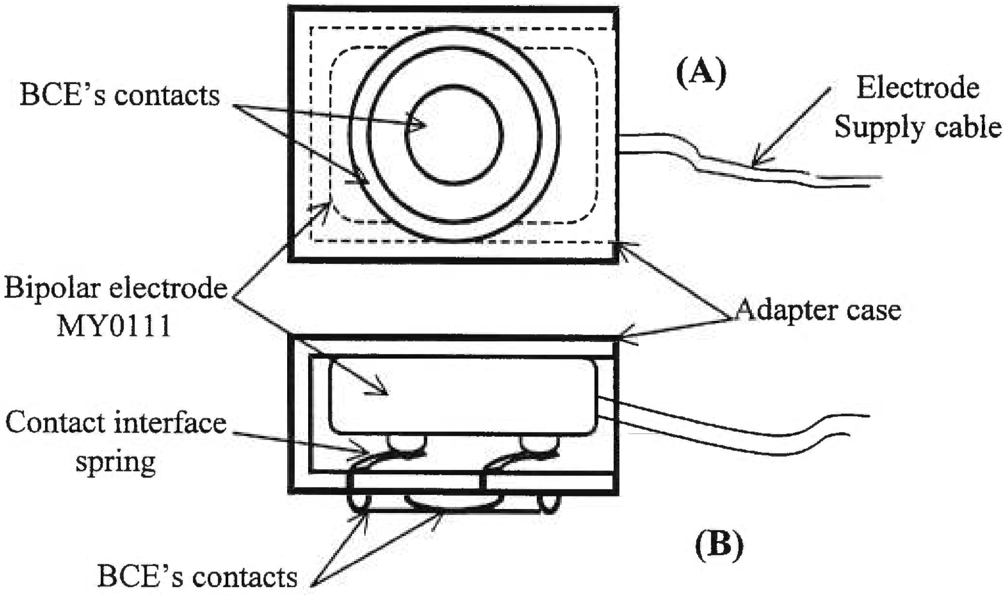

Figure 5.7 Schematic of a BCE assembly. Top (A) and cross section (B) views of the BCE assembly are depicted. BCE's outer ring and centre contacts are mounted on the Plexiglas adapter case. An active bipolar electrode acts as the BCE pre-amplifier.

The position-orientation tracking system is a six degree-of-freedom measuring device called the Flock of Bird (FOB). It can be configured to track the position and orientation of up to thirty receivers by a transmitter. When the receiver is located within 0.91 meter (3 feet) of its transmitter, each receiver is capable of making 10 to 144 measurements per second of its position and orientation. The FOB determines position and orientation by transmitting a pulsed DC magnetic field that is simultaneously measured by all receivers in the flock. From the measured magnetic field characteristics, each receiver independently computes its position and orientation and makes this information available to the host computer.

In turn, this information is translated into the X-Y-Z coordinate system by mean of computer programs written in C language. The physical shape of an object can be described tri-dimensionally by performing positional measurements outputs and later translating this information into the X-Y-Z coordinate system to construct the object's tri-dimensional representation.

The motion analysis system (ExpertVision) is a cinematic data acquisition system that permits to obtain the instant spatial coordinates position of many referential points located on an object in motion, such as selected anatomical sites. These referential points, called point objects, are small light reflecting spheres, (5 to 10 mm in diameter), placed strategically over the object surface by means of double sided tape. The system consists of eight high-speed video cameras furnished with infra-red stroboscopes, four video monitors, four video-processor units, a host SUN computer and a graphics workstation. The system uses stereo-photogrametry principles to track the displacement of point objects in space. Two to several of the light sensible point objects are used to obtain a bi-dimensional image of a motion event. Each video camera records an image of the movement within its field of vision. These images are then filtered by the video-processor unit, leaving visible only the contour reflection of the point objects. Accuracy of cinematic measurements is assured by complete visibility of the point objects at all times within the field of vision of at least two cameras.

Filtered image data from the eight video cameras are digitized and saved on the SUN's hard disk for later processing. A Motion Analysis built-in program permits computation of the point object's centroid and links it to the corresponding spatial coordinates. A geometrical approach is then used to reconstruct the third missing dimension from pre-calibration data obtained from the relative cameras' position with respect to an absolute system of coordinate. Finally, a tri-dimensional reconstruction of the motion is performed using the direct linear transformation technique (DLT). The system permits a choice of sampling frequencies of 60, 120 and 180 Hz.

5.7 METHODOLOGY

A group of three subjects participated in the experiment, one female and two males. Data from one subject would have suffice to offer a proof-of-concept, but one additional male and a female were also tested. This was to confirm whether data collected under similar conditions would show similar results in terms of the technique's predicting abilities. All subjects were healthy, without history of neuro-muscular problems affecting the muscles of the lower limbs. Subjects gave informed consent to the experimental procedures. SEMG data was recorded over the muscles of the right lower leg simultaneously with motion data from five point objects, respectively placed at the greater trochanter (hip joint), head of the fibula (knee joint), external malleolus (ankle joint), head of fifth metatarsal bone (forefoot) and pedal.

SEMG signals were recorded using the 1×12 BCE array configuration in the manner previously described. Signals from the BCE were bandpass pre-amplified between 45 and 550 Hz at a gain of 4200. SEMG data was collected at a sampling frequency of 1024 Hz. After bandpass amplification, data was digitized and displayed on screen for visual inspection prior to storage on disk for subsequent analysis. Position data from five point objects was collected simultaneously with SEMG data at a sampling rate of 180 Hz and stored on disc for later processing and analysis.

Prior to experimentation, the ergometer's seat was adjusted to a level where for the subject's feet could comfortably reach the pedal at its circle's lowest point, with the knee slightly bent. The subject's left leg was shaved and the skin was cleaned with alcohol to provide a low impedance contact between electrodes and skin. The subject sat on the ergometer and the BCE array was first applied laterally to the tibia by means of double sided tape; the BCEs were then equally spaced starting with the first BCE at the tibia's tubercle level and ending with the twelfth BCE at the level of the superior extensor retinaculum. In order to prevent motion artifacs, the BCE array was secured by means of an elastic conforming bandage wrapped around the entire lower leg. Then, a first recording trial was performed: two sets of four seconds of synchronized EMG and cinematic data were collected respectively for fast (100 rpm) and slow (60 rpm) pedaling movements.

Directly after the first recording trial, the BCE array was removed, the skin surface was cleaned with alcohol and each electrode's location was marked for later identification by the BIRD equipment. The electrodes were cleaned, and new double sided tape and fresh electrolyte gel were applied and the BCE array was then re-positioned dorsi-laterally next to the previous position. It was secured with the elastic conforming band and a second recording trial was performed. This procedure was repeated until the entire lower leg had been covered. A total of 17 recording trials were performed, thus producing a "virtual matrix" of 17 by 12 BCEs. For each subject, a total of 34 sets of 4 seconds of synchronized EMG and motion data was obtained (slow and fast movement). Finally, the location of each node of the "virtual matrix" on the lower leg (corresponding to the formal BCEs' spatial location), was obtained by means of the BIRD.

5.8 DATA PROCESSING

5.8.1 Processing of Cinematic Data

Cinematic data from the five point objects (hip, knee, ankle, foot and pedal) was exported from the Motion Analysis System in ASCII format and translated into Matlab format. Inspection of the discrete three dimensional data showed that point objects' motion trajectory -- pedaling action -- occurred chiefly on the sagital plane (X-Y coordinates). Point objects' motion on the coronal plane (Y-Z coordinates) were found to be very small in comparison to those on the sagital plane; consequently, this data was estimated to have a negligible effect on the three dimensional cinematic calculation. Motion data in the Z axis was omitted in the analysis to simplify calculations and save computer time. Cinematic data was smoothed by means of a five points moving average. After removing high frequency noise, data was resample at 512 Hz to match RMS-EMG time increment for further processing and analysis (see next section for EMG data processing).

Given the fact that the pedal point object (PPO) described a perfect circular trajectory, its cinematic data was used to identify the beginning and end of each revolution cycle in each respective trial. PPO motion data was first converted into polar coordinates with the lowest point in the circle identified as the beginning of the cycle, (corresponding to maximum leg extension produced during the cycle). For each trial, the beginning of each cycle as well as cycle length and the average cycle cinematic were recorded in a separate file. The mean average velocity from all slow cycle motions was found to be 61.4 ± 1.5 rpm. Conversely, the mean average velocity for fast cycle movement was 105.4 ± 2.0 rpm.

Individual cycle lengths were normalized to 520 points for slow movements (61 rpm) and 290 for fast movements (106 rpm); and their respective cinematic curves were interpolated to the normalized cycle length using a cubic spline function. This procedure permitted computation of the point object's average cycle cinematic per recording trial. The most likely cinematic for each point object was then found by computing the total mean average from their respective average cycle motions per trial. This latter data was then used to compute the relative knee and ankle joint angles change with respect to the zero phase cycle position (maximum leg extension through one revolution cycle).

5.8.2 Processing of EMG Data

Data from the 34 EMG recorded trials, (slow and fast movement), were processed individually. Data from each BCE was first digitaly bandpass filtered (45 to 350 Hz) with a second order Butterworth filter, (thus 68.4 % of the Nyquist frequency). The RMS was then computed over the 4098 points using a moving square window of 8 points with an overlap of 2 points and later smoothed with a five points moving average. This procedure compressed the EMG data arrays to 2048 discrete points. The next step was to identify individual cycles within each of the 34 arrays of data (fast and slow movement). Given that individual cycles had bee previously identified from the PPO cinematic data, and that the EMG-RMS and cinematic arrays were made of the same length, the same algorithm used to process the cinematic data was applied in this case. Once extracted, EMG-RMS cycles were normalized to their respective average cycle length (290 points for fast movement and 520 points for slow movements). Their respective curves were then interpolated to the normalized cycle length by means of a cubic spline function. The most likely local EMG activity (rms wise) registered by each BCE during a full cycle was found by computing the total mean average from the ensemble of EMG-RMS trial averages.

5.8.3 Processing of Spatio-Temporal Data Matrix

The spatio-temporal EMG data matrix was constructed from the ensemble of EMG-RMS total mean averages. Data was first normalized between the minimum and maximum value found in the entire data ensemble (fast and slow movement). Spatial matrices were then formed with each of the corresponding discrete time sequential elements in the EMG-RMS arrays. That is, for each discrete time instance a spatial matrix (constituted of a 12 by 17 elements) was formed, thus representing one temporal slice of the spatio-temporal data matrix. The sequence of these temporal slices resulted in a tri-dimensional matrix of 12 by 17 by 290 elements, for fast movement cycle and of 12 by 17 by 520 elements for slow movement, respectively.

5.9 RESULTS

We recall that in order to demonstrate and validate the spatio-temporal EMG mapping technique with the resources on hand, two basic assumptions have been made. First, the movement dynamic is presumed to be reproducible through a series of successive trials, and second, muscle activity is also expected to be similar at the various phases of the performed movement during each successive trial. In short, the reliability of the data used to construct the "virtual" spatio-temporal matrix depends directly on the consistency of the dynamic and the EMG data collected. Before the technique can be demonstrated and validated, these two assumptions must be proven.

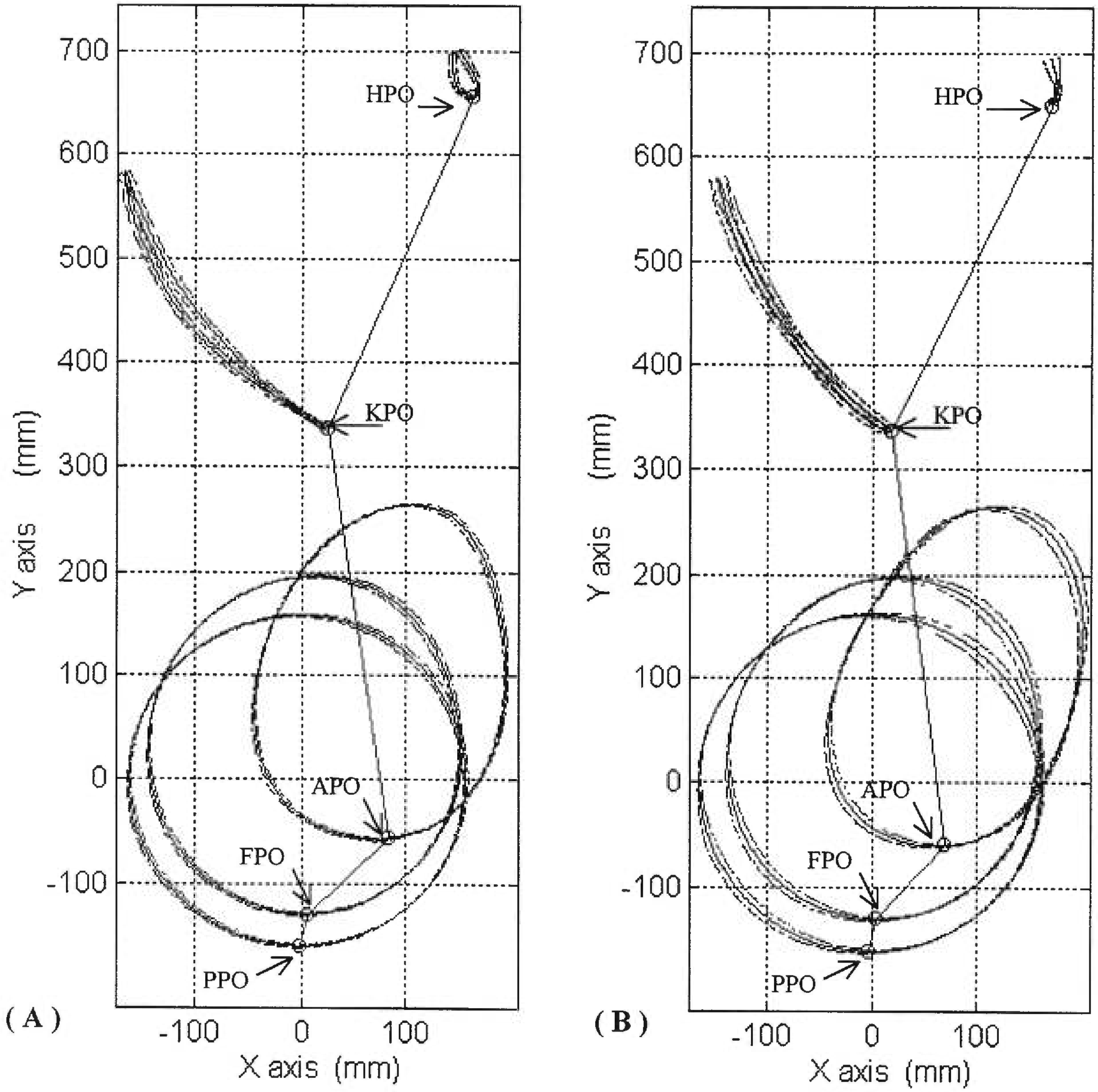

Figure 5.8 **Mean average movement cinematic:** (A) Fast movement. (B) Slow movement. The five point objects are represented by small circles: pedal (PPO); foot (FPO); ankle (APO); knee (KPO); hip (HPO). Point objects are depicted at the beginning of the cycle (0° position, maximal leg extension) and the motion sense is counter clockwise. The computed mean average cycle motion trajectory of the five point objects are shown in solid lines with their respective standard deviations in dashed lines.

Results from cinematic data from the five point objects are shown in Figures 5.8 A and B above for fast and slow movements, respectively. Each mean average cycle trajectory is shown in solid line with their respective standard deviation in dashed lines. Notice that in both cases the standard deviation of the motion cycle trajectory for the pedal, foot and ankle point objects is maximal in the second and the fourth quadrants, (90° to 180°; and 270° to 360°, respectively). However, since the pedal point object was attached to a rigid articulated base, we should have seen a trajectory describing a perfect circle with virtually zero standard deviation. Further, given that similar deviations are observed in the trajectory of the other point objects; such deviations can only be attributed to causes other than inconsistency of the performed movement. The most probable explanation is that the video cameras were not perfectly orthogonal to the plane where most of the performed movement was developed (X-Y plane). This event, plus the omission of the Z axis data in processing the cinematic data, produced the effect of an oval distortion on the description of the point objects circular motion. However, since these variations (standard deviation) are symmetrically consistent along an oblique plane of the circular motion (second and fourth quadrants), they have no bearing in the mean average trajectory described by the point objects in their cycle motion. Similar observations apply for the knee and hip point object cinematic trajectories, only in these cases, a more marked difference between fast and slow movements can be observed from the respective point objects trajectories. We will leave this observation for later discussion.

Regarding the EMG activity, we can observe from the RMS curves in Figures 5.9 A to F that, typically, the standard deviation for the amplitude in the EMG data shows a comparatively larger variation between recorded trials than that observed for the cinematic data. However, since the EMG is a random signal, relatively large variations observed in the signals RMS amplitude values between trials do not necessarily means inconsistency of the data. In fact, such a variation should be expected since different motor units, belonging to the same muscle unit, will be fired in the course of performing the same movement reiteratively; as is the case of the pedaling action. This typical neuro-physiological muscle behavior -- from the point of view of the recording electrode -- produces spatio-temporal variations of the EMG signal without affecting the muscle's total output

Consequently, from the stand point of muscle's output, the important factors to be considered in these cases are consistency in the onset, offset and duration of the EMG activity. Notice that in all six instances, these three mentioned factors are quite consistent; thus, baseline, beginning, duration and end of the EMG activity are clearly defined with virtually no temporal (phase) variations observed in the cycle sequence. Hence, since variations in the intensity (RMS amplitude) of the EMG activity can be explained in neuro-physiological terms from the point of view of the recording electrode, we can infer that the EMG data is also consistent. This demonstrates that the cinematic and EMG data are highly reproducible; and thus, that the assumptions made in the construction of the virtual spatio-temporal matrix are sound.

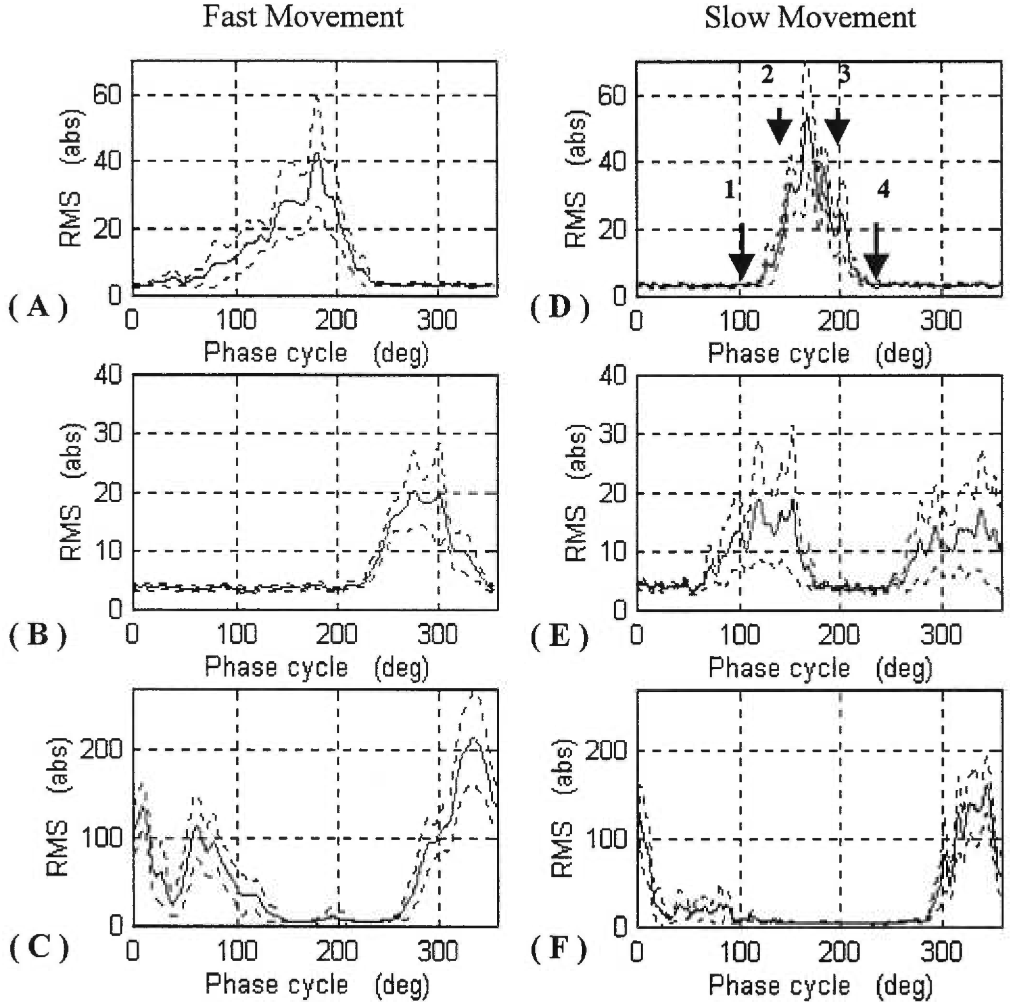

Figure 5.9 **Example of EMG-RMS data**: Typical curves of full cycle EMG activity are depicted from fast (A to C) and slow (D to F) movements. In these particular instances the EMG activity, RMS wise, correspond to that of the following muscles: tibialis anterior (A and D); soleus (B and E) and medial head of gastrocnemius (C and F). Their respective mean average RMS is shown in solid lines with their standard deviations in dotted lines. Figure D illustrates the on-set (1), duration (2-3) and off-set (4) the EMG activity.

5.10 DEMONSTRATION OF THE TECHNIQUE

The ability of the spatio-temporal EMG mapping technique to produce a dynamic representation of the ensemble of muscle contributions at the various stage of performed movement, is demonstrated by the sequence of images that it produces. These are achieved by means of an interactive computer program. The program's algorithm derives from the technique's principles -- previously presented in Section 5.4.

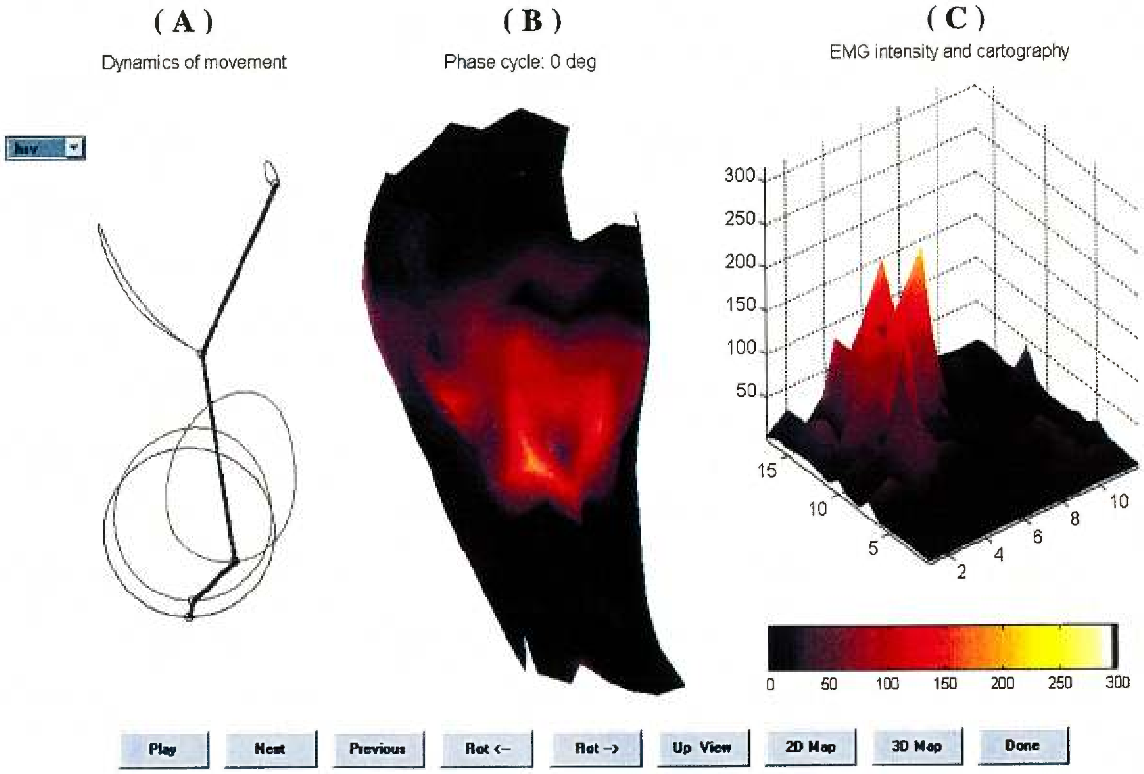

Figure 5.10 **Illustration of the Spatio-Temporal EMG mapping technique program:** A typical set of images as seen displayed on the screen is depicted. (A) Cinematic of movement is described by the point objects position in their respective motion trajectory curves (from top to bottom: HPO, KPO, APO, FPO in red lines and PPO in blue line). Black line represents the limb's posture at the cycle phase (zero degree in this case). (B) The skin surface potential distribution over a tri-dimensional partial representation of the left lower leg surface is depicted at the indicated cycle phase. (C) The intensity and distribution of the SEMG activity as recorded by the BCE matrix at the indicated cycle phase is plotted in a topographic fashion; colors are related to the signals amplitude as per intensity scale on the color bar depicted at the bottom of the plot; black indicates no activity, red indicates medium activity and yellow indicates maximum activity.

A proper demonstration of the dynamic sequence of images requires the computer screen. Here we can only illustrate and explain the program's application. The program itself is interactive, (user friendly), written in Matlab language. It displays three simultaneous dynamic images and thus depicting step by step some of the dynamic and EMG events involved in the multidimensional process of movement execution. Figure 5.10 illustrates a typical example of these images, as well as the nine interactive commands used to run the various program's options. Figure 5.10A depicts the cinematic of the performed movement. The five point object's trajectories described through a single cycle are displayed permanently and each of the point objects position is adjusted at the displayed cycle phase of the movement while a stick representation of the leg gives the exact limb's posture.

Figure 5.10B depicts the corresponding surface potential distribution over a three dimensional partial representation of the observed anatomical area at the given cycle phase. Figure 5.10C is a cartographic representation of the SEMG activity's intensity and distribution. That is, the left lower leg surface from Figure 5.10B has been extended and stretched on a Cartesian plane formed with the 17 by 12 elements (electrodes) matrix and a topographic mapping is generated and depicted using the corresponding instant cycle phase data sensed by each respective electrode in the spatio-temporal matrix.

The program is provided with nine interactive controls permitting the user to: run sequential images continuously (play button) or individually forward and backward (next and previous buttons, respectively); rotate the three dimensional anatomical surface representation over its central axis, clockwise and counter-clockwise (arrow buttons); obtain a top view of the representation (up view button) and; display the matrix's cartography on a two or three dimensional plot (2D map and 3D map buttons, respectively). The 2D map is the stretched-extended version of Figure 4.10B and the 3D map is its topographic representation. In addition, the user can review the EMG activity at any phase of the cycle simply by placing the mouse's pointer arrow over the PPO trajectory circle (blue line, Figure 5.10A) and simultaneously pressing the mouse right button to drag the PPO to the desired phase position.

5. 11 VALIDATION OF THE TECHNIQUE

Validation of the technique is interpreted here as its capability and applicability to identify the ensemble of muscle activities generated through movement execution. In other words, for this technique to be valid, the sequence of images generated by the technique's data recording and processing methodology must permit active muscle identification and elucidation of global spatio-temporal patterns of muscle activation involved in action development. However, a full appreciation of the technique's capabilities in this sense requires, once again, the facilities of a computer. We will consequently be limited here to illustration of a few instances.

These illustrations are presented in Figures 5.11 to 5.16 below for fast (A) and slow (B) movements. Lower leg representations (sub-figures A2 and B2) have been rotated to a plane view where the most active area is depicted. Active muscles identification and description of spatio-temporal patterns will be performed by correlation between the lighter color shapes (active areas) and the lower leg anatomy. Both of these technique's capabilities will be verified using present knowledge on functional muscle anatomy. During a pedalling action, muscles from both the upper and lower leg are solicited at the various stage of motion, however for purposes here we will concentrate only on those of the lower leg, keeping in mind that muscles from the upper leg might also be active at each selected cycle phase.

Figures 5.11 A2 and B2 below depict an interior antero-lateral view of the left lower leg at a cycle phase of 12 degrees for fast and slow movements, respectively. At first glance, in both cases, three active muscles can be identified by a simple anatomical correlation with the lighter areas. By order of their EMG intensity, these are: flexor digitorum longus (FDL); tibialis posterior (TP) and; medial head of the gastrocnemius (MHG). Further, comparing Figures 5.11 A3 and B3, we observe that the number of muscles solicited and the distribution of their respective EMG activity intensities are different in both movements. Fast movement demanded fewer active muscles at a higher EMG intensity, while slow movement required more active muscles but at a much lower EMG intensity.

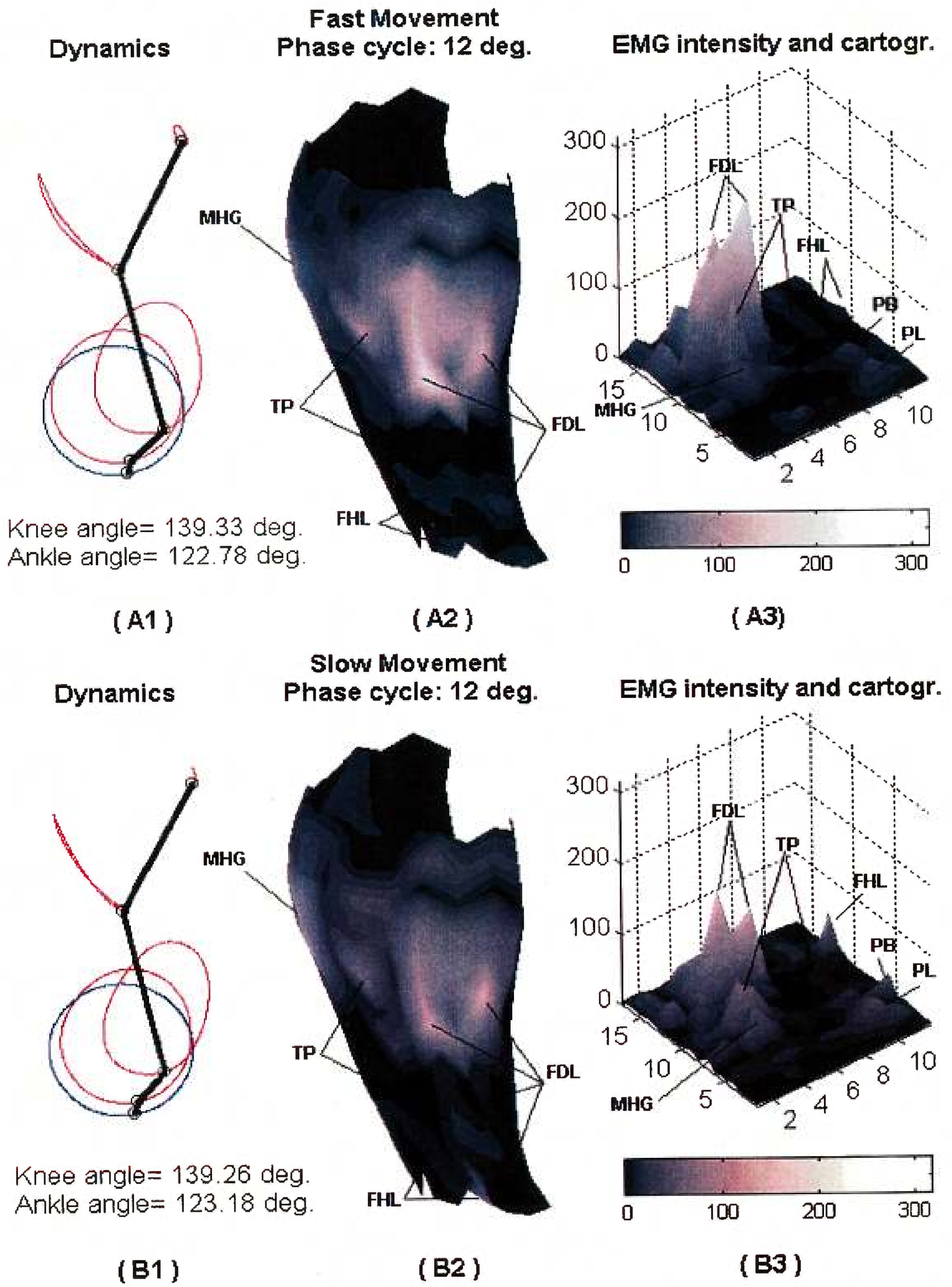

Figure 5.11 **Internal antero-lateral view at 12 deg. cycle phase**. Active muscles identified are: medial head of gastrocnemius (MHG); flexor digitorum longus (FDL); flexor hallucis longus (FHL); tibialis posterior (TP); peroneus longus (PL) and peroneus brevis (PB).

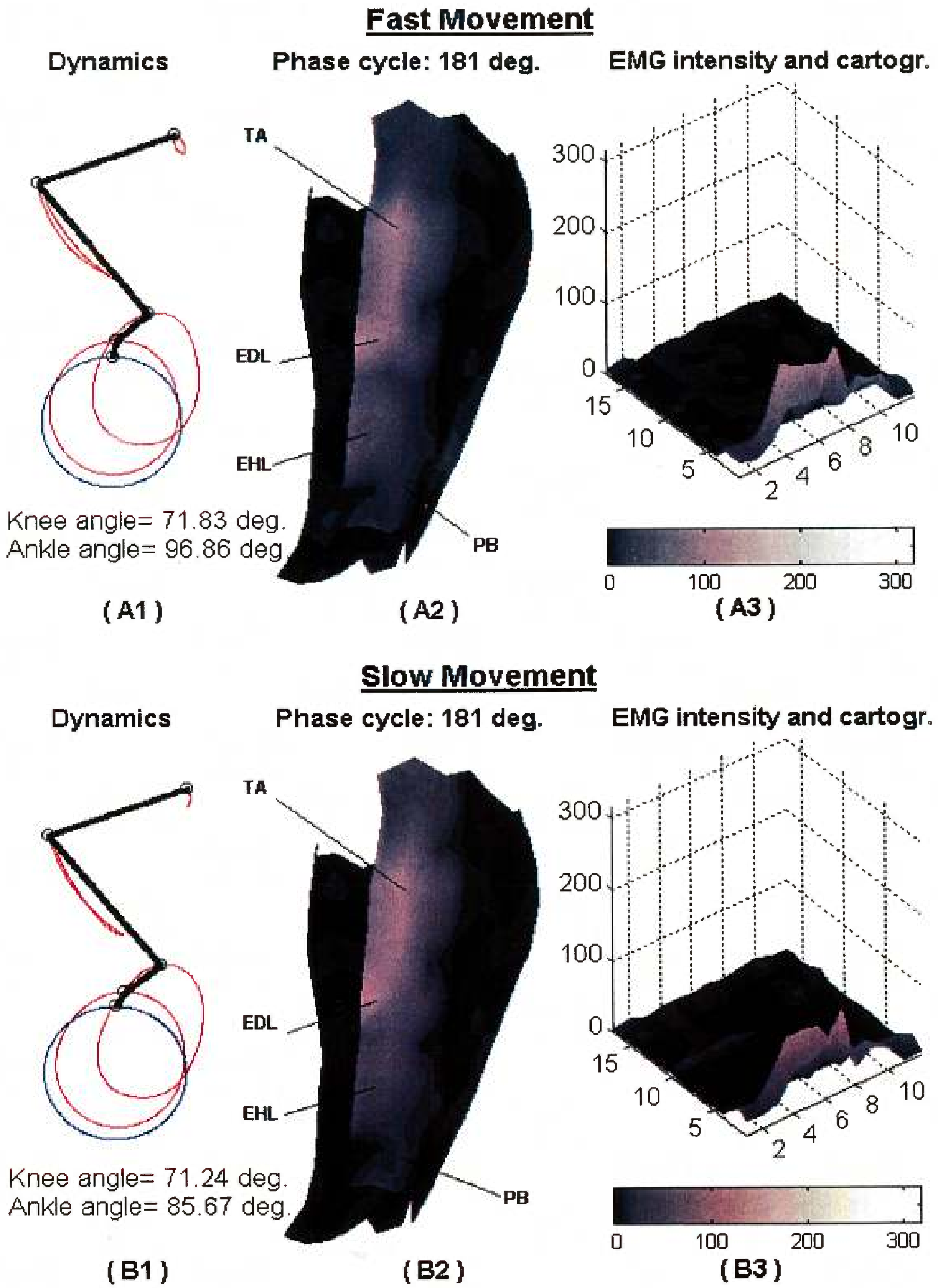

Figure 5.12 <u>External antero-lateral view at 181 deg. cycle phase.</u> Active muscles identified are: tibialis anterior (TA); extensor digitorum longus (EDL); extensor hallucis longus (EHL) and peroneus brevis (PB).

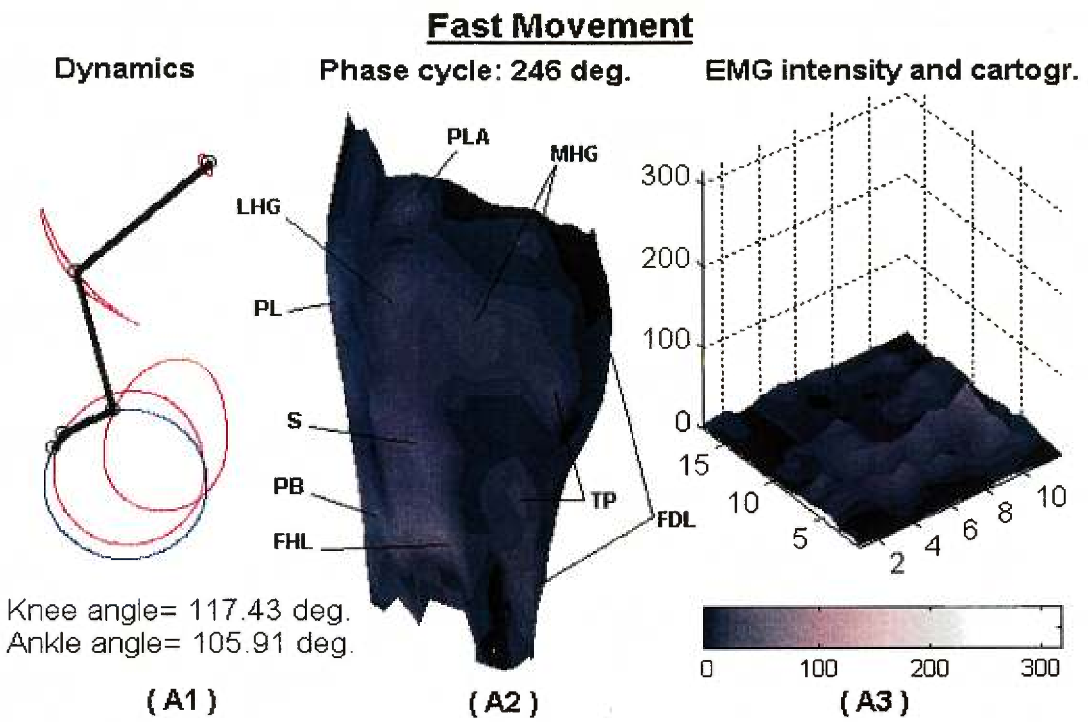
Fast Movement

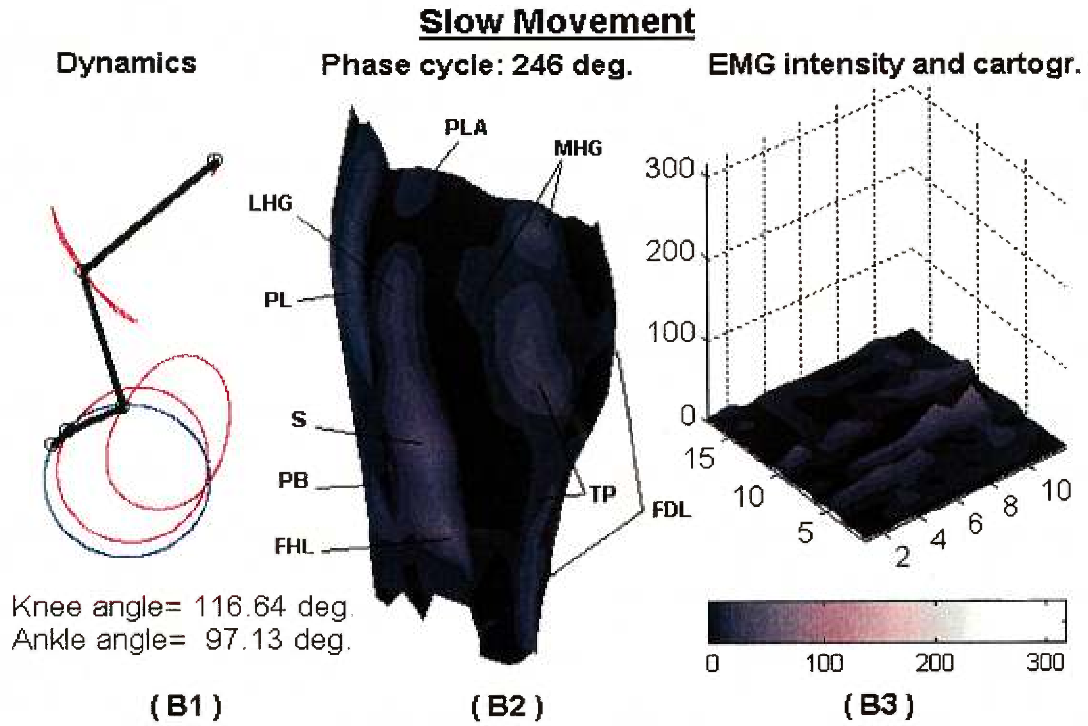
Slow Movement

Figure 5.13 Internal postero-lateral view at 246 deg. cycle phase. Active muscles identified are: plantaris (PLA); medial head of gastrocnemius (MHG); lateral head of gastrocnemius (LHG); soleus (S); tibialis posterior (TP); flexor digitorum longus (FDL); flexor hallucis longus (FHL); peroneus longus (PL) and peroneus brevis (PB).

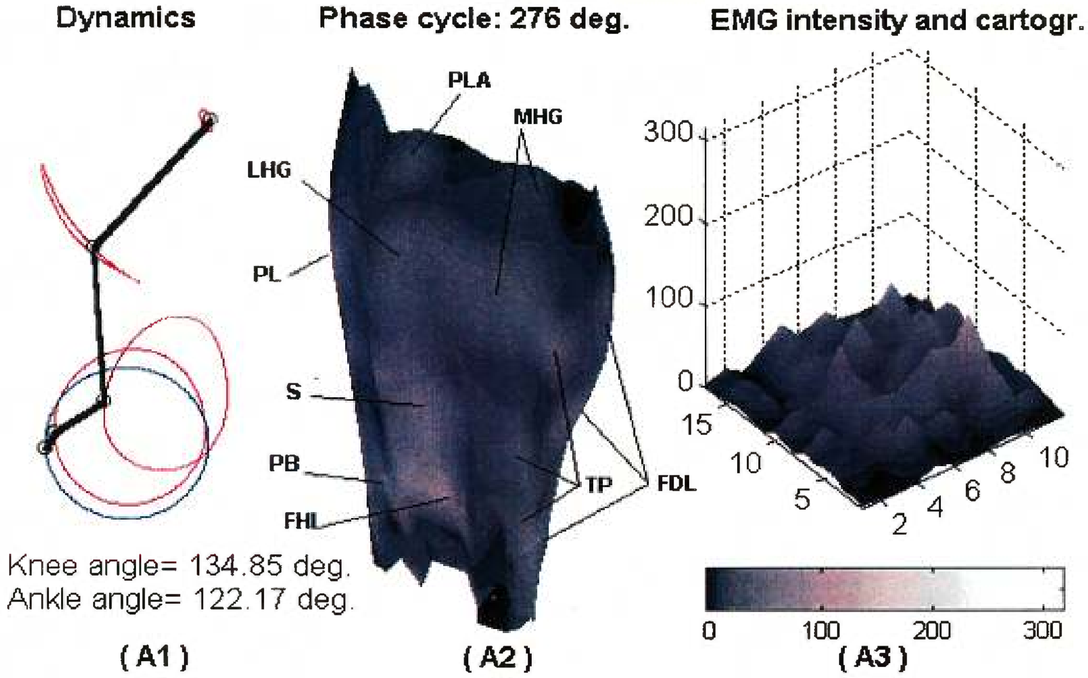

Fast Movement

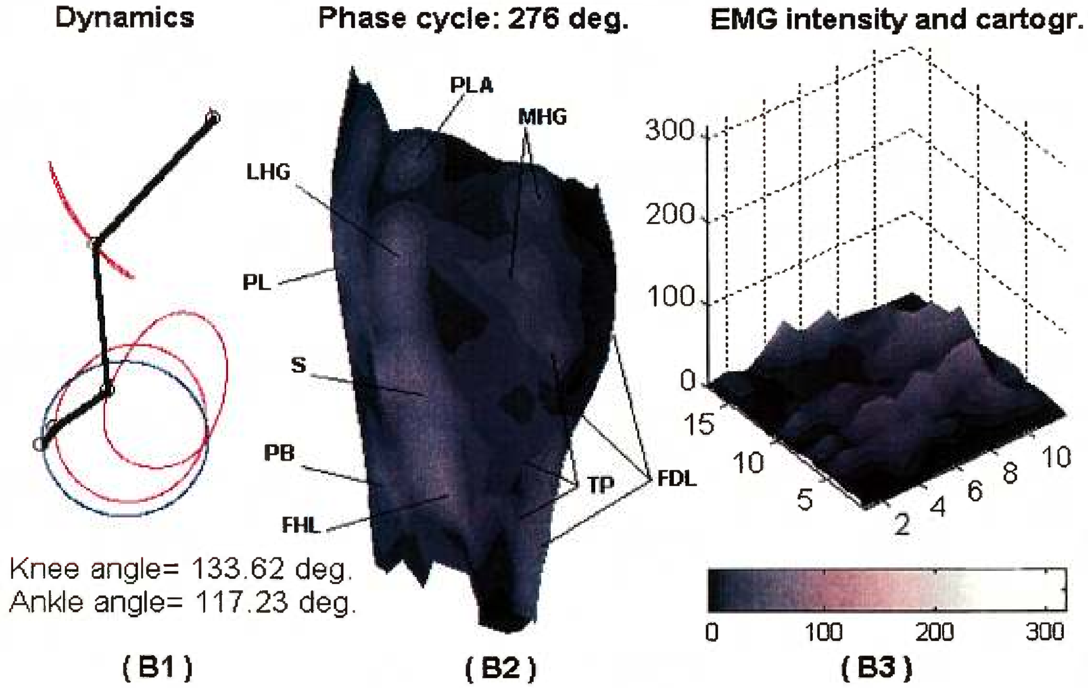

Slow Movement

Figure 5.14 Internal postero-lateral view at 276 deg. cycle phase. Active muscles identified are: plantaris (PLA); medial head of gastrocnemius (MHG); lateral head of gastrocnemius (LHG); soleus (S); tibialis posterior (TP); flexor digitorum longus (FDL); flexor hallucis longus (FHL); peroneus longus (PL) and peroneus brevis (PB).

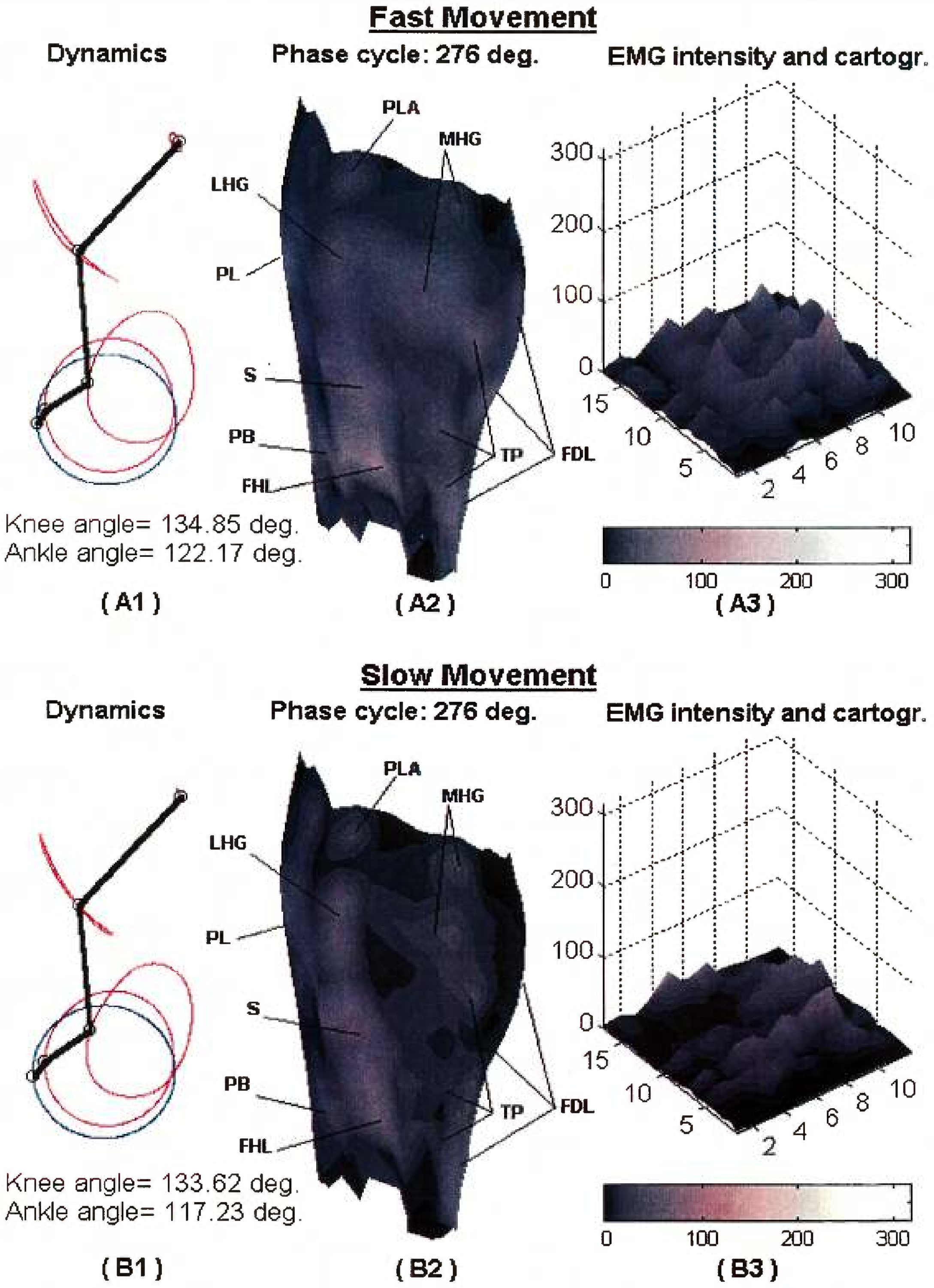

Figure 5.15 Internal postero-lateral view at 305 deg. cycle phase. Active muscles identified are: plantaris (PLA); medial head of gastrocnemius (MHG); lateral head of gastrocnemius (LHG); soleus (S); tibialis posterior (TP); flexor digitorum longus (FDL); flexor hallucis longus (FHL); peroneus longus (PL) and peroneus brevis (PB).

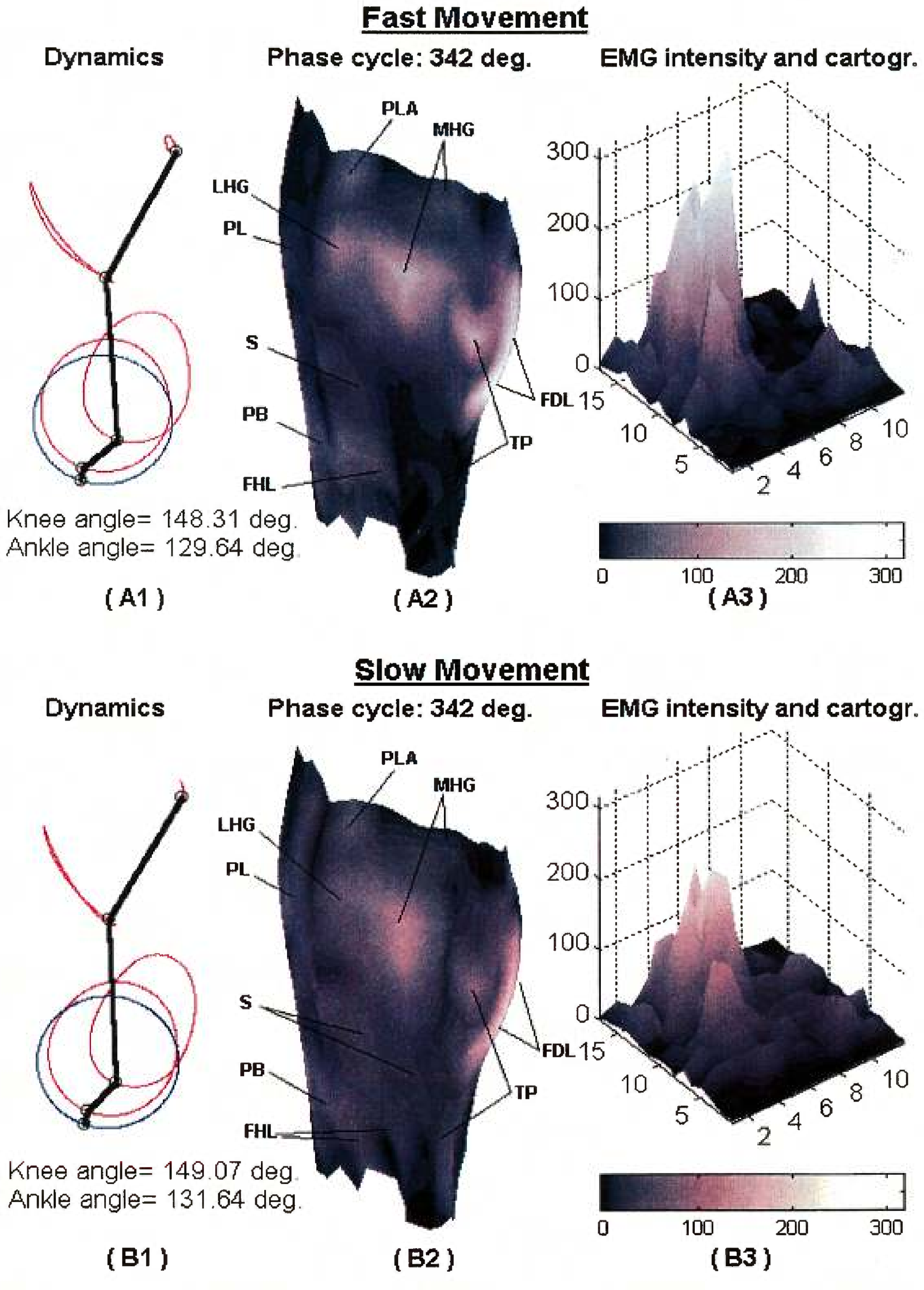

Figure 5.16 Internal postero-lateral view at 342 deg. cycle phase. Active muscles identified are: plantaris (PLA); medial head of gastrocnemius (MHG); lateral head of gastrocnemius (LHG); soleus (S); tibialis posterior (TP); flexor digitorum longus (FDL); flexor hallucis longus (FHL); peroneus longus (PL) and peroneus brevis (PB).

Additional active muscles singled out by their anatomical correlation (Figure 5.11 A3 and B3) can be identified as: peroneus longus (PL), peroneus brevis (PB); flexor hallucis longus (FHL), lateral head of gastrocnemius (LHG) and plantaris (PLA). Notice that, with exception of the FHL, these muscles are hidden on the plan view presented in Figure 5.11 A2 and B2. Identification of these muscles makes sense from a functional anatomic point of view; the active cycle phase (pedal loading) is performed with contributions from the flexor muscles of the lower leg, thus involving plantar flexion (see Figure 5.6 D, page 148). But, at 12 degrees (Figures 5.11 A1 and B1) the active cycle phase is reaching its final stage; the EMG activity from the main flexor muscles (triceps surae group, peroneus longus and brevis) has declined considerably (see Figures 5.15 and 5.16 for comparison). Here, FDL, TP, MHG, LHG, PL and PB are seen working in synergy to produce the remaining plantar flexion required to simultaneously: bring the active phase to an end and; compensate for the passive foot's dorsi flexion motion. Passive dorsi flexion is produced by the foot's angular adjustment on the revolving pedal, as can be verified by the knee and ankle joint angle changes in Figure 5.17 below.

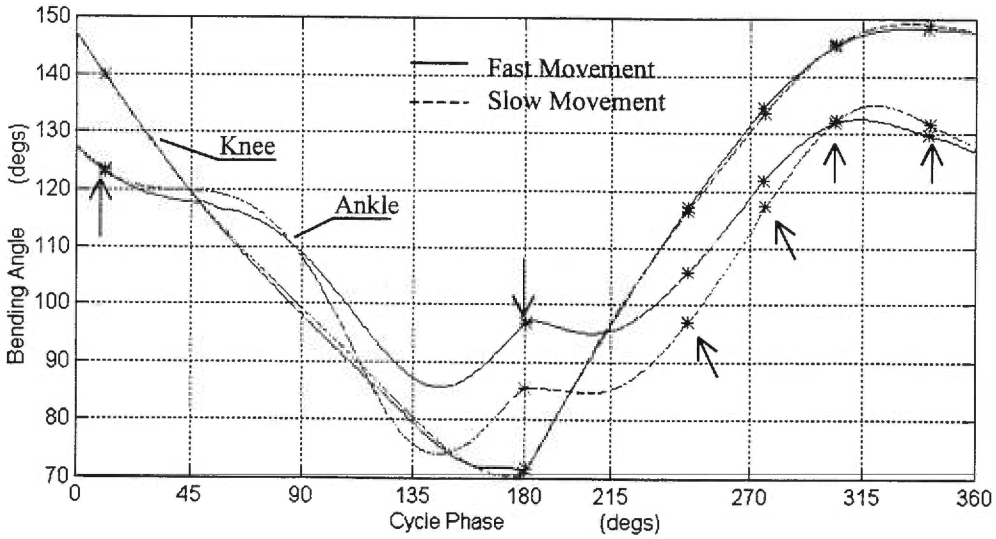

Figure 5.17 **Knee and Ankle joint angles**. Bending angle changes through one full cycle are plotted for fast (solid lines) and slow (dashed lines). Values for the chosen cycle phases (Figures 5.11 to 516) are marked (*). Notice that no significant changes are observed between fast and slow movement for the knee bending angle. Changes observed on the ankle bending angle between fast and slow movement are produced mainly by angles amplitude while the phase changes are basically the same.

On the other hand, the PL and PB act in synergy with the triceps surae and FDL to simultaneously produce plantar flexion and pronation of the foot, while the FHL and FDL together with the TP also act in synergy with the triceps surae to bring about supination of the foot, (see Figure 5.6, page 148). From these movement dynamics (Figures 5.11 A1 and B1), the knee and ankle joint angle changes (Figure 5.17), and the fact that all of these muscles are active, we can infer that at this cycle stage three simultaneous actions are taking place: active plantar flexion, passive dorsiflexion and stabilization of the ankle joint. However, these activities are carried out at different speeds with different intensities, and this explains why these muscles are activated at different intensity rates in both movements.

For fast movement, that is, we can observe less active plantar flexion (strong activity from FDL and mild activity from TP but very low activity from MHG), and therefore, little need to lock or stabilize the ankle joint in place (very low activity from FHL, PL and PB). This allows more ankle joint mobility, hence more passive dorsiflexion (faster decrease of the ankle bending angle, Figure 5.17; 12 deg. cycle phase). Conversely, for slow movement we can observe more active plantar flexion (all flexor muscles but the soleus are active), which is required to stabilize the ankle joint in place (FHL, PL and PB in co-contraction) and thus allow less passive dorsiflexion (much slower decrease of the ankle bending; Figure 5.17, 12 deg. cycle phase). In short, functional muscle anatomy and movements dynamics, both corroborate the capacity of this technique to correctly identify the action of all significant muscles.

Figure 5.12 above shows an exterior antero-lateral view of the lower leg at a cycle phase of 181 degrees. This phase of the pedal loading process, commonly known as the top dead centre (TDC), is characterized by virtually no muscle activity. However, although this holds for most lower leg muscles, we observe from Figures 5.12 A2, A3, B2 and B3 that four active muscles can be distinguished by anatomical correlation with the lighter areas: tibialis anterior (TA), extensor digitorum longus (EDL), extensor hallucis longus (EHL) and peroneus brevis (PB). The TA, EDL and EHL muscles are known to bring about dorsiflexion of the foot; conversely, PB and EDL participate in producing pronation of the foot (see Figure 5.6, page 148). This identification seems possible, since active dorsiflexion and pronation of the foot are indeed required at this stage, as can be corroborated from the knee and ankle joint angle changes depicted in Figure 5.17 above. Here we observe that, between approximately 180 to 215 degrees, the knee has reached its maximum flexing phase and the extension phase begins; the forces produced by the thigh muscles are consequently transmitted through the tibia to the foot. These forces, plus those of the TA and EHL, are effectively exerted on the inner side of the ankle joint and foot, acting to invert the foot and thus calling forth the other component of pronation -- abduction of the foot -- produced by the EDL and PB.

In short, the pedal action produces a balanced set of counter-forces; dorsiflexion and pronation of the foot compensating for the knee's position at the final flexion and commencing extension stages, while stability is maintained to transfer propulsion forces to the revolving pedal. At this particular stage (Figures 5.12 A3 and B3), only minor differences in EMG activity are observable between fast and slow movements. However, it is still possible to distinguish the spatial EMG patterns from the topographic representation of the overall muscle activity and each muscle's respective mode of activation by the distribution and intensity of EMG activity.

We come now to the cycle's active phase (pedal loading), illustrated sequentially from Figures 5.13 to 5.16 for fast and slow movements. These figures use the same lower leg's internal postero-lateral view to show progressives EMG pattern activation changes at 246, 276, 305 and 342 degrees cycle phases. Lower leg flexor muscles commonly responsible for the loading phase have been previously identified by anatomical correlation in the discussion of Figures 5.11 above. Now that we have demonstrated the technique's capability properly to identify individual active muscles, we can concentrate on its capability to describe spatio-temporal EMG pattern activation. According to Burke (1986), the pedal loading phase begins approximately 15 degrees before the TDC with the active participation of the lower leg's extensor muscles (previously discussed in Figure 5.12 above). At about 220 degrees, however, these muscles become silent and the lower leg's flexor muscle group begins to take over the pedal propulsion phase.

Figure 5.13 above illustrates the spatio-temporal EMG muscle activation patterns at the 246 degrees cycle phase; at this moment these patterns begin to make themselves visible. Notice that the same flexor muscle group is active for fast and slow movements but with distinctive EMG activation patterns (compare Figures A2 versus B2 and A3 versus B3). First, in reference to the maximum EMG activity(FHL) found at the 246 degrees cycle phase, we can observe that fast movement demanded a high activity from the S, medium activity from the LHG and a low activity from the MHG, while slow movement required a high activity from the S, a mild activity from the LHG and almost no activity from the MHG. These EMG patterns seem well described by the technique, since with the knee bent, the gastrocnemius is already shortened and thus less efficient in generating force. Under those circumstances, the LHG -- having longer fibers than the MHG -- will be solicited first while the MHG will be called into action only under a high load demand, as is the case here for fast movement. The soleus, on the other hand, has much longer fibers and is therefore more efficient in generating force while the knee is bent.

A closer look at Figures 5.13 A2 and B2 reveals that for slow movement the MHG upper fibers show substantial EMG activity, and the plantaris (PLA) a faint activity while the inverse occurs for fast movement. We know that some of the upper fibers of the MHG and the PLA arise from the capsule of the knee joint. The fact that these upper fibers are active in both muscles implies that the knee joint is in the process of stabilization. Nevertheless, fast and slow movements required different stabilization strategies, which can be explained from a functional perspective. The tibia's natural tendency to rotate inward during pedal loading produces mechanical stress at the knee joint. This triggers three primary compensation mechanisms: adduction of the thigh at the hip joint; reinforcement of the knee joint; and locking abduction of the foot on the pedal. The amount of activity required from these protection mechanisms will depend on the load applied to the joint. A combination of hip adduction and locking foot abduction reduces stress on the knee joint. These actions effectively bring the knee toward the medial plane, thus permitting the propulsion forces line up more closely along the leg's central axis and thus, reducing the lateral component forces responsible for the stress. This occurs at the same time as the leg's central axis approaches its position perpendicular to the foot's flat base on the pedal.

These observations can be verified from Figures 5.13 A1 and B1, and Figure 5.17 above. Here we observe that the trajectories of the hip point object (top) and knee point object (second from the top) show different dynamic behavior in each movement. In the case of fast movement, wider trajectories are described by the hip and knee point objects (implying more hip and knee adduction); the contrary is observed in slow movement. Knee and hip adduction plus the higher load exerted at the ankle joint demands stronger stabilization of the ankle joint, and thus allows less foot dorsiflexion (higher bending angle at the ankle, Figure 5.17). This explains why more activity can be seen in the inferior portion of the TP and PL in fast movement, and in the superior portion of these muscles in slow movement. In both movements, however, EMG activity from the FDL and PB is restricted to the minimum.

Thirty degrees later, we see that in general, muscle activity has increased in intensity while the overall EMG patterns remain much the same as previously described (see Figure 5.14; 276 cycle phase, above). This seems particularly true for fast movement, however some minor strategy adjustments can still be traced from subtle EMG pattern changes for slow movement (compare Figures 5.13 B2-B3 and 5.14 B2-B3, respectively). Here, we see that as the propulsion load is increased in slow movement a higher ankle joint stabilization is required (notice that less difference exists between the ankle bending angle of both movements, Figure 5.17); consequently, the TP EMG activity has been transferred toward the inferior portion of the muscle and the FDL has become quite active at this point, while the PL has increased its activity at a higher rate than the other muscles.

These EMG patterns, however, are considerably modified at the 305 degree cycle phase (Figure 5.15 above). Such an observation better can be appreciated from the topographic representation depicted in Figures 5.15 A3 and B3. In the case of fast movement (Figure 5.15 A2), the triceps surae group is becoming fully active while the stabilizer flexor group (FDL, TP, MHG contributing to supination and PL, PB contributing to pronation) is increasing its activity drastically, thus assisting the triceps surae to lock the foot in position and transfer a higher force to the pedal. Similar observations apply to slow movement (same ankle bending angle for both movements, Figure 5.17 above), with the difference that increases in muscle EMG intensity have been differently modulated spatially; thus the EMG activity from PB, FHL, TP and FDL has increased at a higher rate in the lower muscle portion (Figure 5.15 A3 and B3). As the loading cycle is reaching bottom dead centre (0 deg.), the intensity of muscle activation is further modulated spatially at different rate, as can be seen in Figure 5.16 above. Here we notice significant changes in the way in which the triceps surae is activated for fast movements (Figure 5.16 A2 and A3); the activity of the MHG has reached a peak while that of the LHG has remained essentially the same and of the S has considerably fallen. Similar observations apply to slow movement with exception that the S muscle (Figure 5.16 B2 and B3) is modulated quite differently – the EMG activity of fibers in the muscle's central has portion declined while that of its lateral fibers has been activated.

Further, in Figures 5.16 B2 and B3 for slow movement, we can also see EMG pattern changes from the stabilizer flexor muscles manifested in an activity redistribution; both the FDL and TP have increased their activity at a higher rate on their upper portion. Conversely, the upper portion of both the PL and PB muscles have reduced their activity at a higher rate and the lower portions at a lower rate, while the FHL has increased its activity in its lower portion. Figures 5.16 A2 and A3 for fast movement, show similarly that the FDL also has reached its peak activity and that the TP muscle has become very active in its upper portion while activity has practically disappeared from its lower portion. EMG pattern changes from the PL, PB and FHL muscles are the same as those observed for slow movement.

In conclusion, and without attempting to explain the meaning of these spatio-temporal EMG patterns in terms of the various strategies used by the CNS to execute action movements, we have succeeded in demonstrating the technique's capabilities to identify individual active muscles and to describe their global activation patterns during action development.

5.12 DISCUSSION

Data collected under constant crank load-controlled rpm of slow and rapid speed pedaling conditions permitted a comparative analysis of distinctive spatio-temporal muscle activation patterns. In general terms, we have confirmed that the main contribution of the lower leg to pedal loading is carried by the triceps surae muscle group and that the rest of the lower leg flexor muscles assist synergistically to stabilize the knee and ankle joints, thus allowing the foot to act as an efficient rigid link and transferring force to the pedal (Burke, 1986). However in particular terms, we have also found that fast and slow pedaling speed require different muscle activation strategies to generate propulsive impulse. This was confirmed in Figures 5.8 A and B, page 158, where we noticed that the ankle, knee and hip point objects described -- in both cases -- comparatively different motion trajectories. Further, in Figures 5.9 A to F, page 159 we have observed a different EMG activity in the tibialis anterior, gastrocnemius and soleus muscles through the phase sequences of one full cycle for both movements.

And finally, from Figure 5.17, page 170; we have seen that these strategies were also manifested by the ankle joint angle development changes through the course of one full cycle. In short, the evidence confirms that the CNS uses different strategies for the action development of fast and slow speed pedaling.

In fact, these observation were expected and have been explained by current findings on functional muscle anatomy and so we have just taken advantage of this knowledge to verify if similar conclusions can be drawn from the images produced by the technique. The interesting new fact for the purposes of this thesis is the internal multi-dimensional picture of the muscle activation strategy that we were able to produce. Such images have proved properly to reflect different individual and global EMG muscle activation patterns generated through the phase sequences of one cycle performance. Further, we have treated each Laplacian electrode as an independent sensor in 3-D space and arranged them in a matrix configuration, so as not to be constrained to any particular muscle or specific anatomical surface shape. This means that the technique can be used to study spatio-temporal EMG patterns from different muscle groups in the body.

Possible sources of error in these spatio-temporal images are expected to be due to interpretation of muscle spatial localization. That is, when two or more muscles are anatomically arranged in layers the image might loose resolution. Under these circumstances it might be difficult for the operator to make a proper muscle identification, particularly when two or more of these muscles are active. However, it is also expected that a well trained operator with sufficient experience will have no problem in making a discriminated identification.

5.13 GENERAL CONCLUSIONS

This research has been concerned with achieving two main objectives: consideration of the NMSS as one non-linear open system and development of a tool to study the NMSS in a multi-dimensional fashion. Two basic questions have identified at the foundations of these concerns: how does the neuro-musculo-skeletal system function normally?; and, how and why is normal function disturbed by trauma and disease? In achieving the thesis objectives, no attempt has been made to answer these questions; instead, a series of arguments has been presented and a new tool has been proposed with the intention of opening new avenues in the search for answers to these questions.

In response to the first objective, the principle of interdependence has played a very important role and has therefore been strongly emphasized. Such an interdependence has been seen to apply not only to tissues, but also to individual joints, muscles, and specific regions within the system. Moreover, the functional effectiveness of the entire NMSS has been seen as vitally important because the tasks of everyday life require a complete integration of activity within the system. Behavior of the overall NMSS system has been illustrated not only in the interdependence of its parts, but also in the trauma or disease which affects its parts and consequently the structure as a whole. This is exemplified in any number of pathologies and/or injuries, which may also affect other organ systems. Medical experts need tools that will help them to better understanding of the ways in which muscles produce effort and the effect that they might have in the overall structure. They need, also, tools that will help them to convey the understanding of the principles employed in building muscular strength or endurance, elasticity, normal tonus versus hypertension and relaxation, and numerous other performance factors related to effective action and conservation of energy.

It is from this standpoint that the second objective has been achieved: the development of a visual image to the functional and operational behavior of the NMSS. In this sense, data recorded from a two dimensional matrix of Laplacian electrodes in conjunction with video cinematic and electrodes spatial location have been used to create a 3D dynamic internal image of the multi-dimensional process involved in movement execution. In this sense, results and analysis presented in this chapter are a proof-of-concept. It has been demonstrated that is possible to produce an image depicting multidimensional features of human movement. A match between the referential SEMG activity sources and the muscles' anatomical location in the image can now be obtained without prior commitment to any muscle in particular. A spatio-temporal representation of SEMG distribution sources in a multi-dimensional format permits elucidation of individual and global modes of muscle activation patterns.

It is clear from the results presented here that not only can a movement functional programming mechanism be manifested in a spatio-temporal EMG pattern of muscle activation but also that these patterns change with the tasks. The technique, as a research tool, can be useful to establish relationships between the central nervous system, the muscular system and the skeletal system in a systemic fashion.

5.14 POSSIBLE PRACTICAL APPLICATIONS

In principle, the applications of this technique are limited only by the imagination of the user. However, it is evident that each case the technique requires a suitable representation format that will respond to the needs of the particular application. In general terms, the technique can be applied to study of any phenomena that involves NMSS behavior, normal or abnormal. Direct applications are foreseen in scientific research and clinical environments in four main areas: scientific, medical, para-medical and non-medical.

In the scientific area the technique can be used in: neurophysiological research concerning central and peripheral neural correlates of gestation and the development of voluntary movement programming, in motor control research concerning multi-muscle control and co-ordination of movement and posture, in research and development of biomechanical models closer to reality, etc.

In the medical field, the technique can be applied to any NMSS pathology that can be characterized by abnormal neuro-musculo-skeletal imbalances (idiopathic skeletal malformations, synergetic asymmetries, abnormal co-contraction, neuro-muscular perturbations, fibrillation, neuro-pathologies, etc.). Provided that a suitable representation format is developed, (i.e. easy-to-interpret-image), a wide range of applications is possible in a clinical environment: first, during the different stages of diagnosis, treatment, rehabilitation and prognosis of NMSS pathologies; second, for personalized prescription and adjustment of prostheses/ortheses according to EMG adaptation patterns of the NMSS; and third, for development of new interpretation and evaluation criteria of these diseases. This latter exercise could permit development of new protocols objectively to classify types and statuses of idiopathic conditions. Further, the technique could provide a means to monitor the evolution of the pathology by periodic spatio-temporal EMG testing and at the same time to prescribe simultaneous corrective adjustment of the treatment.

In the para-medical area, the technique can be applied in physiotherapy, particularly, in patient rehabilitation and neuro-muscular re-education. Those affected by scoliosis, lower back pain syndrome, temporal paralysis, muscle deficiencies, neuro-muscular adaptation to prosthesis and orthesis can be particularly helped. This application requires a real time visual bio-feedback system which can be readily obtained through minor modifications and adjustment of the primary 4D EMG mapping system. Re-education of the neuro-muscular system would begin by defining the patient's own functional static/dynamic equilibrium position and later proceed to modify their corresponding EMG patterns of activity to a more efficient and normal pattern.

Finally, the primary non-medical application of the technique will be in the area of sports, particularly in sport medicine diagnosis, athletic selection, control and efficiency of body strategies, analysis and improvement of muscle performance, training programming, etc.

5.15 FUTURE WORK

Projections of future work begin with the basic phase presented in this thesis; first the BCE need further experimental research. It is possible that this type of electrode could have other type of applications in neuro-muscular research; thus other than the visual representation of SEMG potential distribution in time and its graphical correlated with movement dynamics. Comparative test between the BCE and double differential electrode of similar dimensions should be performed under experimental conditions concerning noise disturbance due to skin/electrode, MU studies, etc A second phase will consist in construction of a larger number of BCEs (i.e. 64, 128, etc.) with data acquisition and interface system. This will carry the technique from its present qualitative stage to a quantitative stage. SEMG data recorded by means of a real matrix (as oppose to a "virtual" matrix) will permit the investigation to: improve the signal spatial resolution; manipulate the signal in the time and/or frequency domain; and therefore, give access to additional information concerning EMG activity source location and spatio-temporal EMG patterns. This phase can be further expanded by constructing a full three dimensional representation of the anatomical section including the muscular and skeletal structure. This can be achieved by using digitized images taken from tomographic slices.

BIBLIOGRAPHY

Andreassen S., Arendt-Nielsen L., *Muscle fiber conduction velocity in motor units of the human anterior tibial muscle: A new size principle parameter.* J. Physiol., vol. 391: 561-571, 1987.

Andreassen S., Rosenfalck A., *Relationship of intracellular and extracellular action potentials of skeletal muscle fibers.* CRC Crit. Rev. Bioeng., vol. 6: 267-306, 1981.

Aquelonious S., Askmark H., Gilbert P., Nandedkar S., Olsson Y., Stalberg E. *Topographical localization of motor endplates in cryosections of whole human muscles.* Muscle and Nerve, vol.7: 287-293, 1984.

Arendt-Nielsen L., Mills K.R. Foster A. *Changes in the muscle fiber conduction velocity, mean power frequency and mean EMG voltage during prolonged submaximal contractions.* Muscle Nerve, vol.12:493. 1989.

Balestra G., Knaflitz M., Merletti R. *Comparison between myoelectric signal mean and median frequency estimates.* Proc. Ann. Int. Conf. IEEE Med. Biol., New Orleans, LA, vol.10: 1708-1709, 1988.

Basmajian J.V., De Luca C.J. *Muscles alive: Their functions revealed by electromyography.* Fifth edition. Williams and Wilkins, Baltimore (MD) USA, 1985.

Bean J.C., Chaffin D.B., Schultz A.B. *Biomechanical model calculation of muscle contraction force: A double linear programming method.* J. Boimechanics, vol.21 (1):59-66, 1988.

Bernstein N. *The coordination and regulation of movement.* Oxford: Pergamon Press, 1967.

Bhullar H.K., Loudon G.H. Fothergill J.C. Jones N.B. *Selective noninvasive electrode to study myoelectric signals.* Med. Biol. Eng. Comput. vol.28: 581-586, 1990.

Bigland-Ritchie B. *EMG/force relations and fatigue of human voluntary contractions.* Exerc. Sports Sci. Rev., vol.12: 75-117, 1981.

Blinowska A., Verroust J. *Low frequency power spectrum of the EMG signal.* Electromyogr. Clin. Neurophysiol., vol. 27:349-353, 1987.

Bouisset S. *EMG and muscle force in normal motor activities.* In New developments in EMG and Clinical Neurophysiology, Desmedt J., Ed., Karger, Basel, p547, 1973.

Bogduk N., MacIntosh J.E., Pearcy M.J. *A universal model of the lumbar back muscles in the upright position.* Spine, vol.8: 897-913, 1992.

Brody L.R., Pollock M.T., Roy S.H., De Luca C.J. Celli B. *pH-induced effects on median frequency and conduction velocity on the myoelectric signal.* J. Appl. Physiol., vol.71:1878, 1991.

Broman H., Bilotto G., De Luca C.J. *A note on the non-invasive estimation of the muscle fiber conduction velocity.* IEEE Trans. Biomed. Eng., vol.32: 341-344, 1985a.

Broman H., Bilotto G., De Luca C.J. *Myoelectric signal conduction velocity and spectral parameters: influence of force and time.* J. Appl. Physiol., vol.8: 1428-1437, 1985b.

Burke E.R. *Science of Cycling.* Human Kinetics Publisher Inc. Champaign, Illinois. 1986.

Chang W.H., Hwang C.P. *Autoregressive model to muscle force and fatigue analysis.* Proc. 13th Annu. Int. Conf. IEEE EMBS, vol.13: 481-482,1991.

Christensen E. *Topography of terminal motor innervation in striated muscle from still born infants.* Amer. J. Phys. Med., vol.38: 65-78, 1959.

Clancy, E.A. Hogan, N. *Estimation of joint torque from the surface EMG.* Proc. 13th Annu. Int. Conf. IEEE EMBS., vol.13: 877:878, 1991.

Clancy, E.A. Hogan, N. *Single site electromyograph amplitude estimation.* IEEE Trans. Biomed Eng., vol.41 (2):159-166, 1994.

Clancy, E.A. Hogan, N. *Multiple site electromyograph amplitude estimation.* IEEE Trans. Biomed Eng., vol.42 (2): 203-211, 1995.

Cordo P.J. *Kinesthetic control of a multijoint movement sequence.* J. Neurophysiol., vol.63 (1): 161-172, 1990.

Cordo P.J., Nasher L.M. *Properties of postural adjustments associated with rapid arm movements.* J. Nurophysiol., 47:287-302, 1982.

Crenna P., Frigo C., Pedotti A. *Forward and backward axial synergies in man.* Exp. Brain Res., vol.65: 538-548, 1987.

Cunningham E.A., Hogan N. *Effects of tissue layers on the surface myoelectric signal.* Proc. IEEE Front. Eng. Health Care:3-7. 1981.

De la Barrera E.J., Milner T.E. *The effects of skinfold thickness on the selectivity of surface EMG.* EEG Clin. Neorophysiol., vol.93: 91-99, 1994.

De la Barrera E.J., Milner T.E. *A sensitive technique to optimize recording of surface EMG signal.* Proc. 13th Annu. Int. Conf. IEEE EMBS, vol.13: 837-838, 1991.

De Luca C.J. *Physiology and mathematics of myoelectric signals.* IEEE Trans. Biomed. Eng., vol.26: 313-325, 1979.

De Luca C.J. *Myoelectric manifestations of localized muscle fatigue in humans.* CRC Crit. Rev. Bioeng., vol.11: 251-279, 1984.

De Luca C.J., Noda Y., Matsuzawa I. *The effects of skin desensitization on motor unit recruitment and firing rates.* Soc. Neurosci. Abstr., 1987.

De Weerd J.P.C. *Volume conduction and electromyography.* In Current Practice of Clinical Electromyography, Ed., S.L.H. Notermans. Elsevier Science Publisher B.V.: 9-28, 1984.

Diener H.C., Horak F.B., Nasher L.M. *Influence of stimulus parameters on human postural response.* J. Neurophysiol., vol. 59:1212-1222, 1988.

Diemont B., Maranzana M., Hermens H. *Compression of EMG data.* Proc. 6th ISEK Congr., S-5-5:67, 1985

Dubowitz V., Brooke M. *Muscle biopsy: A modern approach.* Ed. Saunder. Philadelphia, PA. USA, 1973.

Duvoisin M., Convertino V., Buchanan P., Gollink P., Dudley G. *Characteristics and preliminary observations of the influence of electromyostimulation on the size and function of human skeletal muscle during 30 days of simulated micro-gravity.* Aviat. Space. Environ. Med., vol.60: 671, 1989.

Eldeman G. *Neural Darwinism.* New York: Basic Books, 1987.

Englehart K.B., Parker P.A. *Single motor unit myoelectric signal analysis with nonstationary data.* IEEE Trans. Biomed. Eng., vol.41 (2): 168-180, 1994.

Easter S.S., Purves D., Rakic P., Spitzer N. *The changing views of neural specificity.* Science, vol.230: 507-511, 1985

Fattorusso V., Thaon M., Tilmant J. *Contribution a l'etude de l'electrocardiogramme precordial.* Acta Cardiologica, vol.4: 464-487, 1949

Gath I., Stalberg E. *On the volume conduction in human skeletal muscle: In situ measurements.* Electroenceph. Clin. Neurophysiol., vol.43: 106-110, 1977.

Gath I., Stalberg E. *Measurement of the uptake area of small-size electromyographic electrodes.* IEEE Trans. Biomed. Eng., vol.26: 374-376, 1979.

Geddes L.A. Foster K.S., Reilly J., Voorthees W.D., Bourland J.D., Raghed T., Fearnot N.E. *The rectification properties of an electrode-electrolyte interface operated at high sinusoidal* *current density.* IEEE Trans. Biomed. Eng., vol.34: 669, 1987.

Geddes L.A., Baker L.E. *Principles of Applied Biomedical Instrumentation.* 3rd ed., John Wiley and Sons, New York, 1989.

Gielen F.L.H, Cruts H.E.P., Albers B.A., Boon K.L., Wallinga-de Jonge W., Boom H.B.K. *Model of electrical conductivity of skeletal muscle based on tissue structure.* Med. Biol. Eng. Comput., vol.24: 34, 1986.

Graupe D., Cline W.R. *Functional separation of EMG signals via ARMA identification methods for prosthesis control purposes.* IEEE Trans. Syst. Man. Cybern., vol.5: 252, 1975.

Griep P.A.M., Boom K.L., Stegeman D.F. *A study of the motor unit action potential by means of computer simulation.* Cybernetics, vol.30: 221-230, 1978.

Hannaford B., Lehman S. *Short time Fourier analysis of the electromyogram: Fast movements and constant contraction.* IEEE Trans. Biomed. Eng., vol.33: 1173-1181, 1986.

Hary D., Bekey G.A., Antonelli D.J. *Circuit model and simulation analysis of electromyographic signal source- I: The impedance of EMG electrodes.* IEEE Trans. Biomed. Eng., vol.34 (2): 91-96, 1987.

He B., Cohen R.J. *Body surface Laplacian ECG mapping.* IEEE Trans. Biomed. Eng., vol.39 (11): 1179-1191, 1992.

Heffetner G., Zucchini W., Jaros G.G. *The electromyogram (EMG) as a control signal for functional neuromuscular stimulation. I. Autoregressive modelling as a means of EMG signature discrimination.* IEEE Trans. Biomed. Eng., vol.35: 230, 1988.

Helal J.N., Duchene J. *A pseudoperiodic model for myoelectric signal during dynamic exercise.* IEEE Trans. Biomed. Eng., vol.36 (11): 1092-1097, 1989.

Helal J.N., Bouissou P. *The spatial integration effect of surface electrode detecting myoelectric signal.* IEEE Trans. Biomed. Eng., vol.39 (11):1161-1167, 1992.

Higgins S., *Movement as an emergent form: its structural limits.* Human Movement Science, vol. 4:119-148, 1985.

Hilton-Brown P., Stalberg E. *The motor unit in muscular dystrophy, a single fiber EMG and scanning EMG study.* J. Neurol. Neurosurg. Psychiat., vol.46: 981-995, 1983

Hjorth B. *An on-line transformation of EEC scalp potentials into orthogonal source derivations.* Electroenceph. Clin. Neurophysiol., vol.39: 526-530, 1975.

Homma S., Nakajima Y., Hayashi K. *Conduction velocity of action potentials measured from* *unidimensional latency-topography in human and frog skeletal muscle fibers.* Jpn. J. Physiol., vol.36: 15, 1986.

Hunter I.W., Kearney R.E., Jones L.A. *Estimation of the conduction velocity of muscle action potentials using phase and impulse response function techniques.* Med. Biol. Eng. Comput., vol.25: 121-126, 1987.

Inbar G.F., Noujaim A.E. *On surface EMG spectral characterization and its application to diagnostic classification.* IEEE Trans. Biomed. Eng., vol.31: 597, 1984

Inbar G.F., Allin J., Kranz H. *Surface EMG spectral changes with muscle length.* Med. Biol. Eng. Comput., vol.25: 683-689, 1987.

Ju K.H., Minamitani H. *Autoregressive spectrum analysis of EMG signals in muscle fatigue state during a quick movement.* Proc. 12th Annu. Int. Conf. IEEE EMBS, vol.12: 2210, 1990.

Kelly M.F., Parker P.A., Scott R.N. *The application of neural networks to myoelectric signal analysis: a preliminary study.* IEEE Trans. Biomed. Eng., vol.37: 221, 1990.

Knaflitz M., Merletti R., De Luca C.J., Cisari C. *Motor unit recruitment order in voluntary and electrically elicited contractions.* In Electromyographical Kinesiology,. Ed. Anderson P.A., Hobart D.J. and Danoff J.V., Eds., Elsevier, Amsterdam, 1991.

Lindstrom L. *On the frequency spectrum of EMG signals.* Ph.D. thesis, Res. Lab. Med. Electronics, Chalmers Institute of Technology, Goteborg, Swden, 1970.

Lindstrom L., Magnusson R. *Interpretation of myoelectric power spectra: A model and its applications.* Procc.IEEE, vol.65:653-662, 1977.

Lynn P.A. *Direct on-line estimation of muscle fiber conduction velocity by surface EMG.* IEEE Trans. Biomed. Eng., vol.31: 564-571, 1979.

McGill S.M., Norman R.W. *Partitioning of the L4-L5 dynamic moments into ligamentous and muscular components during lifting.* Spine, vol.11 (7): 666-777, 1986.

Merletti R., Knaflitz M., De Luca C.J. *Electrically evoked myoelectric signals.* Crit. Rev. Biomed. Eng., vol.19 (4): 293-340, 1992.

Merletti R., Lo Conte L.R. *Advances in processing of surface myoelectric signals: Part 1.* Med. Biol. Eng. Comput., vol.33: 362-372, 1995.

Merletti R., Lo Conte L.R. *Advances in processing of surface myoelectric signals: Part 2.* Med. Biol. Eng. Comput., vol.33: 373-384, 1995.

Masuda T., Sadoyama T. *Topographical map of innervation zones within single motor units measured with a grid surface electrode.* IEEE Trans. Biomed. Eng., vol.35: 623-628, 1988.

Masuda T., Miyano H., Sadoyama T. *The position of innervation zones in the biceps brachii investigated by surface electromyography.* IEEE Trans. Biomed. Eng., vol.32: 36-42, 1985.

Moritani T., Muro M. *Motor unit activity and surface electromyogram power spectrum during increasing force of contraction.* Eur. J. Appl. Physiol., vol.56: 260-265, 1987.

Muro M., Nagata A., Moritani T. *Analysis of myoelectric signals during dynamic and isometric contractions.* In Matsui H., Kobayashi K., eds. Biomechanics VII-A. Human Kinetics Publishers, III, 1983.

Naeji M., Zorn H. *Estimation of the action potential conduction velocity in human skeletal muscle using surface EMG cross-correlation technique.* Electromyography, vol.23:73-80, 1983.

Nunez P.L. *Electric field of the brain.* Oxford University Press, Oxford, 1981.

Oddsson L., Thorstensson A. *Fast voluntary trunk flexion movements in standing: motor patterns.* Acta Physiol. Scand., vol.129: 93-106, 1987.

Oddsson L., Thorstensson A. *Fast voluntary trunk flexion movements in standing: primary movements and associated postural adjustment.* Acta Physiol. Scand., vol.128: 341-349, 1986.

Okada M. *Effects of muscle length on surface EMG wave forms in isometric contractions.* Eur. J. Appl. Physiol. 56:482-486, 1987.

Paiss O., Inbar G.F. *Autoregressive modelling of surface EMG and its spectrum with application to fatigue.* IEEE Trans. Biomed. Eng., vol.34 (10): 761-770, 1987.

Papoulis A. *Probability, random variables and stochastic processes.* McGraw-Hill, New York, 1965.

Pan Z.S., Zhang Y., Parker P.A. *Motor unit power spectrum and firing rate.* Med. Biol. Eng. Comput., vol.27: 14-18, 1989.

Parker P.A., Scott R.N., Stuller J.A. *Signal processing for the multistate myoelectric channel.* IEEE Proc., vol.65: 662-674, 1977.

Parker P.A., Scott R.N., *Myoelectric control of protheses.* Crit. Rev. Biomed. Eng., vol.13: 283. 1986.

Pedersen D.R., Brand R.A., Cheng C., Arora J.S. *Direct comparison of muscle prediction using linear and nonlinear programming.* J. Biomech. Eng., vol.109: 192-199, 1987.

Perry, J., Bekey, G.A. *EMG-force relationship in skeletal muscles.* CRC Crit. Rev. Biomed. Eng., vol. 7: 1-22, 1981.

Plonsey R. *The active fiber in a volume conductor.* IEEE Trans. Biomed. Eng. BME vol.21 (5): 371-381, 1974.

Platzer W. *Locomotor system.* In Color Atlas and Textbook of Human Anatomy, vol.1, 4th edition. Thieme Medical Publishers Inc., New York, 1992

Polanyi M. *Personal knowledge: towards a post-critical philosophy.* Chicago, IL, The University of Chicago Press, 1958.

Prigogine I., Stengers, I. *Order out of chaos: Man's new dialogue with nature.* Bantam Books, Toronto, 1984.

Rababy N., Kearney R.E., Hunter I.W. *Method for EMG conduction velocity estimation which accounts for input and output noise.* Med. Biol. Eng. Comput., vol.27: 125-129, 1989.

Reed E.S. *Neural regulation of adaptive behavior. Ecological Psychology.*, vol.1: 97-118, 1989.

Reed E.S. *Changing theories of postural development.* In Development of Posture and Gait Across the Life Span. Ed. Woollacott M.H. and Shumway-Cook A., University of South Caroline Press, p3-24, 1990.

Reucher H., Silny J., Rau G. *Spatial filtering of noninvasive multielectrode EMG: Part I – Introduction to measuring technique and Applications.* IEEE Trans. Biomed. Eng., vol.34 (2): 98-105, 1987.

Reucher H., Silny J., Rau G. *Spatial filtering of noninvasive multielectrode EMG: Part II – Filter performance in theory and modelling.* IEEE Trans. Biomed. Eng., vol.34 (2): 106-113, 1987.

Rosenfalck P. *Intra- and extracellular potential fields of active nerve and muscle fibers. A physicomathematical analysis of different models.* Acta Physiol. Scand. Suppl., vol.321: 1-168, 1969.

Rothwell J. *Control of human voluntary movement.* Second edition, Ed. Chapman and Hall, New York, 1994

Roy S.H., De Luca C.J., Schneider J. *Effects of electrode location on myoelectric conduction velocity and median frequency estimates.* J. Appl. Physiol., vol.61: 1510-1517, 1986.

Sadoyama T., Masuda T., Miyano H. *Optimal conditions for the measurement of muscle fiber conduction velocity using surface electrode arrays.* Med. Biol. Eng. Comput., vol.23: 339-342, 1985.

Saitou K., Okada T., Sadoyama T., Masuda T. *Effect on surface EMG wave forms of electrode location with respect to the neuromuscular junctions: Its significance in EMG-muscle length relation.* In Electromyographical Kinesiology. Ed. P.A. Anderson, D.J. Hobart and J.V. Danoff. Elsevier Science Publisher B.V., p27-30, 1991.

Schneider J., Rau G., Silny J. *A noninvasive EMG technique for investigating the excitation propagation in single motor units.* Electromyogr. Clin. Neurophysiol., vol.29: 273-280, 1989.

Schneider J., Silny J., Rau G. *Influence of tissue inhomogeneities on noninvasive muscle fiber conduction velocity measurements: Investigated by physical and numerical modelling.* IEEE Trans. Biomed. Eng., vol38: 851-860, 1991.

Sheriff M.H., Gregor R.J. *Modelling myoelectric interference patterns during mvement.* Med. Biol. Eng. Comput., vol.24: 2, 1986.

Sherrington, C.S., *The integrative action of the nervous system*, New Haven: Yale University Press. 1906

Sollie G., Hermaens H.J., Boon K.L., Wallinga W., Zilvold G. *The boundary condition for measuremnt of the conduction velocity of muscle fibers with surface EMG.* Electroenceph. Clin. Neurophysiol. vol.25: 45-56, 1985a.

Sollie G., Hermaens H.J., Boon K.L., Wallinga W., Zilvold G. *The measurement of the conduction velocity of muscle fibers with surface EMG according to the cross-correlation method.* Electroenceph. Clin. Neurophysiol. vol.25:193-204, 1985b.

Solomonow, M., Baratta, R., Zho, B.H., Shoji, H., D'Ambrosia, D., *The EMG-force model of electrically stimulated muscle: Dependence on control strategy and predominant fiber composition.* IEEE Transc. Biomed. Eng., vol.34: 692-702, 1987.

Solomonow M., Baten C., Smit J., Baratta R., Hermens H., D'Ambrosia R., Shoji H. *Electromyogram power spectra frequencies associated with motor unit recruitment strategies.* J. Appl. Physiol., vol.68: 1177-1185, 1990.

Stalberg E. *Propagation velocity in human muscle fibers in situ.* Acta Physiol. Scand., Suppl. 287: 1-112, 1966.

Stalberg E.V., Antoni L. *Electrophysiological cross section of the motor unit.* J. Neurol. Neurosurg. Psychiat., vol.43: 469-474, 1980.

Stokes, I.A.F., Rush, S., Moffroid, M., Johnson, G.B., Haugh, L.D. *Trunk extensor EMG-torque relationship.* Spine, vol.12: 770-776, 1987.

Stulen F.B., De Luca C.J. *Frequency parameters of the myoelectric signal as a measure of conduction velocity.* IEEE Trans. Biomed. Eng., vol.28: 515-523, 1981.

Van Eijden, T.M., Brugman, W., Weijs, W.A., Oosting, J., *Coactivation of jaw muscles: Recruitment order and levels as function of bite force direction and magnitude.* J. Biomechanics, vol.23 (5): 475-485, 1990.

Van Boxtel A., Goudswaard P., Schomaker L.R.B. *Amplitude and bandwidth of the frontalis surface EMG: effects of electrode parameters.* Psychophysiology, vol.21: 699, 1984.

Van Oosterom A., Strackee J. *Computing the lead field of electrodes with axial asymmetry.* Med. Biol. Eng. Comput., vol.21: 437-481, 1983.

Vitasalo J.T., Luhtanen P., Rahkila P., Rusko H. *Electromyographic activity related to aerobic and anaerobic threshold in ergometer bicycling.* Acta Physiol. Scand., vol.124: 287-291. 1985.

Winter, D. *Concerning the scientific basis for the diagnosis of pathological gait and for rehabilitation protocols.* Physiotherapy Canada, vol.37:245-252, 1985.

Woods, J.J., Bigland-Ritchie B., *Linear and non-linear surface EMG-force relationships in human muscles. An anatomical/functional argument for the existence of both.* Am. J. Phys. Med., vol.62: 287-299, 1983.

Xion F.G., Shwedyk E., *Some aspects of nonstationary myoelectric signal processing.* IEEE Trans. Biomed. Eng., vol.34: 166, 1987.

Yamada M., Kumagai K., Uchiyama A. *The distribution pattern of motor unit action potentials studied by multi-channel surface EMG.* Electroenceph. Clin. Neurophysiol., vol.67: 395-401, 1987.

Zajac, F., *Muscle coordination of movement: a perspective.* J. Biomechanics (26) Supp. 1:109-124, 1993.

Zuk, T., *The role of spinal and abdominal muscles in the pathogenesis of scoliosis.* J. Bone Joint Surg. 44:102-105, 1962.

APPENDIX

SURFACE ELECTRODE TRANSFER FUNCTIONS

In this Appendix, the surface transfer function calculation is detailed for monopolar, bipolar, double differential and bipolar concentric electrodes.

A.1 Monopolar Electrode

From Equation (3.5), the transfer function for a monopolar electrode is defined by:

$$H_m(d,f) = \frac{2}{S}\int_{\rho=0}^{d/2} \rho\left[\int_{\theta=0}^{\pi} e^{j2\pi f\rho\cos\theta/v}\,d\theta\right]d\rho \qquad \text{(A1)}$$

First, let's calculate the inside angular integral:

$$I = \int_{\theta=0}^{\pi} e^{j2\pi f\rho\cos\theta/v}\,d\theta \qquad \text{(A2)}$$

Let's make,

$$\chi = \frac{2\pi f\rho}{v} \qquad \text{(A3)}$$

And by using the Jacobi series development, we have:

$$e^{j\chi\sin\theta} = \sum_{n=-\infty}^{+\infty} J_n(\chi)e^{jn\theta} \qquad \text{(A4)}$$

where $J_n(\chi)$ is the *n*th-order Bessel function of the first kind.

Now let's replace (A3) into (A2), rearrange and use the development (A4) , the integral *I* becomes:

$$I = \int_0^{\pi} e^{j\chi\cos\theta}\,d\theta = \int_{-\pi/2}^{\pi/2} e^{j\chi\sin\beta}\,d\beta = \sum_{n=-\infty}^{+\infty} c(n)J_n(\chi) \qquad \text{(A5)}$$

where

$$c(n) = \int_{-\pi/2}^{\pi/2} e^{j\chi \sin\beta}\, d\beta$$

then, solving *c(n)* as follows:

for $n = 0$: $\quad c(0) = \pi$

and for $n \neq 0$:

$$c(n) = \left[\frac{e^{jn\beta}}{jn}\right]_{-\pi/2}^{\pi/2} = \frac{(j)^n - (-j)^n}{jn}$$

or for $p \neq 0$:

$$c(2p) = 0$$

$$c(2p+1) = (-1)^p \frac{2}{2p+1}$$

Thus, separating zero, positive and negative index terms, I becomes:

$$I = \pi J_0(\chi) + \sum_{p=-\infty}^{+\infty} (-1)^p \frac{2}{2p+1} J_{2p+1}(\chi)$$

$$= \pi J_0(\chi) + \sum_{p=-1}^{-\infty} (-1)^p \frac{2}{2p+1} J_{2p+1}(\chi) + \sum_{p=0}^{+\infty} (-1)^p \frac{2}{2p+1} J_{2p+1}(\chi)$$

Now let $l = 1 - p$ in the negative index summation, I becomes:

$$I = \pi J_0(\chi) + \sum_{l=0}^{+\infty} (-1)^{l+1} \frac{2}{-(2l+1)} J_{-(2l+1)}(\chi) + \sum_{p=0}^{+\infty} (-1)^p \frac{2}{2p+1} J_{2p+1}(\chi)$$

and using the Bessel function property

$$J_{-n}(\chi) = (-1)^n J_n(\chi)$$

I is reduced to

$$I = \pi J_0(\chi) = \pi J_0(2\pi\rho f/v)$$

Now, substituting I in (A.1) we have the transfer function expression as:

$$H_m(d,f) = \frac{2\pi}{S} \int_{\rho=0}^{d/2} \rho J_0(2\pi\rho f/v) d\rho$$

Now, defining a new variable λ as

$$\lambda = \frac{2\pi\rho f}{v}$$

$H_m(d,f)$ becomes:

$$H_m(d,f) = \frac{2v^2}{\pi^2 f^2 d_0^2} \int_0^{\pi fd/v} \lambda J_0(\lambda) d\lambda$$

and solving

$$H_m(d,f) = \frac{2v^2}{\pi^2 f^2 d_0^2} \left[\lambda J_1(\lambda)\right]_{\lambda=0}^{\lambda=\pi fd/v}$$

and finally

$$H_m(d,f) = 2\frac{J_1(\pi fd/v)}{\pi fd/v} \tag{A5}$$

A.2 Bipolar Electrode

From Equation (3.7), the bipolar electrode transfer function is defined by:

$$H_b(d,f,h) = \frac{2}{S_1} \int_{\rho=0}^{d/2} \int_{\theta=0}^{\pi} e^{j2\pi f(-h/2+\rho\cos\theta)/v} \rho d\rho d\theta$$

$$- \frac{2}{S_2} \int_{\rho=0}^{d/2} \int_{\theta=0}^{\pi} e^{j2\pi f(h/2+\rho\cos\theta)/v} \rho d\rho d\theta \tag{A6}$$

which can be rearranged as:

$$H_b(d,f,h) = \frac{2}{S_1} \int_{\rho=0}^{d/2} \int_{\theta=0}^{\pi} \frac{e^{j2\pi f\rho\cos\theta/v}}{e^{j\pi fh/v}} \rho d\rho d\theta$$

$$- \frac{2}{S_2} \int_{\rho=0}^{d/2} \int_{\theta=0}^{\pi} e^{j\pi fh/v} e^{j2\pi f\rho\cos\theta/v} \rho d\rho d\theta \tag{A7}$$

and since $S_1=S_2=S$ and the term $e^{j\pi fh/v}$ can be considered independent from the integral development, then equation (A7) becomes:

$$H_b(d,f,h)=\left[\frac{1-e^{j\pi fh/v}}{e^{j\pi fh/v}}\right]\left\{\frac{2}{S}\int_{\rho=0}^{d/2}\rho\left[\int_{\theta=0}^{\pi}e^{j2\pi f\rho\cos\theta/v}d\theta\right]d\rho\right\} \qquad \text{(A8)}$$

and since the second term in equation (A8) corresponds to equation (A1), therefore it becomes:

$$H_b(d,f,h)=\left[\frac{1-e^{j\pi fh/v}}{e^{j\pi fh/v}}\right]2\frac{J_1(\pi fd/v)}{\pi fd/v} \qquad \text{(A9)}$$

A.3 Double Differential Electrode

From Equation (3.9), the double differential surface electrode transfer function is defined by:

$$\begin{aligned}H_{dd}(d,f,h)=&\frac{2}{S_2}\int_{\rho=0}^{d/2}\int_{\theta=0}^{\pi}e^{j2\pi f(-h+\rho\cos\theta)/v}\rho d\rho d\theta\\&+\frac{2}{S_3}\int_{\rho=0}^{d/2}\int_{\theta=0}^{\pi}e^{j2\pi f(h+\rho\cos\theta)/v}\rho d\rho d\theta\\&-2\frac{2}{S_1}\int_{\rho=0}^{d/2}\int_{\theta=0}^{\pi}e^{j2\pi f\rho\cos\theta/v}\rho d\rho d\theta \qquad \text{(A10)}\end{aligned}$$

which can be rearranged as:

$$\begin{aligned}H_{dd}(d,f,h)=&\frac{2}{S_2}\int_{\rho=0}^{d/2}\int_{\theta=0}^{\pi}\frac{e^{j2\pi f\rho\cos\theta/v}}{e^{j2\pi fh/v}}\rho d\rho d\theta\\&+\frac{2}{S_3}\int_{\rho=0}^{d/2}\int_{\theta=0}^{\pi}e^{j2\pi fh/v}e^{j2\pi f\rho\cos\theta/v}\rho d\rho d\theta\\&-2\frac{2}{S_1}\int_{\rho=0}^{d/2}\int_{\theta=0}^{\pi}e^{j2\pi f\rho\cos\theta/v}\rho d\rho d\theta \qquad \text{(A11)}\end{aligned}$$

and since $S_1=S_2=S_3=S$ and the term $e^{j2\pi fh/v}$ can be considered independent from the integral development, then equation (A11) becomes:

$$H_{dd}(d,f,h)=\left[\frac{1+e^{j4\pi fh/v}-2e^{j2\pi fh/v}}{e^{j2\pi fh/v}}\right]$$

$$\times\left\{\frac{2}{S}\int_{\rho=0}^{d/2}\rho\left[\int_{\theta=0}^{\pi}e^{j2\pi f\rho\cos\theta/v}\,d\theta\right]d\rho\right\} \qquad \text{(A12)}$$

and again since the second term in equation (A12) corresponds to equation (A1), therefore it becomes:

$$H_{dd}(d,f,h)=\left[\frac{1+e^{j4\pi fh/v}-2e^{j2\pi fh/v}}{e^{j2\pi fh/v}}\right]2\frac{J_1(\pi fd/v)}{\pi fd/v} \qquad \text{(A13)}$$

A.4 Bipolar Concentric Electrodes

From Equation (3.11), the transfer function for concentric electrodes is defined as:

$$H_c(d,f,h,e)=\frac{2}{S_2}\int_{\rho=d_1/2}^{d_2/2}\int_{\theta=0}^{\pi}e^{j2\pi f\rho\cos\theta/v}\rho\,d\rho\,d\theta$$

$$-\frac{2}{S_1}\int_{\rho=0}^{d/2}\int_{\theta=0}^{\pi}e^{j2\pi f\rho\cos\theta/v}\rho\,d\rho\,d\theta \qquad \text{(A14)}$$

Again both terms of the Equation can be solve in a similar manner as Equation (A1), just the limits of the first integral is different, as well as the areas S_1 and S_2. Therefore Equation (A14) can be resolved as:

$$H_c(d,f,h,e)=\frac{2d_2}{\pi f(d_2^2-d_1^2)/v}J_1(\pi fd_2/v)-\frac{2d_1}{\pi f(d_2^2-d_1^2)/v}J_1(\pi fd_1/v)$$

$$-\frac{2}{\pi fd/v}J_1(\pi fd/v) \qquad \text{(A15)}$$

but, d_2=2h+e and d_1=2h-e, so replacing d_2 and d_1 into (A15) we have:

$$H_c(d,f,h,e) = \frac{2h+e}{4\pi fhe/v} J_1\left(\pi f(2h+e)/v\right) - \frac{2h-e}{4\pi fhe/v} J_1\left(\pi f(2h-e)/v\right)$$

$$- \frac{2}{\pi fd/v} J_1\left(\pi fd/v\right) \tag{A16}$$